Solid Solution Tetrelides and Pnictides for Thermoelectric Applications

by

Daniel Ramirez

A thesis

presented to the University of Waterloo

in fulfillment of the

thesis requirement for the degree of

Doctor of Philosophy

in

Chemistry

Waterloo, Ontario, Canada, 2023

Examining Committee Membership

The following served on the Examining Committee for this thesis. The decision of the Examining Committee is by majority vote.

External Examiner	Arthur Mar Professor (University of Alberta)
Supervisor	Holger Kleinke Professor (University of Waterloo)
Internal Members	Linda Nazar Professor (University of Waterloo) Dmitry Soldatov Professor (University of Guelph)
Internal-external Member	William Wong Professor (University of Waterloo)

Author's Declaration

I hereby declare that I am the sole author of this thesis. This is a true copy of the thesis, including any required final revisions, as accepted by my examiners.

I understand that my thesis may be made electronically available to the public.

Abstract

Recent major advancements in thermoelectric material performance center around the development and understanding of band structure engineering techniques and phonon scattering mechanisms. Solid solution materials have the potential to access these major strategies simultaneously within a single system. In this thesis, solid solutions of tetrels (C, Si, Ge, Sn, and Pb) and pnictogens (N, P, As, Sb, and Bi) as thermoelectric materials are explored. Electronic structures are examined to understand established materials and propose band engineering strategies. New synthesis approaches for established materials are designed while established methods are utilized to synthesize novel solid solutions. Thermoelectric properties are measured and discussed in terms of the underlying chemistry of the materials. Future work is proposed for the systems studied where improvements can be suggested.

Chapter 1 discusses the various principles and strategies underlying the design and application of thermoelectric materials with a focus on solid solution materials. An overview of current high-performance materials and the principles which provide their status is presented. Finally, the classes of materials which are experimentally studied are discussed to provide background and motivation for the research conducted. Chapter 2 reviews the principles and practices for the experimental methods and instrumentation utilized throughout the course of this study.

The first solid solution material focused on in Chapter 3 is the tetrelide $Mg_2Si_{0.3}Sn_{0.67}Bi_{0.03}$; a high performance, nontoxic, and inexpensive thermoelectric material. A scaled-up reaction process was developed providing the first steps towards large scale applications. Large, condensed pieces of material were pressed on a scale which had not been achieved previously. Statistical analysis of measured thermoelectric properties is performed on the material using samples cut at various positions and orientations. Over 1 kg of material was prepared which displayed a zT_{max} above 1.2 reliably. These methods are used to assure a consistent quality of the process and material which is the first step towards establishing device applications.

Pnictide-tetrel chalcopyrite solid solutions are investigated in Chapters 4 and 5, with $ZnGe_{1-x}Sn_xP_2$ explored in the former, while $ZnSnP_{2-y}As_y$ and $ZnGe_{1-x}Sn_xP_{2-y}As_y$ are explored in the latter. A robust synthesis method for end members and solid solutions was developed using ball milling techniques followed by hot pressing. Successful synthesis and full miscibility of end members and solid

solutions are confirmed with powder X-ray diffraction followed by Rietveld refinements. The synthesis method is primarily discussed in Chapter 4 which is further developed for synthesis of higher order solid solutions in Chapter 5. The methods developed provide a useful tool for low temperature synthesis of solid solutions with differently melting and difficult to synthesize end members.

Structural investigations conducted on resulting $ZnGe_{1-x}Sn_xP_2$ (x = 0, 0.25, 0.5, 0.75, and 1), show a tendency for tetragonality ($c/(2a) = 1$) which maintained high Seebeck coefficients for the Sn rich and equal substituted members. Electronic structure calculations with Boltzmann transport analysis and experimental lattice thermal conductivities were used to predict thermoelectric performance. Doping $ZnSnP_2$ with p-type carriers was predicted to give zT = 1 at 0.002 carriers per formula unit and 900 K (such as with $ZnSn_{0.998}In_{0.002}P_2$), and 1.3 at 0.007 carriers per formula unit. Measured thermoelectric performance was most improved by decreased thermal conductivity due to alloy phonon scattering at equal Ge and Sn substitution (x = 0.5) while maintaining a large Seebeck coefficient. The end members displayed thermal conductivity of 4.4 W m^{-1} K^{-1} and 2.5 W m^{-1} K^{-1} for Ge and Sn respectively which decreased to 1.8 W m^{-1} K^{-1} for x = 0.5 at 875 K. Improvements from zT = $3.9 \cdot 10^{-4}$ and $2.0 \cdot 10^{-3}$ for Ge and Sn end members respectively were achieved to zT = $5.5 \cdot 10^{-3}$ for x = 0.5 at 800 K while increased thermal stability allowed greater performance at higher temperatures.

Chapter 5 focuses on improving the carrier concentration of $ZnSnP_2$ and $ZnGe_{1-x}Sn_xP_2$ by substitution of As for P. The first half of the chapter explores $ZnSnP_{2-y}As_y$ substitutions (y = 0, 0.5, 1, 1.5, and 2) where full miscibility of the solid solutions is achieved. The measured electrical conductivity shows exponential increase with As substitution from 0.03 S cm^{-1} for $ZnSnP_2$ to 10.3 S cm^{-1} for $ZnSnAs_2$ at 715 K. Band gaps as calculated from the activation energies showed a steady decrease with increasing As concentration from 1.4 eV for $ZnSnP_2$ to 0.7 eV for $ZnSnAs_2$. The Seebeck coefficient decreases significantly with As substitution from nearly 1000 μV K^{-1} for the P end member to -100 μV K^{-1} for the As end member at 650 K. Indications of bipolar conductivity are seen starting with the $ZnSnP_{0.5}As_{1.5}$ member which decreases down to 100 μV K^{-1} at 650 K. Thermal conductivity is decreased due to alloy phonon scattering with y = 1 and y = 0.5 showing the lowest values of 1.4 W m^{-1} K^{-1} at 825 K. Figure of merit values are increased at lower temperatures when compared to the $ZnGe_{1-x}Sn_xP_2$ series due to increased electrical conductivity, with y = 1 reaching zT = $2.1 \cdot 10^{-3}$ and y = 2 reaching $2.8 \cdot 10^{-3}$ at 700 K. The $ZnSnP_{2-y}As_y$ series displayed lower thermal stability and therefore overall lower figures of merit were found.

The higher order quinary solid solutions $ZnGe_{1-x}Sn_xP_{2-y}As_y$ (x = 0.5, 0.75, and y = 0, 0.5, 1, 1.5, and 2) are also studied in Chapter 5. Successful synthesis and structural refinements of the solid solutions were performed with a preference for tetragonality again observed. The alloy phonon scattering effect shows additive behavior which decreased the thermal conductivity further to 0.8 W m^{-1} K^{-1} at 775 K for x = 0.75, y = 1 to within the glasslike regime. Transport properties for the x = 0.5 (y = 0, 0.5, 1.5, and 2) series were measured which showed significant improvements compared to properties obtained for quaternary series. Large Seebeck coefficients were maintained despite exponential increase of electrical conductivities with increasing As substitution displaying characteristics similar to high entropy alloys. For $ZnGe_{0.5}Sn_{0.5}P_{0.5}As_{1.5}$ electrical conductivity increases from 0.02 S cm^{-1} to 2 S cm^{-1} while Seebeck coefficient also increases from 500 μV K^{-1} to 575 μV K^{-1} between 325 K and 775 K. The resulting thermoelectric performance of $ZnGe_{0.5}Sn_{0.5}P_{0.5}As_{1.5}$, zT = 0.038, is increased by more than 30-fold of the highest performing end member $ZnSnAs_2$ with greater thermal stability.

The final solid solutions explored are the pnictides $Ca_{11}Sb_{10-x}Bi_x$ and $Ca_{11}Sb_{10-y}As_y$ series in Chapter 6. A direct liquid solid synthesis method is performed which succeeds for many attempted samples while some contained elemental impurities. Single crystals of $Ca_{11}Sb_{10-x}Bi_x$ were obtained and structures solved which display coloring substitution effects. A correlation parameter using electronic structure calculations was developed which predicted the substitution effects well. The highest thermoelectric performance was found for $Ca_{11}Sb_{10}$, with zT = 0.093 at 1000 K, which showed improvement compared to other literature studies of the compound. Evidence of intrastructural suppression of bipolar conductivity is observed resulting in simultaneous increase in Seebeck coefficient and electrical conductivity with increasing temperatures. Bi substitution tended to increase electrical conductivity while decreasing the Seebeck coefficient due to increasing bipolar conductivity. Low thermal conductivity values were measured for all samples with the lowest $Ca_{11}Sb_{10}$ displayed phonon glass electron crystal like behavior of 0.6 W m^{-1} K^{-1} to 0.7 W m^{-1} K^{-1} at 300 K and 1050 K respectively.

Acknowledgements

When I begin forgetting why I am here, I think back to the path that came before, it’s clear yet winding, and often I remember feeling lost along the way but never alone. This is dedicated to all the people I have found along my path and to those who have found me along theirs.

Thank you to my committee members Prof. Linda Nazar, Prof. Pavle Radovanovic, and Prof. Dmitry Soldatov for the ever-important criticism, discussion, and advice. Special thanks to Professor Holger Kleinke for being patient, insightful, and encouraging throughout this endeavor. Thank you to my lab colleagues for stimulating discussions and always being willing to help and work on problems together: Dr. Leilane Macario, Dr. Parisa Jafarzadeh, Dr. Yixuan Shi, Dr. Cheryl Sturm, Luke Menezes, Andrew Golabek, and Xiaoyu Cheng. I had the great opportunity to work directly with some bright undergraduate researchers: Cathy Gao, Raman Sud, and Tony Shi. Thank you to Dr. Jalil Assoud for great insights, discussion, encouragement, and collaboration. Catherine Van Esch for making this process as smooth as possible.

A final thanks to my family for helping me become the person I am. I’d like to thank my mother Cindy for showing me what true strength is, and my father Gregorio for constant and kind support. My siblings Joline, Benjamin, Raymond, and Kevin; thanks for helping keep my head on straight and helping me remember where we came from. San My, Boi, and Thu; you were angels in my greatest time of need, thank you.

Table of Contents

List of Figures

List of Tables

Nomenclature

Symbol	**Description**
a	Unit cell parameter
A	Absorption factor
a_i, b_i, c	Atom/ion specific interaction constants
B	Material quality factor
C_p	Heat capacity
d	Density
d_{hkl}	Distance between crystal planes
D_l	Size at grinding limit
D_t/D_0	Normalized median size
E	Energy
e	Electron charge
E_{elec}	Total electron energy
E_F	Fermi level
E_{gap}	Band gap energy
E_i	Total energy added to material
E_{XC}^{GGA}	Energy functional with XC and GGA approximations
E_{XC}^{LDA}	Energy functional with XC and LDA approximations
f	Fermi-Dirac probability
$f(Q)$	Atomic form factor
f_0	Fermi-Dirac integral
F_{hkl}	Structure factor

f_k	Quantum state populations
g	Density of states
G	Stiffness constant
G_{con}, G_{val}	Density of conduction/valence bands
G_D, G_A	Density of donor/acceptor states
h	Planck constant
H	Grain boundary periodicity
$\hbar$	Reduced Planck constant
$\widehat{H}_{elec}$	Electronic Hamiltonian
I	Electrical current
I_{hkl}	Reflected intensity
$\boldsymbol{J}$	Electrical current of charge carriers
$\boldsymbol{k}$	Wave vector
K	Shorthand for Miller indices (*h k l*)
k_B	Boltzmann constant
K_p	Milling grinding rate
L	Length
L	Lorenz number
l	Sample thickness
L_K	Lorenz polarization factor
M	Device resistance factor
m	Mass
m^*	Effective mass

M_a	Average molar mass
M_A	Atomic mass
m_{DOS}^*	Density of states effective mass
m_I^*	Inertial effective mass
m_p	Specific energy imparted on mass of material
N	Number of electronic states
n	Number of particles
N_A	Avogadro’s number
N_S	Number of electronic states per unit volume
N_V	Valley degeneracy
n_x, n_y, n_z	Quantum numbers
P	Electrical power
P_K	Preferred orientation factor
Q	Heat
q	Particle charge
$\boldsymbol{Q}$	Scattering vector
$\dot{Q}$	Heat flow
R	Electrical resistance
r	Radius
$\boldsymbol{r}$	Particle position
$\boldsymbol{R}$	Direct lattice vector
R_g	Ideal gas constant
R_n	Radius of quantum number space

R_p	Profile residual (reliability factor)
R_{wp}	Weighted profile residual
S	Seebeck coefficient
S	Entropy
s	Scale factor
S_R	Star function for reduced Fermi level
$\overline{SE}$	Average stress energy
SE_j	Stress energy
T	Temperature
$\hat{T}$	kinetic energy
$t_{0.5}$	Half-time
u_{nk}	Periodic potential
V	Voltage
$\hat{V}$	one-body potential energy
$\bar{V}$	Average volume
$\hat{V}_{ee}$	electron-electron repulsion energy
$\vec{v}_{\boldsymbol{k}}$	Group velocity
V_1	One body term
V_c	Unit cell volume
v_j	Impact velocity of colliding bodies
w_i	Statistical weight factor
y_{bi}	Background intensities
y_{ci}	Calculated peak intensities

y_i	X-ray data intensity
Z	Number of formulae per unit cell
zT	Thermoelectric figure of merit
zT_{max}	Maximum achievable figure of merit
α	Thermal diffusivity
$\mathit{\Gamma}$	Point defect scattering factor
γ	Grüneisen parameter
$\mathit{\Delta} SF_j$	Frequency of stress events
ϵ	Reduced energy
ε	Reduced Fermi level
ζ	Distance between grain boundaries
η	Efficiency
θ	X-ray incident/diffracted angle
$\dot{\theta}$	Entropy per charge carrier
θ_D	Debye temperature
κ	Thermal conductivity
κ_{ele}	Electronic thermal conductivity
κ_{lat}	Lattice thermal conductivity
λ	X-ray wavelength
$\mathit{\Lambda}$	Point group rotations
μ	Carrier mobility
$\boldsymbol{\mu}$	Chemical potential
μ_0	Carrier mobility using m_I^*

ν	Phonon wave velocity
ξ	Atomic binding force
Π	Peltier Coefficient
ρ	Electron density
σ	Electrical conductivity
$\sigma_{E,\mu,\nu}$	Mott conductivity
σ_{E_0}	Transport coefficient
$\sigma_{\mu,\nu}$	Energy independent conductivity
τ	Scattering time
τ_0	Average carrier scattering time
T_0	Reduced scattering time
τ_{ph}	Phonon scattering relaxation time
υ	Phonon velocity
Φ	Electrical potential
Φ	Minimization function
ϕ	Multiplicity factor
χ	Goodness of fit
Ψ_{elec}	Electronic wave function
ψ_{nk}	Wave function
ω	Phonon frequency
ω_d	Milling disk rotation frequency
ω_r	Milling jar rotation frequency

Abbreviation	**Meaning**
AOP	Atomic orbital population
BJ	Becke-Johnson
BS	Band structure
CBM	Conduction band minimum
COHP	Crystal orbital Hamilton population
COOP	Crystal orbital overlap populations
CTE	Coefficient of thermal expansion
DFT	Density functional theory
DOS	Density of States
EDAX	Energy dispersive X-ray analysis
GGA	Generalized gradient approximation
GSAS	General structure analysis system
HEA	High entropy alloys
IR	Infrared
LAPW	Linearized augmented plane wave
LDA	Local density approximation
PBE	Perdew-Burke-Ernzerhof
PDOS	Partial density of states
PF	Power factor
PFU	Per formula unit
PGEC	Phonon glass electron crystal
PXRD	Powder X-ray diffraction

SCF	Self consistent field
SCXRD	Single crystal X-ray diffraction
SEM	Scanning electron microscopy
SPB	Single parabolic band
SPS	Spark plasma sintering
TB-mBJ	Tran-Blaha modified Becke-Johnson
TC	Thermal conductivity
TE	Thermoelectric
UC	Unit cell
VBM	Valence band maximum
VEC	Valence electron count

Chapter 1: Introduction

This chapter intends to provide a comprehensive overview of the scientific principles contained within this body of work. Solid state chemistry, material science, and physics are the main fields of study contained within this thesis. Thermoelectric materials are the more specific research topic with a focus on synthesis, applications, investigation of properties, optimization, and calculations. Even more specifically, this work focuses on the development of solid solution materials and synthetic methods for thermoelectric applications. A review of the anti-fluorite Mg_2Si, chalcopyrite, and more obscure $Ca_{11}Sb_{10}$-type thermoelectric materials previews the experimental studies contained within this thesis.

1.1 The Thermoelectric Effect History and Applications

In simple terms thermoelectric effects describe the movement of electronic charge carriers in conjunction with movement of heat. Materials which display thermoelectric properties can be used for direct conversion of heat into electricity and vice versa. The thermoelectric phenomenon was first identified in 1794 by Alessandro Volta and again in 1821 by Thomas Johann Seebeck who described what we know today as the Seebeck effect. The Seebeck effect describes the development of an electromotive force due to a temperature gradient in a material. The inverse Peltier effect was discovered soon after by Jean Peltier in 1834 and describes the absorption and emission of heat in a material due to a flowing current in the material. A complete description of the phenomena was finalized in 1851 by Lord Kelvin who identified the Thompson effect which describes the interaction of the Peltier and Seebeck effects.[1–3]

Thermoelectric phenomena were found to be improvable, with a strong materials-based dependence of transport properties. Analysis performed by A.F. Ioffe provided the groundwork for a figure of merit (zT) which directly relates to the power-heat conversion efficiency of a given material to the material properties.[4] This concise approach allowed scientists to quickly evaluate new and existing materials based on their viability as functional thermoelectric materials. Advancements in material science and particularly the knowledge of semiconductors helped to refine the science of thermoelectric materials.

The Seebeck effect for the generation of electricity using a heat source with the advantage of no moving parts provided motivation for a variety of applications. Radioisotope thermoelectric generators (RTGs) were developed in the late 1950s as energy sources for deep spacecraft far from the sun where solar panels are ineffective. The radioactive decay from a nuclear source such as plutonium-238 produces heat for an array of thermoelectric generators. Other such applications use heat sources such as waste heat from industrial processes, cooking or heating ovens, vehicle exhaust,[1] and even body heat.[5–7] Utilizing these alternative and waste energy sources provides motivation for development of thermoelectric materials. Temperature control using the inverse Peltier effect includes environmental heating/cooling, refrigeration, cryogenic cooling, and active battery cooling all with the distinct advantage of no moving parts.[8–11]

1.1.1 Principles of Thermoelectric Power Generation

Thermoelectric power generation occurs via the Seebeck effect, where the potential difference created in response to the temperature difference is represented by the Seebeck coefficient:

$$S = \frac{\Delta V}{\Delta T} \tag{1-1}$$

Thermoelectric temperature control is achieved with the Peltier effect, often considered the inverse of the Seebeck effect. The Peltier coefficient (Π) is the ratio of heat carried by electronic carriers ($\dot{Q}$) to current passing through the junction (I):

$$\Pi = \frac{\dot{Q}}{I} \tag{1-2}$$

The Seebeck effect describes the development of an electrical potential due to a constant temperature gradient. This situation described above is a state of non-equilibrium within the material. Illustrated in Figure 1.1 (a), the electronic carriers diffuse from the high temperature regions towards low temperature regions where they accumulate creating a potential difference. The potential difference created through each leg is small, however it can be enhanced additively by using both p-type and n-type conductors, where the primary charge carriers are holes in p-type and electrons in n-type materials. The n-type and p-type legs are placed thermally in parallel and electronically in series which allows the potential difference to become additive $\Delta V_T = \Delta V_p + \Delta V_n$. The potential developed for n-type materials is negative versus positive for p-type materials, which is manifested in a negative and positive Seebeck coefficient respectively. The Peltier effect occurs when a current flows through a junction of two different conductors. Heat is absorbed or dissipated at the junction depending on the direction of current flow. A schematic of a Peltier junction can be found in Figure 1.1 (b).

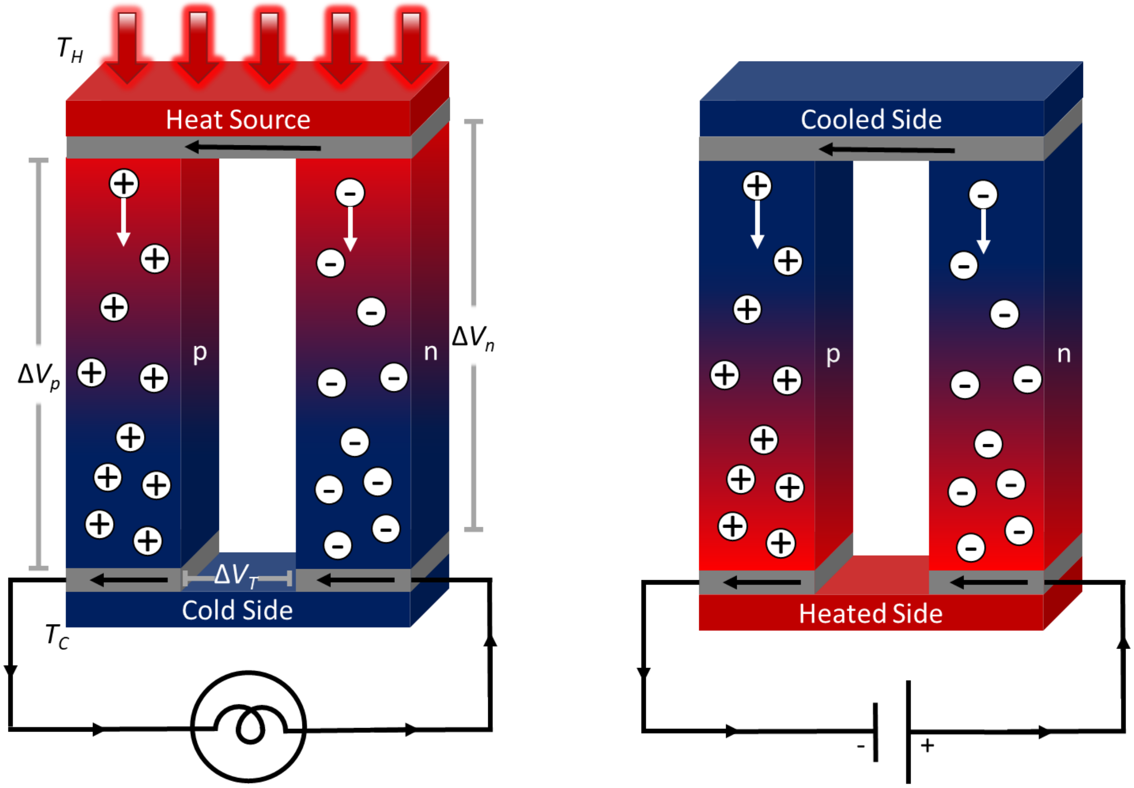

Figure 1.1: Depiction of thermocouple modules for electricity generation via (left) the Seebeck effect and (right) temperature control via the Peltier effect.

Within a single thermoelectric device there are many such thermocouples as described above, allowing for increased electrical generation (heat removal) via increasing leg number as shown in Figure 1.2. The specific geometries of the device can be tailored for a given application, but there must be thermal separation of the hot-side and cold-side of the device. The dimensions (length and cross-sectional area) of each leg of the thermocouples influence performance and power output and are designed according to the application.[1]

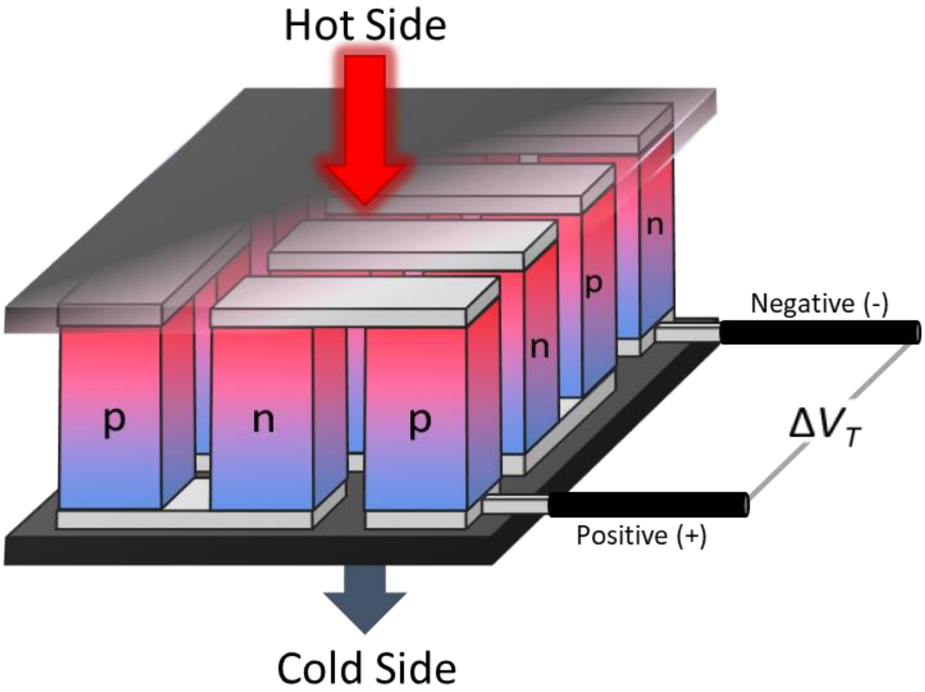

Figure 1.2: Schematic of thermoelectric generator with multiple p-n-thermocouples, the total voltage (ΔV_T) generated is the summation of voltage generated in individual legs.

1.1.2 Conversion Efficiency and Thermoelectric Figure of Merit

Evaluation of thermoelectric device efficiency begins by treating the generator as a simple heat engine:

$$\eta = \frac{P}{Q} \tag{1-3}$$

Where the efficiency (η) is the ratio between the electrical power generated (P) and the heat supplied (Q). The power output is defined as:

$$P = I^2 R_L \tag{1-4}$$

where I is the current and R_L is the load resistance. For a single thermocouple we can use Ohm's law with the resistance of both legs and voltage produced determined from the Seebeck coefficient to obtain the current produced:

$$I = \frac{V}{R_L} = \frac{(S_p - S_n)\Delta T}{R_p + R_n + R_c} \tag{1-5}$$

Here the Seebeck coefficients for the p-type (S_p) and n-type (S_n) become additive due to the negative sign of the n-type coefficient. The resistances of each leg and the contact resistances are added in the denominator.

The total heat input into the device (Q) is evaluated by three main mechanisms: heat conduction from the source to the cold side from (Q_{cond}), Peltier heating (Q_S), and heat returned from Joule heating (Q_{Joule}). Radiative losses can be typically neglected for this evaluation.

$$Q_{cond} = (\kappa_n + \kappa_p)\Delta T \tag{1-6}$$

$$Q_S = \left(S_p - S_n\right)T_h\Delta T \tag{1-7}$$

$$Q_{Joule} = -\frac{1}{2}I^2(R_p + R_n) \tag{1-8}$$

Where T_h is the hot side temperature, κ_n and κ_p are the thermal conductivity for the n-type and p-type legs respectively. Evaluating for the total efficiency gives:

$$\eta = \frac{\left(\frac{\left(S_p - S_n\right)\Delta T}{R_L}\right)^2 R_L}{\left(\kappa_n + \kappa_p\right)\Delta T + \left(S_p - S_n\right)T_h\Delta T - \frac{1}{2}I^2(R_p + R_n)} \tag{1-9}$$

Substituting the terms:

$$M = \frac{R_L}{(R_n + R_p)} \tag{1-10}$$

$$S_{np} = S_p - S_n \tag{1-11}$$

$$\kappa_{np} = \kappa_n + \kappa_p \tag{1-12}$$

can be used to simplify efficiency to:

$$\eta = \frac{\Delta T}{T_h} \frac{M}{1 + M - \frac{\left(R_p + R_n\right)\kappa_{np}}{S_{np}^2} \frac{(1+M)^2}{T_h} - \frac{1}{2}\frac{\Delta T}{T_h}} \tag{1-13}$$

This expression for efficiency shows dependence on materials-based properties, hot and cold side temperatures, and circuit resistance. Normalization of the circuit resistances can be used to reduce the efficiency equation further. A.F. Ioffe evaluated the efficiency for a thermoelectric engine in this way for material properties and temperature gradient to give:[4]

$$\eta = \frac{T_H - T_C}{T_H} \frac{\sqrt{1 + T\sigma S^2/\kappa} - 1}{\sqrt{1 + T\sigma S^2/\kappa} + \frac{T_C}{T_H}} \tag{1-14}$$

Temperature gradient ($T_H - T_C$) is a major contributing factor to efficiency which is typically dependent on the heat source, but as well as material limitations. The efficiency of power generation can be evaluated at a given temperature gradient if the material specific properties are known: the Seebeck coefficient (S), the electrical conductivity (σ) and the thermal conductivity (κ). The material variables are combined at a given temperature into a single dimensionless term to form the thermoelectric figure of merit (zT):[1]

$$zT = T\frac{\sigma S^2}{\kappa} \tag{1-15}$$

Evaluation of the efficiency in this manner provides a clear positive relationship between the figure of merit and the efficiency of electrical power generation, this relationship is illustrated in Figure 1.3. Current state of the art thermoelectric generators have efficiencies no greater than ~10% and materials are considered high performance with $zT > 1$.[12]

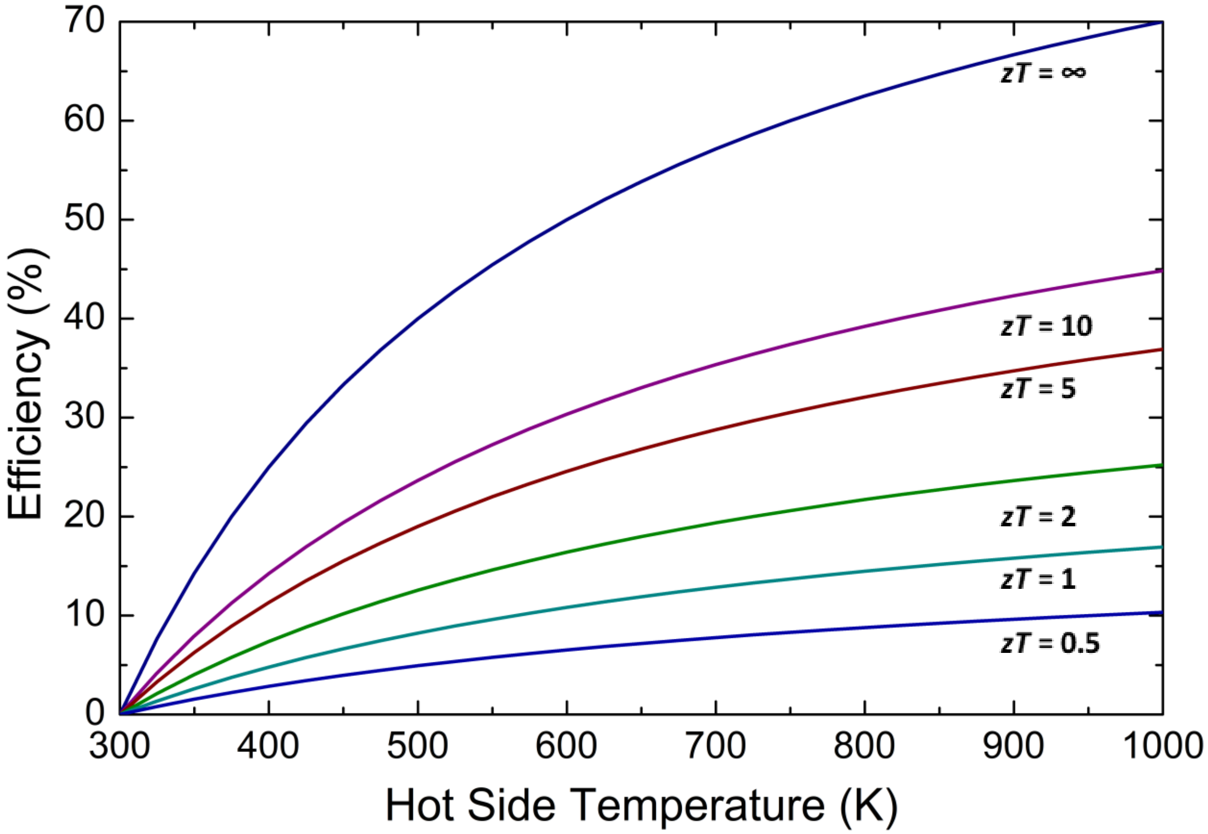

Figure 1.3: The positive relationship between thermoelectric conversion efficiency and thermoelectric figure of merit zT is visualized. Cold side temperature (T_C) is placed at 300 K with efficiency plotted versus hot-side temperature.

A material-based optimization strategy for thermoelectric performance is to maximize electrical conductivity (σ) and Seebeck coefficient (S) while minimizing thermal conductivity (κ). The direct relationship between thermoelectric energy conversion and materials properties has provided researchers with a clear focus for developing and optimizing thermoelectric materials. It was concluded through Ioffe's studies that heavily doped semiconductors are the most promising materials for thermoelectric applications.[4] The various optimization strategies for these material properties will be discussed in subsequent subsections.

1.2 Electronic Structure of Materials

Understanding the interrelationship of the thermoelectric (TE) properties is essential to developing and targeting materials for study. There are many influences on TE properties of a material which includes: atomic structure, electronic band structure, charge carrier concentration, and carrier mobility creating the complex systems which are studied. Understanding structure and chemical composition's contribution to the individual thermoelectric materials properties begins with understanding the electronic structure of materials.

Crystalline semiconductors are the primary materials studied for TE applications. The atomic structure of materials is the resulting arrangement of atoms due to behavior of interacting electron orbitals of the elements composing the structure. The electronic structure is formed by the quantum states available and their corresponding energies which the electrons can occupy in a material. Physical and electrical properties of materials result from their electronic structure, where classes of materials are defined by displaying similar properties.

This section will introduce some basic concepts of electronic structure which can be used for interpretations of band structure and density of states (DOS) calculations. The specific calculation processes will be discussed in the corresponding experimental section in Chapter 2.

1.2.1 Electronic states in crystalline materials

The electronic structure is composed of states at various energy levels which can be occupied by electrons. The number of available electronic states which a material has at a given energy is called its density of states. The density of states is the result of the crystal chemistry of a material and more specifically the orbital interactions of the atoms. The simple free-electron model for density of states in a bulk solid is developed by first treating the system as a particle in a box. The quantum numbers in a 3D system (n_x, n_y, and n_z) can be represented as a space where R_n is a "radius" in the n-space corresponding to a set of quantum numbers. The energy of the box is given as:

$$E = \frac{R_n^2 h^2}{8 m_e L^2} \tag{1-16}$$

Here, L is the length of the box, m_e is the electron mass, and h is the Planck constant. The number of states in a box with an n-space of “radius” R_n, can be solved in terms of energy using a factor of 2 for electron spin states and 1/8 for only positive n-space “volumes”:

$$N = (2)\frac{1}{8}\frac{4}{3}\pi R_n^3 = \left(\frac{8\pi}{3}\right)(2m_e E)^{3/2}\frac{L^3}{h^3} \tag{1-17}$$

Dividing by the box volume gives states per unit volume:

$$N_S = \left(\frac{8\pi}{3}\right)\frac{(2m_e E)^{3/2}}{h^3} \tag{1-18}$$

The density of states as a function of energy is obtained by taking the derivative with respect to energy:

$$g(E) = \frac{dN_S}{dE} = \frac{4\pi(2m_e)^{3/2}}{h^3}\sqrt{E} \tag{1-19}$$

For bulk crystalline materials the density of states function is applicable as it is independent of dimension (L). The probability of an electron occupying an electronic state can be determined by the Fermi-Dirac distribution function:

$$f(E) = \frac{1}{e^{(E-E_F)/k_B T} + 1} \tag{1-20}$$

Where the probability of a state being occupied by an electron $f(E)$ is determined by the energy of a given state (E) with respect to the Fermi level (E_F) at a given temperature (T). The Fermi level is defined as the energy above which there is 0 probability of finding an electron at 0 K in a system. The probability of a state being occupied increases as $f(E)$ approaches 1 ($E < E_F$) and the probability decreases as $f(E)$ approaches 0 ($E > E_F$). When the energy of the state is equal to the Fermi level ($E = E_F$) the state has a 50% chance of being occupied. The availability of states within a material with respect to the Fermi level relates to the electrical properties of the material.

The number of particles occupying states (n) at energy interval dE can be found by factoring the probability function Equation 1-20 and the density of states function Equation 1-19 at the energy interval:

$$n(E)dE = g(E)f(E)dE \tag{1-21}$$

Equation 1-21 can be used to describe the electronic behavior of materials. The Fermi-Dirac distribution is valid in general, however the density of states for a given material varies and is dependent on the atomic structure.[13,14]

1.2.2 Classification of Electronic Materials

When a material has a high density of states which cross the Fermi level (Figure 1.4 (a)) it displays metallic properties, and when only a few states cross the Fermi level (Figure 1.4 (b)) the material exhibits semi-metallic behavior. In the two previous examples electrons can easily become delocalized giving rise to properties such as high electrical conductivity, metallic luster, and malleability. When a material has an absence of electronic states at energies around the Fermi level this is referred to as a band gap. While metals and semi-metals may have band gaps, they are at energies far from the Fermi level.

When the Fermi level exists in a band gap the materials are classified as insulators or semiconductors. The electronic states below the Fermi level are called the valence states, and the electronic states above the Fermi level are referred to as the conduction states. The size of the band gap and its position relative to the Fermi level influence the electronic properties of the material. A material with a wide band gap (> 4.0 eV) is known as an insulator (Figure 1.4 (f)) and shows little to no electrical conductivity as the energy required to delocalize electrons is too large. These materials are typically brittle and transparent to visible light in their crystalline forms.[15]

Semiconductors are a class of materials with band gaps ranging from greater than 0 eV to 4.0 eV and are categorized into three intrinsic types: purely intrinsic (Figure 1.4 (d)), p-type (Figure 1.4 (c)), and n-type (Figure 1.4 (e)). The difference in properties of these semiconductors result from the position of their valence and conduction states relative to the Fermi level. Purely intrinsic semiconductors have conduction and valence states at equal energy difference from the Fermi level, which results in an equal number of conducting holes and electrons. Intrinsic p-type semiconductors have valence states closer in energy to the Fermi level than conduction states, as a result electrical conductivity occurs via ‘empty’ states or holes in the valence band, which have a net positive charge. The alternative n-type semiconductors have conduction states closer to the Fermi level allowing for electrons to occupy the conduction bands resulting in negatively charged electronic carriers. The size of the band gap and density of states around the Fermi level influences the number of active charge carriers and electrical conductivity. These materials have a range of properties based on the size of their band gaps. They are typically brittle with a range of visible colors to metallic like lustre.[15] Most high-performance thermoelectric materials are narrow band gap semiconductors with $E_{gap} = 0.2$ eV to 1.0 eV.[16]

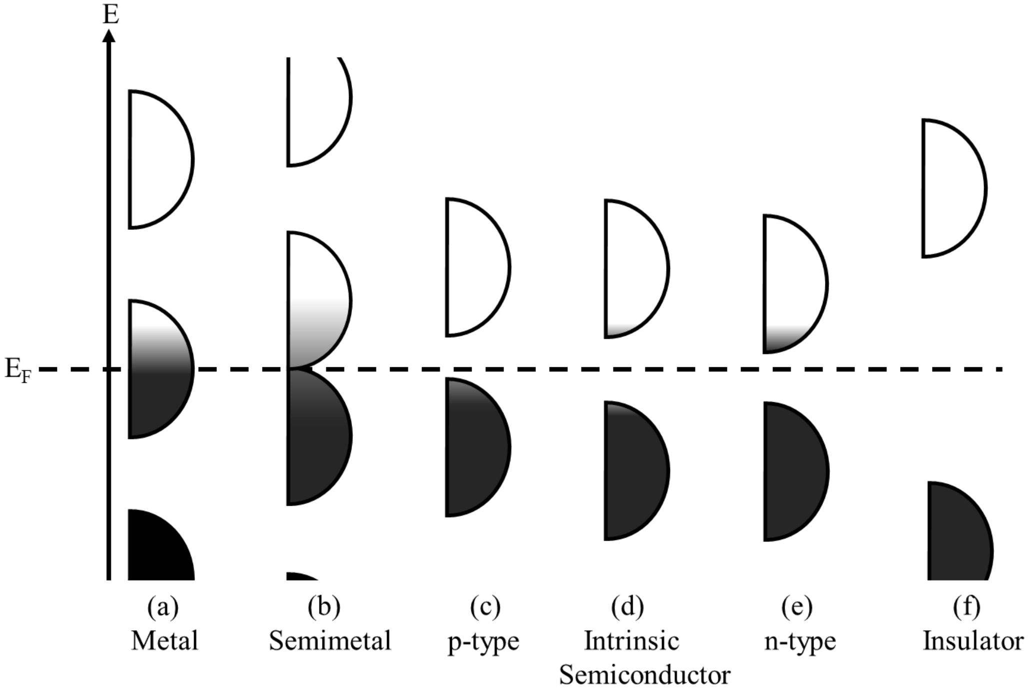

Figure 1.4: Schematic of the Fermi level and density of states relationship with crystalline material electronic properties. The shaded areas indicate states occupied by electrons and the white areas indicate unoccupied or available states.

1.2.3 Electronic Band Structure of crystalline materials

In three dimensional materials the electronic states of electrons are anisotropic, and symmetry of a material influences the dispersion of electrons. The electronic structures of materials can be determined by applying electron wavefunctions to the periodic potentials of a lattice. Energy and direction of electron dispersions form what is known as the band structure which provides useful information for understanding the physical properties of materials.

The primary tool for determining the dispersion of electrons in a crystal is Bloch's theorem:

$$\psi_{n\boldsymbol{k}}(\boldsymbol{r}) = e^{i\boldsymbol{k}\cdot\boldsymbol{r}} u_{n\boldsymbol{k}}(\boldsymbol{r}) \tag{1-22}$$

Where the solution to a wave function ($\psi_{n\boldsymbol{k}}$) at position $\boldsymbol{r}$ is found as a plane wave $e^{i\boldsymbol{k}\cdot\boldsymbol{r}}$ interacting with a periodic potential $u_{n\boldsymbol{k}}(\boldsymbol{r})$. The wave vector $\boldsymbol{k}$ describes the electron's state within an individual energy bands distinguished by n.[14]

The periodic potential of a material is determined by the types of atoms within the lattice. Two extreme models used to describe electron interaction within a periodic potential are the nearly-free electron and the tight-binding approximations. These models have their limitations in real systems with different types of atoms and interactions.[17] Density functional theory (DFT) with molecular orbital theory (MO) is a modern approach to modeling the periodic potential, which considers the shape of atomic orbitals and their interactions in a lattice.[18] Details of the specific DFT method for calculations used in this thesis will be discussed in Chapter 2.

A Fourier transform of the direct lattice is used to develop a reciprocal lattice. Mathematically, the reciprocal lattice is useful for representing the movement of waves in the real lattice with wave vectors. Due to the periodic nature of the structure, wave function solutions will repeat beyond a given set of wave vectors. The reciprocal lattice points forming the unit cell can be reduced to a zone which is translationally equivalent to all other zones as seen in Figure 1.5 (left), this is called the first Brillouin zone. The wave vectors which provide unique solutions for the Schrödinger equation are all contained within the first Brillouin zone.[13,14]

Three dimensional Brillouin zones used for calculating the band structure of a crystalline material, provide points and directions of interest of the various electronic bands. The first Brillouin zone for a face-centered cubic (FCC) lattice is seen in Figure 1.5 (right) with special points and directions labeled. Electron dispersion within a material is represented by plotting the energy of individual bands versus wave vector as we move between special points in the Brillouin zone. Electronic bands are constructed by calculating the electron dispersion for example by moving from the center of the zone Γ to the edge X along the line Δ. Band structures plots are formed by plotting electron dispersion while moving between various high symmetry points. The number of electron states are fixed by valence electrons within the first Brillouin zone and therefore fixed for a given ***k*** interval.[13,14]

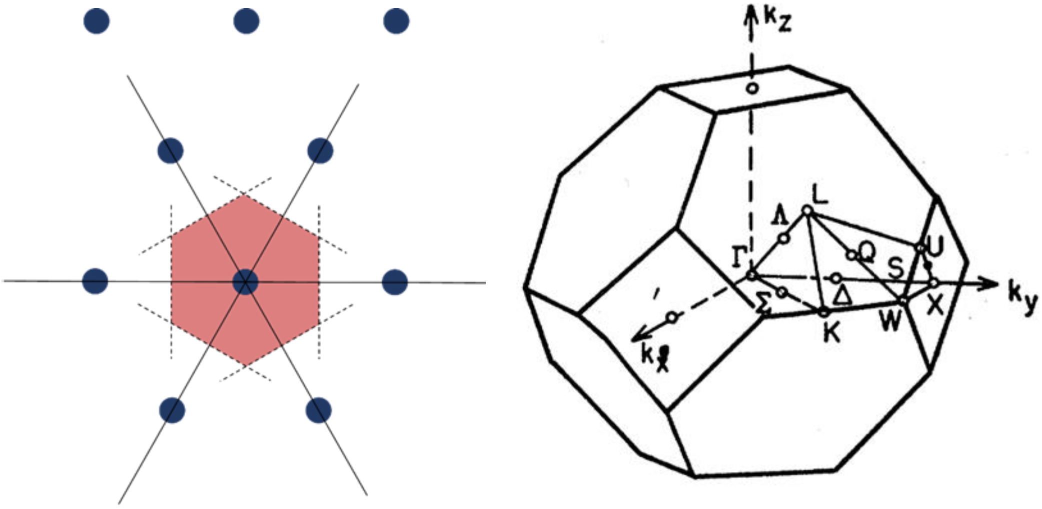

Figure 1.5: First Brillouin zone: (left) of hexagonal two-dimensional lattice formed by drawing line from central lattice point to all other lattice points a normal line is drawn at the midpoint and the enclosed space is the first Brillouin zone. (right)† Brillouin zone of FCC Bravais lattice with special high symmetry wave vectors labeled.[19]

The shape of the resulting bands describes the dynamics of electrons within the bands, for example the effective mass of an electron in the band is found by:

$$m^* = \frac{1}{4\pi^2}\frac{h^2}{\frac{d^2E}{d\boldsymbol{k}^2}} \tag{1-23}$$

Where the effective mass is inversely proportional to the second derivative of energy with respect to wave vector. This translates to electrons within shallow curved bands having a larger effective mass and within steep curved bands having light effective mass. This is graphically depicted in Figure 1.6. Given that the number of states which can be occupied at a wave vector is fixed in a single band, the

---

† Reprinted with permission from (P.M. Lee, Physical Review, 135, A1110, 1964) Copyright (1964) by the American Physical Society

density of states as described in Equation 1-19 is greater for a band with small changes in energy with respect to wave vector.[13,14] An electron with a lower effective mass (small density of states) moves easier through the bands than one with a larger effective mass (large density of states).

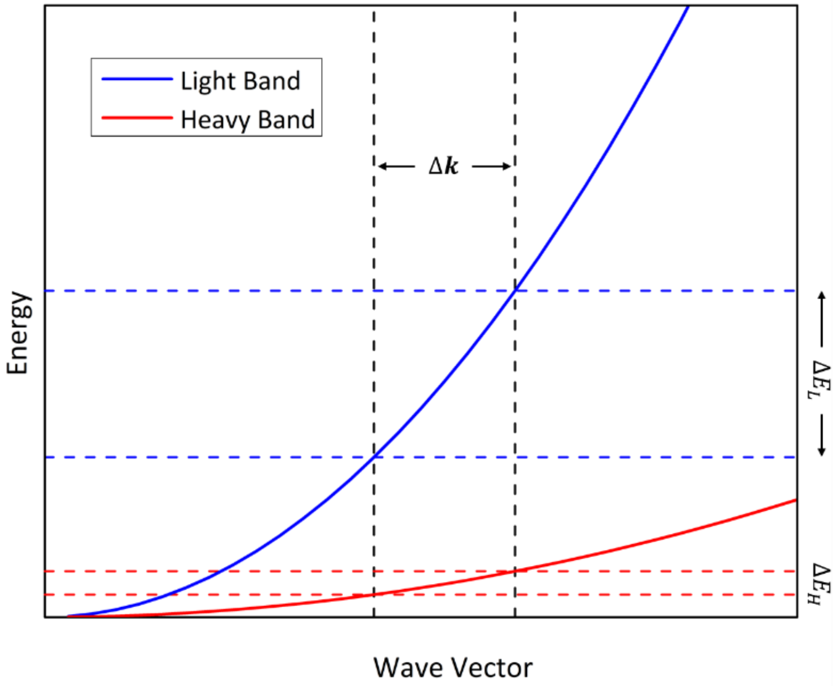

Figure 1.6: Schematic of parabolic bands with heavy effective mass (red) and light effective mass (blue). The difference in energy for a light band ΔE_L is greater than the difference in energy for a heavy band ΔE_H in the same k-space interval Δk corresponding to differences in the density of states.

Individual electronic bands which are equal in energy are considered degenerate and electrons can move easily between the bands. The calculation of electronic structures is performed at 0 K and therefore bands close in energy ($\Delta E < k_B T$) can be considered degenerate at room temperature as the energy required for electron transfer is smaller than the thermal energy of the system. Band degeneracy serves to increase the total density of states in those energy and wave vector intervals.[20]

Local maxima of the valence band and minima of the conduction bands are referred to as valleys and are key features of band structures. Valley degeneracy (N_V) occurs when two or more valleys are degenerate increasing the density of states at the band edges. This is an important aspect of band engineering in thermoelectrics as it may increase the Seebeck coefficient while maintaining carrier mobility.[21]

1.3 Thermoelectric Properties of Materials

This section will discuss the individual thermoelectric properties which contribute to zT and their dependence on other material properties. Interdependence of material properties with charge carrier concentration is discussed followed by derivation and creation of charge carriers in semiconductors. The electrical conductivity and Seebeck coefficient are discussed in terms of their dependence on charge carrier concentration and carrier effective mass. Band engineering and carrier effective mass are considered for optimization strategies for S and σ. Thermal conductivity and phonon scattering are discussed with strategies for reducing lattice thermal conductivity.

1.3.1 Interdependence of Thermoelectric Materials Properties

The greatest challenge for optimizing zT in thermoelectric materials arises from the interdependence of material properties on charge carriers. This difficulty arises because charge carriers themselves carry heat with them through the system. Optimizing the charge carrier concentration (n) of TE materials is important as it directly effects all thermoelectric properties.

The electrical conductivity (σ) of a material can be modeled simply as the product of the number of available charge carriers (n), the carrier mobility (μ), and the charge carried (e):

$$\sigma = ne\mu \tag{1-24}$$

The above equation suggests that higher carrier concentration would be preferred as zT is directly proportional to σ. The mobility of the charge carriers tends to decrease slightly with increasing carrier concentrations due to electron-electron scattering.

For a degenerate semiconductor with single parabolic bands (SPB) the Seebeck coefficient can be modeled using the Mott equation:

$$S = \left(\frac{8\pi^2 k_B^2}{3eh^2}\right) m^* T \left(\frac{\pi}{3n}\right)^{\frac{2}{3}} \tag{1-25}$$

Where k_B is the Boltzmann constant, h is the Planck constant, m^* is the effective mass of the charge carriers, and e is the electron charge. Here we see the Seebeck coefficient is greatest for insulating materials and low for metallic materials as there is an inverse 2/3 power relationship with charge carriers.[16,22] The thermoelectric figure of merit is proportional to the Seebeck coefficient squared; this provides a strong incentive to maximize the Seebeck effect for a given TE material. The Seebeck coefficient quickly drops off with carrier concentration however, and as illustrated in Figure 1.7, the power factor ($S^2\sigma$) is maximized for an intermediate carrier concentration. This balance of carrier concentration is achieved in degenerate semiconductors and can be tuned with doping levels. To make the optimization process of zT complete however we must consider the effect of carrier concentration on the thermal conductivity.

Thermal conductivity (κ) is composed of two main mechanisms in an electronically active material lattice and electronic thermal conductivity. Lattice thermal conductivity (κ_{lat}) occurs via atomic vibrations through the atomic structure of a material. These atomic vibrations called phonons are the only component of zT which can be decoupled from the charge carrier concentration. The next component is the electronic contribution to thermal conductivity (κ_{ele}) which occurs due to the thermal energy which charge carriers distribute through the material. Total thermal conductivity sums both these components:[16,22]

$$\kappa = \kappa_{lat} + \kappa_{ele} \tag{1-26}$$

and the Weidemann-Franz relation can be used to estimate the effect charge carriers have on the electronic thermal conductivity:[22–25]

$$\kappa_{ele} = L\sigma T = Lne\mu T \tag{1-27}$$

where L is the Lorenz number and σ is the electrical conductivity which can be related to charge carrier concentration as before in Equation (1-24). To maximize zT the thermal conductivity needs to be minimized which becomes entangled with its relationship with electrical conductivity. The total dependence on carrier concentration is illustrated in Figure 1.7, where due to the electronic contribution of κ, the thermoelectric figure of merit is not maximized at the maximum power factor.

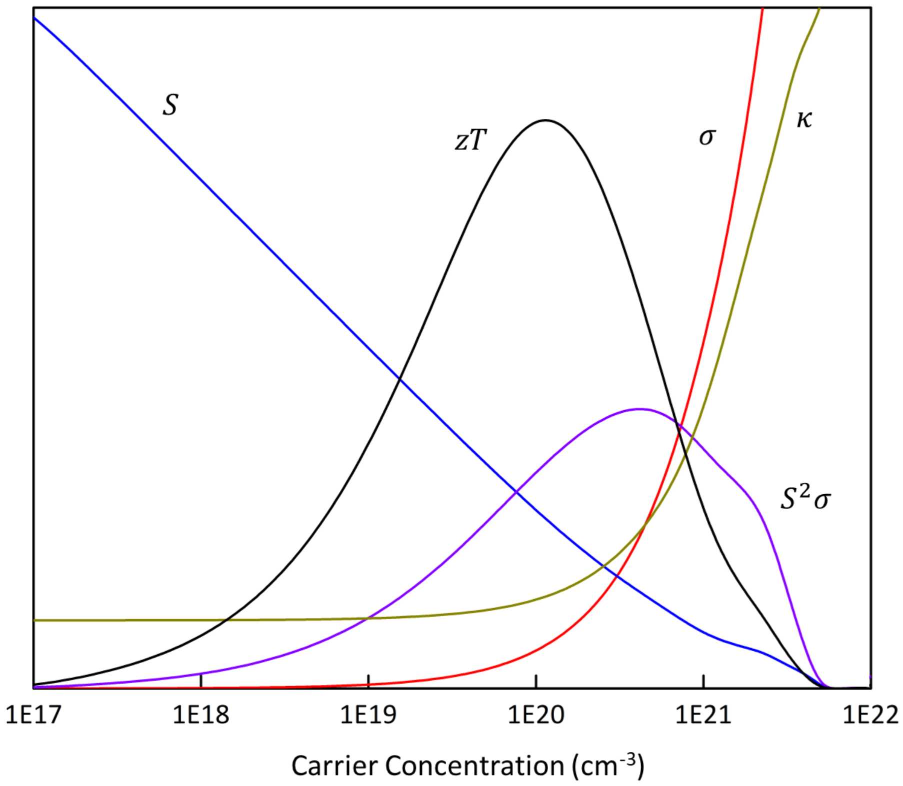

Figure 1.7: Example of thermoelectric properties versus carrier concentration showing the optimal figure of merit (zT) requires a compromise between electrical conductivity (σ), Seebeck coefficient (S), and thermal conductivity (κ). The difference in optimal carrier concentration for the power factor ($S^2\sigma$) and zT is due to increasing electronic contribution to thermal conductivity. Results obtained from simulation of p-type $ZnSnP_2$.

From the equations presented above it can be concluded that the number of charge carriers is an important contributing factor to all the thermoelectric properties. Increasing the number charge carriers increases the electrical conductivity and electronic thermal conductivity while decreasing the Seebeck coefficient. Modeling the above-mentioned properties as a function of charge carriers as shown in Figure 1.7. Insulators which are classified in the less than 10^{17} cm^{-3} regime have the largest Seebeck effect and lowest electronic thermal conductivity yet lack the appropriate electrical conductivity. Metallic materials (greater than 10^{21} cm^{-3}) have high electrical conductivity but suffer from low Seebeck coefficient and high electronic thermal conductivity. Heavily doped semiconductors (10^{19} to 10^{21} cm^{-3}) display the optimal thermoelectric properties, providing regions of optimal power factor and optimal zT.[4,16]

1.3.2 Determination of Carrier Concentration in Semiconductors

The active carrier concentration in an undoped semiconducting material is dependent on the density of states near the valence and conduction band edges, the temperature, and the size of the band gap. As discussed previously the number of carriers can be found using the density of states and Fermi-Dirac equation:[14]

$$n(E)dE = \int_0^\infty g(E)f(E)dE = \frac{8\sqrt{2}\pi m^{*3/2}}{h^3}\int_0^\infty \frac{\sqrt{2E}}{1+e^{(E-E_F)/k_BT}}dE \tag{1-28}$$

Here it can be seen that the number of charge carriers at energy E is proportional to the value of the Fermi level divided by temperature and Boltzmann constant, often referred to as the reduced Fermi level: $n(E) \propto E_F/k_BT$. For an n-type semiconductor with a single parabolic band (SPB):

$$n(E)dE = \int_0^\infty g(E)f(E)dE = \frac{8\sqrt{2}\pi m^{*\frac{3}{2}}}{h^3}\int_0^\infty \sqrt{E-E_{gap}}\frac{1}{1+e^{(E-E_F)/k_BT}}dE \tag{1-29}$$

For nondegenerate semiconductors with bands far enough away from the Fermi level ($E - E_F \gg k_BT$) the Fermi-Dirac part of the function can be reduced by realizing the 1 in the denominator becomes insignificant. This turns the Fermi-Dirac distribution into the classical Maxwell-Boltzmann distribution. For a purely intrinsic semiconductor the Fermi level is at the center of the band gap ($E_F = E_{gap}/2$), and the density of charge carriers can then be written:

$$n(E)dE = \frac{8\sqrt{2}\pi m^{*\frac{3}{2}}}{h^3}\int_0^\infty \sqrt{E-E_{gap}}e^{-(E-E_{gap}/2)/k_BT}\,dE \tag{1-30}$$

The number of electrons in the conduction band (n_e) can then be found by integrating from the bottom of the conduction band using the effective mass of the band (m_e^*):

$$n_e = \int_{E_{gap}}^\infty n(E)dE = \frac{2^{\frac{5}{2}}(m_e^*\pi k_BT)^{\frac{3}{2}}}{h^3}e^{-E_{gap}/2k_BT} \tag{1-31}$$

For the number of holes in p-type conductivity the derivation is similar, with the use of the effective mass of the valence band and integrating for energies below the valence bands. For an intrinsic semiconductor which conducts both electrons and holes the carrier concentration can be found by multiplying the equations for n-type and p-type:[26]

$$n_i = \sqrt{G_{con} G_{val}} e^{-E_{gap}/2k_B T} \tag{1-32}$$

The above equation applies assuming the law of mass action where the intrinsic carrier concentration squared is equal to the product of the electron and hole carrier concentration $n_i^2 = n_e n_h$.[14,20,26,27] Electrical conductivity for an intrinsic semiconductor is then found by combining Equation 1-32 and Equation 1-24:

$$\sigma = \sigma_0 e^{-E_{gap}/2k_B T} \tag{1-33}$$

Where

$$\sigma_0 = 2(G_{con} G_{val})^{\frac{1}{2}} e\mu \tag{1-34}$$

and

$$G_{con} = \frac{2^{\frac{5}{2}}(m_e^* \pi k_B T)^{\frac{3}{2}}}{h^3}, \tag{1-35}$$

$$G_{val} = \frac{2^{\frac{5}{2}}(m_h^* \pi k_B T)^{\frac{3}{2}}}{h^3} \tag{1-36}$$

The density of states at the conduction (G_{con}) and valence (G_{val}) band edges and carrier mobility (μ) influence the overall electrical conductivity through the σ_0 term. The exponential term describes the temperature dependent activation of charge carriers. Equation (1-33) is often used to calculate the band gap from electrical conductivity measurements where the pre-exponential term is estimated as temperature independent.[28]

For a semiconductor with the Fermi level directly in the center of the band gap the number of n-type and p-type carriers are equal ($n = p$). Which can be represented in terms of the density of states and Fermi-Dirac equation by:

$$G_{con}e^{-\left(\frac{E_C - E_F}{k_B T}\right)} = G_{val}e^{-\left(\frac{E_F - E_V}{k_B T}\right)} \tag{1-37}$$

Rearranging Equation 1-37 and solving for the Fermi level (E_F) gives:

$$E_F = E_{val} + \frac{1}{2}E_{gap} - \frac{1}{2}k_B T ln\left(\frac{G_{con}}{G_{val}}\right) \tag{1-38}$$

Given that the density of states depends on the effective mass of the conducting bands and therefore the carriers:[26]

$$E_F = E_{val} + \frac{1}{2}E_{gap} - \frac{1}{2}k_B T ln\left(\frac{m_e^*}{m_h^*}\right) \tag{1-39}$$

It can be seen from Equation 1-39 that the effective mass of the conduction and valence bands influence the Fermi level and therefore the type of carriers in a material. Purely intrinsic semiconductors make poor thermoelectric materials as the carrier concentrations for holes and electrons are equal as the Seebeck coefficient would be net zero. Materials with heavier conduction bands shift the Fermi level lower producing more p-type carriers and vice versa, this is schematically shown in Figure 1.4 (c) and (e) for p-type and n-type respectively.[20]

Degenerate semiconductors are classified as semiconductors in which the classical methods discussed above cannot accurately determine carrier concentration. This is often considered to occur when the Fermi level is close to either or both the conduction band and valence band. More specifically when: $(E_{con} - E_F)/k_B T \leq 0$ and $(E_F - E_{val})/k_B T \leq 0$. The classical Maxwell-Boltzmann approach produces an error in determining carrier concentration by the previously discussed methods of more than 20% and 8% when $(E_F - E_{val})/k_B T$ or $(E_{con} - E_F)/k_B T = 0$ and 1.4 respectively. To solve for the carrier concentration of a degenerate semiconductor Fermi-Dirac statistics must be applied completely and solved for numerically.[20]

1.3.3 Electronic Doping of Materials

The band gap and density of states of a given material is fixed by its chemical and structural properties as such so are the activated charge carriers. However, charge carriers and electrical conductivity can be affected through chemical doping. A dopant is an elemental substitution, vacancy or interstitial that adds or removes electrons from the system. Removal or addition of electrons is used for p-type and n-type doping respectively. Vacancy doping of cations resulting in holes or anions resulting in electrons are typical, however cation vacancies tend to be more chemically favorable. Interstitial doping is almost always achieved with cations as they have smaller ionic radii which results in extra electrons or n-type doping. Substitutional doping is performed by substituting an atom in the structure with a different valence state than is natural in the charge balanced structure. The chosen dopant has similar ionic radii, is typically a neighboring group, and behaves chemically like the substituted atom. Doping is typically performed at low concentrations so as to not destabilize the inherent structure or form undesirable side products.

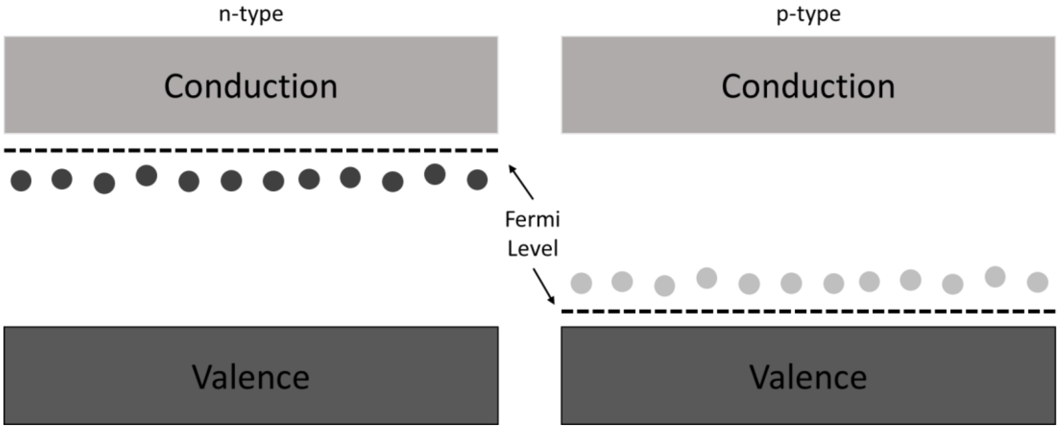

Figure 1.8: Schematic of addition of donor states in n-type (left) and acceptor states in p-type (right) for semiconductors. Doping shifts the Fermi level between the impurity states and conduction bands (n-type) or valence bands (p-type) allowing.

Dopants in semiconductors affect the charge carrier concentration adding hole energy levels and electron energy levels in the band gap for p-type and n-type respectively. The addition of energy states in the band gap shifts the Fermi level between the added states and the conduction band (n-type) or valence band (p-type). This is shown schematically in Figure 1.8. The energy required to activate these added carriers is reduced greatly and for n-type doping at low temperatures the donor carrier concentration (n_D) is given as:[26]

$$n_D = \sqrt{\frac{G_D G_{con}}{2}} e^{\frac{-(E_C - E_D)}{2k_B T}} \tag{1-40}$$

Which closely resembles the carrier concentration of intrinsic semiconductors where G_D is the density of states for the donor atoms and E_D is the energy of those states. The energy difference between the conduction states and donor states ($E_C - E_D$) is small. Complete thermal activation of the donor states occurs at relatively low temperatures, for example at room temperature (298 K) when $k_B T$ is 25.7 meV. Once all the donor states are activated the carrier concentration of doped semiconductors becomes:

$$n_D = \frac{1}{2}\left[(G_D - G_A) + \sqrt{(G_D - G_A)^2 + 4n_i^2}\right] \tag{1-41}$$

For heavily doped n-type semiconductors in which the density of donor states (G_D) is greater than the density of acceptor states (G_A) ($G_D \gg G_A$) and even so greater than activated intrinsic carriers $|N_D - N_A| \gg n_i$ the number of charge carriers is reduced to: $n_D \approx G_D$. The charge carrier concentration is roughly equal to the density of donor states.[20]

As the temperature of the doped semiconductor continues to increase the intrinsic charge carriers dominate. Temperature dependent carrier concentration behavior of a doped semiconductor is classified by three distinct regions. At low temperatures a “freeze out” region displays increasing concentration with increasing temperature and is defined by Equation 1-40. A Saturation region follows where the carrier concentration is relatively constant and is defined by Equation 1-41. Finally, as temperature increases further the carrier concentration behaves intrinsically and is modeled by Equation 1-31 with the addition of the doped carriers. The specific temperature ranges of these regions are dependent on the doping level, band gap, impurity density of states, and intrinsic density of states. A schematic of the carrier concentration versus temperature for a doped semiconductor is shown in Figure 1.9.[20]

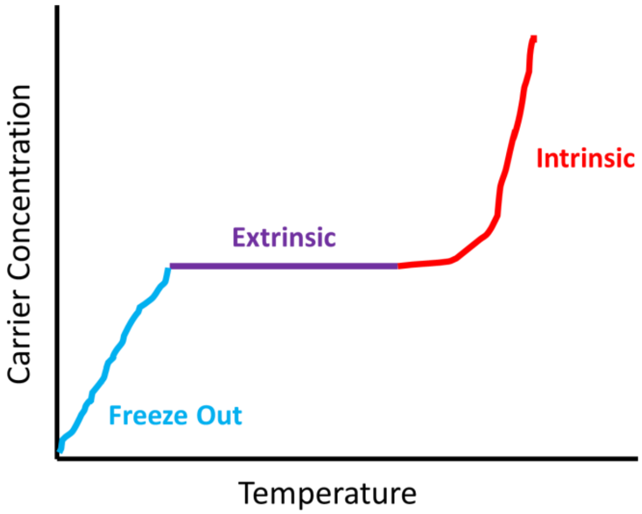

Figure 1.9: Schematic diagram of the charge carrier temperature dependence for an extrinsic semiconductor. The freeze out region (blue) is the low temperature region where the donor or acceptor impurities are not fully activated. The extrinsic region (purple) is a plateau where few intrinsic carriers are thermally activated, and all impurity carriers are active. Finally, the Intrinsic region (red) begins when the intrinsic carriers dominate as the majority carriers.

1.3.4 Electrical Conductivity

With the origins of carrier concentration defined, the mobility of charge carriers should be discussed as it influences electrical conductivity as seen in Equation 1-24. The carrier mobility (μ) describes how fast an electron moves through a material given an external electromotive force and is typically given in units of cm^2 V^{-1} s^{-1}. Carrier mobility can be found from the ratio of the average carrier scattering time (τ_0) by charge (e) to its effective mass (m^*):

$$\mu = \frac{e\tau_0}{m^*} \tag{1-42}$$

Therefore, electrical conductivity is found by:

$$\sigma = \frac{ne^2\tau_0}{m^*} \tag{1-43}$$

The relation assumes that after each scattering event the movement of a carrier becomes randomized before continuing in the direction of the external force. Therefore, mobility increases when there is longer time between scattering events and the effective mass of the carrier is low.[20]

Scattering time can also be represented as the velocity of the electrons and the mean free path before a collision. The frequency of scattering events is typically influenced by impurities, lattice defects, and phonons which are additive according to Matthiessen's rule as long as the scattering events are independent:[29]

$$\frac{1}{\tau_0} = \frac{1}{\tau_{impurities}} + \frac{1}{\tau_{defects}} + \frac{1}{\tau_{phonon}} + \cdots \tag{1-44}$$

and therefore:

$$\frac{1}{\mu} = \frac{1}{\mu_{impurities}} + \frac{1}{\mu_{defects}} + \frac{1}{\mu_{phonon}} + \cdots \tag{1-45}$$

Scattering events due to phonons or lattice vibrations increase in frequency with increasing temperature ($1/\tau_0 \propto T$) and therefore μ_{phonon} is proportional to $T^{-3/2}$.[20] Individual scattering mechanisms can be treated and resolved using statistical mechanics for each type of scattering event which is beyond the scope of this thesis.

The electrical conductivity of semiconductors is dependent on the charge carrier concentration and in turn the temperature which activates intrinsic carriers. While intrinsic mixed carriers are effective in increasing the electrical conductivity, a majority carrier type is necessary for good thermoelectric performance. To produce carriers of a single type in undoped materials, an imbalance in the conduction edge and valence edge density of states, and therefore effective mass (m^*), is preferred. Intrinsic carriers in semiconductors require small band gaps to produce a high enough carrier concentration for optimal zT as seen in Figure 1.7. Impurity doping is often necessary to produce high performance thermoelectric materials by increasing the electrical conductivity through a single charge carrier type. This is especially important for semiconductors with a relatively wide band gap.[16]

The carrier mobility is affected by the effective mass which is in turn dependent on the shape of the valence or conduction bands. Heavily doped materials with low effective mass of the carrier bands benefit the electrical conductivity. While increasing carrier concentration and decreasing effective mass might seem beneficial the resulting Seebeck coefficient will trend negatively.

1.3.5 The Seebeck Coefficient

The Seebeck effect describes the development of an electromotive force (emf) in a material due to a temperature gradient. Electronic carriers on the hot side of the material have higher thermal energy and diffuse to the cold side of the material. The gradient produced by this temperature difference is an entropy per unit charge and can be defined thermodynamically as:[27]

$$\frac{\partial \boldsymbol{\mu}}{\partial T} = -\frac{\partial \boldsymbol{S}}{\partial N} = -\dot{\theta} \tag{1-46}$$

i.e., the chemical potential ($\boldsymbol{\mu}$) change with temperature (T) is equal to negative entropy ($\boldsymbol{S}$) with number of particles (N) which is equal to the entropy per charge carrier ($\dot{\theta}$). The change in electrical potential (Φ) due to the movement of carriers can be equated as the difference of chemical potential per charge of the particle (q):

$$\Delta\Phi = \frac{\Delta\boldsymbol{\mu}}{q} \tag{1-47}$$

The Seebeck coefficient can then be realized in terms of the chemical potential as:

$$S = \frac{\partial \Phi}{\partial T} = \frac{\dot{\theta}}{q} = -\frac{1}{q}\frac{\partial \boldsymbol{\mu}}{\partial T} \tag{1-48}$$

To evaluate the development of electrical potential with movement of particles Boltzmann transport theory can be used. For an n-type material with a SPB and negligible perturbations, the electrical current (I) exposed to a temperature gradient (∇T) is found to be:[27]

$$I = \frac{e}{3\pi^2 m^*}\int_0^\infty \boldsymbol{k}^3 \frac{\partial f_0}{\partial k}\tau_0(\boldsymbol{k})\left[\frac{E - E_F}{T}\nabla T + \nabla(E_F - e\phi)\right] d\boldsymbol{k} \tag{1-49}$$

Where f_0 is the Fermi-Dirac function, $\boldsymbol{k}$ is the wave vector, and ϕ is the electrostatic potential. For steady state condition $I = 0$, and applying Sommerfeld's model for a SPB where $E = \frac{h^2\boldsymbol{k}^2}{8m^*\pi^2}$:

$$0 = \frac{e}{3\pi^2 m^*}\left\{\frac{\nabla T}{T}\int_0^\infty E^{\frac{5}{2}}\frac{\partial f_0}{\partial E}dE - E_F\frac{\nabla T}{T}\int_0^\infty E^{\frac{3}{2}}\tau_0(E)\frac{\partial f_0}{\partial E}dE + \nabla(E_F - e\phi)\int_0^\infty E^{\frac{3}{2}}\tau_0(E)\frac{\partial f_0}{\partial E}dE\right\} \tag{1-50}$$

The Seebeck coefficient is found by dividing the total emf by the temperature gradient and integrating by parts to obtain:

$$S = \frac{\nabla\left(\phi - \frac{E_f}{e}\right)}{\nabla T} = -\frac{k_B}{e}\left[\frac{\int_0^\infty \epsilon^{5/2}\,\tau_0(\epsilon)\,\frac{\partial f_0}{\partial \epsilon}d\epsilon}{\int_0^\infty \epsilon^{3/2}\,\tau_0(\epsilon)\,\frac{\partial f_0}{\partial \epsilon}d\epsilon} - \frac{E_F}{k_B T}\right] \tag{1-51}$$

Where the term $\epsilon = E/k_B T$ is the reduced energy. If the scattering time (τ_0) is considered energy dependent it further reduces the equation:[27]

$$S = -\frac{k_B}{e}\left[\frac{\int_0^\infty \epsilon^{5/2+\mathrm{T}_0}\,\frac{\partial f_0}{\partial \epsilon}d\epsilon}{\int_0^\infty \epsilon^{3/2+\mathrm{T}_0}\,\frac{\partial f_0}{\partial \epsilon}d\epsilon} - \frac{E_F}{k_B T}\right] \tag{1-52}$$

The above equation describes the Seebeck coefficient using Fermi-Dirac statistics where the integrals are the Fermi functions which change order based on the scattering mechanisms (T_0). The Fermi-Dirac statistics in Equation 1-52 can be treated as in the previous section using classical Maxwell-Boltzmann statistics for non-degenerate semiconductors ($E - E_F \gg k_B T$) resulting in:

$$S = -\frac{k_B}{e}\left(\left(\frac{5}{2} + \mathrm{T}_0\right) - \frac{E_F}{k_B T}\right) \tag{1-53}$$

Here the reduced scattering time (T_0) is dependent on the dominant scattering mechanism with dimensionless values of 3/2 or -1/2 for impurity or lattice phonon scattering mechanism respectively. Equation 1-53 shows that as $E_F/k_B T$ increases the Seebeck coefficient decreases in magnitude. As discussed previously, following Equation 1-28 the number of charge carriers is proportional to reduced Fermi level $n(E) \propto E_F/k_B T$, seen here it follows that the Seebeck coefficient decreases with increasing charge carriers.[27]

Equation 1-53, known as the Pisarenko relation,[27] does not have any dependence on the density of states of that material. To evaluate the Seebeck coefficient in a more modern way band theory of solids rather than a free electron model is used. The Mott relation utilizes Fermi-Dirac statistics with band energies to evaluate the Seebeck coefficient:[30]

$$S = \frac{k_B}{e}\frac{1}{\sigma_{\mu,\nu}}\int_0^{\infty} \sigma_{E,\mu,\nu}(E)\left(\frac{E-E_F}{k_BT}\right)\left(\frac{\partial f}{\partial E}\right)dE \tag{1-54}$$

Where $\sigma_{\mu,\nu}$ and $\sigma_{E,\mu,\nu}$ is the energy independent and Mott conductivity respectively. The result for a degenerate semiconductor with a single parabolic band is found as:[16,31]

$$S = \frac{8\pi^2 k_B^2}{3eh^2} m^* T \left(\frac{\pi}{3n}\right)^{2/3} \tag{1-55}$$

From the above equation the negative dependence of Seebeck coefficient on carrier concentration can be realized where $S \propto n^{-2/3}$. The relationship of Seebeck coefficient with density of states is found in the effective mass term (m^*) where a high effective mass or flat high-density bands at the band edge improve the Seebeck coefficient.

Large effective mass in materials occurs when the band edge density of states is “flat” as described previously, meaning for a single electronic band there is little variance in the energy with respect to direction. Flat bands are typically found in materials containing f-shell electron orbitals or heavy fermion materials. Aside from individual heavy bands a high density of states at the band edge would increase the Seebeck coefficient. Overlapping or degenerate bands as is seen in highly symmetric crystal systems. Degenerate bands have the added advantage in that the individual bands may have low effective mass yet when overlap occurs at the band edge the density of states increases without increasing the effective mass of the charge carriers.[32] The latter case is found to occur in PbTe materials one of the highest performance TE materials to date.[33,34]

1.3.6 Effective Masses

Much like the contradicted relationships of Seebeck coefficient and electrical conductivity with charge carrier concentration, such a relationship exists for effective mass, where increasing effective mass increases the Seebeck coefficient while decreasing electrical conductivity. As discussed in Section 1.2.3 the effective mass of a carrier is well defined by the shape and density of the electronic bands with respect to energy versus wave vector. In rigorous examination of electronic structure, two distinct types of effective masses can be determined. The inertial effective mass (m_I^*) describes the movement of carriers while the density of states effective mass (m_{DOS}^*) describes the effective mass of the electronic bands.

The effective mass which directly contributes to electrical conductivity defined in Equation 1-43 is m_I^* ($\sigma = ne^2\tau/m_I^*$) while the carrier scattering time (τ_0) is decreased with increasing m_{DOS}^*. Steep band valleys will result in low inertial effective mass while flatter bands increase inertial effective mass. As detailed in Equation 1-55 the Seebeck coefficient is dependent on the effective mass, which is the m_{DOS}^*. This distinction of effective masses allows the development of band engineering strategies to further improve thermoelectric performance.

Band valley degeneracy serves to increase the density of states and therefore m_{DOS}^* while maintaining low m_I^* with steep bands. The band valley degeneracy relates to the effective masses by:

$$N_V^{2/3} = \frac{m_{DOS}^*}{m_I^*} \tag{1-56}$$

Many well-established high-performance TE materials contain intrinsic band valley degeneracies. Developing band valley degeneracies is often achieved by formation of solid solutions through band convergence in many high-performance TE materials.[35–39]

1.3.7 Thermal Conductivity

Thermal conductivity is a measure of the heat transfer rate of a given material. Heat transfer occurs through a material via two main mechanisms: lattice vibrations (phonons) and electronic carriers. High performance thermoelectric materials are poor thermal conductors. Strategies to reduce thermal conductivity mostly focus on the reduction of phonons via scattering as the electronic thermal conductivity is dependent on the carrier concentration through electrical conductivity.

1.3.7.1 Electronic Thermal Conductivity

The heat carried by electronic carriers can be evaluated with the Wiedemann-Franz law ($\kappa_{ele} = LT\sigma$) as discussed previously which applies most accurately to metals and degenerate semiconductors. This simple relation shows that as charge carriers and therefore conductivity increase the electronic thermal conductivity increases relating to Figure 1.7. The proportionality constant (L) is known as the Lorenz number and is based on the heat capacity of a free electron gas at 0 K where:[24,25,40]

$$L = \frac{\pi^2}{3}\frac{k_B^2}{e^2} = 2.44 \times 10^{-8}\, V^2 K^{-2} \tag{1-57}$$

In real materials with electronic bands and not at 0 K the Lorenz number can vary significantly from the theoretical value. The Lorenz number can be modeled numerically for various systems using a SPB approximation, Boltzmann transport equations, band effective mass, and various scattering mechanisms.[24,41] Using this method the Lorenz number (10^{-8} V^2 K^{-2}) ranges from 1.5 to 3 for non-degenerate semiconductors with acoustic phonon scattering and degenerate semiconductors with impurity scattering mechanisms.

A more convenient approach to estimating the Lorenz number by Kim et al. utilizes the Seebeck coefficient assuming a SPB and acoustic phonon scattering to give:

$$L = 1.5 + e^{\left[-\frac{|S|}{116}\right]} \times 10^{-8}\, V^2 K^{-2} \tag{1-58}$$

Where S is in μV K^{-1} with 1.5 as the acoustic scattering limit; Equation 1-58 is accurate within 5% of the SPB model. [23] It can be seen clearly here that as Seebeck coefficient increases in magnitude the Lorenz constant decreases thus decreasing the electronic contribution to thermal conductivity. The model uses the assumption that the electronic carriers are all a single type which is not always the case but allows for temperature dependent estimation of the Lorenz number rather than using a constant value.

1.3.7.2 Lattice Thermal Conductivity

Lattice thermal conductivity (κ_{lat}) plays an important role in thermoelectric materials because it is the most disentangled thermoelectric property. Reduction of lattice thermal conductivity can be achieved with little influence on other key TE properties. Reducing κ_{lat} serves to both increase the figure of merit and reduce the optimal carrier concentration required for zT_{max} as shown in Figure 1.10. This shift in optimal carrier concentration reduces κ_{ele} and increases Seebeck coefficient increasing zT further.[16]

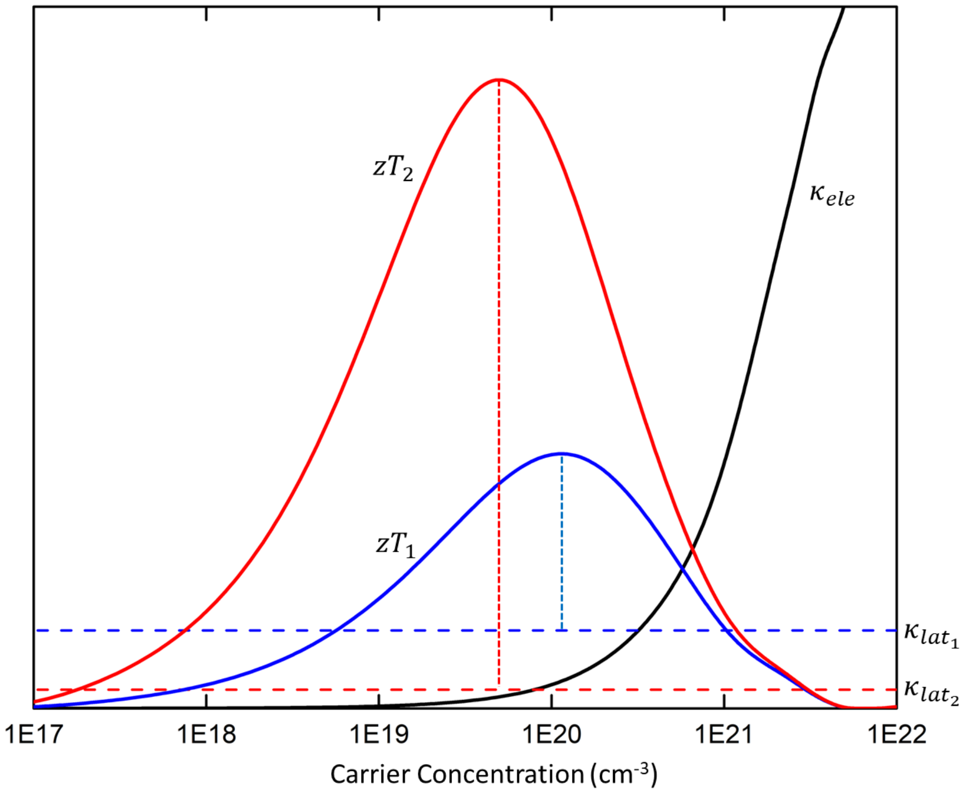

Figure 1.10: Lower lattice thermal conductivity (κ_{lat}) shifts the optimal carrier concentration for zT_{max} lower while also shifting the overall value higher. Here κ_{lat_2} is set 4 times less than κ_{lat_1} shifting the optimal carrier concentration from $1.2 \cdot 10^{20}$ cm^{-3} to $4.7 \cdot 10^{19}$ cm^{-3} and zT from 0.83 to 2.1 respectively. Figure obtained from BoltzTraP simulation on compound ZnSnP$_2$.

The electronic contribution to thermal conductivity is most highly dependent on the number of charge carriers while the lattice component is mostly dependent on various phonon scattering mechanisms. Phonons are the particle representation of the wavelike movement of lattice vibrations which transfer heat. Thermal conductivity is defined in terms of heat transfer particles by:

$$\kappa_{lat} = \frac{1}{3} N_{ph} C_p v^2 \tau_{ph} \tag{1-59}$$

Where the number of phonons (N_{ph}) with heat capacity (C_p) is multiplied by the phonon scattering kinetics ($\lambda_{ph} = \upsilon\tau$) and phonon velocity ($\upsilon$) with scattering relaxation time (τ_{ph}). The factor of 1/3 is assuming anisotropic movement given three dimensions of freedom.[14]

Heat capacity can be modeled using the Debye model for low temperatures which reduces to the Dulong-Petit approximation for high temperatures. Heat capacity is considered constant above the Debye temperature which describes the activation barrier for acoustic phonons. For the purposes of this work the Dulong-Petit method is used for its simplicity, accuracy, and applicability at high temperatures, which is given by:[42]

$$C_P = \frac{3R}{M_a} \tag{1-60}$$

Where R is the universal gas constant and M_a is the average molar mass of the material. As seen here the heat capacity and therefore κ_{lat} decreases with increasing average molar mass. This means that materials composed of heavier atoms tend to have lower thermal conductivity than those with light atoms.

1.3.7.3 Phonon Scattering Processes

Scattering mechanisms for phonons are abundant in imperfect bulk crystalline solids and are considered additive using Matthiessen's rule assuming they do not interact.[29] Within a crystalline material there are various phonon frequencies (ω) or modes of vibration, and interaction of phonons with scattering mechanisms dependent on the phonon frequency. For normal processes a scattered phonon is annihilated, and a new phonon is created at the same frequency in a different direction or wave vector. When a scattered phonon moves in a different direction than the heat flux then thermal resistance is created.[14,43–45]

The frequency of scattering events is inverse relaxation time $1/\tau$, therefore as the frequency of phonon scattering increases the thermal conductivity decreases. P. G. Klemens developed relations describing the various normal scattering processes in crystals at low temperatures using perturbation theory.[46] For scattering due to substitutional atoms of different mass (ΔM_A) the scattering frequency is given by:

$$\frac{1}{\tau_{MF}} = \frac{a^3}{G}\left(\frac{\Delta M_A}{M_A}\right)^2 \frac{\omega^4}{4\pi v^3} \tag{1-61}$$

Where a is the unit cell parameter or a^3 is the volume of unit cell and G is the average stiffness constant of neighboring bonds, M_A is the mass of the original atoms being substituted for, ω is the phonon frequency, and ν is the phonon wave velocity. It can be seen here that as the mass difference of substituted atoms increases the thermal conductivity decreases. This is typically referred to as mass fluctuation effects. For substituted atoms with different bonding force ($\Delta\xi$):

$$\frac{1}{\tau_{BF}} = \frac{a^3}{G}\left(\frac{\Delta\xi}{\xi}\right)^2 \frac{2\omega^4}{\pi v^3} \tag{1-62}$$

Where ξ is the bonding force of the original atoms in the cell. Like the mass fluctuation effect, as differences in bonding energy increases the thermal conductivity decreases. Scattering frequency for a point defect within a crystal system is given by:

$$\frac{1}{\tau_{PD}} = \frac{a^3}{G}\Gamma^2 \frac{3\omega^4}{\pi v^3} \tag{1-63}$$

Where Γ is a combination of the differences in mass, bond energy and elastic strain field of the given point defect from the other lattice atoms. The ω^4 dependence in the above three equations indicate interaction with high-frequency phonons.

Scattering due to dislocations: single, edge, and core are proportional to phonon frequency by ω, ω, and ω^3 respectively interacting most strongly with mid-frequency phonons. For grain boundaries the scattering frequency is given as:

$$\frac{1}{\tau_{GB}} = \frac{v}{\zeta}\gamma^2\left(\frac{b}{H}\right)^2 \frac{1}{36} \tag{1-64}$$

Where ζ is the distance between intersections of grain boundaries, H describes the periodicity of the grain boundaries which is the inverse of the angle of misfit with a periodic lattice, and b is the Burgers vector describing the size and direction of dislocations. The Grüneisen parameter (γ) which effects other dislocation scattering similarly is a measure of the anharmonicity of the crystal structure and is proportional to the complexity of the structure. Equation 1-64 shows no dependence on phonon frequency or ω^0 which indicates interaction with low-frequency phonons. Grain boundary scattering of phonons increases with decreasing distance between their intersections and increasing grain boundary sizes and angle of misfit.

The models outlined above are based on normal phonon scattering where energy is conserved which is primarily at low temperatures below the Debye temperature of the material. This does not mean that these scattering processes are inactive at high temperatures, but instead the above models are not accurate for a complete description of lattice thermal conductivity.[45] The temperature dependencies of the of the above normal scattering processes vary. For mass fluctuations, bonding energy fluctuations, and point defects there is a positive temperature dependence ($1/\tau_{MF} \propto T,\ 1/\tau_{BF} \propto T$, and $1/\tau_{PD} \propto T$) due to their interactions with high frequency phonons. Scattering from grain boundaries has a negative cubic temperature dependence ($1/\tau_{MF} \propto T^{-3}$) due to its interaction with low frequency phonons. The other dislocation scattering processes have little dependence on temperature due to their interaction with mid-frequency phonons.[45,47]

At high temperatures the dominant scattering processes are three-phonon, four-phonon, and Umklapp scattering ($1/\tau_U$) which result from phonon-phonon interactions.[48] These interactions give rise to various scenarios, where phonons can either combine or split into other phonons. For two phonons with momentum q_1 and q_2 they can combine resulting in a third phonon with momentum q_3. When the third phonon produced from this process has a momentum outside of the first Brillouin zone the translational symmetry replaces the phonon with a reduced momentum (q'_3) phonon. This process is referred to as Umklapp scattering, which is not a normal scatting process as it does not conserve momentum. This can occur in three or four phonon interactions. As temperature increases phonons with greater momentum interact, increasing the likelihood that the resulting phonon will be outside the first Brillouin zone ($1/\tau_U \propto T$). The resulting effect on thermal conductivity is a negative temperature dependence ($\kappa \propto T^{-1}$).[48]

Slack's model was developed to estimate the lattice thermal conductivity considering many factors contributing to phonon scattering:[43]

$$\kappa_{lat} = A\frac{M_a \theta_D \bar{V}^{1/3}}{\gamma^2 n^{2/3} T} \tag{1-65}$$

Where M_a is the average molar mass, $\bar{V}$ is average volume, and n is the number of atoms in the unit cell showing a positive dependency for large heavy tightly packed atoms. The Debye temperature θ_D here has a positive contribution to thermal conductivity since it describes the transition from normal to phonon-phonon dominated scattering regimes. The Grüneisen parameter (γ) measures the anharmonicity which correlates to crystal structure complexity, the negative dependence provides a basis for the trend of decreasing thermal conductivity with increasing crystal complexity.[49] This model is useful when considering materials which are relatively defect free, however neglects the contribution of scattering due to defects.[47] While defects reduce thermal conductivity, they also contribute to carrier scattering reducing the electrical conductivity through carrier mobility.

1.4 Solid Solutions as Thermoelectric Materials

The body of this work focuses on synthesis and analysis of solid solutions as thermoelectric materials. There are distinct advantages which solid solutions have with respect to thermoelectric performance. Electronic band engineering and mass fluctuation effects are achieved with many solid solutions and are primary strategies in many high-performance TE materials.[1] Solid solution principles, synthetic methods, and improvements to thermoelectric performance by band engineering will be discussed in this section.

1.4.1 Solid Solution Principles

Solid solutions are crystalline materials which contain a mixture of elemental components that share the same crystallographic sites. Nomenclature represents solid solution chemical formula by $A_{1-x}B_x$ where component A and B are distinct elements and x is the degree of substitution. Two isostructural compounds having the same structure but different isovalent elemental components can typically form a solid solution. Two pure materials which when mixed maintain a single phase for the full range of substitution are termed fully miscible. Miscibility gaps are areas or degrees of substitution where a solid solution is not thermodynamically stable and therefore forms two distinct solid solutions with differing stoichiometry. Substitution of atoms with different valence states than the parent structure tends to have very limited miscibility, however miscibility gaps occur for mixtures which are both isovalent and isostructural.

Solid solutions of more complicated binary, ternary, or greater compounds maintain similar reasoning for each individual atom type. The pure isostructural compounds are often referred to as the end members of the solid solutions. Alloys and solid solutions are often used synonymously and are used so in this thesis. The technical distinction arises on the atomic scale where alloys can be a mixture of typically metallic compounds with varying structure, whereas solid solutions maintain a single crystal structure.[50]

Solid solutions can be characterized in much the same way as other crystalline phases using powder X-ray diffraction (PXRD) and single crystal X-ray diffraction (SCXRD). The degree of miscibility of a solid solution can be easily identified by PXRD. A 'splitting' of peaks indicates the presence of two separate phases; however, the indications can often be more subtle such as a shoulder around an expected peak. Complete miscibility of a solid solution results in singular PXRD peaks as in a pure crystalline phase.[51] Resulting peak intensities will become the result of the average degree of component atom substitutions.

The mixing of atomic positions by substituted elements results in unit cell expansion or contraction due to differences in size and bonding behavior of the substituted elements. Standard isovalent substitution typically results in linear unit cell expansion or contraction with degree of substitution. The lattice parameter changes are linear and can be approximated using Vegard's law $a_{A_{(1-x)}B_x} = (1-x)a_A + x\, a_B$, where a_i is the unit cell parameter of the end member i, this applies most accurately to cubic systems but has validity in lower symmetry systems.[50,52,53]

Higher order substitutions such as various elements on a single site or multiple substitutions on different sites are often termed as high entropy alloys (HEA) due to their high mixing entropies. The highly disordered lattices give rise to decreased thermal and electrical conductivity, increased mechanical and chemical stability, and other emergent properties not inherent to the pure components.[54–56] Studies of these solid solutions have been often limited to metallic materials, however some examples have been demonstrated in TE materials showing improvement to performance.[56–59] These solid solutions are often composed of five or more elemental substitutions with similar stochiometric proportions.

In solid solutions with complex crystal structures, preferred occupancy of crystallographic sites can result due to differences in bonding energies of the various sites. The arrangement and occupancy of atoms resulting in the lowest energy atomic structures is referred to as the "coloring problem" in chemistry.[60] The coloring problem can be used to resolve the expected bonding structure of materials, however in the context of solid solutions, refers to the preferred occupancy at specific atomic positions within a known crystal structure. Coloring effects are particularly interesting for the development of superconducting materials due to spin, charge, and orbital ordering effects which results in correlated electrons.[60,61]

1.4.2 Solid Solution Synthetic Methods

Synthesis of solid solutions usually requires careful consideration of heating and cooling rates to achieve miscibility. In these cases, it is very helpful to develop or reference a phase diagram of the target systems. For ternary and higher order solid solutions the availability of phase data is fairly limited as the systems become increasingly complex. Consideration of the end member melting and/or decomposition temperatures is needed to develop appropriate strategies. Various approaches can be taken for solid solution synthesis with distinct advantages and disadvantages.

Most commonly a liquid-solid synthesis approach is used where the solution at desired stoichiometry is melted into a homogenous liquid then cooled at a quick rate to achieve a homogenized polycrystalline solid solution. A fast-cooling rate is often used to avoid any two-phase liquid-solid regions however sintering can be used to correct for undesired side products. This method works best for materials with congruent melting behaviors of the solid solutions and end members. The resulting material is typically in the form of a polycrystalline ingot.[50] A liquid-solid synthesis approach was taken for the scaled-up processing of the high-performance $Mg_2Si_{0.32}Sn_{0.6}Bi_{0.08}$ materials discussed in Chapter 3.

Some flux methods have proven successful in producing solid solution compounds, however the solubility of the elemental components within the flux must be similar. Flux methods are typically utilized for the formation of single crystals. If there are differences in constituent solubilities within the flux the precipitated crystals will have compositional gradients. The cores of the crystals will contain the least soluble mixtures while the outside would contain the most soluble constituents. Controlled doping of materials by this method proves similarly difficult due to the above-mentioned reasons, but also due to formation of side products.[62]

Solid-solid synthesis of solid solutions poses certain challenges but is a viable method. Starting constituents are ground together into a fine powder in their solid forms. Grinding works best for brittle constituents where crushing into a powder is achieved rather than the deformation and agglomeration of malleable components. The reaction is limited by diffusion of constituents in their solid form therefore a very fine homogenized powder is pressed into a bulk solid at high pressures to reduce diffusion lengths. Heat is applied to thermally activate the material below its melting temperature forming a bulk polycrystalline pellet. Often, due to homogenization difficulties or diffusion barriers the sample will be reprocessed into powder form and the steps are repeated until the desired product is achieved.[50]

The primary difficulty in the formation of solid solutions by this method is due to incomplete material homogenization. A solid solution is a crystalline mixture at the atomic scale and therefore advanced grinding and mixing or comminution methods are required. Ball milling is a mechanochemical synthesis technique which achieves very fine grinding of samples. High energy ball milling of materials is an established approach for the formation of alloys in metallurgical fields.[63–68] The primary body of this work utilizes ball milling techniques followed by high pressure sintering to achieve solid solution synthesis by solid-solid methods.

1.4.3 Solid Solutions for Band Engineering

Electronic band engineering through the formation of solid solutions has produced some of the highest performance thermoelectric materials to date. Some examples will be discussed in later sections of this chapter. As discussed previously, the tuning of charge carriers is an important aspect of developing high performance thermoelectric materials. Band gap engineering to tune charge carriers by increasing or decreasing the band gap can be achieved through formation of solid solutions. A decrease in the band gap can be beneficial for increasing the carrier concentration for wide band gap materials, while increasing the band gap is useful for inhibiting the formation of undesired carrier types in small band gap or degenerate semiconductors.[31,69]

The band gap of isostructural materials tends to decrease when moving down a group on the periodic table. This is due to an increasing unit cell size and therefore decreasing amount of electron orbital overlap of the atoms resulting in bands with more spread-out energies. Large differences in electronegativity of the constituent atoms result in more ionicity and closer atoms giving rise to greater orbital overlap and larger band gaps which occur more often with lighter elements. The expected band gap of solid solutions is an intermediate of the end members based on the degrees of substitution.[14,50]

Solid solution band engineering can also be used to change the effective mass of the conduction and valence bands. As discussed previously, changes to effective mass can be used to influence carrier type, Seebeck coefficient, and carrier mobility. When multiple valence band minima (or conduction band maxima) are equal in energy at the same or different k-vectors, the bands are considered degenerate and the effective mass increases. Degeneracy can be induced if one end member of the solid solution has band valleys greater or less than another band valley and the other end member has opposite energy differences. At an intermediate solid solution substitution level, the band extrema will be equal in energy. Degeneracy can occur for band extrema at the same or different k-vectors.[31,32,36–38]

Band convergence approaches allow for increases in the Seebeck coefficient without decreasing carrier concentration or carrier mobility. The degeneracy induced here has the advantage over flat band degeneracies due to maintaining a relatively low inertial effective mass (m_I^*) while increasing the overall effective mass (m_{DOS}^*). This is achieved by aligning the energy of steep parabolic bands increases the overall effective mass while maintaining low inertial effective mass, also known as band valley degeneracy (N_V).[32,37] This band engineering strategy has been utilized to produce record thermoelectric performance in materials.

1.4.4 Solid Solution Effects on Thermal Conductivity

Optimization of thermoelectric performance through solid solutions can be realized by decreasing the lattice thermal conductivity of a given material. Reduction in thermal conductivity is achieved through increased phonon scattering as discussed in Section 1.3.7.3, specifically Equation 1-61. Solid solutions achieve increased phonon scattering through mass fluctuation, bond energy fluctuation, and generally increased disorder within the structure.[70] Mass fluctuation effects occur when there are differences in the atomic weight of the substituted atoms, where greater differences in mass increase scattering effect. The contribution of these effects to phonon scattering is quadratic, resulting in an inverse parabolic trend, with the lowest thermal conductivity typically found in the solutions with equal mixing of substituted atoms.

1.5 High Performance Thermoelectric Materials

High performance thermoelectric materials are those which display zT > 1 and are therefore viable for technological applications. There are many such materials which have been developed since the 1960s where Bi_2Te_3-based compounds reigned as high-performance materials with zT ~ 1 for decades. Advances in the material science and design of thermoelectrics improved greatly starting in the early 2000s. Use of targeted atomic scale defects through nano-structuring allowed for zT > 1.5

starting in 2010, $zT > 1.75$ was followed in 2015 using secondary phase band alignment, and finally band convergence materials were coupled with doping to achieve $zT > 2.25$ in 2013 and most recently $zT > 2.75$ in 2020.[2,3] Over the past couple decades there has been a revival in interest and promise for thermoelectric applications. Such materials and key innovations will be discussed in this section.

1.5.1 Metal Chalcogenide Thermoelectric Materials

Chalcogenide compounds are a diverse class of materials containing group VI (S, Se, Te) anions which gives rise to variety of structures and therefore properties. Metal chalcogenides, particularly those containing p-block elements (Sn, Pb, Bi, etc.) are well studied for thermoelectric applications. Many of these compounds have low thermal conductivity due to complex structures while still allowing for fine-tuning of electrical properties. This section will focus on some important structures and material properties which give rise to high thermoelectric performance.[2,16,71]

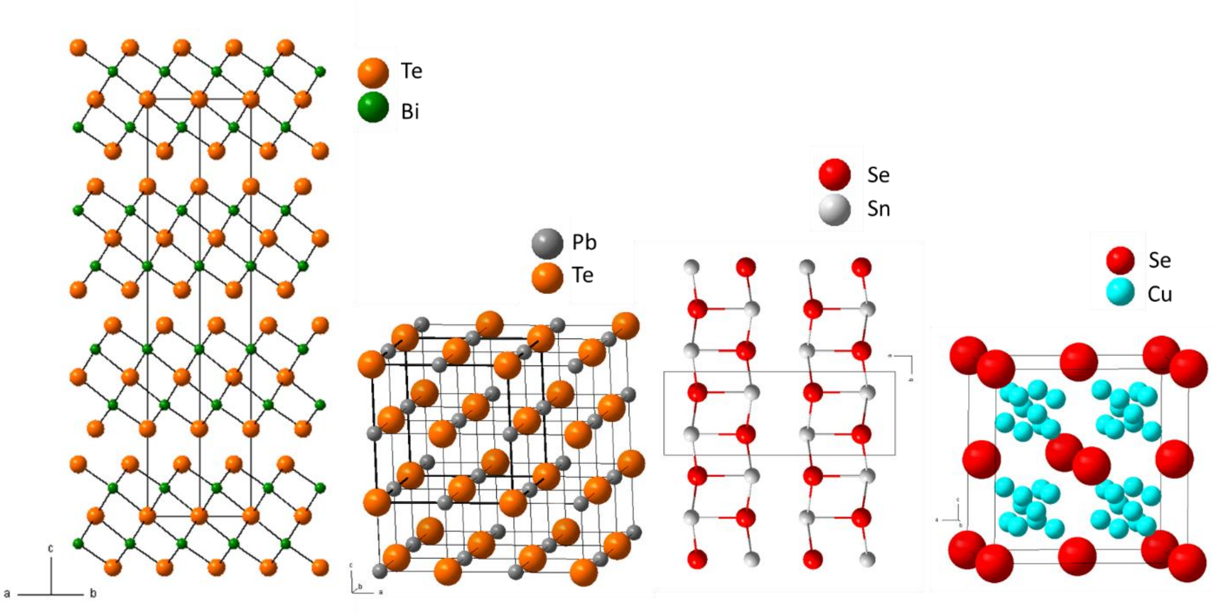

Figure 1.11: Crystal structures of high thermoelectric performance metal chalcogenides, from left to right: (a) Bi_2Te_3, (b) PbTe, (c) SnSe, and (d) β-Cu_2Se.

Bismuth telluride and similar isostructural relatives (Bi_2Te_3, Bi_2Se_3 and Sb_2Te_3) form in the $R\bar{3}m$ space group as rhombohedral crystals (Figure 1.11(a)) and can easily form solid solutions. The distorted rock-salt type layers are held together with Van der Waals forces creating a large, layered structure. This material has been used for decades in thermoelectric applications, particularly for cooling, and performs well near and below room temperature.[72] High thermoelectric performance is achieved due to the presence of six valleys on both the conduction and valence bands.

High performance of p-type $Bi_{0.5}Sn_{1.5}Te_3$ is achieved $zT = 1.86$ at 320 K through the formation of nano grain boundaries and dislocation arrays.[70] n-type $Bi_2Se_{0.3}Te_{2.7}$ achieves $zT = 1.20$ at 445 K by decreasing thermal conductivity through defect engineering.[73] While Bi_2Te_3 type materials have performed well for many decades the rarity of the elemental constituents in particular tellurium makes them expensive to produce. Due to instability at high temperatures these materials are also limited to lower temperature applications. These materials are still studied extensively and have been improved upon using modern nano structuring techniques.[71]

Lead chalcogenides form in the cubic $Fm\overline{3}m$ space group with a rock-salt structure type (Figure 1.11 (b)) which leads to anisotropic transport as bulk materials. Both valence and conduction bands display a 4-fold degeneracy at the L-point in the Brillouin zone improving the Seebeck coefficient.[74] Shifts in the valence bands of PbTe with increasing temperature widens the band gap reducing bipolar conductivity while increasing band degeneracy.[74] Alloying and formation of solid solutions is achievable with isostructural and more complex rock-salt structure types.[75] Band engineering and defect engineering through formation of solid solutions and synthesis techniques has stationed PbTe based materials as some of the best performing thermoelectric materials.[12,71]

High performance of p-type $(PbTe)_{0.8}(PbS)_{0.2}$ is achieved with 3% Na doping resulting in $zT = 2.30$ at 923 K due to the formation nano-scale precipitates reducing thermal conductivity below 1.0 W m^{-1} K^{-1}.[33] Doping with Al on the Pb site to produce n-type $Pb_{0.99}SeAl_{0.01}$ achieves $zT = 1.30$ at 850 K by increasing the Seebeck through creating resonant states within the conduction band.[76] There are many examples of high performance PbTe based materials employing a variety of optimization strategies.[71] These materials are of great interest as they are formed from cheap elements and perform well in relatively high temperature ranges.

In moving up the periodic table from Pb to Sn the formation of SnSe occurs in a layered orthorhombic structure (Figure 1.11(c)) with $Pnma$ space group from earth abundant elements. The layers are formed by strong Sn-Se zig-zag-like bonding in the b-direction and are held together with weaker Sn-Se bonds in the a-direction creating a chain-like structure. These materials display high thermoelectric performance as single crystals due to low thermal conductivity resulting from Peierls distortion (electron-phonon coupling) and weak bonding between the layers. The band structure of these materials can be manipulated through Se vacancies altering the structure of the bonding chains. Due to these properties, single crystals of SnSe have displayed p-type and n-type performance of $zT = 2.60$ at 973 K[77] and $zT = 2.20$ at 773 K[78] respectively along their b-axis. In a very similar manner of manipulating a chainlike structure through Peierls distortions, Se deficient $In_4Se_{2.67}Cl_{0.03}$ achieves an n-type $zT = 1.53$ at 700 K with formation nanocomposites.[79]

Copper selenide has recently attracted attention due to its outstanding thermoelectric performance and composition of earth abundant elements.[71] Below 396 K, Cu_2Se crystallizes in a Se close packed cubic structure with Cu tetrahedrally coordinated forming the α-phase.[80,81] Above this temperature the Cu atom sites become disordered (Figure 1.11 (d)) having differing occupancy at the sites forming the β-phase in an antifluorite structure. The disordered ionic lattice is responsible for very low glass-like thermal conductivity (0.8 $W\ m^{-1}\ K^{-1}$) but gives rise to material instability.[82] Interest in the material was heightened when copper deficient ($Cu_{2-x}Se$) p-type materials were shown to result in $zT = 1.6$ at 1000 K. Since then, various alloying, doping, nanocomposite, and addition of scattering mechanisms have been employed,[71] however the Al doped material $Cu_{1.94}Al_{0.02}Se$ has shown the highest performance with $zT = 2.62$ at 1029 K.[83]

1.5.2 Zintl Pnictide Thermoelectric Materials

Complex materials are well suited for thermoelectric applications due to their large structural anharmonicity which decreases thermal conductivity as discussed. Zintl phases are a diverse class of intermetallic compounds which are typically complex semiconductors fitting well into low thermal conductivity requirements. These materials are characterized by covalently bonded anionic substructures that are held together by a cationic matrix resulting in an overall charge balanced structure.[84–86]

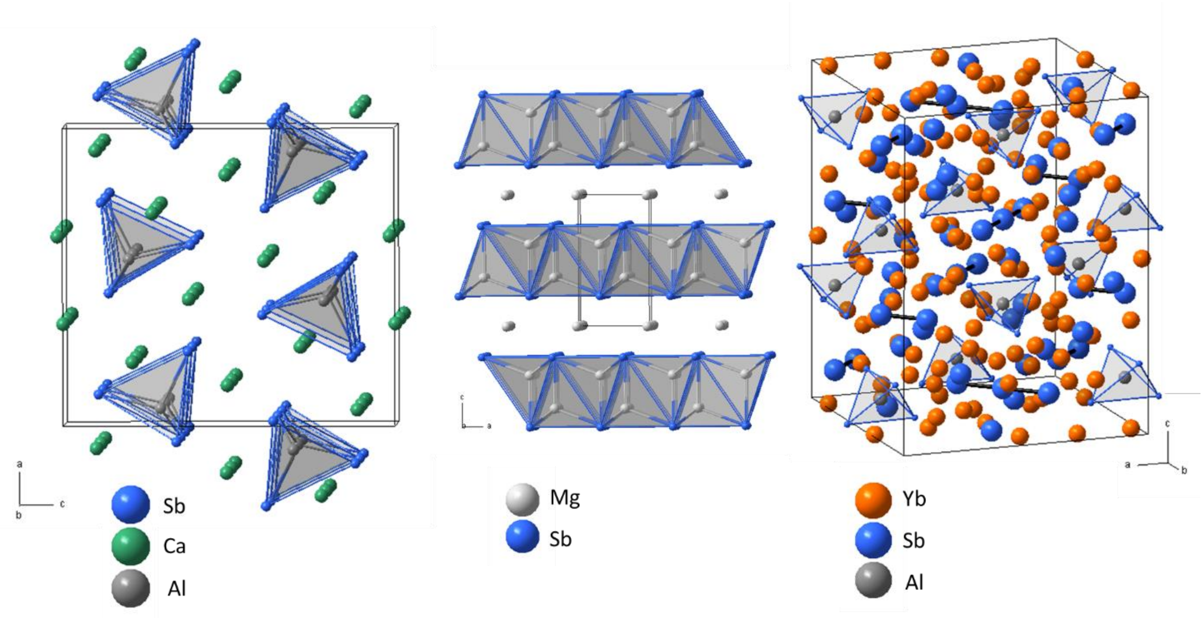

Figure 1.12: Crystal structures of the thermoelectric Zintl pnictides (a) Ca_3AlSb_3, (b) Mg_3Sb_2, and (c) $Yb_{14}AlSb_{11}$.

Ca_3AlSb_3 and similar structures ($Ca_5In_2Sb_6$, $Ca_5Sn_2As_6$, etc.) are intermetallic Zintl phases which are formed from $AlPn_4$ tetrahedra chains within a metal AE^{2+} matrix. The anionic chained substructure in Ca_3AlSb_3 has a formula of $[AlSb_3]^{6-}$ formed by $Al^{-1}Sb^{-1}(Sb^{-2})_2$ anions which are charge balanced by three Ca^{2+} cations. The resulting electronic structure is highly anisotropic and contains three valence band maxima. High anharmonicity leads to low lattice thermal conductivity ranging from 1.3 at 300K to 0.6 at 1000 K.[85,87] Doping with Na to produce $Ca_{2.97}Na_{0.03}AlSb_3$ results in p-type performance of $zT = 0.8$ at 1000 K.[88] Limited doping concentrations were achievable due to formation of undesired side products limiting TE performance. Similar performance is found in compounds such as Sr_3GaSb_3 ($zT = 0.9$ at 1000 K) and $Ca_5In_2Sb_6$ ($zT = 0.75$ at 900 K) with similar structures.[87,89]

Some of the most successful thermoelectric Zintl phases are the $CaAl_2Si_2$-type materials which includes Mg_3Sb_2 and many others.[90,91] These phases crystalize in the $P\overline{3}m1$ space group (Figure 1.12 (b)) with anionic $[Al_2Si_2]^{2-}$ slabs separated by single cationic Ca^{2+} layers. A distinct advantage that these phases have over other Zintl phases is the high degree of tunability through formation of solid solutions and doping. The valence bands contain N_V = 3 valleys, whereas the conduction bands contain up to N_V = 9 valleys which can be converged through alloying. p-type doping can be performed using cation vacancies or substitutions with alkali metals, whereas n-type doping has been achieved using excess cations and group VI substitutions. Thermoelectric performance of p-type $YbCd_{1.6}Zn_{0.4}Sb_2$ achieves $zT = 1.2$ at 700K through reduction of thermal conductivity while leaving carrier mobility intact.[92] The alloys $Mg_3Sb_{2-x}Bi_x$ have produced impressive performance with $zT = 1.6$ at 600 K for x = 1 due to reduction of bipolar carriers and band convergence. This performance of $Mg_3Sb_{2-x}Bi_x$ is the highest performing n-type material within the 300 K to 600 K temperature range.[93]

Discovery of the complex Zintl material $Yb_{14}AlSb_{11}$ ($zT = 1$ at 1200 K) was exciting due high temperature (> 900 K) thermoelectric performance breaking a 20-year stagnation.[94] The $Ca_{14}AlSb_{11}$-type materials crystallize in $I4_1/acd$ space group (Figure 1.12 I) which consists of $[AlSb_4]^{9-}$ tetrahedra, $[Sb_3]^{7-}$ linear units, and isolated Sb^{3-}, charge balanced in a Ca^{2+} cation matrix. There are many analog compounds with this structure type that have been studied however p-type $Yb_{14}MnSb_{11}$ shows the best TE performance with $zT = 1.2$ at 1275 K.[95] High TE performance of these materials is attributed to the phonon glass electron crystal (PGEC) characteristics which scatter phonons without disrupting carrier movement reaching thermal conductivity as low as 0.5 W m^{-1} K^{-1}.[96] Some of the phonon scattering is attributed to the interesting Sb_3^{7-} units which display high thermal fluctuations.[91]

Structural complexity of Zintl intermetallic phases provides a good starting basis for thermoelectric optimizations due to low thermal conductivity and high temperature stability. Some downsides of this class of materials include low carrier mobility and limited band engineering options. Most Zintl phases are p-type materials which can be easily doped with p-type carriers, however there are few n-type options.[85–87]

1.6 Magnesium Silicide-Stannides as High-Performance Thermoelectrics

Magnesium silicide based materials Mg_2Cn (Cn = Si, Sn, Pb) have attracted increasing attention since 2006 due to their high chemical stability and high efficiency,[97] particularly since a zT of above unity was achieved in Sb-doped $Mg_2(Si,Sn)$ solid solutions,[36,69,98] comparable with the state-of-the-art high temperature TE materials such as PbTe and filled skutterudites.[34,99] These materials display optimal properties within temperatures ranging from 500 K to 800 K, are comprised of abundant raw materials, very cheap, benign to the environment, and stable at relatively high temperatures, which makes them ideal for device applications.[100–102]

Mg_2Cn-type (Cn = Si, Sn, Pb) materials crystallize in the relatively simple antifluorite structure-type (Figure 1.13), where the 8c (¼, ¼, ¼) and 4a (0, 0, 0) sites are occupied by Mg and Cn, respectively.[103] Mg atoms have also been observed interstitially at the 4b (½, ½, ½) site, which significantly influences the physical properties, and are more likely to occur than other point defects.[100,104,105] As discussed previously the interstitial point defects increase phonon scattering and can act as a source of electron doping.

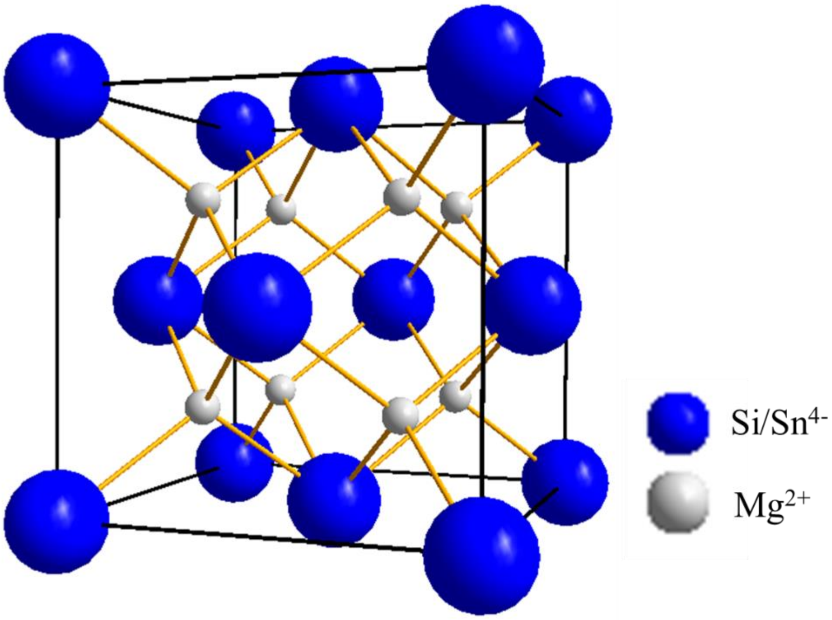

Figure 1.13: Antiflourite crystal Structure of Mg_2(Si, Sn)

Alloys of Mg_2Si and Mg_2Sn have been studied extensively showing excellent TE performance with n-type dopants.[105–107] Band structures for Mg_2Si and Mg_2Sn are shown in Figure 1.14. Here there are two distinct bands at the X point, a heavy (blue) and light (red) formed from hybridized Mg 3s and Cn d-t_{2g} and hybridized Mg 3p, Cn s, and Cn d-e_g orbitals respectively. For Mg_2Si the light band is lower in energy than the heavy band and for Mg_2Sn the heavy band is lower in energy. Therefore, there will be an intermediate solid solution where these two bands have equal minimum energy at the band edge. The existence of a miscibility gap in the Mg_2Si-Mg_2Sn phase space limits stoichiometry options and complicates synthetic procedures.[108] However, the degenerate conduction bands result from a solid solution of $Mg_2Si_{1-x}Sn_x$ ($0.6 \le x \le 0.7$) allowing for an enhanced Seebeck coefficient due to an increased density of states, and the solid solution is fully miscible at these stoichiometries.[108]

Pnictogen based dopants are readily incorporated into the structure on the Cn-sites, allowing for control and optimization of the n-type electrical properties. Mass fluctuation effects are expected from the significant difference between the masses of silicon and tin, which contribute to a lowering of the lattice thermal conductivity, ideal for TE materials.

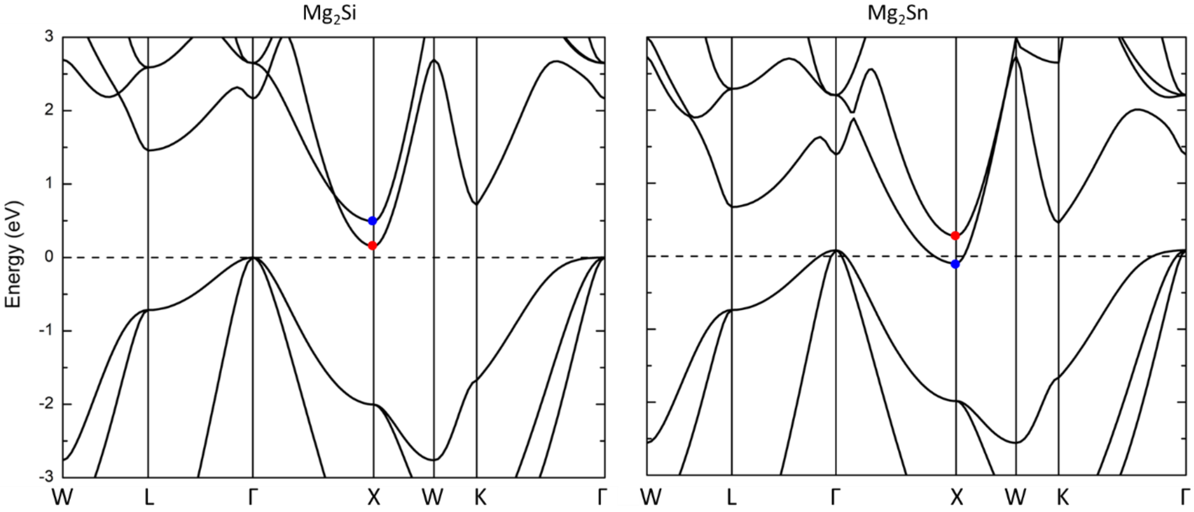

Figure 1.14: Electronic band structure of Mg_2Si (left) and Mg_2Sn (right). The parabolic conduction bands at the X point are highlighted, where the "light" band (red) is lower in energy for Mg_2Si, whereas the "heavy" band (blue) is lower in energy for Mg_2Sn.

Due to the above stated properties, n-type materials such as $Mg_{2.15}Si_{0.28}Sn_{0.71}Sb_{0.006}$,[109] $Mg_{2.16}(Si_{0.4}Sn_{0.6})_{0.97}Bi_{0.03}$,[110] $Mg_2Si_{0.53}Ge_{0.05}Sn_{0.4}Bi_{0.02}$,[111] and $Mg_2Si_{0.3}Sn_{0.665}Bi_{0.035}$,[112] all achieve outstanding figures of merit values between 1.2 and 1.4 from 750 K to 850 K.[113] Performance of p-type materials $Mg_{1.86}Li_{0.14}Si_{0.3}Sn_{0.7}$ by doping with Li is significantly lower (0.5 at 773 K) due to fewer converging bands.[114] Overall, Bi-doped $Mg_2Si_{1-x}Sn_x$ samples have shown some of the best thermoelectric properties compared to Cu-, Al-, P-, and Sb-doped samples.[115–117] This is likely due to a heavier mass and a larger radius causing local distortions (M_{Bi} = 208.9 g mole^{-1}, r_{Bi} = 1.60 Å) in comparison to the host atoms (M_{Si} = 28.1 g mole^{-1}, r_{Si} = 1.10 Å; M_{Sn} = 118.7 g mole^{-1}, r_{Sn} = 1.45 Å), further contributing to a reduction in thermal conductivity.

A breadth of synthetic methods has been performed to obtain Mg_2Cn based compounds and to improve the thermoelectric properties including solid state reaction,[115] flux synthesis method,[118] mechanical alloying,[119] hot pressing,[112] spark-plasma-sintering (SPS),[100,117] melt casting,[120,121] and nano-composites.[113,122] The use of expensive sacrificial reaction crucibles such as BN or tantalum crucibles is standard to avoid Mg volatilization and reaction with the container.[112] Similar processes employ heating under argon flow with non-reusable small scale graphite containers.[123] More recent studies recognize the viability of doped Mg_2(Si,Sn) for device applications[124] and some propose methods to scale-up synthetic processes.

A 2017 report focused on Al- and Bi-doped Mg2Si; batches of 1 kg were prepared via ball-milling of the elements, followed by cold-pressing and heating of 100 g pellets in alumina crucibles in parallel quartz tubes at 823 K for 6 hours under vacuum. Thereafter, the samples were again ball-milled and then sieved to use only particles with a diameter below 53 µm. Finally, the samples were consolidated into round 2.5 cm pellets by either hot-pressing or spark-plasma-sintering, both at 1023 K. The best performance was found for hot-pressed $Mg_{1.96}Al_{0.04}Si_{0.97}Bi_{0.03}$ with a peak zT value of 0.98 at 873 K.[125]

In 2019, large samples of $Mg_2Si_{0.3}Sn_{0.675}Bi_{0.025}$ were prepared by spark-plasma-sintering three times between 973 and 1273 K, followed by ball-milling for 12 hours, and finally consolidated again by spark-plasma-sintering at 973 K into round pellets with diameters of 5 and 7 cm, respectively, resulting in reproducible peak zT values of 1.3 at 773 K.[126] The work presented in Chapter 3 will focus on the development of a similar scaled-up synthesis technique as a step towards utilizing Mg_2Cn based materials in thermoelectric devices. The aim of the developed process is to simplify synthesis and produce consistent high performance TE material.

1.7 Chalcopyrite as Thermoelectric Materials

Chalcopyrite materials have been studied for technological applications since the middle of the 20th century with applications including nonlinear optics,[127–130] photovoltaics,[131–135] and LEDs[136] among others.[137,138] Thermoelectric application of chalcopyrite was first explored in the 1960s for pure compounds due to the availability of p- and n-type dopants and inexpensive elemental constituents. While the materials studied displayed high carrier mobility the performance was not competitive enough for applications.[139] Recently chalcopyrite have been revisited as thermoelectric materials by applying band engineering and nano structuring strategies.[138] High thermoelectric performance (zT) has been achieved using chalcopyrite materials some in line with state-of-the-art materials.[140–148]

Chalcopyrite compounds crystallize in $I\bar{4}2d$ space group symmetry (Figure 1.15 (c)) with a charge balanced stoichiometry ABX_2, where A and B are cations and X are anions. Two families of chalcopyrite are the chalcogenide and pnictide compounds consisting of group constituents $A^{I}B^{III}C^{VI}_{2}$ and $A^{II}B^{IV}C^{V}_{2}$ respectively. There are 26 known chalcogenide compounds (A = Li, Cu, Ag; B = Fe, B, Al, Ga, In, Tl; and X = S, Se, Te) while there are 17 known pnictide compounds (A = Mg, Zn, Cd; B = Si, Ge, Sn; and X = P, As, Sb).[149]

The structures can be thought of as an extension of the zinc blende structure type (Figure 1.15 (b)) which in turn is an extension of the diamond structure type (Figure 1.15 (a)). Diamond structure type is formed by two interpenetrating fcc lattices offset by (¼, ¼, ¼) with all atoms tetrahedrally coordinated. The interpenetrating fcc lattices in zinc blende are of the differing atom types. For chalcopyrite structure the interpenetrating lattices are formed from the cations and anions similarly to zinc blende. The anions are tetrahedrally coordinated by alternating cation type. The lattice is doubled in the c-direction because the cation fcc lattices are rotated 90 degrees and inverted about a central atom also known as an S_4 improper rotation.[150]

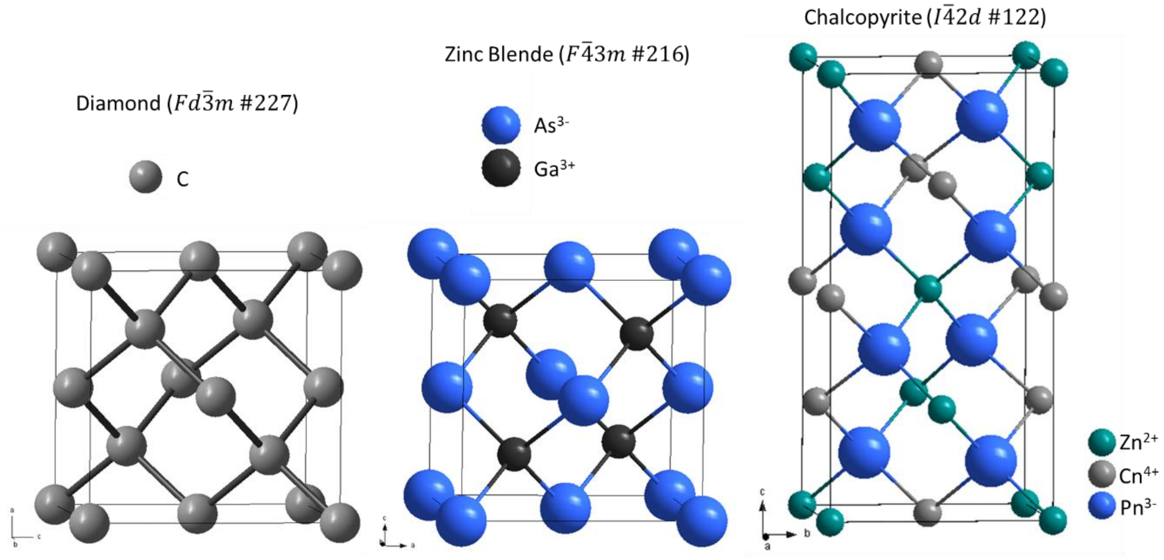

Diamond ($Fd\bar{3}m$ #227)

Zinc Blende ($F\bar{4}3m$ #216)

Chalcopyrite ($I\bar{4}2d$ #122)

Figure 1.15: Crystal structures of Diamond, GaAs, and $ZnSnAs_2$ from left to right. Chalcopyrite structures can be thought of as derived from zinc blende which can also be thought of as an extension of the diamond structure semiconductors silicon and germanium.

The chalcopyrite family provides an interesting template for development as thermoelectric materials. The large tetragonal structure compared to the zinc blende family of semiconductors has double the atoms per unit cell providing lower thermal conductivity. Constituents for the formation of solid solutions are readily available due to the variety of isovalent and isostructural members allowing for further reduction of thermal conductivity through the mass fluctuation effect. Band gaps of the compounds range from nonexistent to 3.5 eV offering tunability of the electronic properties. Doping of the three available sites allows for the addition of either n-type or p-type carriers.

The electronic band structures of the compounds display multiple converging bands at both the valence and conduction band edges. Some compounds display steep parabolic bands which are degenerate improving the Seebeck coefficient while maintaining high carrier mobility while others display flat bands reducing carrier mobility but improving Seebeck. Through solid solutions intermediate band structures should be attainable. Band degeneracies are closely related to the tetragonality ($c/2a$) of the structure. When $c/2a = 1$ the structure is perfectly tetragonal and pseudocubic. The convergence of bands under these criteria can be seen at the W point in the band. Band engineering has been performed through the formation of solid solutions where one end member has $c/2a > 1$ and the other has $c/2a < 1$and an intermediate composition has $c/2a = 1$. This technique has been used to significantly improve Seebeck coefficient and therefore thermoelectric performance.

The characteristics described above have resulted in the development of some high TE performance in chalcopyrite chalcogenides. $CuGaTe_2$ is a p-type material with a relatively high Grüneisen parameter $\gamma = 1$ resulting in low Thermal conductivity due to Umklapp scattering, and band degeneracy is expected due to high tetragonality ($c/2a = 0.99$) resulting in improved Seebeck coefficient. This material achieves $zT = 1.4$ at 950 K without doping.[144] Similar high performing chalcopyrite materials include n-type $Ag_{0.9}Cd_{0.1}InSe_2$ ($zT = 1.1$ at 900 K),[147] $CuIn_{1-x}Ga_xTe_2$

Little work has been performed on pnictide based chalcopyrite materials for thermoelectric applications. Of the 64 possible combinations of the $A^{II}B^{IV}C^{V}_2$ only 48 have been calculated to be stable and only 17 have been confirmed.[149,151] Some of the reason for this is due to the difficult synthesis due to high volatility of the group II and group V elements. Low temperature stability of the Sn based materials is another limitation for both synthesis and application.[152] Recently there has been promising first principles calculations performed on the $A^{II}B^{IV}C^{V}_2$ compounds suggesting competitive thermoelectric performance.[142,153–155] The abundance of raw elemental constituents of these compounds makes them appealing for TE applications.

The work presented in Chapters 4 and 5 are focused on the development of pnictide chalcopyrite solid solutions $ZnGe_{1-x}Sn_xP_2$, $ZnSnP_{2-x}As_x$, and $ZnGe_{1-x}Sn_xP_{2-y}As_y$. A novel study of the synthesis of these compounds and their solid solutions via mechanochemical methods is conducted. The structural, electronic structure, and thermoelectric properties of these materials are examined.

1.8 Zintl Compound $Ca_{11}Sb_{10}$

$Ca_{11}Sb_{10}$ is an interesting Zintl compound with potential as a thermoelectric material due to structural complexity, high temperature stability, and semiconducting behavior. The material crystallizes in the $Ho_{11}Ge_{10}$ structure type (Figure 1.16) in the $I4/mmm$ space group.[156] The large body-centered tetragonal unit cell contains an unusual charge balanced stoichiometry. A unit cell contains two Sb_2^{4-} dumbbells, 0.5 Sb_4^{4-} anionic square subunits, and four Sb^{3-} isolated anions for a total anion charge of -22; these are balanced by 11 Ca^{2+} cations. The Sb_4^{4-} subunits are like those found in filled Skutterudites,[157] and Sb_2^{4-} subunits like those found in Zn_4Sb_3 materials;[158] both established thermoelectric materials with low thermal conductivity. There are a few pnictide based isostructural analogs to $Ca_{11}Sb_{10}$ with the formula $M_{11}Pn_{10}$ (M = Ca, Sr, Ba, Yb, Eu; and Pn = As, Sb, Bi). Until recently the structure was not known to accommodate lower mass pnictides (As and P) as they rarely form the dumbbell and square subunits. However, in 2022 the $Ca_{11}As_{10}$ compound was synthesized and structurally characterized.

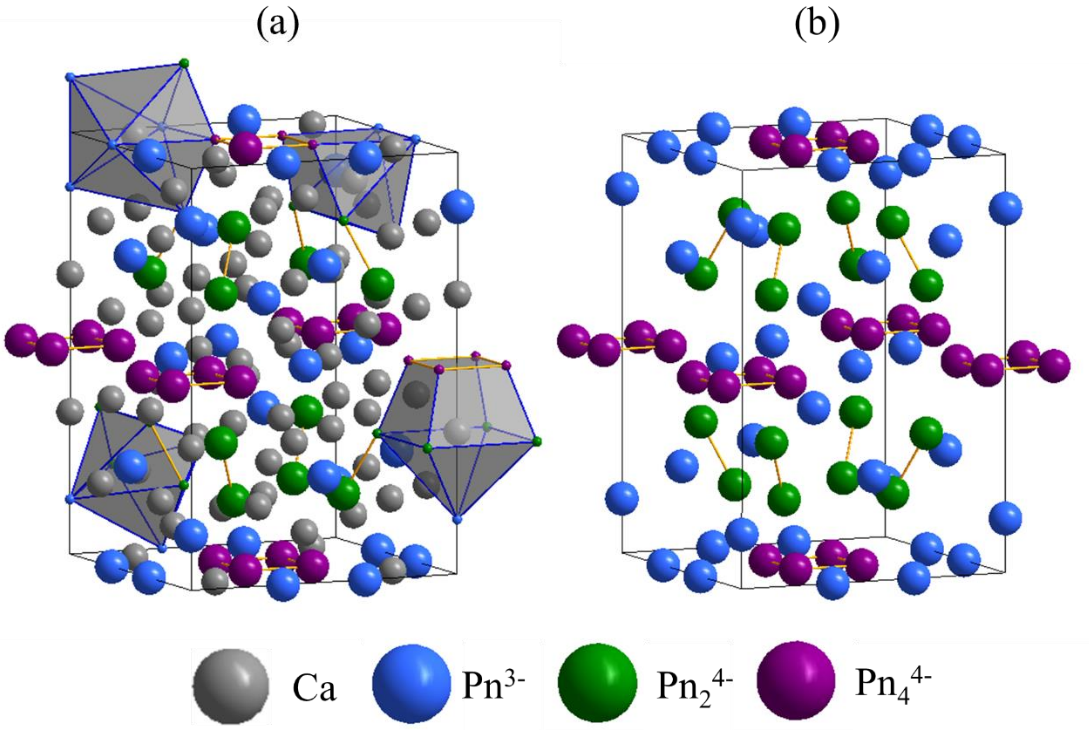

Figure 1.16 : Crystal structure for $Ca_{11}Sb_{10}$ (a) complete structure with unique polyhedral of the Ca environments and (b) anionic sublattice displaying connectivity through the cell.

Synthetic methods for these compounds have been limited to off stochiometric approaches,[156,159] tin flux,[160,161] and arc melting[162] to obtain single crystals. Direct synthesis of $Ca_{11}Bi_{10}$ is especially difficult due to incongruent melting behavior at 1075 °C, while $Ca_{11}Sb_{10}$ congruently melts at 985 °C.[163] The highly reactive and volatile calcium metal poses synthetic challenges as it comprises most of the chemical formula. Standard fused silica reaction ampules react with calcium at elevated temperatures while the high vapor pressure requires closed reaction systems.

Thermoelectric performance of these compounds has been underwhelming despite reports of low glasslike thermal conductivity of less than 1.0 W m^{-1} K^{-1} for all compounds.[160,162] The Seebeck coefficients in studies of these materials display p-type conductivity with indications of a high degree of bipolar conductivity. Two separate studies of Sn-flux synthesized $Ca_{11}Sb_{10}$ show very different results such as n-p transitional behavior (S = -7 at 300 K to ~20 at 1100 K)[160] with another displaying bipolar p-type behavior (20 μV K^{-1} at 300 K to 15 at 700 K).[162] The low Seebeck coefficients found have resulted in poor TE performance with a highest reported value of $zT = 0.025$ at 1200 K for

$Yb_{11}Sb_{9.3}Ge_{0.5}$.[161] Indications of residual tin flux may be a contributing factor for increasing bipolar conductivity resulting in poor thermoelectric performance.[160,161]

Chapter 6 of this thesis focuses on the development of a direct synthetic method for $M_{11}Pn_{10}$ compounds, specifically $Ca_{11}Sb_{10}$, $Ca_{11}Bi_{10}$, and $Ca_{11}As_{10}$ which attempts to avoid sources of contamination. The solid solutions $Ca_{11}Sb_{10-x}Bi_x$ and $Ca_{11}Sb_{10-y}As_y$ are explored for miscibility ranges, structural effects, and thermoelectric properties.

1.9 Scope of Thesis

Recent major advancements in thermoelectric material performance center around the development and understanding of band structure engineering techniques and phonon scattering mechanisms. Solid solution materials have the potential to access these major strategies simultaneously within a single system. Band convergence to increase the Seebeck coefficient is achieved by optimizing the composition of a solid solution while site mixing creates mass fluctuation effects decreasing the thermal conductivity. Electrical carrier tuning can also be achieved through solid solution strategies which are essential to optimizing TE materials.

In this thesis solid solutions as thermoelectric materials are explored. Electronic structures are examined to understand established materials and propose band engineering strategies. New synthesis approaches for established materials are designed while established methods are utilized to synthesize novel solid solutions. Thermoelectric properties are measured and discussed in terms of the underlying chemistry of the materials. Future work is proposed for the systems studied where improvements can be suggested.

This chapter discussed the various principles underlying the design and application of thermoelectric materials with a focus on solid solutions for thermoelectric applications. Strategies which will be followed and discussed for the materials studied in Chapters 3-6 are outlined. An overview of current high-performance materials and the principles which provide their status is presented. Finally, the classes of materials which are experimentally studied are discussed to provide motivation for the research conducted. Chapter 2 provides principles for the theoretical methods, experimental methods, and instrumentation utilized to study the properties of thermoelectric materials.

The first solid solution material studied is $Mg_2Si_{0.3}Sn_{0.67}Bi_{0.03}$ presented in Chapter 3, a well-established TE material. A scaled-up reaction process was developed providing the first steps towards device applications. A large, condensed piece of material was pressed on a scale which had not been achieved previously. Statistical analysis of measured TE properties is performed on the material using samples cut at various positions and orientations. These methods are used to assure a consistent quality of the process and material which is the first step towards establishing device applications.

Pnictide chalcopyrite solid solutions are investigated in Chapters 4 and 5 with $ZnGe_{1-x}Sn_xP_2$ explored in the former and $ZnSnP_{2-y}As_y$ and $ZnGe_{1-x}Sn_xP_{2-y}As_y$ explored in the latter. A primary focus in Chapter 4 is overcoming the synthesis challenges posed by the end members as well as the solid solutions. The developed synthesis method is therefore primarily discussed in Chapter 4 but utilized for synthesis in Chapter 5. Structural investigations are conducted on the solid solutions using Rietveld refinement results of PXRD data. Electronic structure calculations (BS, DOS, and BoltzTraP) are explored for comparison with measured properties and to develop strategies for future optimizations. Finally thermoelectric properties of the solid solutions are measured and discussed with respect to the solid solution composition.

The final solid solutions explored are the $Ca_{11}Sb_{10-x}Bi_x$ and $Ca_{11}Sb_{10-y}As_y$ series in Chapter 6. A direct liquid solid method is used to synthesize the materials which have not been previously studied. Single crystals of $Ca_{11}Sb_{10-x}Bi_x$ are obtained and the structural properties are studied with respect to substitution. The electronic properties are calculated for the purpose of developing future strategies and understanding the resulting properties. Thermoelectric properties of the solid solutions are measured and discussed, and $Ca_{11}Sb_{10}$ results compared to other literature studies of the compound.

Chapter 2: Experimental Methods

This chapter will discuss the background and techniques utilized during the experimental work for this thesis. The procedures and theories outlined here describe the general approaches taken in the laboratory setting, while the project-specific methods will be addressed in their respective chapters. Synthesis, instrumentation, and simulation techniques will be discussed in principle and practice ordered with respect to the overall experimental process.

2.1 Material Preparation

All synthetic techniques outlined below used elemental reagents as starting constituents for sample preparation. Powdered samples and starting reagents were handled and stored in an argon atmosphere MBRAUN glove box to prevent oxidation. Weighing of samples and starting reagents was achieved using a precision microbalance within the glove box. The loading of samples and reagents was also performed inside the glove box to properly control reaction vessel atmosphere. Constant circulation purification typically kept the H_2O and O_2 levels below 0.1 and 0.6 ppm, respectively.

2.1.1 Liquid-Solid Synthesis

Liquid-solid synthesis is a synthesis process in which the reactant constituents are brought to melt at high temperatures and then cooled down to form a solid, typically polycrystalline product. The molten liquid solution is considered homogenized and uniform and must be higher in temperature than the desired products melting temperature. Cooling of the liquid solution ideally crystallizes the material uniformly without formation of undesired side products. Phase diagrams of the constituent reactants are important for planning liquid-solid synthesis processes such as in Figure 2.1. The formation of undesired side products can occur when the target product melts incongruently. Liquid solutions containing liquidus phase curves at temperatures higher than the desired product and composition are unideal for liquid-solid synthesis. Fast cooling or crash cooling through a liquidus region can be used to limit the formation or undesired side products.

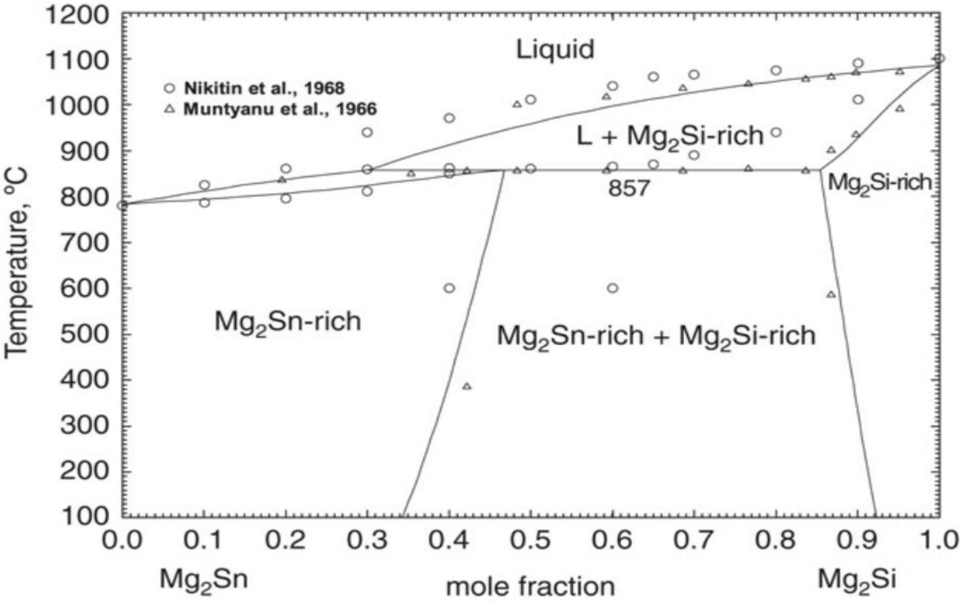

Figure 2.1: Liquid-Solid phase diagram of the Mg_2Sn-Mg_2Si system with component composition versus temperature used to plan reaction conditions[‡].[108]

Solid solutions can be formed from liquid-solid synthesis if constituent compounds are congruently melting, and the solution is miscible. In some cases, there will be a liquidus region in which the constituent compounds will separate, however solid annealing within a miscible region can be used to form the complete solid solution.

Reaction vessels for liquid-solid synthesis must be unreactive to the liquid mixture, withstand any increases in vapor pressure, and withstand any thermal expansion from the reactants or products. In this work, an in-house liquid-solid reactor was developed for magnesium-silicide-stannide and will be discussed in a subsequent chapter in detail.

Most liquid-solid and solid-solid reactions were performed in evacuated fused silica ampules. If the starting elemental reagents were reactive with silica, then a graphite coating was fused to the unloaded tubes. Starting elements were loaded into the open tubes with a funnel for powdered materials and directly for larger solid pieces. Specific heating profiles and techniques were used based

---

[‡] Reprinted with permission from (In-Ho Jung, Dae-Hoon Kang, Woo-Jin Park, Nack J. Kim, SangHo Ahn CALPHAD 31, 192–200, 2007) Copyright (2007) by Elsevier

on the targeted materials and starting constituents. Scaled-up liquid-solid synthesis was performed in specially designed graphite crucibles, placed in a vertical tube apparatus under constant argon atmosphere.

2.1.2 Mechanochemical Synthesis

Mechanochemical synthesis is the process of using high energy kinetic collisions to mechanically react reagents together. The method crushes material into fine powders which mix and undergo chemical reaction by increasing material stress, surface area, and local temperature. Fine powdered products can be formed on the low micro scale which can be advantageous for targeted applications. Typically, brittle starting materials are chosen, as ‘soft’ materials tend to deform and agglomerate inhibiting crushing and reactions. This work utilizes a planetary ball-milling process to achieve successful formation of solid solutions.

In planetary ball-mills, the jars are attached to a disk that rotates around a central axis while the jars rotate around their own axis in the opposite direction as seen in Figure 2.2(a). High rotation speeds of the jars and disk creates large impact energies of the milling balls, which crush powder samples between ball and jar surfaces. The ratio of the disk revolution frequency (ω_d) and the jar rotation frequency (ω_r) is defined by the ratio which is specific to the milling instrument used:[164]

$$k = \frac{\omega_r}{\omega_d} \tag{2-1}$$

Several milling conditions influence the outcome of the mechanochemical process; these parameters are as follows: revolution/rotational speed, milling time, filling ratio of milling balls, and filling ratio of grinding material. These parameters are not independent from one another and should be varied to optimize the specific process.[165,166] The movement of balls within are influenced by the operating parameters and manifest in different motion patterns: cascading, cataracting, or rolling; the cataracting motion (Figure 2.2 (b)) produces the largest number of high intensity impacts.[164,167–169]

The specific energy imparted on a mass of material (m_p) is a useful variable as it is independent of the type of milling process used. A generalized relation of the total energy to the powder mass can be used:

$$E_i = \frac{\sum_{j=1}^{n} SE_j \Delta SF_j}{m_p} \times t = \frac{SN \times \overline{SE}}{m_p} \tag{2-2}$$

Where the total specific energy (E_i) is given by the stress energy (SE_j) and frequency of stress events (ΔSF_j) at intervals (j) for a given time (t) divided by the mass; this is equal to the number of stress events (SN) multiplied by the average stress energy ($\overline{SE}$) for the total process. The milling parameters mentioned above relate to the stress energy by:

$$SE = \frac{v_j^2 m_1 m_2}{2(m_1 + m_2)} \tag{2-3}$$

with v_j as the impact velocity of two colliding bodies with masses m_1 and m_2.[170,171] The specific energy increases linearly with the number of collisions and therefore the number of balls and is also proportional to the revolution speed. Higher mechanochemical activation is achieved when the specific energy increases, and maximum specific energy is the critical energy before ball rolling motion occurs.

The grinding rate (K_p) is the rate of particle breakage and it has been shown to have a linear relationship with specific energy for planetary ball-mills.[172–174] Experimental data has been used to develop the empirical relation for particle size with respect to grinding rate:

$$\frac{D_t}{D_0} = \left(1 - \frac{D_l}{D_0}\right) e^{-K_p t} + \frac{D_l}{D_0} \tag{2-4}$$

The normalized median size (D_t/D_0) decreases rapidly in the initial stages of grinding and tends to level off as the process continues toward the median size at the grinding limit (D_l). There is a strong positive relationship for grinding rate for revolution speed.[175]

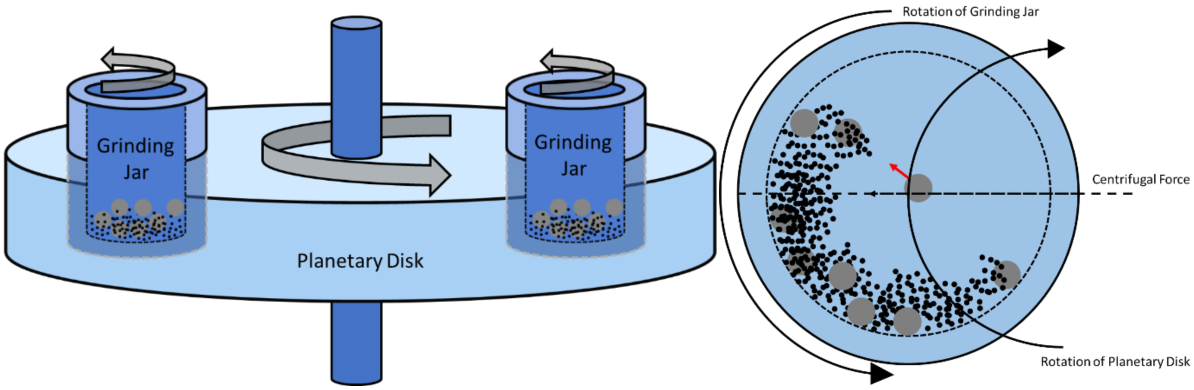

Figure 2.2: Schematic diagram of a planetary ball-mill process where (a) the planetary disk rotates with revolution speed ω_d and the grinding jars counter rotating at a speed ω_r (b) the cataracting movement of milling balls in the jar producing high energy collisions.

Mechanochemical techniques in this work were performed as comminution and reaction steps which were often followed by solid-solid reaction and sintering. Zirconia lined mill jars were loaded with reaction components and zirconia grinding balls under argon atmosphere. A typical ball to sample mass ratio of 10:1 was used, with some variations depending on sample. The sealed jars were placed into a FRITSCH Pulverisette 7 planetary micro mill. Comminution is achieved by the grinding of the loaded sample between the mill jar and grinding balls. The planetary action creates centrifugal forces which allow for high energy impacts resulting in fine particle sizes and homogeneity of the samples. Specific ball-milling details are discussed in the experimental methods section for the corresponding project chapters.

2.1.3 Sintering and Densification

Powdered samples were densified into bulk samples for the analysis of their physical properties. Densification of samples were performed via an Oxy-Gon FR-210-30T-ASA-160-EVC hot press furnace system. The schematic diagram of the system is shown in Figure 2.3. A sample is placed into a hardened graphite die between hardened graphite plungers under inert gas or reducing atmosphere. A hydraulic press applies a user specified force to the sample while heating elements apply controlled heat to the samples. The high-pressure sintering technique produces a flat cylindrical polycrystalline pellet with near single crystal densities.

Bulk polycrystalline samples are densified to near single crystal densities for physical property measurements. The applied pressure scales with the expected sample density, where for higher crystal densities higher pressures are required. Sintering temperatures are typically below the melting or decomposition temperature of the targeted compound. The amount of time which pressure and temperature are applied with depend on the sintering kinetics which is proportional to the temperature.[176] Increasing time of applied conditions also increases the size of grain boundaries in the materials which effects the material's density and bulk properties. A pressure free cool down is used to prevent pellet cracking due to differences in the coefficient of thermal expansion (CTE) between the die/plunger and the sample. The specific experimental details for each sample will be discussed in the corresponding chapters.

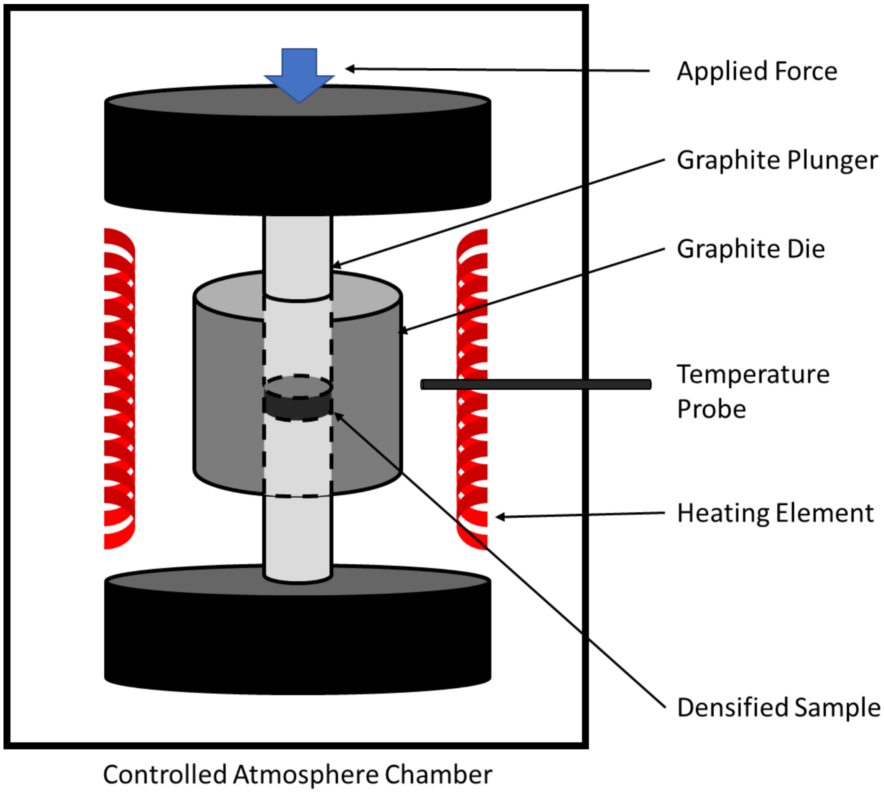

Figure 2.3: Schematic diagram of the OXY-GON hot-pressing system operation with labeled elements

2.2 Chemical and Structural Analysis

Chemical and structural identification methods are essential tools for developing targeted synthesis procedures and understanding structure-property relationships. Various techniques were used to analyze and characterize the obtained samples. These methods are discussed in this section in a broad context to allow for more specific discussions in the following chapters.

2.2.1 Density Measurements (Archimedes' method)

The density of crystalline materials is a property inherent to the atomic structure where for a perfect crystal:

$$d = \frac{ZM_a}{V_c N_A} \tag{2-5}$$

with M_a as the formula mass, Z is the number of formulae per unit cell, V_c is the unit cell volume, and N_A is Avogadro's number. Polycrystalline materials are bulk materials formed from many single crystallites separated by grain boundaries and empty space. The amount of empty space in the material is called porosity and is 100% less the density. The measured density is an indication of the quality of the densification process and is ideally 95% or above of the single crystal density.

The method used to measure density is the Archimedes method which is used to determine the specific gravity of a solid submerged in a liquid. The Archimedes method is advantageous in that the measurement doesn't require the sample to have regular geometry.[177] The equipment used is the Sartorius YDK01 density determination kit which is used for solids with specific gravity greater than that of a reference liquid. The liquid acts on the solid with a buoyant force and the weight of the liquid displaced is proportional to the volume of the solid:

$$d_{solid} = \frac{m_{air} \times d_{liquid}}{m_{air} - m_{liquid}} \tag{2-6}$$

Here the density of the solid, d_{solid}, can be determined from the sample weight in air (m_{air}) and weight in liquid (m_{liquid}) measured by a hydrostatic balance, with the density of the liquid (d_{liquid}) enacting the buoyant force. Ideally this measurement provides an accuracy one percent for density.

It is difficult to obtain ideal conditions for this process however, and certain other conditions must be considered for accuracy. This includes temperature dependence of liquid density, buoyancy of air, level of the sample holder immersion, liquid adhesion on the assembly, and air trapped on the sample or holder.

The temperature of the immersion liquid needs to be measured to determine its density. The effect of temperature on the liquid density is in the range of 0.1%/degree for alcohols or hydrocarbons and

0.02%/degree for distilled water. Tables and equations can be used to estimate the liquid density at a given measured temperature. The immersion liquid used should be considered per sample for distilled water is widely available with low density temperature dependence, whereas alcohols and hydrocarbons are typically unreactive with bulk samples sensitive as opposed to water.

To correct for errors due to air buoyancy the density of air under standard conditions, $d_{air} = 0.0012$ g/cm^3, is included in the formula:

$$d_{solid} = \frac{m_{air} \times (d_{liquid} - d_{air})}{m_{air} - m_{liquid}} + d_{air} \tag{2-7}$$

A correction for the submersion level of the sample holder and sieve must be considered. For this, the geometry of the sample holder in the measurement setup with respect to its immersion depth is factored in. A correction factor of 0.99983 for the errors from changing immersion depth is applied to give the final density equation:

$$d_{solid} = \frac{m_{air} \times (d_{liquid} - d_{air})}{0.99983 \times (m_{air} - m_{liquid})} + d_{air} \tag{2-8}$$

Errors due to liquid adhesion are prevented by unloading the balance at the beginning of each measuring step to remove the effect of the menisci, with the weight recorded immediately after the stability symbol is displayed. Large air bubbles on the sample can be removed with a brush or other utensil to prevent buoyancy errors.[178] Aside from the Archimedes method, the sample density can be verified or checked with dimensional analysis for regular geometries.

2.2.2 Scanning Electron Microscopy (SEM) and Energy Dispersive X-ray Analysis (EDAX)

Scanning electron microscopy (SEM) is a microscopy technique which utilizes electrons to image samples at high resolution on the scale typically between 50 Å and 500 Å. Generation of a beam of electrons starts via thermionic emission from a tungsten filament under vacuum and accelerated at the sample using high voltage. The electrons are focused into a beam using condenser lenses then deflected by scanning coils or deflector plates which use the beam to scan the sample in a rectangular area. The electron beam ranges in energy (typically 0.2 keV to 40 keV) and penetrates the sample to a depth based on the energy.[15,179]

Electrons interact with the samples resulting in elastic (backscattered) and inelastic (secondary) scattering of electrons. Inelastically scattered electrons are low energy electrons ejected from the electronic bands of the material. Secondary electrons are detected via a scintillator-photomultiplier system and provide high resolution topographical images. Elastically scattered electrons are high-energy electrons backscattered from core electrons of the atoms, and therefore interact proportionally to the atomic number. The differing interactions allow for compositional analysis of the sample which is seen as a contrast in the image produced. Backscattered electrons are detected by semiconducting or scintillator type detectors. The images produced by SEM are informative for crystalline materials in observing grain boundaries and morphology.

Energy-dispersive X-ray spectroscopy (EDAX) utilizes characteristic X-rays emitted from the sample to identify the atomic composition of the material. Electrons hitting the sample eject inner shell electrons resulting in the relaxation of outer shell electrons into the vacancies. The energy released from this relaxation is in the form of X-rays which have frequencies that are characteristic to the orbital energies of the interacting atom. An X-ray detector determines the energy of the photon emitted, which is then used to determine the atomic composition of the sample.[179]

Principles of EDAX are demonstrated in Figure 2.4(a). The characteristic X-ray emitted receives a label based on the shell energy of the relaxing and vacant electrons. Shells are labeled as K, L, and M of principal quantum numbers n = 1, 2, 3, respectively. Relaxation from a higher energy shell into a lower energy shell is labeled as α for one shell higher, β for two shells higher, and γ for three shells higher in energy. An X-ray produced from the relaxation of an electron from the L shell into the K shell is labeled as K_α radiation. Due to the energy differences of the shells from atom to atom, the wavelength (energy) of the emitted photon is specific in energy to the atom, however there is often overlap in the energies of characteristic X-rays of various atoms (eg. Mn K_β and Fe K_α). Resulting spectrums are complete and include all activated characteristic emissions which allow deciphering of the chemical composition of the sample as seen in Figure 2.4(b).

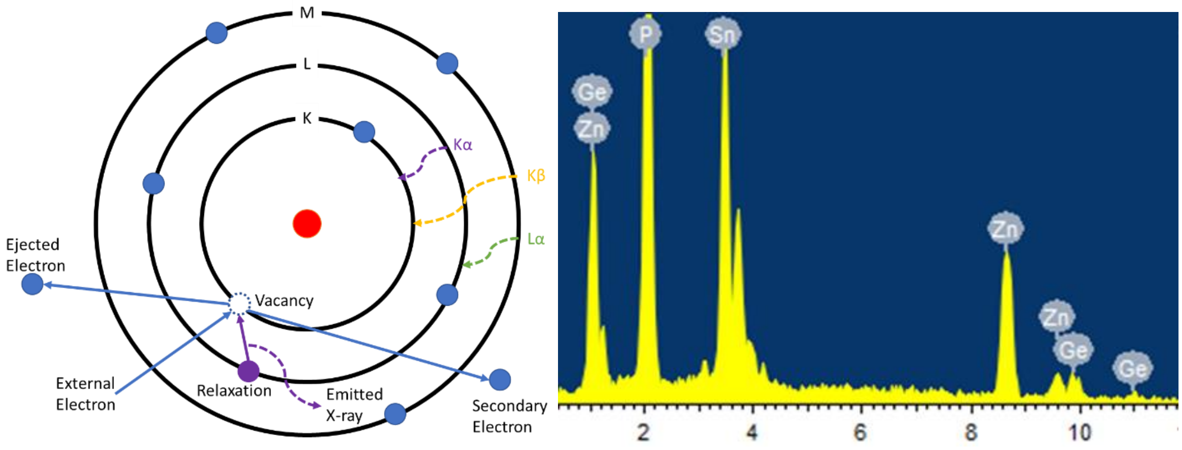

Figure 2.4: Principles of EDAX and inelastic electron scattering (a) the ejection of an inner core electron produces X-ray radiation characteristic to the energy levels of the ejected and relaxing electron. (b) EDAX spectrum where the Ge L_α (1.188 keV) and the Zn L_α (1.012 keV) overlap significantly, however the Ge K_α (9.874 keV) and Zn K_α (8.630 keV) have no overlap and therefore can be quantified easily.

2.2.3 Powder X-ray Diffraction (PXRD)

Structure and phase verification of samples studied within this body of work were examined using the powder X-ray diffraction (PXRD) technique. An INEL X-ray powder diffractometer with a position-sensitive detector was used. X-rays were generated from a Cu source with a current of 30 mA and acceleration voltage of 30 kV. Samples were measured at ambient conditions with 2θ between 5° and 120°.

The process of X-ray diffraction requires the generation of electromagnetic radiation with wavelengths on the scale of the spacing between atoms in the crystalline solid. There are several ways to produce X-rays, however this work focuses on vacuum tube anode generation. X-rays are generated this way by first producing electrons from a cathode by thermionic emission or ‘boiling’ electrons from a metal filament. The emitted electrons are accelerated into a cathode target made of copper where they produce bremsstrahlung and characteristic X-rays. Bremsstrahlung radiation is produced from the deceleration of electrons as they interact with the metal and are wide spectrum, whereas characteristic X-rays are spectral lines specific to the excitation of inner shell electrons within the metal atoms as discussed before. The resulting X-rays from this process are typically monochromated to produce a beam of X-rays of a single wavelength, in the case of the Inel diffractometer, by a Ge single crystal.

A powder crystalline sample is struck by the beam of X-rays where constructive interference between the repeating crystalline plane produces a coherent reflected beam of X-rays. The reflected X-rays spread into a three-dimensional pattern which are then detected with respect to their angle and intensity. The resulting pattern is characteristic to the sample measured and can be used to determine the atomic structure of new materials as well as the presence of known materials.

Crystalline materials are composed of repeated atomic arrangements which form specific structures based on the chemical behavior of the elemental components. The three-dimensional periodic nature of crystalline solids allows for the interference between reflected waves or Bragg diffraction. The principles of refining crystalline structures require that X-rays reflect coherently from crystalline materials as Bragg conditions are met:[180]

$$2d_{hkl}\sin\theta = n\lambda \tag{2-9}$$

Miller indices ($h\ k\ l$) designate planes within a crystal unit cell and the spacing between planes is given as d_{hkl}. When the incident X-rays wavelength (λ) matches the distance between repeating planes at angle θ, the reflected X-rays constructively interfere and reflect at the same angle θ. Resulting reflections are a reciprocal lattice representation of the crystal, Bragg's law is demonstrated in Figure 2.5.

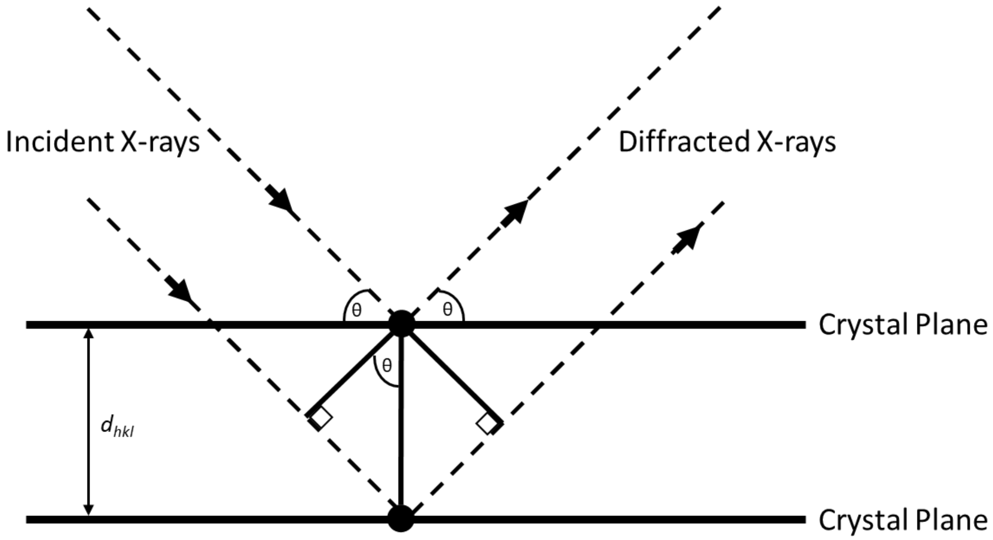

Figure 2.5: Schematic of X-ray diffraction where incident radiation is reflected constructively when the Bragg conditions are met.

The intensity of the reflected X-rays is proportional to the interaction of the electromagnetic radiation with the electrons surrounding the atoms within a plane which is represented by the atomic form factor:

$$f(Q) = \sum_{i=1}^{4} a_i e^{-b_i\left(\frac{Q}{4\pi}\right)^2} + c \tag{2-10}$$

Where the values of a_i, b_i, and c are atom or ion specific, and Q is the scattering vector which is dependent on the wavelength of radiation (λ) and scattering angle (2θ). Finally, the reflected intensity is a function of the atomic form factors and positions of atoms within the lattice which is determined by the structure factor squared $I_{hkl} = |F_{hkl}|^2$:

$$F_{hkl} = \sum_{j=1}^{N} f_j e^{[-2\pi i(hx_j+ky_j+lz_j)]} \tag{2-11}$$

Here the sum over all atoms in the unit cell is considered, where x_j, y_j, and z_j are the coordinates of atom j's position, with its atomic scattering factor f_j. The reflected intensities (I_{hkl}) and positions (2θ) are used to determine the crystal structure from the diffracted pattern. Structural refinement details and software will be covered in the subsequent section.[181]

2.2.4 Rietveld Refinement

Rietveld refinement is a method for analysis of powder X-ray diffraction (PXRD) data using a least squares approach to match experimental data to theoretical patterns derived from a crystal model.[182,183] This modelling and fitting can be performed using the General Structure Analysis System (GSAS) GSAS-II software.[184]

The data for a pattern is processed by intensity (y_i) at increment (i) of the scattered angle (2θ), and the model used by GSAS calculates the intensity (y_{ci}) based on the theoretical model:

$$y_{ci} = s\sum_{K} L_K |F_K|^2 \phi(2\theta_i - 2\theta_K) P_K A + y_{bi} \tag{2-12}$$

Here K is used as shorthand for Miller indices ($h\ k\ l$), s is the scale factor, L_K is the Lorenz, polarization, and multiplicity factor, $\phi(2\theta_i - 2\theta_K)$ is the reflection profile function, P_K is the preferred orientation function, A is the absorption factor, and y_{bi} is the background intensity.

The least squares method of refinement uses non-linear minimization to solve the system:

$$\begin{pmatrix} y_{ci} & = & ky_i \\ \vdots & & \vdots \\ y_{cn} & = & ky_n \end{pmatrix} \tag{2-13}$$

Where y_{ci} is the calculated intensity, y_i is the observed intensity, k is a scaling factor, and n is the number of observed data points. The minimization function (Φ) is given as:

$$\Phi = \sum_{i=1}^{n} w_i (y_i - y_{ci})^2 \tag{2-14}$$

With the statistical weight factor (w_i) the calculated model's dependent variables are continuously refined to minimize the above function until the observed data (y_i) matches the calculated model (y_{ci}).[182]

Several measures of the accuracy of the model are used to evaluate the quality of the refinement: profile residual (reliability factor) (R_p), weighted profile residual (R_{wp}), and goodness of fit squared (χ^2).

$$R_p = \sum_{i}^{n} \frac{|y_i - y_{ci}|}{\sum_i^n y_i} \times 100\% \tag{2-15}$$

$$R_{wp} = \sqrt{\sum_{i}^{n} \frac{w_i (y_i - y_{ci})^2}{\sum_i^n w_i (y_i)^2}} \times 100\% \tag{2-16}$$

$$\chi^2 = \left(\frac{R_{wp}}{R_e}\right)^2 \tag{2-17}$$

Where,

$$R_e = \sqrt{\frac{N - P}{\sum_i^n w_i (y_i)^2}} \times 100\% \tag{2-18}$$

Where N is the number of data points and P is the number of varied parameters. These figures of merit are used during the refinement process to track the progress of the fit of the data to the model. Ideal values these parameters are as low as possible for R_p and R_{wp} and low but no less than 1 for χ^2. Typical values indicating a good match of a model with data is for $R_p, R_{wp} < 10\%$ and $\chi^2 \cong 1$, however may vary based on the complexity of the material studied.[185]

Refining crystal structures range in difficulty based on the material being studied. The most difficult structures to refine are ones in which the structure type is unknown and complicated as pattern decomposition must be performed to solve the structure type. The easiest structural refinements are for materials of known composition and structure type as the Bragg reflections are fixed. Structures refined by GSAS-II in this work are all known structure types with some of known composition.

2.3 Thermoelectric Property Measurements

Thermoelectric effects are transport processes and as such transport measurements are required to adequately characterize thermoelectric materials. Obtaining the figure of merit ($zT = T\sigma S^2/\kappa$) is the typical goal of such measurements. This section will discuss the instruments and methods for obtaining temperature dependent data for thermoelectric properties.

2.3.1 Electrical Conductivity

Electrical conductivity (σ) is the measure of a material's ability to conduct electrical current and given the units of Siemens per meter (S/m), this is the reciprocal of electrical resistivity ($\sigma = 1/\rho$). Measuring this property begins by applying Ohms Law: $V = IR$, where a potential difference (V) results from an applied current (I) through a material with a resistance (R). To obtain the more meaningful material specific resistivity (ρ), the dimensions of a measured sample must be considered. The relation between resistance (R) and resistivity (ρ) is: $\rho = R\frac{A}{l}$, where A is the cross-sectional area and l is the length of the sample between the measuring probes.

In practice this measurement is achieved with the four-probe technique. This approach has the advantage of negating the resistances of the probing devices which results from a two-probe method. A current source is used to apply a current through the sample at the electrodes. The resulting voltage is measured at the probe contacts at a measured distance, and the cross-sectional area of a sample is taken prior to the measurement. This entire apparatus can be sealed in an inert atmosphere, while temperature probes are used to monitor the sample.[186]

Measurements taken on the ULVAC ZEM-3 are performed under an inert helium atmosphere. Pressure contacts are made for both the electrode and voltage probes. The entire system is heated with an infrared furnace and the temperature is monitored with R-type thermocouples which double as the voltage probes. Data acquisition is performed using the ULVAC instrument provided software through LabView. This measurement is performed in conjunction with the Seebeck coefficient measurements.

2.3.2 Seebeck Coefficient Measurements

The value of the Seebeck coefficient was obtained using the direct method and is typically given in units of μV K^{-1}. This technique is performed by applying a temperature gradient through a sample and measuring the resulting potential difference: $S = \frac{\Delta V}{\Delta T}$.[187] While simple in principle; in practice this measurement poses a unique set of challenges.

The ULVAC ZEM-3 (schematic Figure 2.6) is a specialized instrument designed specifically to perform these measurements. A heater is used to apply a temperature gradient through the sample while convection is quickly stabilized due to a helium atmosphere. The temperature gradient is measured at two contact points with specially calibrated R-type thermocouples, and the potential difference is subsequently measured through the same thermocouple probes. The probes are in direct pressure contact with the sample. Three Seebeck measurements are taken at varying temperature gradients as there should be proportional voltage responses. A least squares analysis is performed on the resulting data to account for the temperature dependence of the Seebeck coefficient.[186] This measurement is performed in conjunction with electrical conductivity measurements.

The squeezing pressure contacts of the electrodes is a primary source of inconsistency with temperature in these measurements. This occurs if a sample becomes soft at high measurement temperatures which distorts the dimensions of the samples on the macro scale or causes microstructural changes.

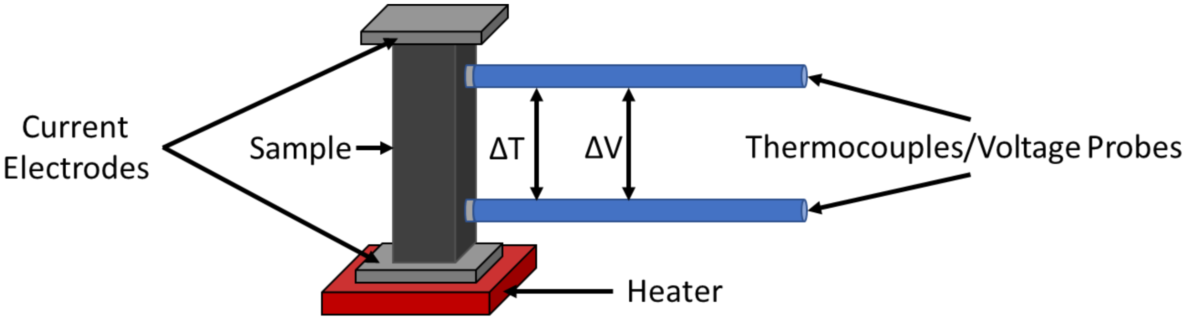

Figure 2.6: Schematic diagram of the ZEM-3 measurement system, heat is applied to the sample unidirectionally allowing for the measurement of Seebeck coefficient, and electrodes supply current to measure electrical resistivity of a regular square prism.

2.3.3 Thermal Conductivity

There are many techniques for measuring the thermal conductivity of a given material. This work utilizes the laser flash technique for obtaining thermal conductivity. These experiments typically follow the densification of a sample. A pellet of determined density is coated in a thin layer of graphite using an aerosol spray. The samples are placed in an inert high purity argon atmosphere at a constant purge rate. A class 1 neodymium:glass laser pulse with up to 17 Joules of energy is focused onto the sample from below heating the sample. Heat diffusion through the sample follows:

$$\alpha = c \times l^2 \times t_{0.5}^{-1} \tag{2-19}$$

Where the thermal diffusivity (α) is calculated by the thickness of the sample (l), the time for reaching half the maximum temperature ($t_{0.5}$), and a proportionality constant (c). The constant is based on heat loss where for the Parker model $c = 0.139$ assuming little to no heat loss.[188]

The resulting heat is detected with an InSb infrared detector where a voltage signal is recorded with respect to time, and the time to reach half maximum signal is calculated.[189] The thermal conductivity (κ) of a given sample can then be calculated by:

$$\kappa = \alpha\ d\ C_P \tag{2-20}$$

The heat capacity can be estimated with viable accuracy using the Dulong-Petit law:

$$C_P = \frac{3R_g}{M_a} \tag{2-21}$$

Where R_g is the ideal gas constant and M_a is the average molar mass of the material.[190] Calculation of the thermal conductivity therefore requires measurement of material density and knowledge of chemical composition. A schematic of the measurement is provided in Figure 2.7 with an example histogram of the detector response.

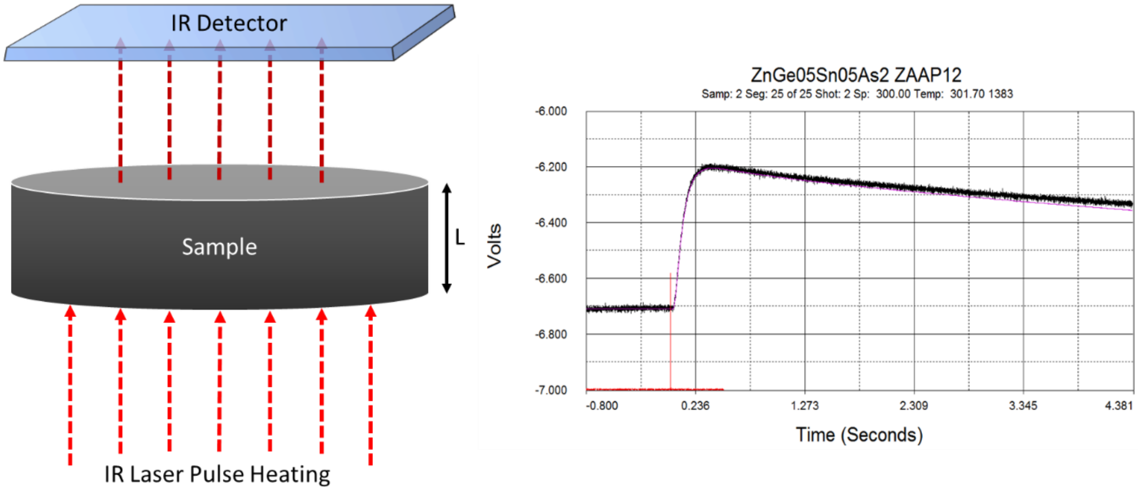

Figure 2.7: Schematic of laser flash diffusivity measurement (left) a cylindrical sample is heated unidirectionally with an IR laser which is detected with respect to time (right) a typical histogram obtained, where voltage response of the detector is measured versus time.

2.3.4 Error Analysis of Thermoelectric Properties

Thermoelectric measurements are like all other property measurements that contain experimental errors and deviations. It is important to be aware of the sources errors while analyzing the data as the calculation of the figure of merit propagates the errors.[191] The errors are based on the instruments used and for use in this thesis are: 5%, 3% and 2.3% for electrical conductivity, Seebeck coefficient and thermal diffusivity measurements, respectively. The estimated error in crystal density measurement is 2%. Based on these values the approximate error for the figure of merit zT can be evaluated to be around 10% using:[16]

$$\frac{dZ}{Z} = \sqrt{\left(2\frac{dS}{S}\right)^2 + \left(\frac{d\sigma}{\sigma}\right)^2 + \left(\frac{d\kappa}{\kappa}\right)^2} \tag{2-22}$$

To better understand the standard deviation of these data, an international round robin study has been performed and the standard deviations based on the 2σ method were around, ±7%, ±6.5%, ±3.5% and ±14% for electrical resistivity, Seebeck coefficient, thermal diffusivity and zT, respectively.[42,186,192]

2.4 First Principles Methods and Calculations

The development of computational techniques has allowed for further understanding of structure-property relationships in solid state systems. Such computational methods can be used to calculate ab-initio properties to target and optimize materials properties. This section will discuss the techniques, software, and theory used to obtain meaningful calculation results.

2.4.1 Density Functional Theory

Density functional theory (DFT) is a computational method used for modelling the electronic structure of materials by quantum mechanical functionals. The electronic structure of materials can be used to predict physical properties by understanding the contributions electrons have to certain energy levels as DFT focuses on the electron density (ρ).

The Hohenberg-Kohn theorems form the basis of DFT which stays accurate if the electron system is not within a magnetic field. The first theorem postulates that the electron density determines the Hamiltonian operator, which uniquely coincides with the ground-state properties of the system. This can be realized by solving the many-electron time-independent Schrödinger equation:

$$\hat{H}_{elec}\Psi_{elec} = E_{elec}\Psi_{elec} \tag{2-23}$$

where Ψ_{elec} is the electronic wave function, and E_{elec} is the total electronic energy of the system, and $\hat{H}_{elec}$ is the electronic Hamiltonian:

$$\hat{H}_{elec} = \hat{T} + \hat{V}_{ee} + \hat{V} = -\frac{1}{2}\sum_{j=1}^{N} \nabla_j^2 + \frac{1}{2}\sum_{i\neq j} \frac{1}{|\boldsymbol{r}_i - \boldsymbol{r}_j|} + \sum_{j=1}^{N} V_1(\boldsymbol{r}_j) \tag{2-24}$$

Here $\hat{T}$, $\hat{V}_{ee}$, and $\hat{V}$ are the kinetic energy, electron-electron repulsion, and one-body potential energy, respectively. The second theorem states that the ground state electron density minimizes the energy functional for a given system: $E_{ele} = \min_{\Psi}\langle\Psi|\hat{H}|\Psi\rangle$ over all antisymmetric N-particle wavefunctions.[193]

One major limitation of DFT is that the interactions between electrons (exchange and correlation) do not have defined functionals. These interactions are important to consider for determining the electronic band structure of a material. Correlation interactions describe the Coulombic force an electron experiences in the presence of other electrons, while exchange interactions describe the force resulting from two electrons with the same spin. Approximation of the functionals can be realized using local-density approximation (LDA). The assumption made is that the exchange-correlation energy depends on the local electron density using and can be modeled as a free-electron gas:

$$E_{XC}^{LDA}[\rho] = \int \varepsilon_{XC}(\rho)\, \rho(\boldsymbol{r}) d\boldsymbol{r}^3 \tag{2-25}$$

LDA assumes the electron density is uniform, however in actuality there is a gradient of electron energies throughout the material. As a result, LDA tends to underestimate the exchange energies and overestimate the correlation energies. Generalized gradient approximation (GGA) is a method used to account for the electron density gradients having the form:

$$E_{XC}^{GGA}[\rho_\uparrow, \rho_\downarrow] = \int \varepsilon_{XC}(\rho_\uparrow, \rho_\downarrow, \nabla\rho_\uparrow, \nabla\rho_\downarrow)\, \rho(\boldsymbol{r}) d\boldsymbol{r}^3 \tag{2-26}$$

Here the energy functionals consider the electron spin densities indicated by the spin up (↑) and spin down (↓) subscripts. In this research, the type of GGA used is the Perdew-Burke-Ernzerhof (PBE) method which is simple yet accurate compared to other GGA methods. While the GGA method is an improvement to LDA, it is known to underestimate the band gap of semiconductors and insulators. To calculate more accurate band gaps, the Becke-Johnson (BJ) exchange-correlation potential is employed which is a semi-local model. This model is further improved with the Tran-Blaha modification (TB-mBJ) which uses orbital dependent potentials. The GGA functionals discussed allow for inexpensive and accurate calculations of large systems.[194] These calculations are performed using the Wien2k package where known structural information is used to develop and apply the functionals discussed, to calculate the electronic structure of materials.[18,195]

The Wien2k package contains several independent programs linked which work together to perform DFT calculations. The initialization suite is a set of small programs used to generate the inputs for the main programs. This includes: NN, SGROUP, and SYMMETRY which generate and check the structural inputs from atomic positions and symmetries; LSTART defines the atomic densities and orbitals; KGEN generates the k-mesh in the first Brillion zone; and DSTART creates a starting electron density for the next set of programs.

The body of programs used next is referred to as the self-consistent field (SCF) are the main calculation programs. These programs are repeated iteratively until convergence is achieved when energy (functionals) of the system is minimized. Necessary programs include: LAPW0, LAPW1, LAPW2, LCORE, and MIXER. LAPW0 receives the density from the previous cycle and generates the total potential for the sum of Coulomb and exchange-correlation potentials. LAPW1 calculates the valence bands from the potential in the form of eigenvectors and eigenvalues, which are fed into LAPW2 which computes the valence densities. LCORE receives the potential from LAPW0 to compute the core state densities. The valence and core densities are fed into the MIXER program which uses the density from the previous iteration to stabilize the cycle and generate a new total density. Densities are then used to determine if the self-consistent cycle has converged. Optional programs can be included if the studied material requires it such as: spin-polarization, fixed-spin-moment, and anti-ferromagnetic calculations. A flowchart of a basic program operation is illustrated with Figure A.1 in the Appendix.[196]

2.4.2 Boltzmann Transport Properties

Standard DFT calculations provide valuable information about the electronic structure of materials which becomes useful for designing and reviewing new materials. Efforts to translate electronic structures into physical properties have been made with success using Boltzmann theory. A code called BoltzTraP can be used with the Wien2k package to calculate these band-structure dependent properties.[197]

Transport functions are used to physically describe the processes which underlie the electronic properties of materials (S, σ, κ_{ele}) or transport coefficients.[197,198] To relate these properties to the electronic structure of materials, we observe the electrical current of charge carriers as:

$$\boldsymbol{J} = e\sum_{\vec{\boldsymbol{k}}} f_{\boldsymbol{k}}\vec{v}_{\boldsymbol{k}} \tag{2-27}$$

with e the charge of the carriers, and $\boldsymbol{k}$ being the wave vector. $f_{\boldsymbol{k}}$ is the population of the quantum state and $\vec{v}_{\boldsymbol{k}}$ is the group velocity at $\boldsymbol{k}$. Group velocity is the gradient electronic bands in reciprocal space:

$$\vec{v}_{\boldsymbol{k}} = \frac{1}{\hbar}\frac{\partial \varepsilon_{\boldsymbol{k}}}{\partial \boldsymbol{k}} \tag{2-28}$$

The Boltzmann equation is used to find the population of a quantum state $f_{\boldsymbol{k}}$

$$\frac{\partial f_{\boldsymbol{k}}}{\partial t} = -\vec{v}_{\boldsymbol{k}}\cdot\frac{\partial f_{\boldsymbol{k}}}{\partial \boldsymbol{r}} - \frac{e}{\hbar}\left(\boldsymbol{E} + \frac{1}{c}\vec{v}_{\boldsymbol{k}} \times \boldsymbol{H}\right)\cdot\frac{\partial f_{\boldsymbol{k}}}{\partial \boldsymbol{k}} + \frac{\partial f_{\boldsymbol{k}}}{\partial t}_{scatt.} \tag{2-29}$$

which states that the rate of change of population of a quantum state depends on diffusion, electric field, magnetic field, or scattering. The above equation can be linearized using relaxation (scattering) time $\tau_{\boldsymbol{k}}$ and solved for under various transport conditions to define the transport coefficients:

Electrical conductivity

$$\sigma = e^2\int d\varepsilon\left(-\frac{\partial f_0}{\partial \varepsilon}\right)\sum_{\vec{\boldsymbol{k}}} \vec{v}_{\boldsymbol{k}}\vec{v}_{\boldsymbol{k}}\tau_{\boldsymbol{k}} \tag{2-30}$$

Seebeck coefficient

$$S = \frac{ek_B}{\sigma}\int d\varepsilon\left(-\frac{\partial f_0}{\partial \varepsilon}\right)\sum_{\vec{\boldsymbol{k}}} \vec{v}_{\boldsymbol{k}}\vec{v}_{\boldsymbol{k}}\tau_{\boldsymbol{k}}\frac{\varepsilon - \boldsymbol{\mu}}{k_BT} \tag{2-31}$$

Electronic thermal conductivity

$$\kappa_{ele} = k_B^2T\int d\varepsilon\left(-\frac{\partial f_0}{\partial \varepsilon}\right)\sum_{\vec{\boldsymbol{k}}} \vec{v}_{\boldsymbol{k}}\vec{v}_{\boldsymbol{k}}\tau_{\boldsymbol{k}}\left[\frac{\varepsilon - \boldsymbol{\mu}}{k_BT}\right]^2 \tag{2-32}$$

The Fermi distribution function ($f_0(\varepsilon_{\boldsymbol{k}})$) is used here as it is the solution to the Boltzmann equation in the absence of fields, and $\boldsymbol{\mu}$ is the chemical potential. Relaxation time is an unknown material dependent property which cannot be determined using the transport equations outlined above; therefore σ and κ_{ele} are determined with respect to relaxation time. Although relaxation time is dependent on both k-vector and band index, in practice τ is directionally independent. This allows the relaxation time to be removed from the integrals in the Seebeck equation and canceled, providing direct calculation of the Seebeck coefficient.[198]

To reduce the computational cost of evaluating the group velocity as a numerical derivative, BoltzTraP uses a Fourier expansion of the band energies, in which the group symmetry always remains constant.

$$\varepsilon_i(\boldsymbol{k}) = \sum_{\boldsymbol{R}} c_{\boldsymbol{R}i} S_{\boldsymbol{R}}(\boldsymbol{k}) \qquad (2\text{-}33)$$

where

$$S_{\boldsymbol{R}}(\boldsymbol{k}) = \frac{1}{n}\sum_{\{\Lambda\}} e^{i\boldsymbol{k}\cdot\Lambda\boldsymbol{R}} \qquad (2\text{-}34)$$

here $\boldsymbol{R}$ is a direct lattice vector, and $\{\Lambda\}$ are the n point group rotations. The star functions are also used to stabilize the calculation by using more star functions than available band energies. The band energies at the various k-points are used to generate conductivity tensors which are then used to calculate the transport coefficients as a function of chemical potential.[197]

Chapter 3: Large-Scale Synthesis of High-Performance Magnesium Silicide Solid Solution $Mg_2Si_{0.3}Sn_{0.67}Bi_{0.03}$

This chapter is adapted with permission from Large Scale Solid State Synthetic Technique for High Performance Thermoelectric Materials: Magnesium-Silicide-Stannide. Daniel C. Ramirez, Leilane R. Macario, Xiaoyu Cheng, Michael Cino, Daniel Walsh, Yu-Chih Tseng, and Holger Kleinke, *ACS Applied Energy Materials*, **2020**, 3 (3), 2130-2136 DOI: 10.1021/acsaem.9b02146. Copyright 2020 American Chemical Society.

This chapter discusses the development of a large-scale batch synthesis process for the high-performance thermoelectric material $Mg_2Si_{0.3}Sn_{0.67}Bi_{0.03}$. An in-house liquid-solid reactor was developed and employed to produce ingots of uniform and consistent composition. The ingot material was crushed and sintered under high pressure and temperature into a large 10.2 x 10.2 x 1.0 cm^3 piece by hot-pressing for analysis. Relevant thermoelectric properties were measured on parallelepiped pieces machined at different orientations and positions from the pressed pellet. Large dimensionless figure of merit (zT) values was achieved for all samples, with values greater than $zT = 1.2$ at 773 K. Statistical analysis revealed consistent material properties, which are necessary for device application of the given material.

3.1 Experimental Methods

3.1.1 Synthesis

Elemental starting reagents were used for the reactions detailed in this work, namely magnesium chips (99.98%, Aldrich Chemistry), silicon powder (99.9%, Alfa Aesar), tin shots (99.8%, Strem), and bismuth needles (99.99%, Alfa Aesar). Stoichiometric amounts for the formula $Mg_2Si_{0.3}Sn_{0.67}Bi_{0.03}$ were used with 10% excess magnesium to account for vaporization expected at high temperatures. All reactants and products were handled in an inert atmosphere argon glovebox. Reactants with total masses of 25 g – 35 g were placed into cylindrical graphite crucibles (50 mL) lined with thin graphite foil.

The crucibles were placed into a closed cylindrical alumina tube under constant argon flow at atmospheric pressure. The entire setup was placed into a vertical tube furnace for heat treatment. The furnace was ramped to 1193 K in 5 hours to create a melt as expected from the phase diagrams,[108] and held at 1193 K for 6 hours. The reaction furnace was then cooled through the liquidus region to 973 K to dwell for 12 hours to 18 hours annealing the solid solution $Mg_2Si_{0.3}Sn_{0.67}Bi_{0.03}$. The entire alumina tube was then removed from the furnace to cool to room temperature under argon flow. A schematic of the reaction setup is seen in Figure 3.1(c). The products were sand cleaned to remove excess graphite foil and crucibles were reused, while the foil was discarded after each reaction. The resulting ingots (Figure 3.1(a)) were visibly porous with large crystallite sizes and displayed a metallic lustre. After long annealing times (~18 h), ingots with the largest crystallite sizes were observed, these ingots were typically more difficult to separate from the graphite foils resulting in some loss of material, thereafter shorter (~12 h) annealing times were used improving quality. Multiple surface and internal powder samples were taken from the ingot, combined, and analyzed with PXRD to confirm phase purity before utilizing for further reaction.

High pressure sintering was performed at the CANMET facility by combining crushed ingots from multiple reaction batches. The hot-press used is the FCT Ingenieurkeramik GmbH model HP W 400 SD/KD. The press uses an indirect hot-pressing method where the heating occurs through the mold by convection. The molds are solid graphite, and the powder to be compacted is separated from the graphite by a graphite foil about the perimeter, on top, and bottom pressing surfaces. 300 grams of material was placed into a 10.16 cm x 10.16 cm square die to be pressed at 900 K for 4 hours under an applied pressure of 60 MPa, followed by a pressure-free cool-down resulting in a large dense polycrystalline piece seen in Figure 3.1 (b) with 1 cm thickness.

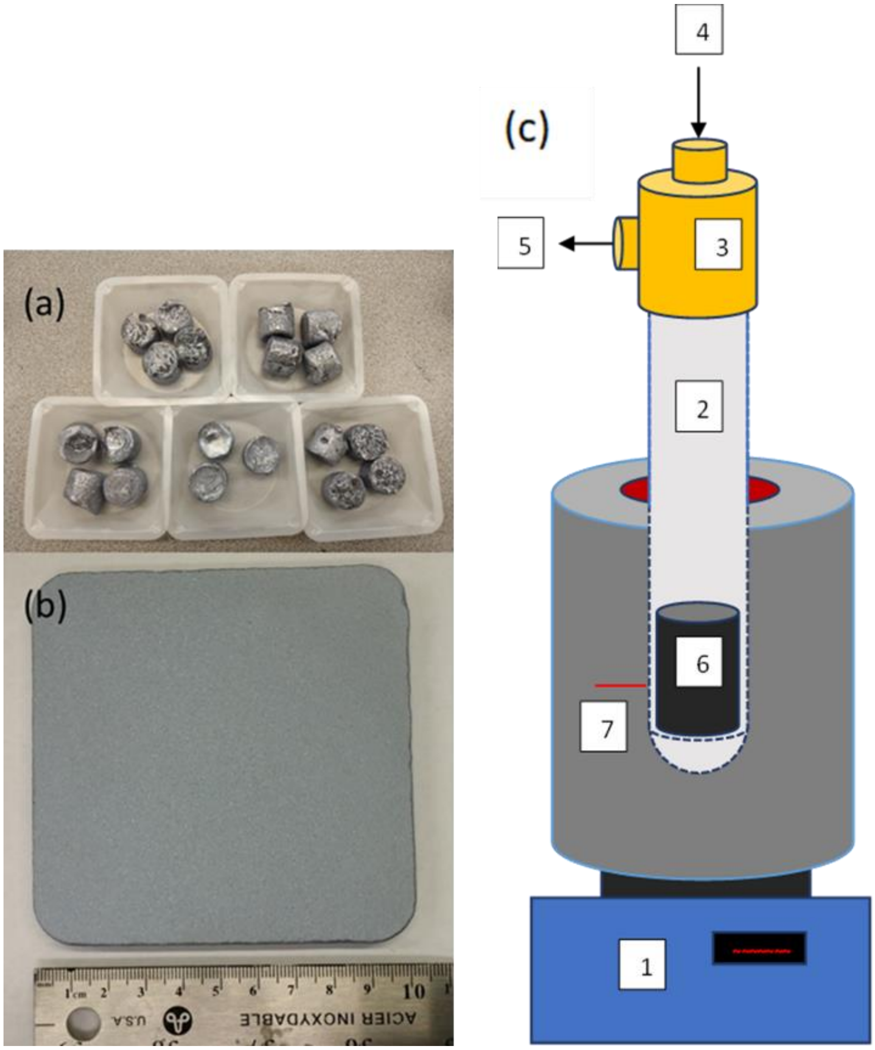

Figure 3.1: Synthesis of $Mg_2Si_{0.3}Sn_{0.67}Bi_{0.03}$ materials: (a) ingots cleaned and removed from crucibles; (b) large hot-pressed square piece. (c) Furnace setup for production of Mg_2(Sn, Si) materials: A semi-programmable muffle tube furnace (1) with alumina (Al_2O_3) closed-end tube (2), sealed by compression fitted KF hose adaptor (3) placed under argon flow (4, 5). Reaction crucible and reactants (6) were placed close to thermocouple (7) during reaction.

3.1.2 Analysis

Powder X-ray diffraction (PXRD) performed on an Inel powder X-ray diffractometer with Cu K_{α_1} radiation was used to verify phase purity of the pre-pressed material. Data were collected at room temperature for 20 minutes for a total of 35 sample ingots and two small batch-combined and pressed pellets. The phase composition of the solid solution and the lattice parameters was verified by comparing to a calculated standard pattern.

After pressing, the resulting material was cut into quadrants and further into various orientations and positions for analysis. Shown in Figure 3.2 is the machining diagram for the 20 parallelepipedal pellets: a total of 20 bars were cut, nine were cut with lengths perpendicular and 11 with lengths parallel to the pressing direction. A total of 13 flat square pellets were cut from the large piece for thermal diffusivity measurements at different orientations and positions on the piece, the samples are named accordingly. The density of each bar and pellet was measured using dimensional analysis by massing the bar with a balance accurate to 0.1 mg and measuring lengths with a micrometer accurate to 0.001 mm. The dimensions, masses, and densities of all measured samples are found in Table A.1 through Table A.3 in the Appendix.

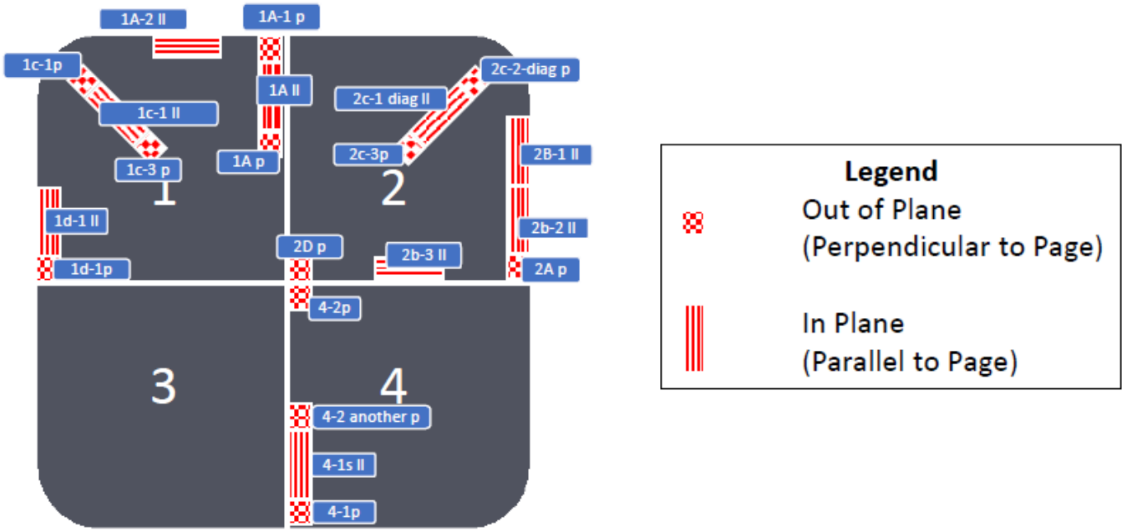

Figure 3.2: Machining diagram of the large pellet of $Mg_2Si_{0.3}Sn_{0.67}Bi_{0.03}$ with parallelepiped samples cut for Seebeck coefficient and electrical conductivity measurements as performed on ULVAC-RIKO ZEM-3 apparatus.

Electrical conductivity and Seebeck coefficient measurements on the parallelepipedal sections were performed using an ULVAC-RIKO ZEM-3 apparatus from 323 K to 773 K under a helium atmosphere. Thermal diffusivity measurements were performed between 323 K and 773 K under an argon atmosphere by using a Netzsch LFA457 thermal properties analyzer. Thermal conductivity was calculated from the equation $\kappa = \alpha \rho C_p$, where $\alpha =$ thermal diffusivity, $\rho =$ density of pellets, and $C_p =$ specific heat capacity. The Dulong–Petit approximation was applied for determining C_p values, which has been shown to work well for these materials.[199]

3.2 Results and Discussion

3.2.1 Phase Characterization

The PXRD patterns for each ingot were measured for 10 minutes as shown in Figure 3.3, to verify the expected powder pattern for $Mg_2Si_{0.3}Sn_{0.67}Bi_{0.03}$. Phase purity of the material is consistent for most ingots measured and match expected and previous results well. There were no issues with phase separation, and complete miscibility is seen throughout. Some residual elemental magnesium is found to remain in the material after the initial reaction. The argon atmosphere provided a pressure which reduced the magnesium vaporization, thus a lower excess of 5-10% would likely be sufficient to account for magnesium volatility, however this is dependent on the length of time used for the annealing and melting steps.

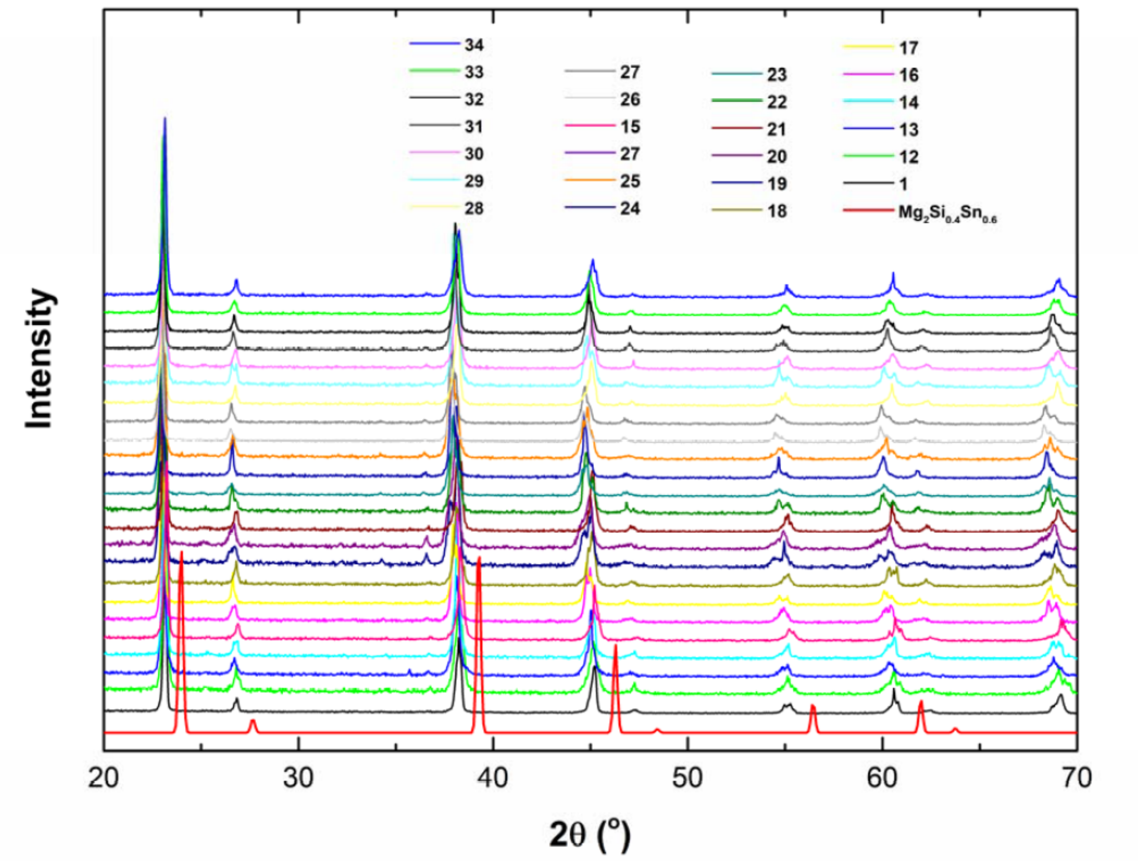

Figure 3.3: PXRD verifying quality of as synthesized ingots of $Mg_2Si_{0.3}Sn_{0.67}Bi_{0.03}$ by comparing to calculated $Mg_2Si_{0.4}Sn_{0.6}$ (red). The expected phase shift from the difference in solid solution stoichiometry is seen. Most samples display a small impurity peak at 2θ = 37° associated with the presence of elemental magnesium. Samples containing large amounts of magnesium (19, 20) or other impurities (13, 25) were omitted from further experiments.

The powder from different ingots was combined and pressed on a small scale before large scale pressing to test process conditions. The final condensed material retained complete miscibility and formed a single solid phase. The excess magnesium is no longer visible from PXRD after the pressing (Figure 3.4); therefore, it is likely lost during the process or at low interstitial concentrations as seen in previous work.[100] Magnesium evaporation is usually evidenced by a grey-white residue on the pressing die and inside the oil bubbler. The densities of all samples are close to the expected values with an average value and deviation of 3.147 g cm^{-3} ± 0.004 g cm^{-3}. The large, pressed piece (Figure

3.1(b)) showed no signs of cracking; however, the surfaces were slightly uneven; and upon polishing the material appeared metallic silver blue.

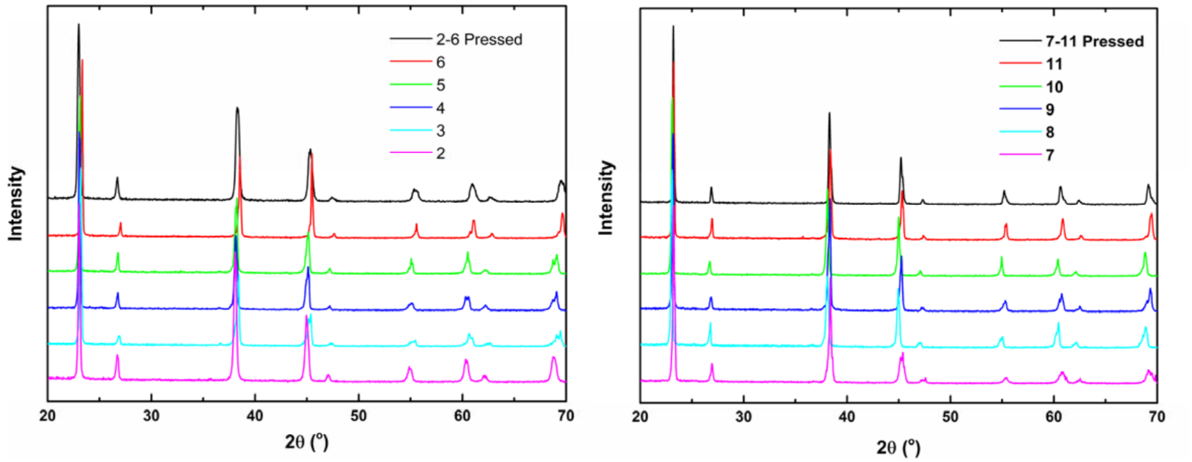

Figure 3.4: PXRD of as synthesized ingot samples (left) 2-6, (right) 7-11, and pressed (sintered) pellets obtained from combined powders of $Mg_2Si_{0.3}Sn_{0.67}Bi_{0.03}$. The sintering results display complete miscibility of all samples indicated by singular peaks. Disappearance of the elemental magnesium peaks ($2\theta = 37^{o}$) in the pressed sample is observed. Samples were measured for 20 minutes.

Energy dispersive analysis of X-ray (EDAX) studies were performed on three randomly chosen pellets after the physical property measurements utilizing the FEI Nova SEM with an acceleration voltage of 20 kV. The samples appeared to be homogeneous on that scale (Figure 3.5), and the obtained atomic % were in line with the nominal values (Table 3.1). While the Bi content seems to be lower than expected, it is noted that such small peaks in the EDX spectrum corresponding to a concentration below 3% are notoriously difficult to quantify.

Table 3.1: Nominal and Experimentally Determined Compositions (at. %) from the EDAX Studies

Element	Mg	Si	Sn	Bi
Nominal	66.7	10	22.3	1.0
Pellet 1	67.4	10.1	21.9	0.6
Pellet 2	67.8	9.2	22.4	0.6
Pellet 3	68.0	10.6	20.8	0.6

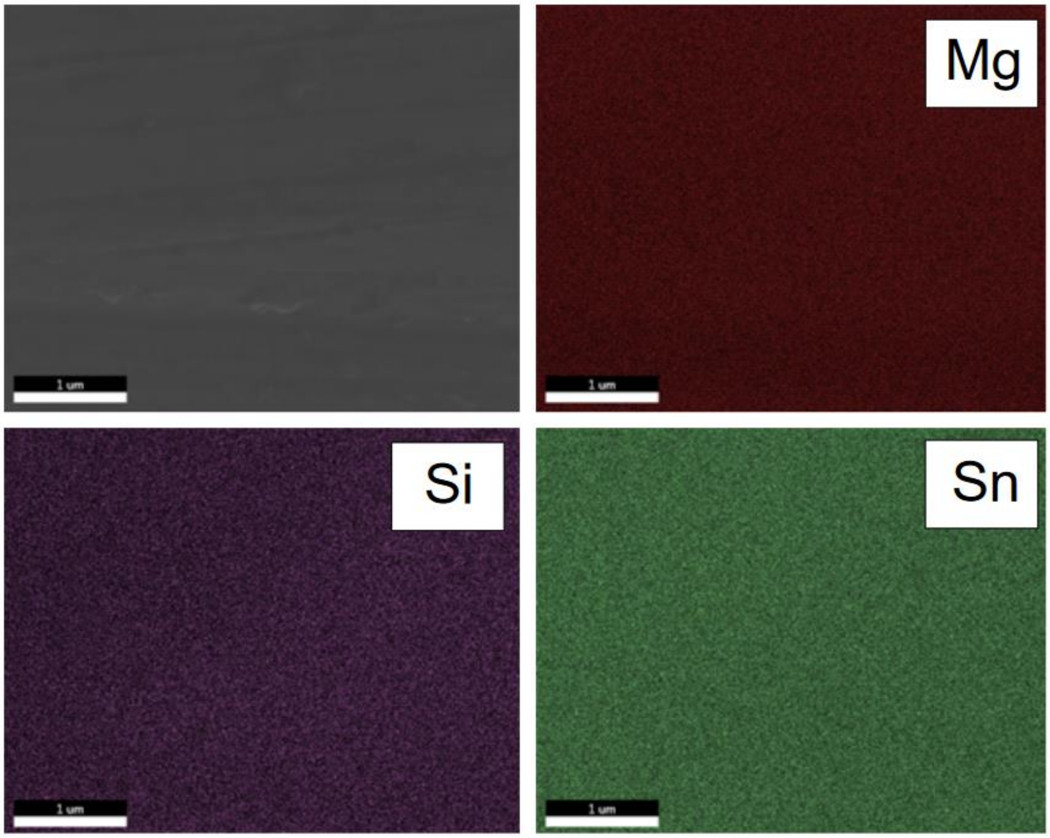

Figure 3.5: Low magnification SEM and EDAX compositional mapping of a hot-pressed pellet of $Mg_2Si_{0.3}Sn_{0.67}Bi_{0.03}$ after the property measurements showing distribution of Mg, Si, and Sn.

3.2.2 Thermoelectric Properties

The temperature dependence of the electrical conductivity was measured for $Mg_2Si_{0.35}Sn_{0.67}Bi_{0.03}$ on a total of 20 samples. Figure 3.6(a) shows the averages with consideration to their orientation to the direction of pressing with the standard deviation represented by error bars (3.8% - 4.3%). Very similar results were obtained for samples oriented perpendicular and parallel to the pressing direction with a slightly larger standard deviation for the samples taken parallel to pressing direction. There is no clear relationship between the sample orientation or position and electrical conductivity within the large, pressed piece. The samples display electrical conductivity characteristics of heavily doped semiconductors observed by the decreasing conductivity with increasing temperature due to decreased carrier mobility. The electrical conductivity values range from 2550 S cm^{-1} ± 95 S cm^{-1} at 323 K to 1125 S cm^{-1} ± 79 S cm^{-1} at 773 K, slightly higher yet consistent with those observed in other Mg_2(Si, Sn)-doped materials. For Bi doped materials with similar alloying average values range from 2195 S cm^{-1} (323 K) to 975 S cm^{-1} (773 K).[36,112,118,123,126] Electrical conductivity values of differently doped but similarly alloyed samples include 1950 S cm^{-1} (323 K) to 950 S cm^{-1} (773 K) for Sb-doped samples[109] and 1050 S cm^{-1} (323 K) to 600 S cm^{-1} (773 K) for p-type Li-doped materials.[114]

Seebeck coefficient measurements show the expected temperature dependence: the absolute value of Seebeck coefficient increases with temperature as seen in Figure 3.6(b). The extra electrons from the Bi atoms occupying the Sn sites populate the conduction bands, and therefore the Seebeck coefficient is negative as expected. The Seebeck coefficient values range from -115 $\mu V K^{-1}$ ± 3 $\mu V K^{-1}$ at 323 K to -190 $\mu V K^{-1}$ ± 1 $\mu V K^{-1}$ at 773 K; these values are overall smaller in magnitude compared to Bi-doped materials with similar alloying, which is consistent with higher electrical conductivity. For similar materials average values include -120 $\mu V K^{-1}$ (323 K) to -210 $\mu V K^{-1}$ (773 K) for Bi-doped samples,[36,112,118,123,126] -120 $\mu V K^{-1}$ (323 K) to -170 $\mu V K^{-1}$ (800 K) for Sb-doped samples,[109] and 75 $\mu V K^{-1}$ (323 K) to 165 $\mu V K^{-1}$ (800 K) for p-type Li-doped samples.[114] The standard deviations of the Seebeck measurements (1.1% - 3.0%) are much lower than those found for electrical conductivity measurements, which suggest some error in conductivity measurements may be resulting from length measurements, either from voltage/temperature probe distances or sample dimensions. This analysis of errors is consistent with observations from other studies.[186,192]

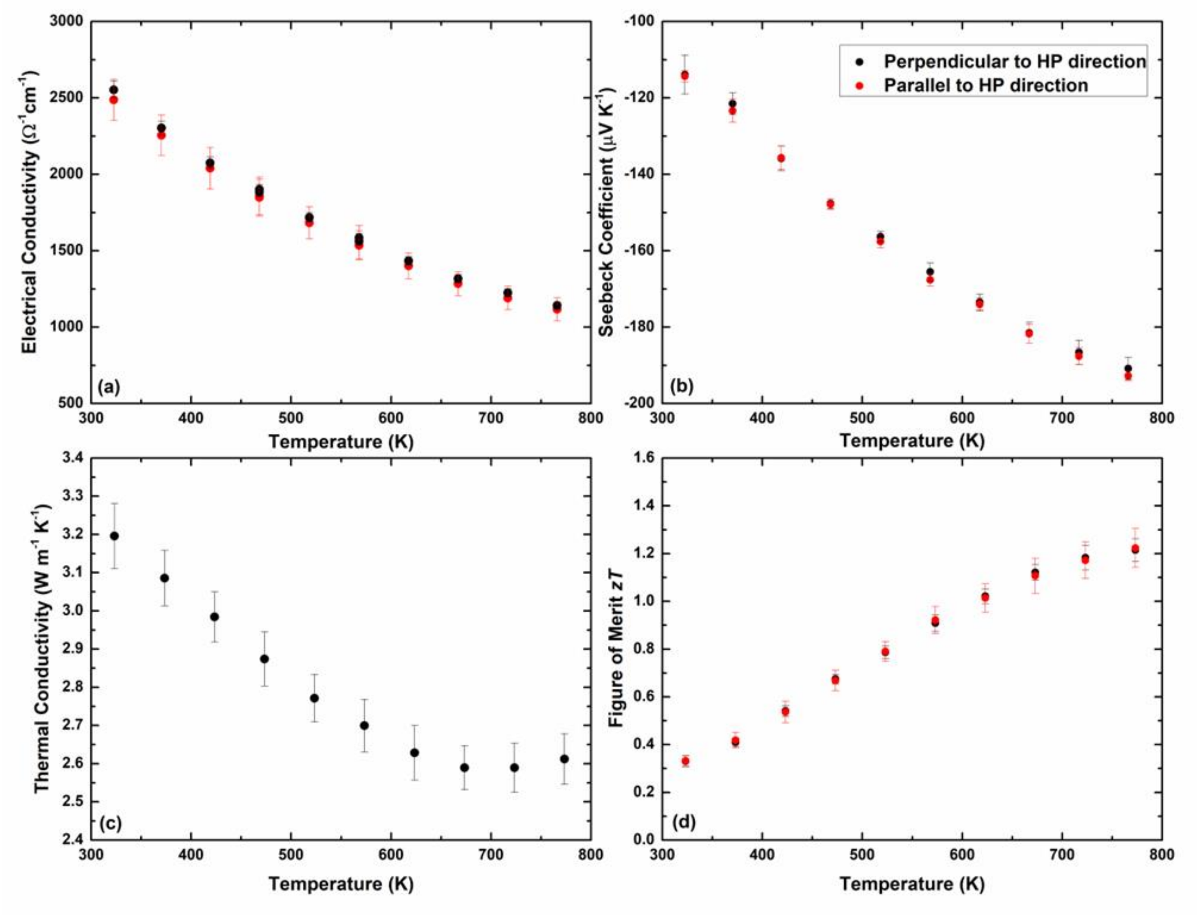

Figure 3.6: Thermoelectric properties of $Mg_2Si_{0.3}Sn_{0.67}Bi_{0.03}$ grouped with lengths perpendicular (black) and parallel (red) to pressing direction with standard deviations of the samples as error bars. (a) Electrical conductivity averaged over 20 pellets; (b) Seebeck coefficient of the same pellets; (c) thermal conductivity of sample averaged over 20 pellets. (d) *zT* of the material with $zT_{max,\,avg}$ = 1.22 at 773 K.

Figure 3.6(c) displays the average temperature dependence of thermal conductivity κ for the 13 measured samples. The thermal conductivity decreases with increasing temperature from 3.2 W m^{-1} K^{-1} ± 0.08 W m^{-1} K^{-1} at 323 K to a local minimum value of 2.6 W m^{-1} K^{-1} ± 0.05 W m^{-1} K^{-1} at 673 K. For most of the similarly doped and alloyed samples, the same behaviour in thermal conductivity is observed with average values ranging from 2.9 W m^{-1} K^{-1} (323 K) to 2.3 W m^{-1} K^{-1} (673 K);[36,112,126] while others observe no local minimum with similar values in thermal conductivity: 2.6 W m^{-1} K^{-1}

(323 K) to 2.2 W m^{-1} K^{-1} (773 K),[118] and 3.4 W m^{-1} K^{-1} to 2.4 W m^{-1} K^{-1} (773 K).[123] In these compounds the electronic thermal conductivity is a major contributor to the total thermal conductivity; therefore, a higher thermal conductivity is expected in the studied material compared to some other studies due to higher electrical conductivity.

The temperature dependence of the dimensionless figure of merit, zT, is shown in Figure 3.6(d), zT rises with increasing temperature, starting with zT = 0.33 ± 0.02 at 323 K and gradually increasing up to 1.22 ± 0.07 at 773 K. These values match well to those found in literature for similarly doped and alloyed samples; with some average values from 0.4 (323 K) to 1.4 (800 K),[36,112,126] and for other scale-up processes with 5-7 cm round pellets 0.3 (323 K) to 1.3 (773 K), i.e., within experimental error.[123,126] These results can also be compared to other non-Bi-doped samples with zT values of 0.3 (300 K) to 1.2 (800 K) for Sb-doped materials[109] and 0.08 (300 K) to 0.5 (800 K) for Li-doped p-type materials.[114] A complete table of the average of thermoelectric properties at 323 K and 773 K is found in Table 3.2 with similarly alloyed and doping levels.

Table 3.2: Comparison of relevant thermoelectric properties for Mg_2(Si, Sn)-doped materials with similar alloying and doping levels.

Sample Formula	σ (S cm^{-1}) 323 K, 773 K	S (µV K^{-1}) 323 K, 773 K	κ (W m^{-1} K^{-1}) 323 K, 773 K	zT 323 K, 773 K	*Ref*
$Mg_2Si_{0.3}Sn_{0.67}Bi_{0.03}$	2550, 1125	-115, -190	3.2, 2.6	0.35, 1.21	this work
$Mg_2Si_{0.3}Sn_{0.675}Bi_{0.025}$	2500, 1000	-115, -200	2.8, 2.3	0.32, 1.30	126
$Mg_{2.16}(Si_{0.4}Sn_{0.6})_{0.97}Bi_{0.03}$	1950, 950	-125, -210	2.7, 2.3	0.39, 1.43	110
$Mg_2Si_{0.3}Sn_{0.67}Bi_{0.03}$	2125, 1000	-120, -210	3.1, 2.3	0.30, 1.32	112
$Mg_{2.08}Si_{0.37}Sn_{0.6}Bi_{0.03}$	2250, 1050	-140, -205	2.6, 2.2	0.55, 1.55	118
$Mg_2Si_{0.3}Sn_{0.67}Bi_{0.03}$	2150, 875	-120, -225	3.4, 2.4	0.32, 1.30	123
$Mg_{2.16}(Si_{0.4}Sn_{0.6})_{0.97}Sb_{0.03}$	1950, 950	-120, -200	2.7, 2.3	0.30, 1.25	109
$Mg_{1.86}Li_{0.14}Si_{0.3}Sn_{0.7}$	1050, 600	80, 155	2.8, 2.2	0.07, 0.50	114

3.2.3 Error Analysis

Intersample errors are displayed in Table 3.3 for relevant physical parameters using relative standard deviations calculated from the mean and error propagation methods. The standard deviations found in samples measured in this work are relatively low with 1.9% - 2.3%, and there is also no clear connection between pressing direction or sample position and thermal conductivity within the large, pressed piece. Minor variations do occur due to the pressing direction; however, the results are equal within error. The errors here are lower than those of inter-laboratory round robin studies[42,186,192] and considering expected instrument errors (~5%), these results display an intra-sample consistency that is more than satisfactory for device fabrication. Complete plots of TE properties versus temperature for all tested samples can be found in the Appendix in Figure A.2 to Figure A.5. The plots are differentiated by machining direction as shown in Figure 3.2.

Table 3.3: Uncertainty of thermoelectric parameters of $Mg_2Si_{0.3}Sn_{0.67}Bi_{0.03}$, calculated from standard deviation divided by the mean values with appropriate error propagations.

Temperature (K)	σ (% dev)	S (% dev)	κ (% dev)	zT (% dev)
323	3.79	3.01	2.41	5.41
373	3.97	2.46	1.88	5.03
423	4.26	2.28	1.92	5.19
473	4.14	0.89	2.06	4.70
523	4.03	1.06	1.90	4.58
573	4.00	1.31	2.19	4.75
623	3.99	1.09	2.27	4.72
673	4.07	1.40	2.19	4.84
723	4.24	1.41	2.00	4.89
773	4.23	1.21	1.91	4.79

3.3 Conclusion

High performing TE material $Mg_2Si_{0.3}Sn_{0.67}Bi_{0.03}$ was synthesized using a scaled-up and simplified reaction process at low cost. Around 1 kg of raw ingot material was synthesized and characterized, and 33 separate property measurements were performed on the processed material. Repeatability and consistency of the material was observed throughout characterization. Overall, the average values of the measured thermoelectric properties are consistent with earlier studies and are in line with viable high performance thermoelectric materials. The large-scale process allowed for thorough analysis using statistical methods concluding that the quality and performance of the material was reproducible and robust. Minor variations of the physical parameters occur due to the pressing direction; however, the results are equal within error.

The process described here provides an inexpensive, simple, and high turnover alternative to other scale-up methods previously described, especially considering the use of reusable crucibles and the replacement of spark-plasma-sintering with the more readily scalable hot-pressing. Consequently, we obtained the largest pellet ever of this material, and ultimately obtained an averaged figure of merit of 1.21(6) at 773 K, equal within error to the zT = 1.30 of the spark-plasma-sintered $Mg_2Si_{0.3}Sn_{0.675}Bi_{0.025}$.[126] These synthetic techniques here developed constitute therefore another step toward creating devices on an industrial scale for energy production via waste heat recovery.

Chapter 4: Synthesis, Structure, and Thermoelectric Properties of the Chalcopyrite Solid Solutions $ZnGe_{1-x}Sn_xP_2$

This chapter focuses on the formation of the solid solutions $ZnGe_{1-x}Sn_xP_2$ using mechanochemical synthesis methods. As discussed in Chapter 1, the motivation for chalcopyrite compounds as thermoelectric materials stems from the tunability of key thermoelectric properties through doping and formation of solid solutions. The melting behavior of the end member compounds compared to their elemental constituents has made them notoriously difficult to synthesize. This work achieves direct synthesis of the end members and solid solutions using the mechanochemical synthesis technique followed by hot-press sintering. Ab-initio electronic structure calculations are performed for the series and Boltzmann transport theory is applied to calculate thermoelectric properties. The synthesis process, development, conditions, and results are discussed. Experimental studies of the structural changes and thermoelectric properties with varying substitution follows. The effect of band degeneracies due to the changes in tetragonality on TE properties is considered and discussed.

4.1 Experimental Methods

Preparation of all materials was performed in a purified argon glovebox using stochiometric amounts with -100 mesh zinc powder (99.9% Alfa Aesar), -100 mesh tin powder (99.998% Alfa Aesar), germanium pieces (99.999% STREM Chemicals) were pre-milled to fine powder for use; -100 mesh phosphorus powder (99% Alfa Aesar). The powders were loaded into zirconia ball mill jars with 20 count of 1 mm zirconia balls under argon atmosphere and sealed. The reactions were milled in cycles at 600 rpm for 5-minute increments with 1-minute rest times reversing in direction after each cycle. Three milling steps were used: first for 5 hours, the jars were then opened in an argon glovebox and agglomerated material was mechanically reincorporated before two subsequent 2 hour milling steps. The reacted material was mechanically removed and ground into a uniform powder. High pressure sintering was performed as a final reaction step, various sintering temperatures were used based on the alloying levels of the material. A pressure of 56 MPa was applied using and OXYGON industries hot press, temperatures used for various alloying levels can be found in Figure 4.2; the temperature was ramped over two hours and applied for 2.5 hours with a pressure free cooldown. The resulting pellets were 12.5 mm in diameter and densities were measured using Archimedes' method with ethanol.

Powder X-ray diffraction was performed on polished pellets, ground, and milled samples. Measurements were obtained using an Inel powder X-ray diffractometer equipped with a position sensitive arc detector and Cu Kα radiation source (30 kV, 30 mA), monochromated to K_{α_1} with Ge single crystal. Measurements in 2θ were collected from 5° to 120°. EDAX measurements were performed using an FEI Quanta FEG ESEM with an acceleration voltage of 20 kV. Four point measurements were averaged for each sample, and element mapping was performed on a 150x150 μm^2 area. Thermal diffusivity of the pressed pellets was measured using the TA-instruments DLF-1200 system. Seebeck coefficient was measured by the direct method, and electrical conductivity measured by a standard 4-point method using the ULVAC RIKO ZEM-3 apparatus. Rietveld refinements were performed using GSAS-II analysis software. The refined parameters were background, lattice parameters, atomic positions, sample displacement, isotropic temperature factors, crystallite size, microstrain and occupancy of substituted (Ge, Sn) sites. Electronic structure calculations were performed using the Wien2k package using the full potential linearized augmented plane wave (LAPW) method.[195] The BoltzTraP2 package in Wien2k was used to calculate thermoelectric properties from the electronic structure.[197]

4.2 Development of Synthesis Procedures

4.2.1 Overview

Typically, $ZnSnP_2$ synthesis is performed by the flux method, utilizing a tin self-flux at greater than 94 mole %, cooling to acquire single crystals, and removing residual flux from the material.[200–203] Due to the peritectic melt behavior of $ZnSnP_2$ (700 °C) direct stoichiometric liquid-solid synthesis is not possible.[203] This work demonstrates the viability of mechanical milling to achieve direct synthesis of pure $ZnSnP_2$ powder and bulk polycrystalline material. Synthesis of $ZnGeP_2$ poses challenges despite congruently melting at 1085 °C. The difficulty in the synthesis arises due to the high vapor pressure of the elemental phosphorus and zinc constituents. Some synthetic approaches for this compound involve the use of temperature gradients and or excess elemental phosphorus with complex apparatus.[204–210] This work demonstrates the viability of mechanical milling for overcoming vapor pressure challenges while allowing for much lower reaction temperatures of bulk $ZnGeP_2$.

Solid solution miscibility of chalcopyrite compounds has thus far been limited to congruently melting compounds,[153,211–214] while full miscibility of incongruently melting compounds is rarely achieved in crystalline materials.[50] Miscibility is typically achieved through homogenization in a liquid phase which is maintained by quickly cooling the samples into their solid forms. Liquid-solid synthesis is not viable for these solid solutions as the end members have drastically different melting behaviors: incongruent ($ZnSnP_2$ at 700 °C) versus congruent melting ($ZnGeP_2$ at 1085 °C) and at large temperature differences. Utilizing a high energy ball milling process direct synthesis of the solid solutions is achieved at low temperatures using the elemental constituents as starting materials.

Previously considered structural limitations of chalcopyrite alloying suggests a difference of tetragonality in end members greater than 0.13 ($\Delta c/(2a) > 0.13$) results in miscibility gaps due to bonding stress.[215] In this work, the end members meet the previously hypothesized miscibility criteria, so full miscibility is expected. The ball milling process allows for much lower reaction temperatures due to greatly increased surface area of reactants. As will be discussed below full miscibility is achieved in the series using the developed process.

4.2.2 Synthetic Procedure

Attempts to form the solid solutions through ball milling together the end members were performed with little success. Graphite coated fused silica tube reactions of the end members were performed, where the starting elemental reagents were layered from lowest melting at the bottom to higher melting placed on top. The primary difficulties which arose were high Zn and P vapor pressure in the case of $ZnGeP_2$ resulting in many exploding reactions and the mass of excess tin required for low yield single crystals of $ZnSnP_2$. Doping via this conceived method would also likely prove difficult due to the solution synthesis required for $ZnSnP_2$.

The direct combination of elemental constituents via ball milling was then attempted followed by a high temperature sintering and reaction step in fused silica. Handling of milled material within an inert environment was necessary due to the small particle size and therefore large surface area making them reactive in ambient conditions. Initially, solid elemental chunks were used as starting materials to reduce potential of oxygen contamination. After milling however, larger pieces of tin and zinc were left unincorporated in the milling jar, and smaller pieces tended to agglomerate heavily onto the milling jar walls. Mechanical reincorporation was used and after three to four, 5-hour milling attempts a uniform material was formed. Analysis of the tube reactions which followed showed reactions contained numerous elemental and binary impurities suggesting incomplete homogenization.

A switch to powdered starting materials followed, which greatly improved the homogenization, reduced agglomeration, and following a tube reaction produced little to no side products. A single milling step was used initially, however due to the emergence of tin impurities after sintering, a multi-step milling process was used. Powder X-ray diffraction was performed on milled powder to develop the process. The milling patterns can be found in Figure 4.1 for exploratory experiments displaying the progressive conversion to the target phase. After 5 hours of milling the pattern of target chalcopyrite phase is observed (28°, 47°, and 55°), however there is a major presence of β-tin (30.6° and 32°). Subsequent 2-hour millings display reduction of β-tin relative to the target phase (7 hours), eventually β-tin becomes unidentifiable (9 hours), and further milling primarily produces peak broadening of the target phase (12 hours).

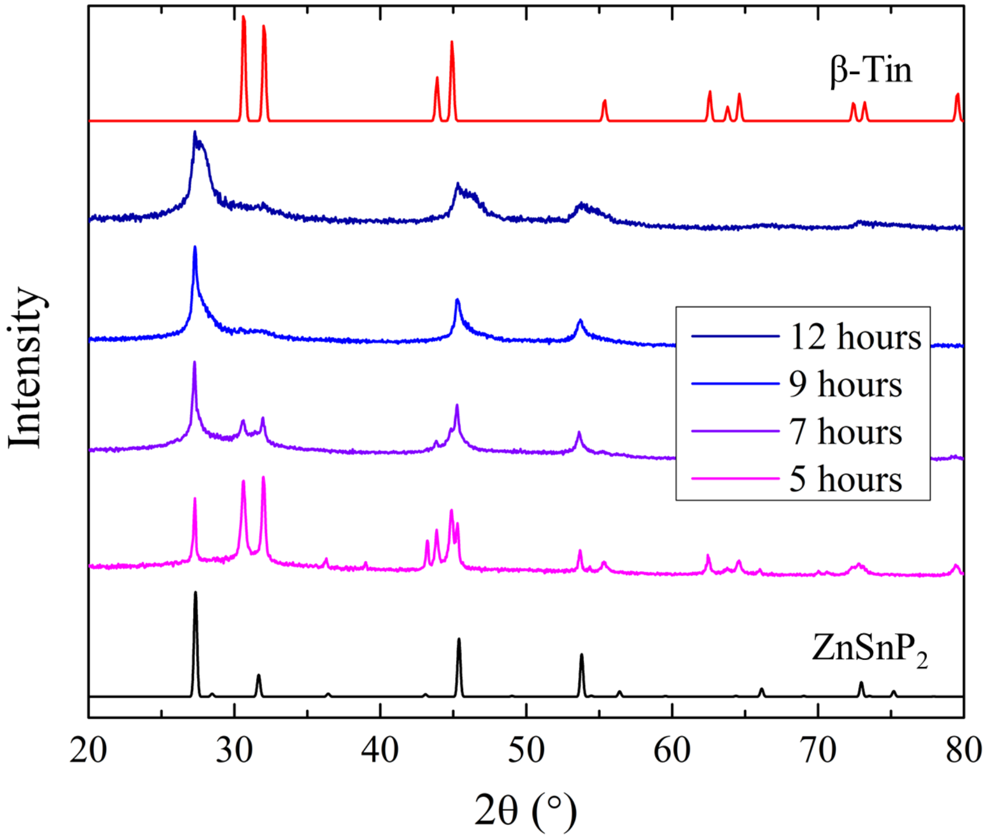

Figure 4.1: Progression of $ZnGe_{0.5}Sn_{0.5}P_2$ synthesis by ball milling of elemental constituents. The development of the target phase can be seen forming from the main (112) peak at 28° as β-tin peaks reduce.

The finalized process used for successful synthesis of the solid solutions $ZnGe_{1-x}Sn_xP_2$ (x = 0, 0.25, 0.5, 0.75, 1) is as follows. Milling of starting materials was performed in three steps, a long 5-hour milling followed by two 1-hour millings. The agglomerated material was mechanically reincorporated into the milling jar in the glovebox between milling steps. Silica tube reaction steps were circumvented, and milled material was directly placed into a graphite die and transported under inert atmosphere to the hot-pressing apparatus and purged with argon gas. The sintering process conditions are visualized in Figure 4.2 for each of the members of the series. The material was pressed under 58 MPa and raised to the target temperature over 2 hours which varied per sample and held for 2.5 hours. Pressure was released and the heating elements were turned off allowing the sample to cool pressure free preventing cracking due to differing thermal expansion between the die and material. PXRD verification of pellet was performed followed by properties analysis, after which a long PXRD was performed on ground samples for Rietveld refinements.

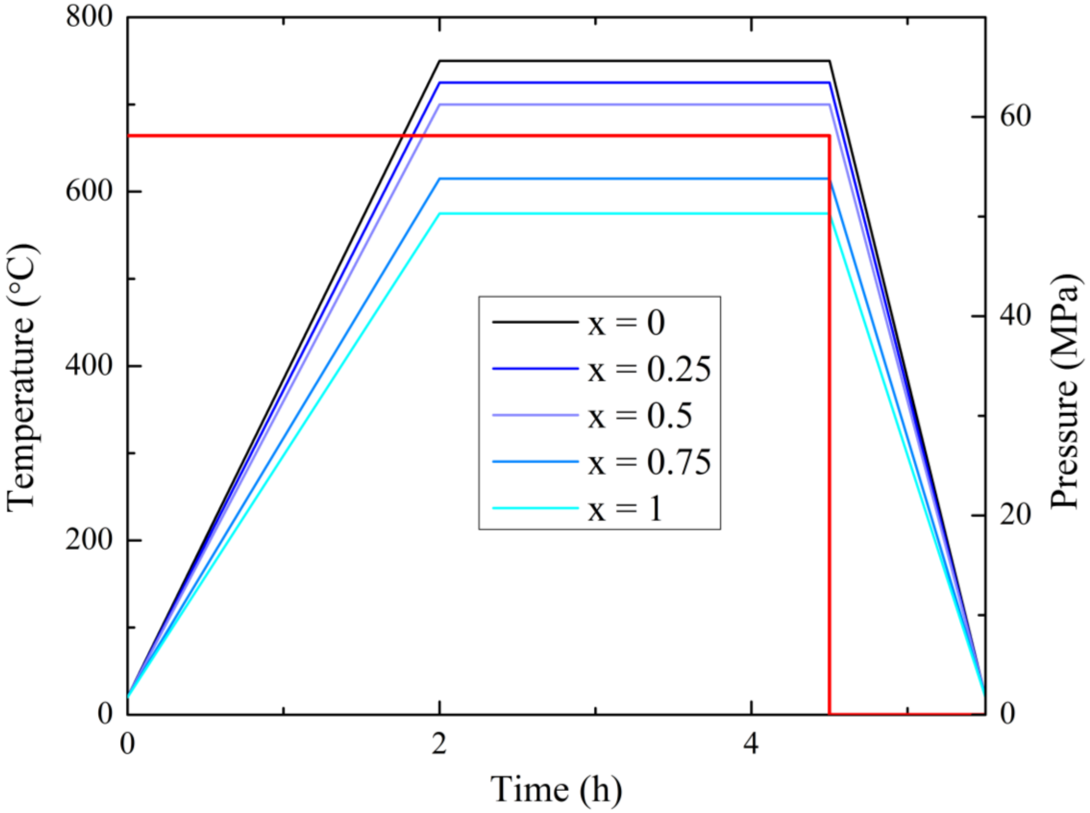

Figure 4.2: Hot-pressing conditions for the solid solution series $ZnGe_{1-x}Sn_xP_2$ with temperatures displayed in blue and pressure in red.

4.3 Chemical and Structural Characterization

The target phases were not fully realized until after sintering upon which the broad peaks narrowed suggesting the growth of grain size in the material. Successful acquisition of the target phase was found to be sensitive to sintering temperature for the alloyed phases and pure $ZnSnP_2$, however $ZnGeP_2$ was less sensitive due to its congruently melting behavior. Ideal sintering temperatures varied dependent on the level of alloying with a narrow range for successful synthesis. If the temperature was too high decomposition was observed, while if the temperature was too low miscibility was not achieved and double sets of peaks were observed.

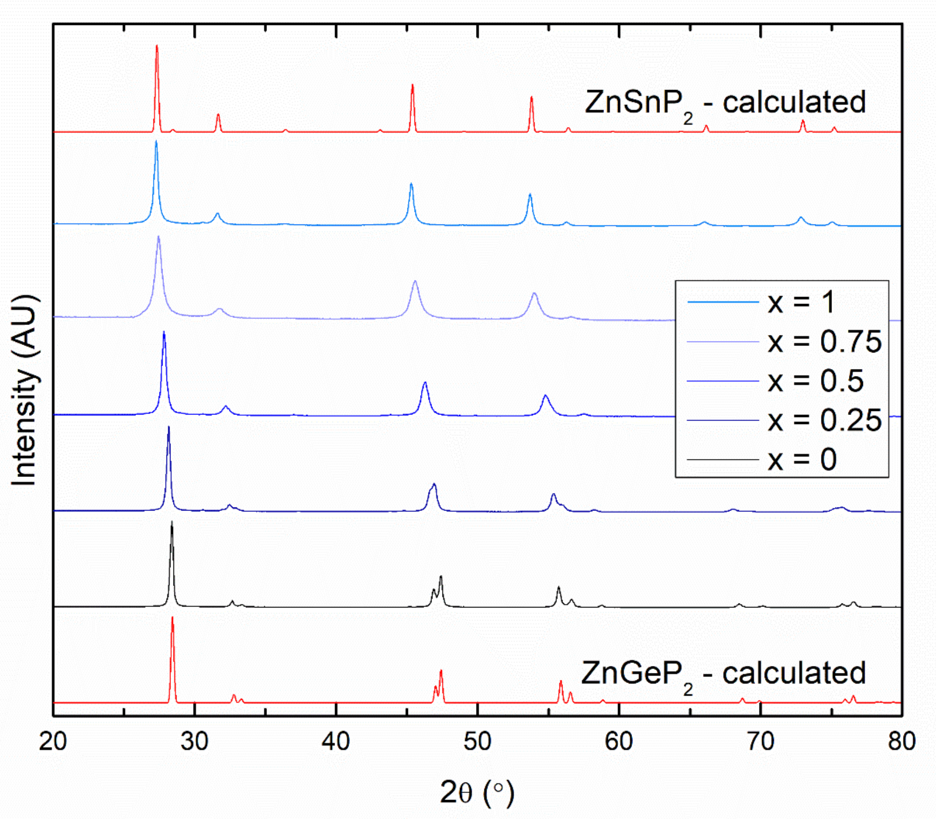

Figure 4.3: PXRD of the solid solutions after sintering and densification. Systematic peak shifts in 2θ and intensity can be seen as the concentration of Cn group changes. The double peaks at 33°, 47°, and 56° shift into a single peak as the system becomes more tetragonal ($c/(2a) = 1$).

Successful alloying of the compound produces a systematic peak shift towards lower 2θ values with increasing tin concentration. Figure 4.3 displays the PXRD pattern data for the full series and the refinement statistics can be found in Table A.4 in the appendix. Rietveld refinements on the obtained data reveal changes in the unit cell parameters with alloying as shown in Figure 4.4(a, b). The volume changes slowly between the end members x = 0-0.25 and x = 0.75-1 then quickly for Sn concentrations between x = 0.25 and x = 0.75. This behavior as a deviation from Vegard's law has been explained previously for complex compounds.[216] A summary of the unit cell parameters for all members are shown in Table 4.1.

Table 4.1: Summary of structure parameters for $ZnGe_{1-x}Sn_xP_2$ series obtained from Rietveld refinements.

x	***a, b* (Å)**	***c* (Å)**	***V* (Å^3)**	***c*/2*a***
0	5.4703(1)	10.7221(3)	320.84(1)	0.9800
0.25	5.5039(2)	10.8561(5)	328.86(2)	0.9862
0.5	5.5601(3)	11.0209(8)	340.71(3)	0.9910
0.75	5.6298(9)	11.229(3)	355.89(6)	0.9973
1	5.6584(1)	11.290(4)	361.5(3)	0.9976

Expansion of the *c*-axis is found to be much greater than that of the *a*-axis as seen in Figure 4.4(c), where $\Delta c/2$ is nearly double Δa between x = 0 and x = 0.75 and between x = 0.75 and x = 1 the relative change in the UC parameters is the same. Due to these relative changes, tetragonality is rapidly increased reaching a plateau at x = 0.75 as seen in Figure 4.4(d). Changes for bond distances with alloying are seen in Figure 4.4(e), where Zn-P bonding distance remains relatively unchanged while the Ge, Sn-P bond distances increases significantly with increasing tin concentration.

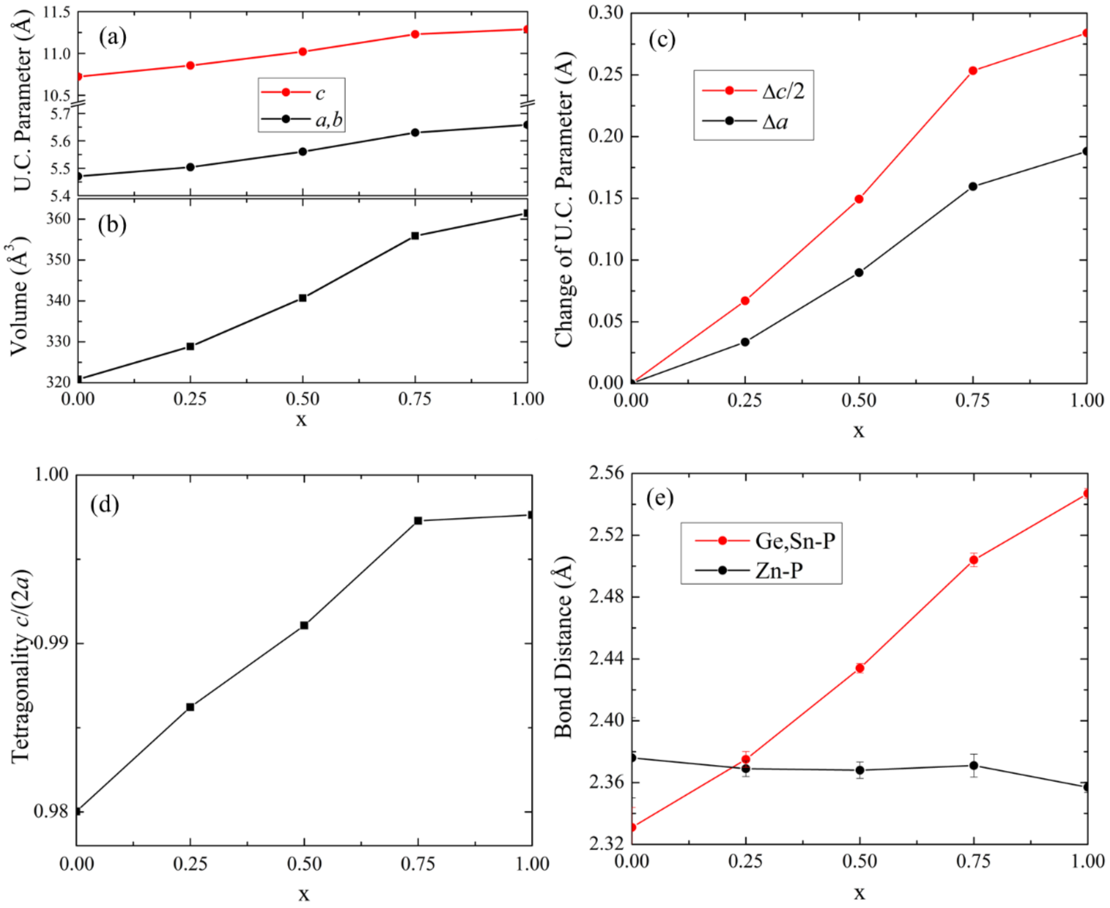

Figure 4.4: Effect on structure with changes in concentration x of $ZnGe_{1-x}Sn_xP_2$ results in expansion of (a) unit cell parameters and (b) volume with increasing tin concentration. (c) Comparing the increase in unit cell parameters *a* and *c*/2 and (d) resulting changes to tetragonality with composition. (e) Changes in bond distances with increasing Sn show Ge, Sn–P bonds increase while Zn–P remains relatively unchanged.

The bonding angles of the tetrahedra influence the changes in unit cell parameters differently. Shown in Figure 4.5(a), the crystal structure is viewed along the *b*-axis. As bonding angles in the *c*-direction (black) decrease it tends to increase the length of the *c*-axis and decrease the length of the *a*, *b*-axis. The alternative occurs for the bonding in the *a*, *b* direction (red). As seen from Figure 4.5(b) the bonding angles of the zinc-centered tetrahedra (solid lines) increase the length of the *c*-axis (decrease *a*-axis) while the tin-centered tetrahedra (dashed lines) decrease the length of the *c*-axis (increase *a*-axis). Angles of the zinc centered tetrahedra decrease 5° in the *c*-direction and increase 2.5° in the *a*, *b*-direction versus the Ge,Sn centered tetrahedra which increase 2.9° in the *c*-direction and decrease 1.5° in the *a*,*b*-direction. The changes in zinc-phosphorus bonding angles have a greater influence on the unit cell parameters than tin-phosphorus bonding angles resulting in preferred tetragonality.

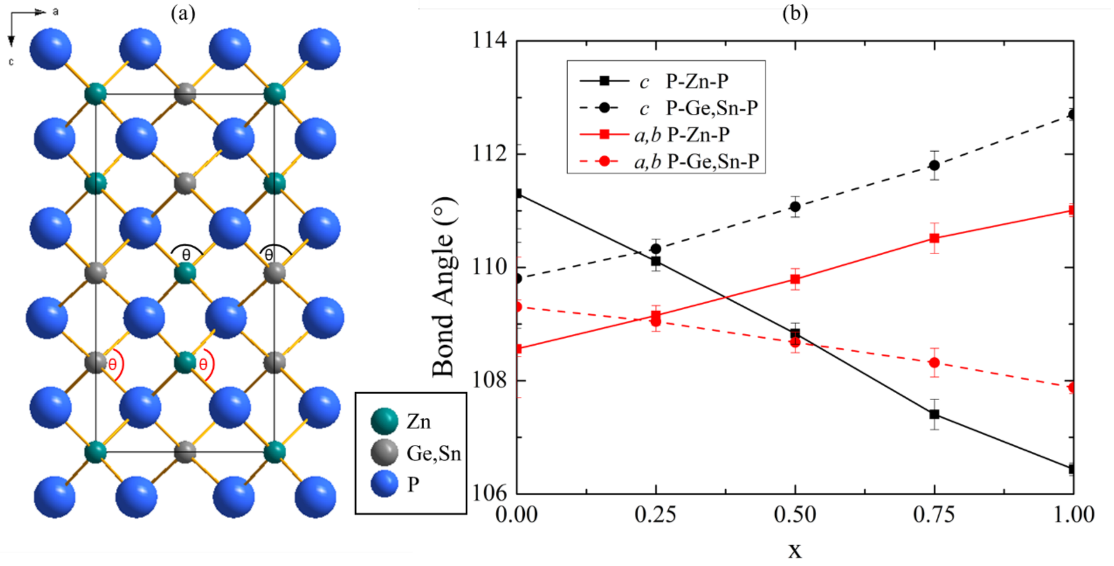

Figure 4.5: Changes in bond angles with Sn concentration influence on UC parameters. (a) Decreases to *a, b*-directional bonds (red) will decrease the *c*-axis, while decreases to *c*-directional bonding (black) will increase the *c*-axis, and vice versa. (b) The Zn-centered tetrahedra (solid lines) tend to increase the *c*-axis, while the Ge, Sn tetrahedra (dashed lines) tend to increase the *a, b* axis.

Statistical results of the Rietveld refinements can be found in Table A.4 in the Appendix, where R_p, R_{wp}, R_{exp}, x_{calc}, and χ^2 are shown. The poorest refinement results were obtained for $ZnGeP_2$ with R_{wp} = 18.5% while all other samples R_{wp} ranged from 4.4% to 8.5%. The chemical composition of the series was evaluated by refining occupancy parameters during Rietveld refinements and energy dispersive x-ray spectroscopy (EDAX) analysis. Sn occupancy from Rietveld refinements of the solid solutions were determined as x_{calc} = 0.223, 0.454, and 0.737 with relative discrepancies of 11%, 9%, and 2% from the target composition. EDAX results for the solid solutions and end members can be found in Table 4.2, where atomic percent, and empirical formula of the constituent atoms are shown. Sn concentrations determined from EDAX measurements match well with expected atomic percent showing differences of less than 2%, however Zn and Ge values were lower than expected while P was larger than expected for the measured compounds. Ge and Zn differences may be due to significant overlap of the dispersion peaks for Zn-Kα_1 and Ge- Kα_1 which were quantified. Further quantifThese discrepancies may also indicate systematic loss of Zn, Ge, and Sn during the reaction process. Excess amorphous P would be difficult to detect with PXRD, however at such significant losses of Ge and Sn the formation of crystalline ZnP_2 would likely occur and be easily detected. In the following chapters EDAX area scans are used versus the point measurements used here which show significant improvement to these discrepancies. EDAX atomic mapping can be found in Figure A.6 in the Appendix.

Table 4.2: EDAX analysis results obtained using average of four point measurements on the $ZnGe_{1-x}Sn_xP_2$ series. The table is sorted by compound nomenclature with atomic percent (At. %) and empirical formula (Emp.) for each set of measurements.

	x = 0		**x = 0.25**		**x = 0.5**		**x = 0.75**		**x = 1**	
Elem.	**At. %**	**Emp.**	**At. %**	**Emp.**	**At. %**	**Emp.**	**At. %**	**Emp.**	**At. %**	**Emp.**
Zn	23.1	0.92	24.7	0.99	25.2	1.01	24.1	0.97	22.9	0.92
Ge	24.1	0.96	17.2	0.69	9.7	0.39	5.36	0.22	--	--
Sn	--	--	6.14	0.25	12.4	0.49	18.4	0.74	25.3	1.01
P	52.9	2.12	51.9	2.08	52.6	2.11	52.1	2.08	51.7	2.07

4.4 Electronic Structure and Properties

Electronic band structure calculations and density of states (DOS) of the end members are displayed in Figure 4.6. The electronic structures display band gaps with Fermi levels close to the valence band resulting in p-type semiconducting behavior. The primary contributions to the band structure from the valence band maximum (VBM) to about -5 eV consist of the P *3p*-states, with some mixing of Zn *sp*-states and Sn/Ge *p* states. The conduction bands from conduction band minimum (CBM) to 6 eV are primarily composed of Sn/Ge *s* states with some mixing of the P *p* states where $ZnGeP_2$ has less mixing than $ZnSnP_2$ due to a larger degree of ionic bonding. Calculated band gaps are 1.25 eV and 0.93 eV for $ZnGeP_2$ and $ZnSnP_2$ respectively; which are significantly lower than experimental results of 2.2 eV and 1.66 eV respectively found in literature,[217,218] but are in line with other calculations.[219,220] Partial density of states (PDOS) calculations for $ZnGeP_2$ and $ZnSnP_2$ for each atomic position and their orbitals are found in the Appendix Figure A.7 and Figure A.8. The direct band gap is found along the Γ direction for both compounds. Underestimation of band gaps is a typical result with semiconductor and insulator calculations from DFT calculations.[194]

It is informative to compare the valence edge bands for both materials at the Γ point. For $ZnSnP_2$, band convergence due to tetragonality is observed, whereas the bands of $ZnGeP_2$ are slightly separated. Degeneracy of bands and high density of states at the band edge is known to result in greater Seebeck effect in TE materials.[38] The conduction bands for $ZnGeP_2$ display a higher degree of degeneracy, whereas the valence bands of $ZnSnP_2$ show greater degeneracy. Band convergence of the conduction bands should also be possible through solid solution formation by convergence of extrema. The conduction band minimum for $ZnGeP_2$ at the S point (Figure 4.6(a)) is lower than the minimum at the Γ point while for $ZnSnP_2$ (Figure 4.6(b)) the alternate occurs. In principle there should be an intermediate composition at which these bands are degenerate. The conduction band degeneracy would be most noticeable in an n-type material; however, the Fermi level close to the valence bands indicates p-type behavior. These various pathways to obtain band degeneracy in these compounds provide motivation for the formation of solid solutions of the end members.

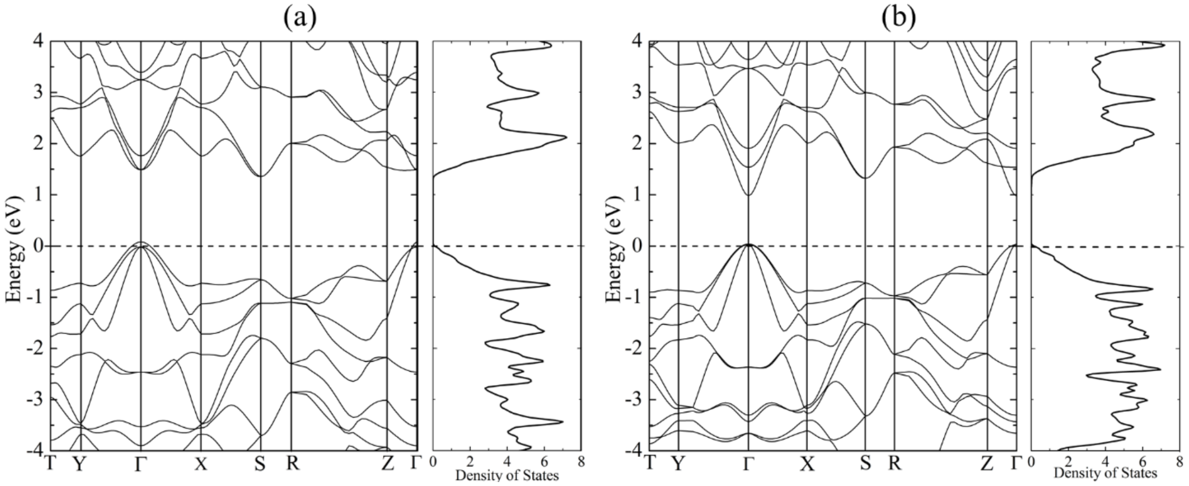

Figure 4.6: Electronic band structure and density of states for $ZnGeP_2$ (a) and $ZnSnP_2$ (b).

Ab initio electronic structure calculations were performed on all members of the $ZnGe_{1-x}Sn_xP_2$ solid solution series. Manual substitution of Sn onto the four Ge sites was used, and symmetry was considered to eliminate duplicate structures. The resulting structures had $P\bar{4}$ symmetry for x = 0.25

and 0.75, and two unique symmetries $I\bar{4}$ and $P222_1$ for x = 0.5. Volume optimization calculations were performed starting from the unit cell parameters of the end members. Energy, force and charge were minimized while changing the atomic coordinates. The lowest energy structures were determined and used to perform electronic structure calculations. The unit cell parameters remained constant however, which were initialized using the $ZnSnP_2$ parameters. A low symmetry orthorhombic basis was used for band structure plots to allow for comparison of the bands. The band structures for x = 0.25 and 0.75 are comparable to the end members, while for x = 0.5 the resulting band structure shows considerable differences. These band structure plots are shown in Figure A.9 through Figure A.12 in the Appendix.

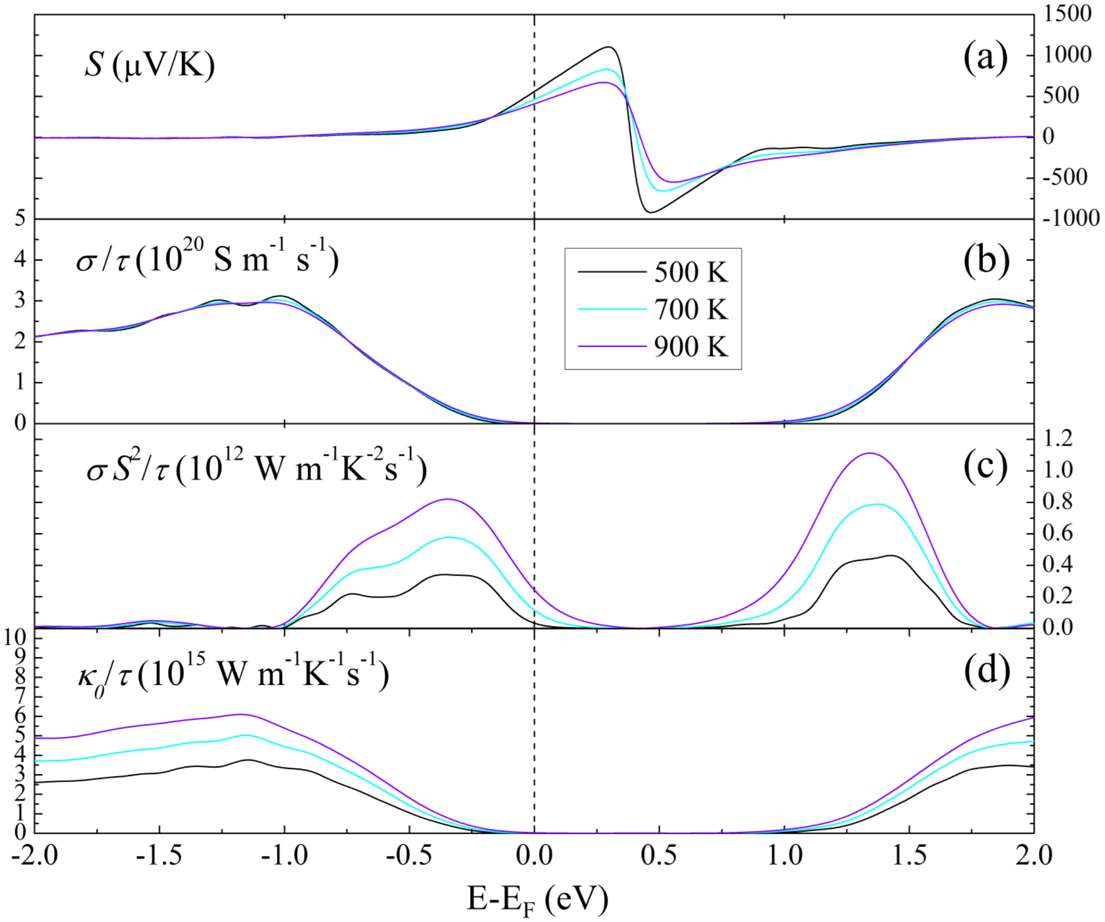

Figure 4.7: BolzTraP2 calculation results of TE parameters versus energy level for $ZnSnP_2$. (a) Seebeck coefficient, and scattering independent (b) electrical conductivity, (c) power factor, and (d) electronic thermal conductivity.

Boltzmann transport calculations were performed using the BoltzTraP2 package on all members of the series. Temperature increments of 100 K were used to display the changes of the calculated properties versus energy level with changing temperature. Calculated Fermi energies were used to derive the expected Seebeck coefficients, and with respect to the relaxation time, electrical conductivity, electronic thermal conductivity, and power factor as seen in Figure 4.7 for $ZnSnP_2$.

Applying a scattering time estimate of τ = 10 fs, which is typical for these materials,[221] allows an estimate of the TE properties. Using these values along with lattice thermal conductivity (κ_{lat}) obtained experimentally (Section 4.5.4) allows for the calculation of zT:

$$zT = T \frac{(\sigma S^2/\tau) \cdot \tau}{(\kappa_0/\tau) \cdot \tau + \kappa_{lat}}$$

These obtained values can be plotted versus Fermi level, carrier concentration, and doping levels. Using the doping level per unit cell and dividing by formula units per cell (Z = 4), zT as a function of dopant is obtained (Figure 4.8). Here the negative values indicate electrons and the positive values holes. For $ZnSnP_2$ zT_{max} is achieved by doping of 0.01 electrons and 0.007 holes per formula for a n-type and p-type material respectively. This level of doping is readily achievable in materials without destabilization of the structure and/or formation of side products.[50]

The p-type zT_{max} found in Figure 4.8 is significantly greater than n-type which can be interpreted using the band structure (Figure 4.6 (b)), where the valence band edge contains a greater number of degenerate valleys centered at the Γ direction, while the conduction bands contain no direct degeneracies. The relatively steep parabolic band degeneracies would increase Seebeck coefficient by increasing the density of states while maintaining low inertial effective mass leading to higher values of zT. Similar analysis of $ZnGeP_2$ predicts that n-type performance is greater than p-type (Figure A.18) which can again be interpreted from the band structure (Figure 4.6(a)) as the conduction band edge displays more degenerate (direct and indirect) behavior than the valence band edge. Analysis for all members of the series was performed which can be found in Table 4.3 using the experimentally determined thermal conductivities.

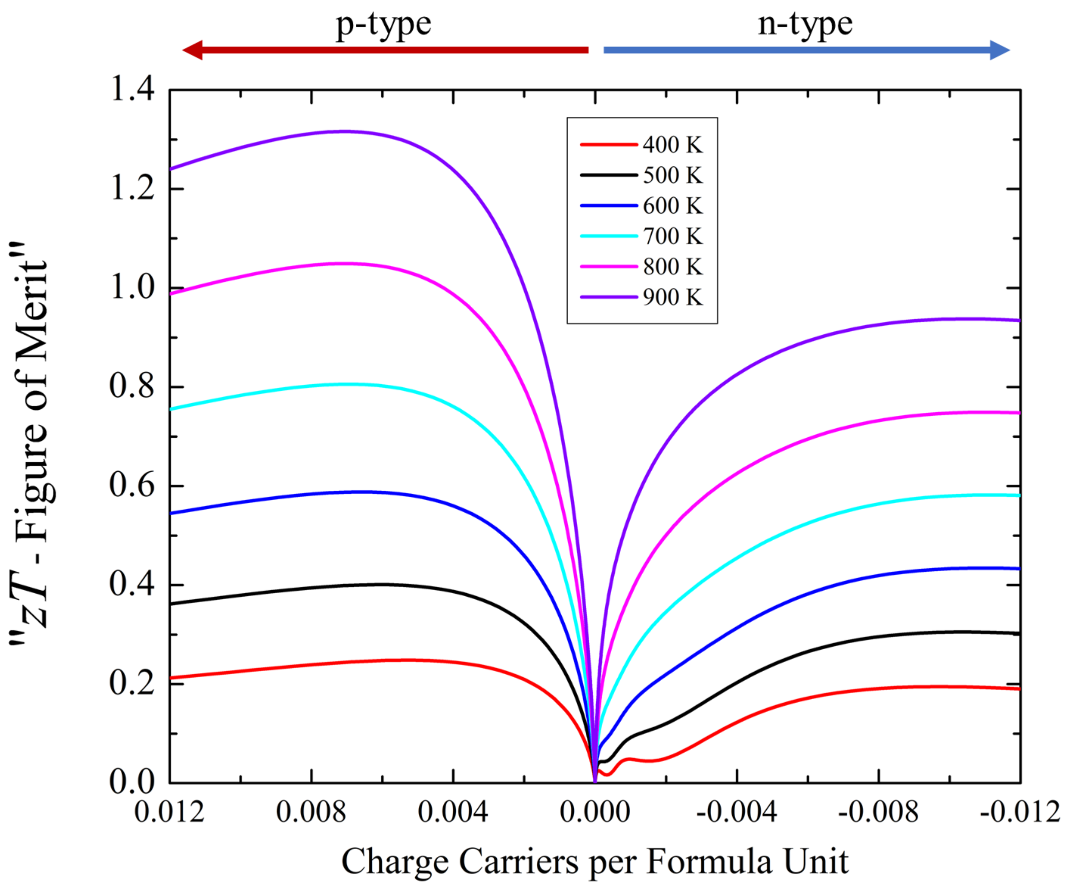

Figure 4.8: Calculated zT versus charge carriers per formula unit of $ZnSnP_2$. The figure of merit is obtained from BoltzTraP calculations and experimental data for lattice thermal conductivity with a constant relaxation time (τ) of 10 fs.

While the doping required to produce zT_{max} may be achievable in these materials, a significant improvement to the TE properties is seen for even smaller doping levels. Table 4.3 contains the minimum doping levels (N_{min}) to achieve $zT = 1$ for all members of the series which is found to range from 0.001 to 0.003 carriers per formula unit. These levels of p-type doping have been achievable in the chalcogenide chalcopyrite materials,[222,223] and would have chemical formulas such as $ZnSnP_{1.98}S_{0.002}$ or $ZnSn_{0.98}In_{0.002}P_2$. The complete BoltzTraP results are shown for all calculations with Figure A.13 through Figure A.22 in the Appendix.

Table 4.3: Results of BoltzTraP analysis for Figure of Merit for $ZnGe_{1-x}Sn_xP_2$ series. The dark rows of the table are for n-type and light rows for p-type. N is the number of charge carriers per formula unit, and N_{min} is the minimum carriers PFU required to achieve *zT* = 1.

x	Carrier type	N	zT_{max}	N_{min} (900 K)
0	n	-0.008	1.4	-0.002
	p	0.007	1.1	-
0.25	n	-0.012	0.6	-
	p	0.015	1.3	0.003
0.5	n	-0.002	0.8	-
	p	0.006	1.7	0.001
0.75	n	-0.013	0.5	-
	p	0.013	1.4	0.003
1	n	-0.007	0.9	-
	p	0.007	1.3	0.003

4.5 Thermoelectric Properties

4.5.1 Electrical Conductivity

Measurements of electrical conductivity (Figure 4.9) were taken at elevated temperatures due to the high resistance of the samples and instrument limitations. The thin samples required for thermal conductivity measurements resulted in small cross-sectional areas and thus increased resistance of the samples. Above 800 K, the samples containing more than x = 0.25 tin produced inconsistent results after thermal cycling likely due to softening as temperatures approached decomposition of $ZnSnP_2$ (~980 K). Inconsistent measurements may also be the result of the well-known high temperature transition to disordered sphalerite-like structure for chalcopyrite compounds.[139,150]

The range of electrical conductivities is low for thermoelectric application with 0.01 S cm^{-1} – 0.5 S cm^{-1} at 600 K and increasing to 0.1 S cm^{-1} at 750 K and up to 1 S cm^{-1} at 950 K for x = 0.25. A desirable range of electrical conductivity for typical thermoelectric materials vary, but for high performance chalcopyrite TE materials is typically in the range of 10 S cm^{-1} to 100 S cm^{-1} around 800

K.[31,90] The electrical conductivity of $ZnGeP_2$ displays behavior least consistent with the other compounds, where the conductivity crosses the other members of the series which may be due to impurities in the sample which were not detected with PXRD. The other members of the series display consistent behavior, where $ZnSnP_2$ has the lowest conductivity with members increasing in conductivity as Sn concentration decreases. This behavior is somewhat unexpected as the band gap for $ZnGeP_2$ (1.18 eV) is determined to be larger than that of $ZnSnP_2$ (0.70 eV), however these values were measured optically.[213]

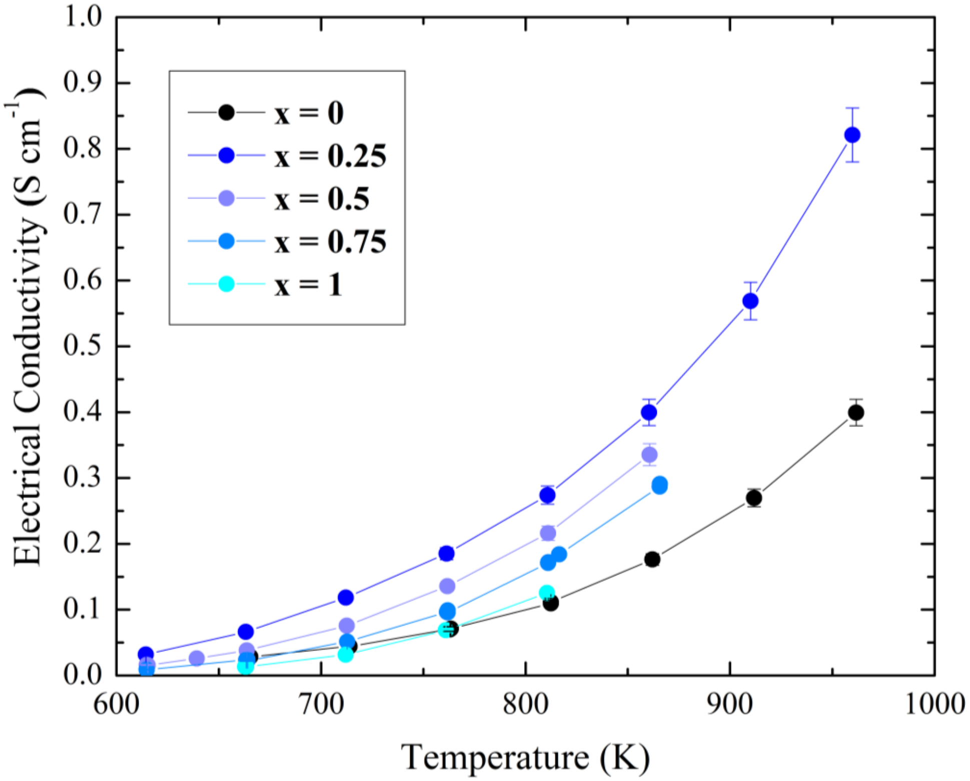

Figure 4.9: Electrical conductivity for $ZnGe_{1-x}Sn_xP_2$ series (x = 0, 0.25, 0.5, 0.75, 1). $ZnGeP_2$ displays behavior not on trend with the other members of the series.

Intrinsic semiconducting behavior is observed in the compounds displaying an exponential increase in conductivity with increasing temperature. The intrinsic conductivity is confirmed in Figure 4.10(a) by plotting ln (σ) versus 1/T to obtain an Arrhenius plot. Both x = 0 and x = 0.25 show significant deviation from linearity at lower temperatures. The band gaps of the materials are obtained by fitting the linear region and using Equation 1-33 which is at higher temperatures as expected. The unexpected band gap trend seen in Figure 4.10(b) shows an increasing band gap with increasing Sn concentration. The band gaps obtained in literature are significantly higher than calculated for both end members 1.92 eV versus 1.16 eV and 1.66 eV versus 1.43 eV for Ge and Sn respectively which may suggest impurities in the samples.[150] These band gap values obtained from the activation energies of the samples differ from the optically measured band gaps, and therefore are expected to differ. Due to the high temperatures required for these measurements this method has not been performed for these materials prior to this study.

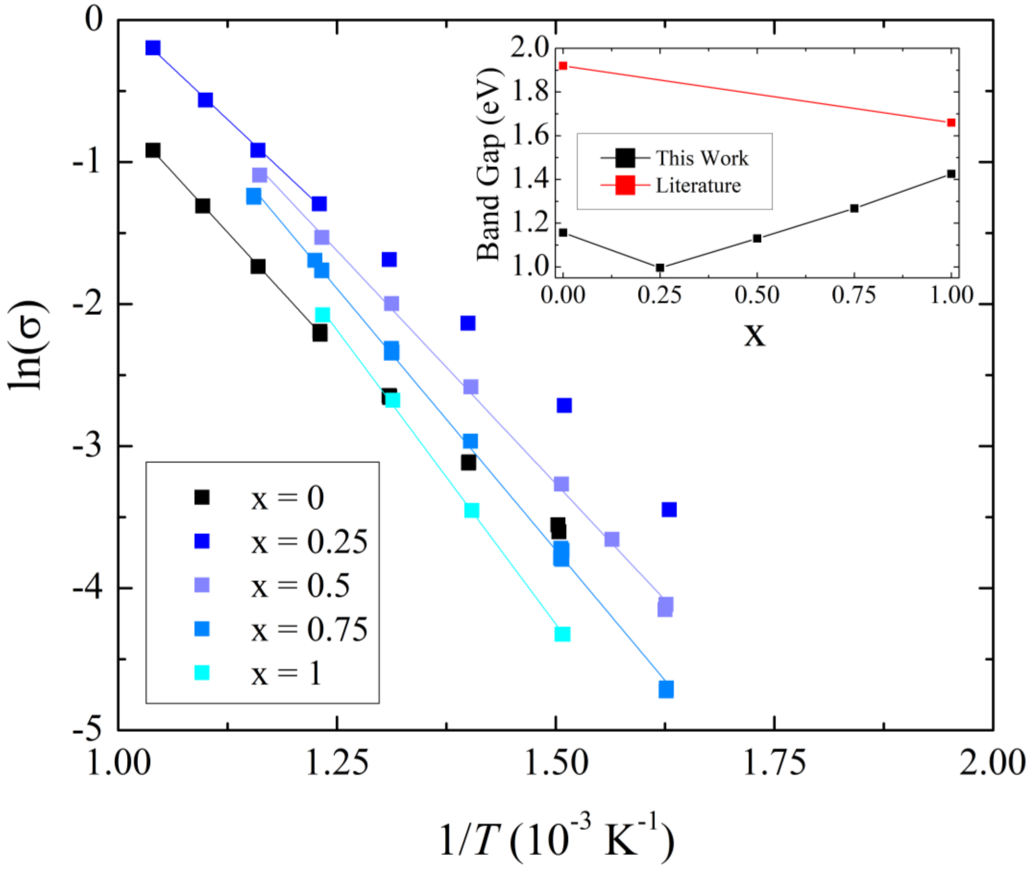

Figure 4.10: Calculation of band gap using the Arrhenius method for $ZnGe_{1-x}Sn_xP_2$ series (main) ln (σ) versus 1/T with linear fits for the intrinsic regions (inset) calculated band gaps (eV) versus Sn concentration x.

4.5.2 Seebeck Coefficient

The Seebeck coefficient for chalcopyrite materials benefits greatly from the pseudo-cubic structure, which leads to parabolic band degeneracies as previously discussed.[224] Seen in Figure 4.11, the Seebeck coefficient varies significantly over the range of solid solutions and is indicate of p-type behavior. The Seebeck coefficient values trend inversely with electrical conductivity as expected for x = 0.5, 0.75, and 1. Ge-rich members (x = 0, 0.25) have significantly lower values due to the lower the higher electrical conductivity, however a lower degree of tetragonality may also contribute. In comparable temperature ranges starting at 650 K, the Seebeck coefficient values are 250 μV K^{-1} and 650 μV K^{-1} for x = 0 and 0.25 respectively, increasing with temperature to 500 μV K^{-1} and 600 μV K^{-1} at 925 K. The temperature dependent behavior observed is consistent with extrinsic semiconductors, which is unexpected. The other members have similar values of Seebeck coefficient to each other; with 925 μV K^{-1}, 933 μV K^{-1}, and 970 μV K^{-1} at 650 K for x = 0.5, 0.75, 1, respectively. The Seebeck coefficient decreases more for $ZnSnP_2$ than for the other members to 740 μV K^{-1} at 800 K. The other members decrease less and are almost equivalent with 815 μV K^{-1} and 800 μV K^{-1} for x = 0.5 and 0.75, respectively at 800 K. The degree of tetragonality might be considered here as a significant contributor to the value of the Seebeck coefficient, where the members with higher degrees of tetragonality have higher significantly higher Seebeck coefficients due to expected band degeneracies. The temperature dependence is typical for intrinsic semiconductors for the tin rich compounds.

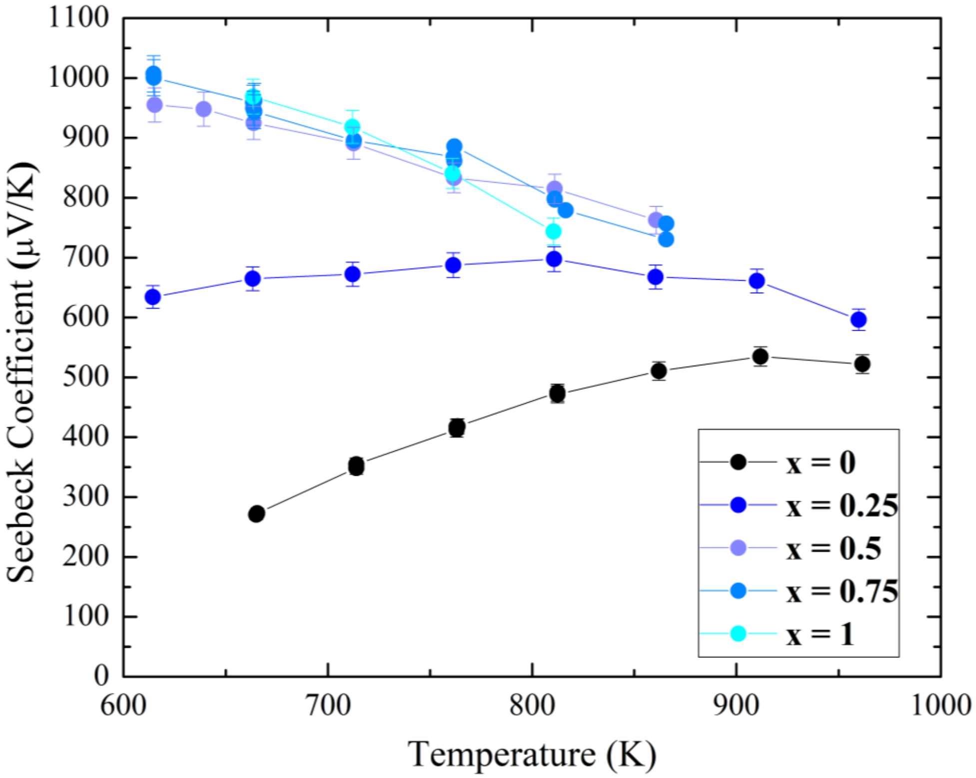

Figure 4.11: Seebeck coefficient measurements vs temperature for the $ZnGe_{1-x}Sn_xP_2$ series, typical negative linear response with temperature is seen for x = 0.5, 0.75, and 1 for intrinsic semiconductors. Members with x = 0 and 0.25 display more extrinsic semiconducting like behavior.

4.5.3 Power Factor

The power factor ($S^2\sigma$) versus temperature is displayed for the series in Figure 4.12. The end members have the lowest power factors with $ZnGeP_2$ the lowest due to low Seebeck coefficient and $ZnSnP_2$ due to low electrical conductivity. The solid solution members with x = 0.25, 0.5 and 0.75 have similar values at comparable temperatures with 1.28 $\mu W\ m^{-1}\ K^{-2}$, 1.51 $\mu W\ m^{-1}\ K^{-2}$, and 1.08 $\mu W\ m^{-1}\ K^{-2}$ at 615 K respectively, rising to 13.3 $\mu W\ m^{-1}\ K^{-2}$, 14.3 $\mu W\ m^{-1}\ K^{-2}$, and 12.7 $\mu W\ m^{-1}\ K^{-2}$ at 815 K. The x = 0.25 member displays the largest power factor of 29.2 $\mu W\ m^{-1}\ K^{-2}$ at 960 K due to high temperature stability. Power factors are quite low for these compounds as expected due to low electrical conductivity despite the large Seebeck coefficients. As seen in the Boltzmann transport calculations, considerable improvement is expected by increasing the carrier concentration.

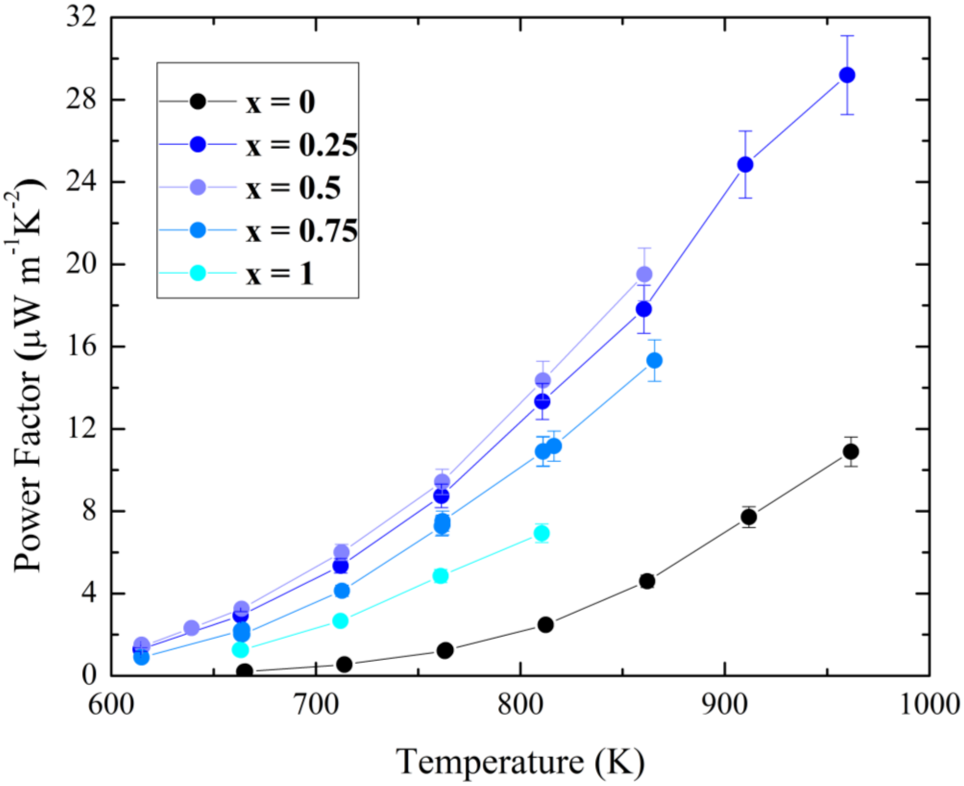

Figure 4.12: Power factor versus temperature for the $ZnGe_{1-x}Sn_xP_2$ series. Power factor is the highest for the solid solutions and lower for the end members.

4.5.4 Thermal Conductivity

Thermal conductivity measurements are displayed in Figure 4.13 for the series. The measurements show that the two end members of the solid solution have the highest values, with $ZnGeP_2$ having the largest thermal conductivity by more than two times that of the other compounds at low temperatures. Alloy scattering of phonons reduce the thermal conductivity of the solid solutions leading to lowest thermal conductivity at x = 0.5 and 0.75.[213] Typical negative temperature dependence is observed with $ZnGeP_2$ starting highest at 9.6 W m^{-1} K^{-1} at 320 K decreasing to 3.8 W m^{-1} K^{-1} at 875 K. For $ZnSnP_2$ and the solid solutions, the thermal conductivity starts at 2.9 W m^{-1} K^{-1} to 4.1 W m^{-1} K^{-1} at 320 K decreasing slightly to 1.8 W m^{-1} K^{-1} to 2.3 W m^{-1} K^{-1} at 875 K. The overall change in thermal conductivity follows a parabolic trend with concentration typical of solid solutions, where the lowest thermal conductivity occurs at x = 0.5 and highest for the end members.

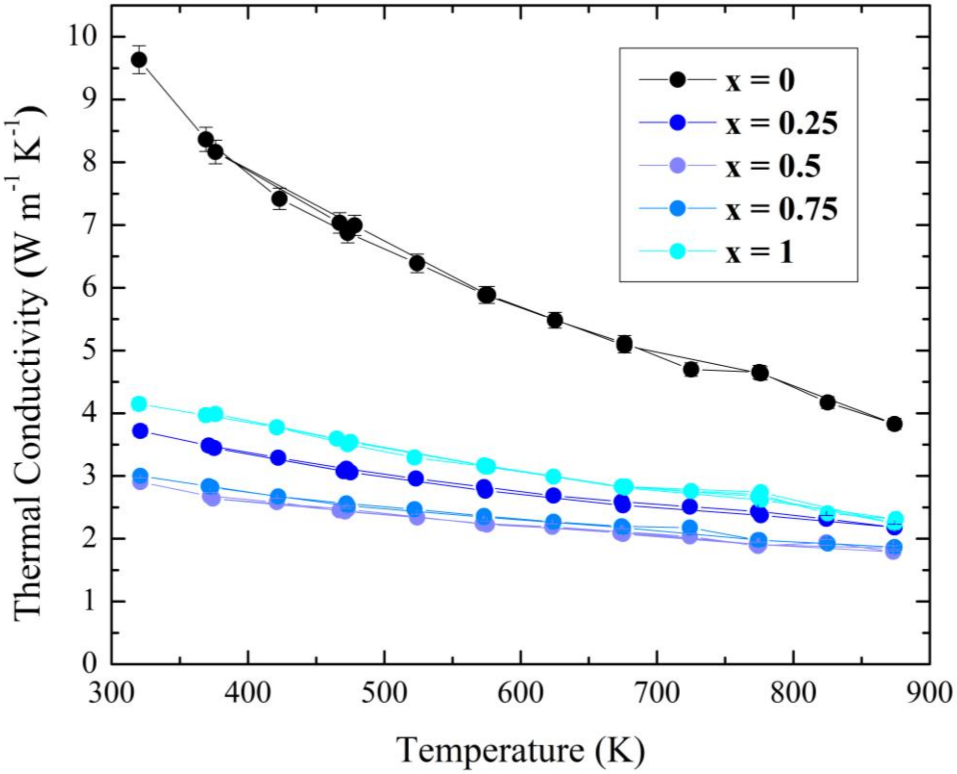

Figure 4.13: Thermal conductivity for $ZnGe_{1-x}Sn_xP_2$ series (x = 0, 0.25, 0.5, 0.75, 1). End members display the largest thermal conductivity, while the solid solutions display decreased thermal conductivity due to alloy scattering.

The electronic and lattice thermal conductivities were determined for the members of the series using Equation 1-58 and the Wiedemann-Franz law displaying low electronic thermal conductivities less than 0.001 W m^{-1} K^{-1}. The resulting lattice thermal conductivities determined followed the same trend with substation as the overall thermal conductivity. The lattice thermal conductivity (Figure A.23) and electronic thermal conductivity (Figure A.24) are displayed in the Appendix.

4.5.5 Thermoelectric Figure of Merit, zT

The thermoelectric figure of merits follows a similar temperature and compositional trend to the power factors with the end members having the poorest performance rising to only zT = 0.003 at 950 K and 0.0015 at 750 K for $ZnGeP_2$ and $ZnSnP_2$ respectively. In comparable ranges however, the performance of $ZnSnP_2$ is much better than $ZnGeP_2$. The solid solutions have better thermoelectric performance with x = 0.25 rising to 0.008 at 875 K. In comparable temperature ranges, x = 0.25 and x = 0.75 have nearly identical performance, where we see the lower thermal conductivity of the Sn-rich solution balancing the higher power factor of the germanium rich member. The best performance is found in the x = 0.5 member, where both the power factor and thermal conductivity are most favorable producing zT = 0.009 at 850 K. The overall thermoelectric performance of these solid solutions is poor due to low electrical conductivity. Increases in overall performance are seen in the solid solutions, however, due to decreased thermal conductivity and increased electrical conductivity, while maintaining a high Seebeck coefficient. The zT versus temperature results are displayed in Figure 4.14 and a summary of relevant thermoelectric properties in comparable temperature ranges are found in Table 4.4.

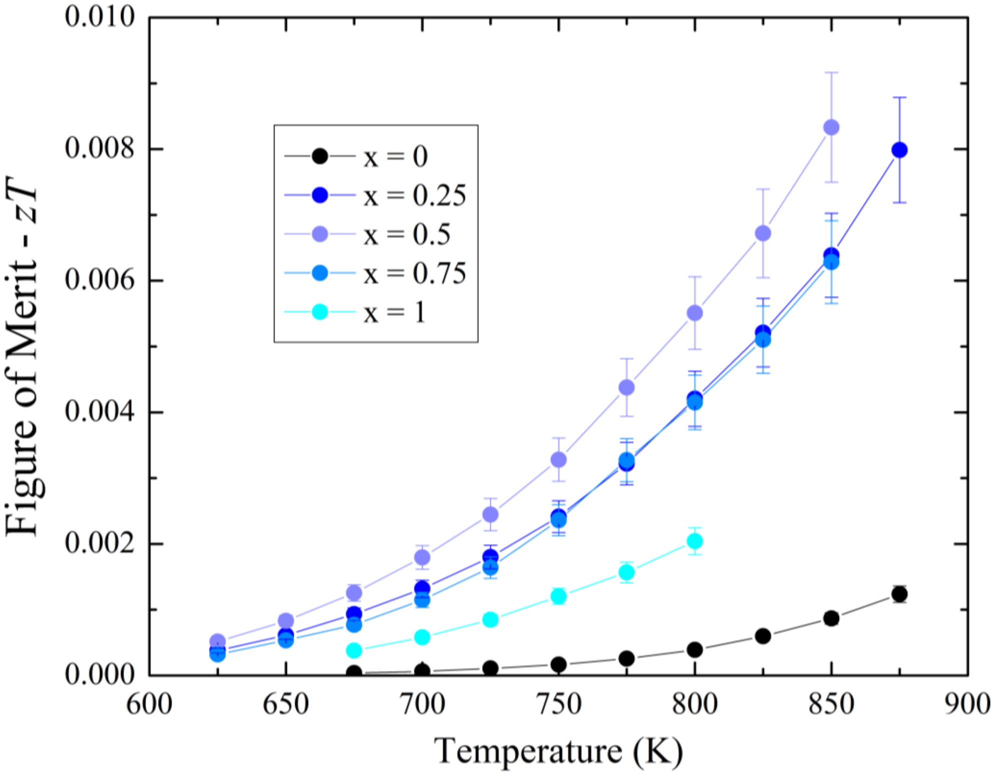

Figure 4.14: Thermoelectric figure of merit vs temperature for the $ZnGe_{1-x}Sn_xP_2$ series. Data calculated from linear interpolation of measured properties at comparable temperatures.

Table 4.4: Summary of thermoelectric properties for $ZnGe_{1-x}Sn_xP_2$ solid solutions within comparable temperature ranges.

x	σ (S^{-1} cm^{-1}) 660 K, 810 K	S (µV K^{-1}) 660 K, 810 K	$S^2\sigma$ (µW m^{-1} K^{-2}) 660 K, 810 K	κ (W m^{-1} K^{-1}) 325 K, 875 K	zT 675 K, 800 K
0	0.028, 0.109	275, 475	0.19, 2.47	9.64, 4.41	3.7E-5, 3.9E-4
0.25	0.066, 0.274	665, 697	1.28, 13.3	3.70, 2.18	9.3E-4, 4.2E-3
0.5	0.038, 0.216	925, 815	3.26, 14.4	2.88, 1.82	1.3E-3, 5.5E-3
0.75	0.022, 0.171	950, 798	2.02, 10.9	2.99, 1.87	7.7E-4, 4.2E-3
1	0.013, 0.125	975, 744	1.25, 6.93	4.13, 2.54	3.8E-4, 2.0E-3

4.5.6 Thermal Conductivity after Refined Synthesis

Thermoelectric property measurements discussed above were performed on materials synthesized by the method described previously: ball milling to ampule sintering to hot-pressing. A streamlined and more effective method was later developed as described previously: ball milling three times followed directly by hot-pressing. Thermal conductivity measurements were performed on the end members of the series which produced considerable improvements as seen in Figure 4.15.

The thermal conductivity of the samples decreases by more than a factor of 2 at low temperatures compared to the previous method. For $ZnSnP_2$ TC at 325 K decreases from 4.13 W m^{-1} K^{-1} to 1.73 W m^{-1} K^{-1} and at 825 K decreases from 2.40 W m^{-1} K^{-1} to 1.21 W m^{-1} K^{-1}. For $ZnGeP_2$ TC at 325 K decreases from 9.51 W m^{-1} K^{-1} to 4.45 W m^{-1} K^{-1} and at 825 K decreases from 4.17 W m^{-1} K^{-1} to 2.56 W m^{-1} K^{-1}. This decreased thermal conductivity is likely the result of decreased particle size and sintered grain boundaries. Required miscibility sintering temperatures for the materials synthesized by the newer method were reduced, which also serves to decrease the size and number of grain boundaries. The temperature dependence for thermal conductivities of the samples shows flatter curves suggesting an increase in boundary scattering which tends to decrease with increasing temperature.[46,48] Thermoelectric properties of the full series of solid solutions synthesized by the refined method were not measured.

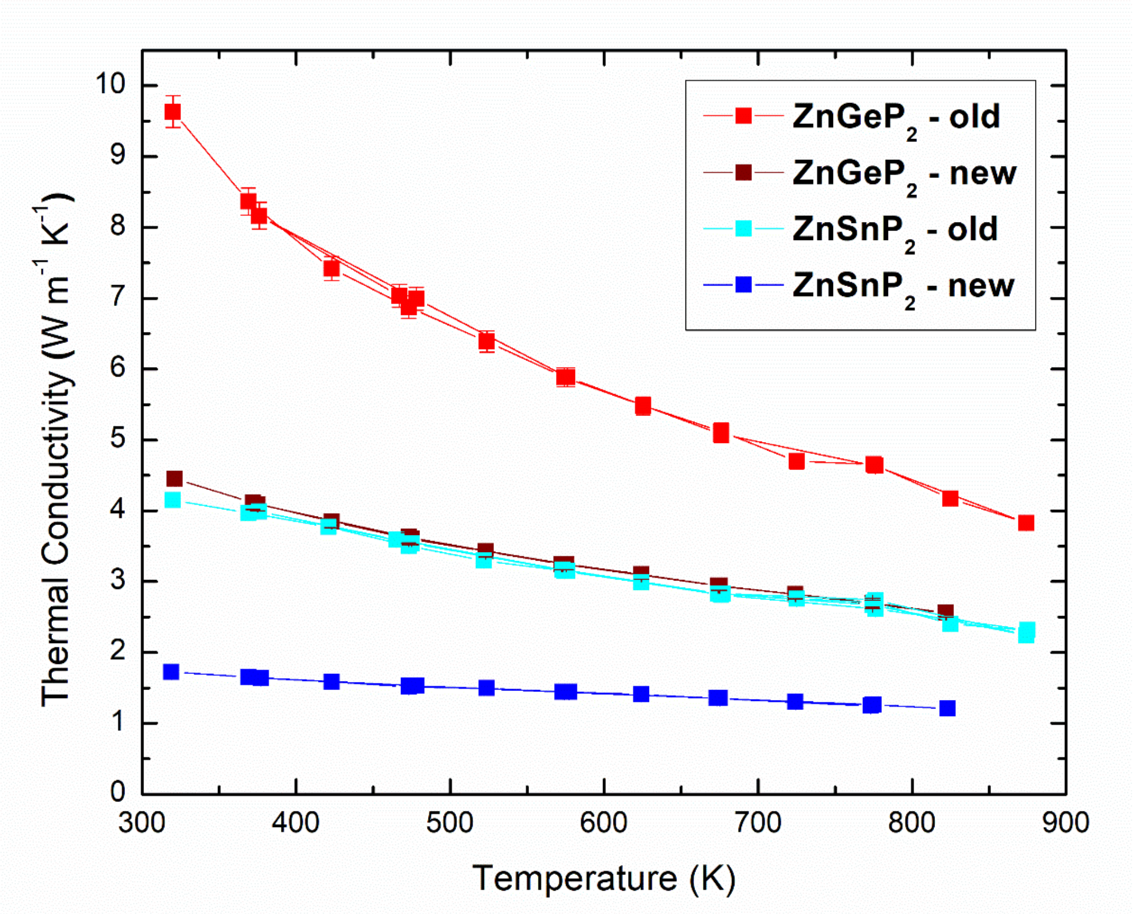

Figure 4.15: Comparing thermal conductivity for end members of series using newly developed synthesis methods. A dramatic reduction in thermal conductivity is seen for both members.

Analysis of the BoltzTraP results were performed using these achievable lattice thermal conductivities obtained from the refined synthesis methods. Combining the Seebeck coefficient, electrical conductivity, and electronic thermal conductivity values calculated from BoltzTraP with these experimentally determined lattice thermal conductivity values results in the figure of merit curves shown in Figure 4.16 for $ZnSnP_2$. Peak zT = 1.1 at 900 K is found for n-type doping of 0.007 electrons per formula such as in $ZnSnP_{1.993}S_{0.007}$, while more promising p-type doping of 0.004 holes per formula could lead to zT = 2.1 at 900 K such as in $Zn_{0.996}Cu_{0.004}SnP_2$. With increased thermal stability of the solid solutions these temperatures and doping levels may be achievable.

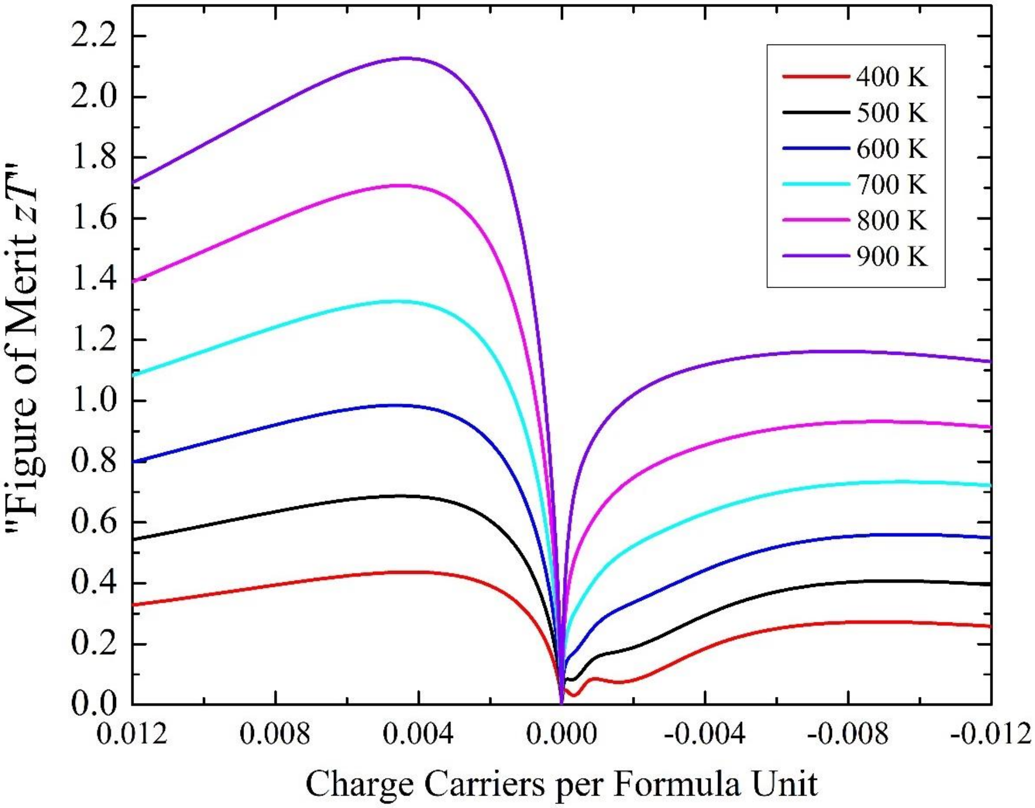

Figure 4.16: *zT* versus charge carriers per formula unit of $ZnSnP_2$ using the lattice thermal conductivity obtained from the refined synthesis method. The figure of merit is obtained from BoltzTraP calculations and experimental data for lattice thermal conductivity with a constant relaxation time of 10 fs.

4.6 Conclusion

Solid solutions are important for the development of high-performance thermoelectric materials. Synthesis of these solid solutions provided challenges due to extreme differences in the end member melting behavior. Mechanochemical methods and careful sintering processes were utilized to perform direct synthesis of all targeted members of the series. Application of mechanical milling to form these solid solutions is a novel method with distinct advantages that are applicable for overcoming significant synthesis hurdles. Full miscibility of the differently melting end members was achieved using low temperature methods which expands viable solid-state methods for solid solutions that cannot be accessed via traditional liquid-solid methods synthesis.

The overall poor thermoelectric performance of the material is not surprising due to low electrical conductivity resulting from low carrier concentration. The solid solutions formed here showed minor differences in electronic transport behavior with levels of substitution. Larger Ge concentrations in $ZnGe_{1-x}SnP_2$ served to stabilize the compounds at much higher temperatures, while larger Sn concentrations shifted the system quickly towards a higher degree of tetragonality. A tendency towards tetragonality was observed in the system which is beneficial for design of high-performance thermoelectric materials due to increased band degeneracies. The large Seebeck coefficient values in the Sn-rich compounds are likely due to the increased tetragonality of the system, however lower electrical conductivity values may also suggest other contributing factors such as decreased carrier concentration.

From calculations and observed measurements, electronic doping of these materials would be required to improve thermoelectric properties. There are many available dopants due to the diversity of the crystal sites as well as the known formation of the I-III-VI_2 chalcopyrite material. Doping of Cu on Zn-sites is a common approach for p-type doping as Cu^{1+} (91 pm) has a similar ionic radius to Zn^{2+} (88 pm). Doping of Ga, In, or Al on the IV-site would also produce more p-type carriers.[225] n-type carries could be introduced as well with chalcogenides on the IV-site adding electrons to the system. As seen from the BoltzTraP2 calculations, both p-type and n-type doping would improve the thermoelectric properties considerably with p-type doping providing higher performance. The Seebeck coefficient values calculated via BoltzTraP were considerably lower than those achieved from experimental measurements which may indicate even greater potential TE performance than calculated.

Development of the outlined ball milling synthesis method provides a useful tool for synthesis of future thermoelectric materials, and specifically for II-IV-V_2 chalcopyrite materials and their solid solutions. For example: $ZnSnSb_2$ shows potential for TE application but has low temperature stability and is difficult to synthesize. Ball mill alloying with germanium in this system may be possible to a certain degree for stability higher temperatures; while phosphorus alloying may widen the band gap reducing the charge carriers which is expected to increase TE performance in this material.[226] The flexibility of the chalcopyrite structure should allow for multiple substitutions on the various sites allowing for various tuning strategies. Potential elemental substitutions for the materials would include Zn and Cd on the II-site, Ge, Sn, and Pb on the IV-site, and P, As, and Sb on the V-site.

Chapter 5: Synthesis and Thermoelectric Properties of Chalcopyrite Solid Solutions $ZnSnP_{2-y}As_y$ and $ZnGe_{1-x}Sn_xP_{2-y}As_y$

In the previous chapter the solid solutions $ZnGe_{1-x}Sn_xP_2$ were studied with respect to synthesis, structure and thermoelectric properties. Thermoelectric performance of the materials was found improvable through alloying, however low electrical carrier concentration limited performance. This chapter explores the synthesis and thermoelectric properties of $ZnSnP_{2-y}As_{2y}$ with the goal of improving the carrier concentration of the previously studied II-IV-V_2 chalcopyrite compounds through band gap tuning. The calculated band gap of $ZnSnAs_2$ is (0.75 eV) which is considerably lower than that of $ZnSnP_2$ (1.66 eV) and $ZnGeP_2$ (1.92 eV).[217] For distinction within this thesis the nomenclature “y” will be used for the degree of As substitution, while “x” indicates degree of Sn substitution. The analogous I-III-VI_2 compound $CuInSe_2$ has shown promise as a p-type thermoelectric material achieving zT_{max} = 0.3 at 750 K providing motivation for the study of $ZnSnAs_2$ compounds.[222,227]

$ZnGe_{1-x}Sn_xP_{2-y}As_y$ solid solutions are also explored in this chapter using the synthetic methods developed in Chapter 4 to examine the viability of forming quinary chalcopyrite solid solutions using ball milling techniques. The $ZnGe_{1-x}Sn_xP_{2-y}As_y$ higher order solid solution series is of interest for increasing stability of the $ZnSnP_{2-y}As_y$ series. Further reduction of thermal conductivity from alloy phonon scattering is another motivating force for the study. Synthesis of higher order solid solutions becomes complex due to number of components and therefore potential impurities. This study therefore explores the synthesis of the compounds $ZnGe_{1-x}Sn_xP_{2-y}As_y$ using the milling, heating, and pressing process developed in Chapter 4 for $ZnGe_{1-x}Sn_xP_2$ for x = 0.5 and x = 0.75. Structural and thermoelectric properties for the higher order solid solutions are discussed in the second half of this chapter.

5.1 Experimental Methods

Preparation of all materials was performed in a purified argon glovebox using stochiometric amounts of -100 mesh zinc powder (99.9% Alfa Aesar), -100 mesh tin powder (99.998% Alfa Aesar), germanium pieces (99.999% STREM Chemicals) were pre-milled to fine powder for use, -100 mesh phosphorus powder (99% Alfa Aesar), and -100 mesh arsenic powder (99.98 Alfa Aesar). The powders were loaded into zirconia lined ball mill jars with ~10g of 1 mm zirconia balls under argon atmosphere and sealed. The reactions were milled in cycles at 600 rpm for 5-minute increments with 1-minute rest times reversing in direction after each cycle. Three milling steps were used: first for 5 hours, the jars were then opened in an argon glovebox and agglomerated material was mechanically reincorporated before two subsequent 2 hour milling steps. The reacted material was mechanically removed and hand ground into a uniform powder. High pressure sintering was performed as a final reaction step, for all $ZnSnP_{2-y}As_y$ compounds a sintering temperature of 575 °C was found to produce the target phase. A pressure of 56 MPa was applied using an OXYGON industries hot press; the temperature was ramped over two hours and applied for 6 hours with a pressure free cooldown. The resulting pellets were 12.5 mm in diameter and densities were measured using the Archimedes' method with ethanol.

PXRD was performed on polished pellets and ground samples using the Inel powder X-ray diffractometer. The diffractometer is equipped with a position sensitive arc detector and Cu Kα radiation source (30 kV, 30 mA), monochromated to K_{α_1} with Ge single crystal. Measurements in 2θ were collected from 5° to 120°. EDAX measurements were performed using an FEI Quanta FEG ESEM with an acceleration voltage of 20 kV. Five point measurements were averaged for each sample, area scans, and element mapping was performed on a 150x150 μm^2 area. Thermal diffusivity of the pressed pellets was measured using the TA-instruments DLF-1200 system. Seebeck coefficient was measured by the direct method, and electrical conductivity measured by a standard 4-point with the ULVAC RIKO ZEM-3 apparatus. Rietveld refinements were performed using GSAS-II analysis software.[184] Electronic structure calculations were performed using the Wien2k package using the full potential linearized augmented plane wave (LAPW) method.[18] The BoltzTraP2 package in Wien2k was used to calculate thermoelectric properties from the electronic structure.[197]

5.2 Results and Discussion $ZnSnP_{1-y}As_y$

5.2.1 Chemical and Structural Characterization

Phase verification of the compounds was performed after the densification steps before proceeding to property measurements. After thermal diffusivity measurements were performed the samples were cut into bars for transport measurements, and PXRD was performed on the leftover pellet pieces hand ground into powders. The powder was measured for greater than 8 hours providing adequate data for Rietveld refinements. Long PXRD measurements for $ZnSnP_{2-y}As_y$ (x = 1) were performed, for y = 0, 0.5, 1, 1.5, and 2 (Figure 5.1). A standard shift of the characteristic peaks to lower angles due to unit cell expansion while reduction of the (020) peak around 2θ = 32° is seen with increasing As concentration. The patterns are very consistent and do not have signs of impurities.

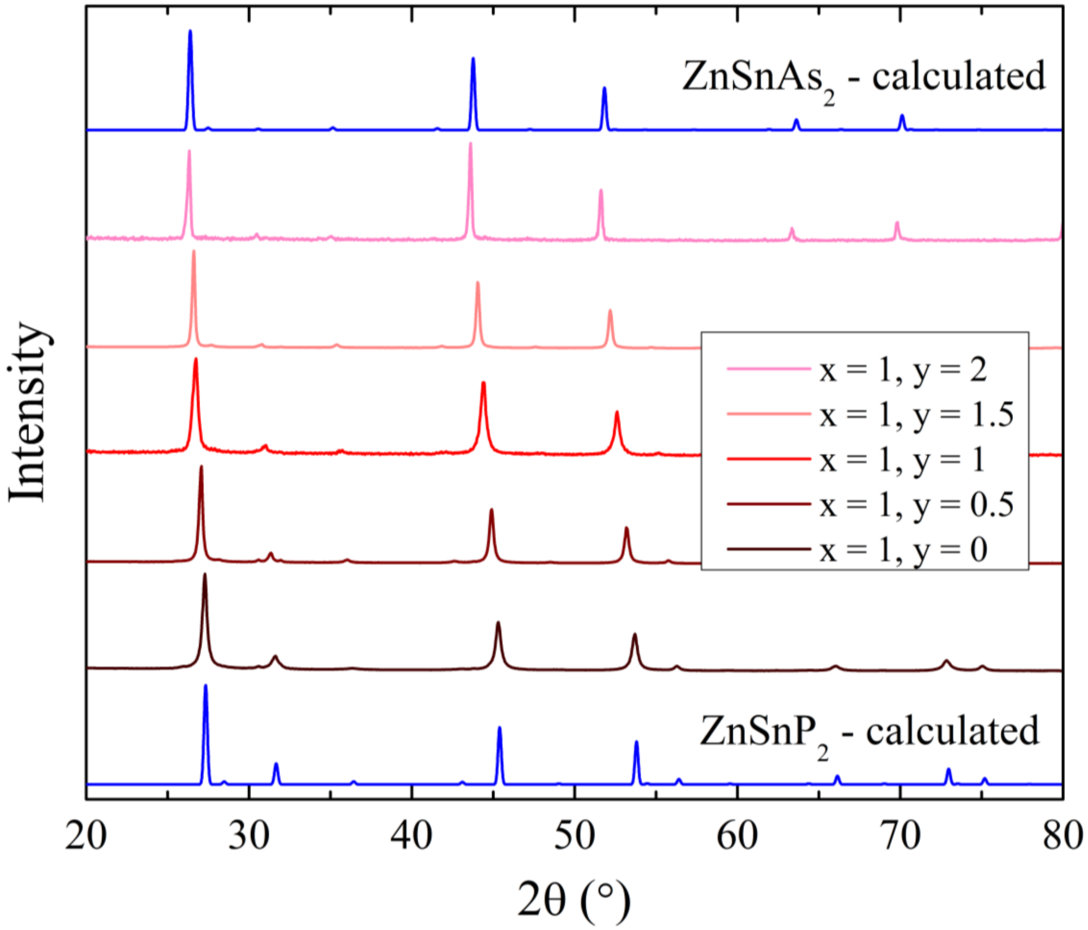

Figure 5.1: PXRD patterns of ZnSnP$_{2-y}$As$_y$ series (y = 0, 0.5, 1, 1.5, 2) with calculated patterns for comparison

The expansion of unit cell parameters can be seen in Figure 5.2(a) obtained from Rietveld refinements, a steady increase with increasing As concentration is observed from y = 0 to y = 1.5. A larger increase is seen when moving from y = 1.5 to y = 2 end member, and unit cell volume displays a similar trend (Figure 5.2 (b)). The tetragonality of the system (Figure 5.2(c)) is constant around 0.998 between y = 0 and y = 1, with a slight decrease at y = 1 which is within error of the other values. Between y = 1 and y = 2 the increase in tetragonality is linear from 0.998 to 1.000. Both end members of the solid solutions are highly tetragonal, therefore significant changes with composition is not expected as with $ZnSnP_{2-y}As_y$ solid solutions.

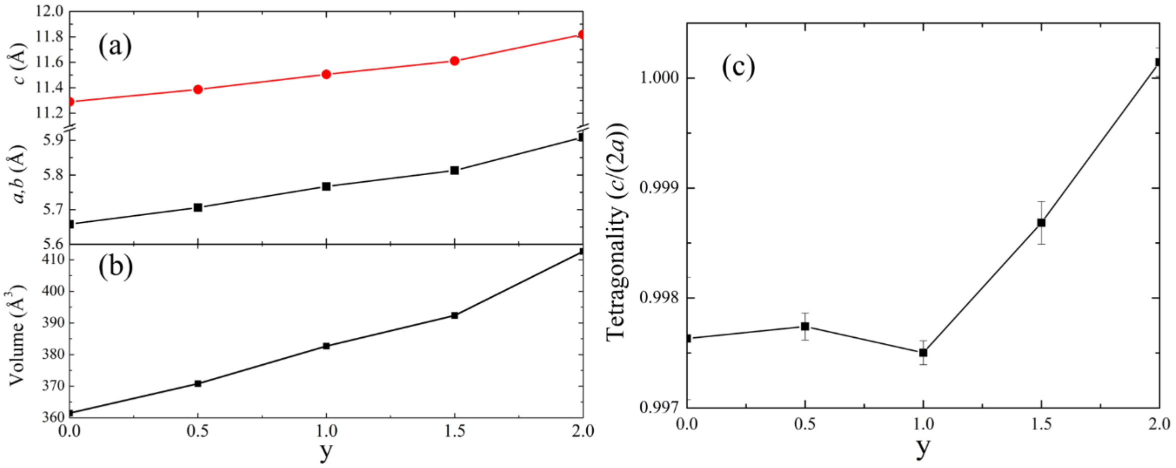

Figure 5.2: Rietveld refinement results for $ZnSnP_{2-y}As_y$ (a) unit cell parameters, (b) volume, and (c) tetragonality versus arsenic concentration y.

The results of Rietveld refinement measurements

Table 5.1: Rietveld refinement results for $ZnSnP_{2-y}As_y$ solid solution series.

y	*a, b* (Å)	*c* (Å)	*V* (Å^3)	*c*/(2*a*)
0	5.658(1)	11.290(4)	361.4(3)	0.9976
0.5	5.7063(3)	11.3869(9)	370.78(2)	0.9977
1	5.7672(3)	11.5055(8)	382.67(3)	0.9975
1.5	5.8131(4)	11.611(2)	392.36(4)	0.9987
2	5.9087(3)	11.819(1)	412.64(3)	1.0001

Statistical results of the Rietveld refinements can be found in Table A.5 in the Appendix, where R_p, R_{wp}, R_{exp}, y_{calc}, and χ^2 are shown. Refinement results showed R_{wp} = 7.5%, 21.8%, 9.5%, and 14.4% for y = 0.5, 1, 1.5 and 2 respectively. Data obtained for y = 1 had a large background resulting in χ^2 = 1.07 and poor refinement statistics. Peak intensities for y = 2 differed significantly from refinement calculations suggesting systematic error in sample preparation such as improper grinding or preferred orientation.

The chemical composition of the series was evaluated by refining occupancy parameters during Rietveld refinements and energy dispersive x-ray spectroscopy (EDAX) analysis. As occupancy from Rietveld refinements of the solid solutions were determined as y_{calc} = 0.533, 0.959, and 1.521 with relative discrepancies of 7%, 4%, and 1% from the target composition. Refinement of As occupancy was also performed on the $ZnSnAs_2$ end member which showed y_{calc} = 1.84, significantly lower (8%) than expected. EDAX results for the solid solutions and end members can be found in Table 5.2, where atomic percent, and empirical formula of the constituent atoms are shown. Atom concentrations determined from EDAX measurements match well for the solid solutions with expected atomic percent showing differences of less than 8%. The end member $ZnSnAs_2$ displayed significantly lower than expected Zn and As (higher Sn) concentration reflecting the results found from Rietveld refinements. EDAX atomic mapping for these measurements can be found in Figure A.25 in the Appendix.

Table 5.2: EDAX analysis results obtained using five point measurements and area scans on the $ZnSnP_{2-y}As_y$ series. The table is sorted by compound nomenclature with atomic percent (At. %) and empirical formula (Emp.) for each set of measurements.

x = 1	y = 0.5		y = 1		y = 1.5		y = 2	
Elem.	**At. %**	**Emp.**	**At. %**	**Emp.**	**At. %**	**Emp.**	**At. %**	**Emp.**
Zn	24.8	0.99	23.9	0.96	24.8	0.99	21.9	0.88
Sn	25.8	1.03	24.8	0.99	25.6	1.02	32.1	1.28
P	37.5	1.50	27.1	1.08	12.7	0.51	-	-
As	11.9	0.47	24.2	0.97	36.9	1.48	45.9	1.84

5.2.2 Electronic Property Calculations

Electronic band structure (BS) and density of states (DOS) for $ZnSnAs_2$ material are displayed in Figure 5.3. The high tetragonality of the system ($c/(2a) = 1$) creates three band valley degeneracies at the valence edge in the Γ-direction with a single steep band at the conduction band edge forming a direct band gap. Density of states calculates a band gap of 0.245 eV with the Fermi energy closest to the valence states suggesting p-type conductivity. The steep valley in the conduction band at the Γ-point has a very low density of states as seen by comparing the BS with the DOS. The valence structure primarily consists of Sn *p* states, Zn *p* states, and As *p* states from the VBM to -6 eV with minor contributions from Zn *s*-states between -1 to -5 eV. The conduction band consists of Zn *s* and *p* states and As and Sn *s, p,* and *d* states with primary contributions from Sn *s* states and As *p* states from then CBM to 3 eV. The higher energy conduction bands (>3 eV) are primarily composed of Sn *d* and *p* states, and Zn *s* and *p* states with minor contributions from As *s*, *p*, and *d* states.

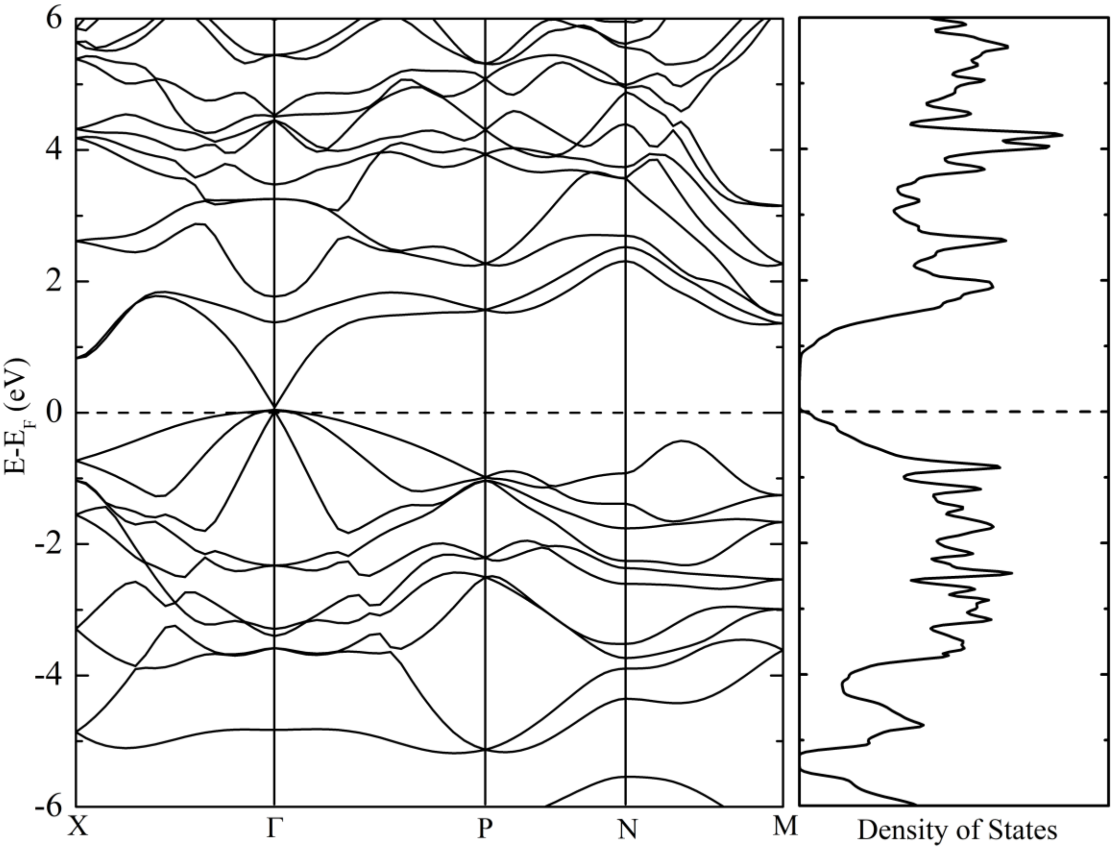

Figure 5.3: Calculated band structure and density of states for $ZnSnAs_2$ with Fermi level subtracted energy E-E$_F$.

BoltzTraP calculations were performed (Figure 5.4) and analyzed in a manner similar to the previous chapter to determine optimal carrier concentrations (Figure 5.5). The resulting p-type $zT_{max} = 1.1$ is found by doping 0.1 holes per formula unit (PFU), while n-type $zT_{max} = 0.5$ is found by doping 0.15

electrons PFU; however, a $zT = 1$ is achieved by doping 0.06 holes PFU. In comparison to the $ZnGe_{1-x}Sn_xP_2$ series calculations, $ZnSnAs_2$ displays lower zT_{max} for both n-type and p-type with higher doping concentrations required to achieve $zT = 1$. The low potential zT of this material is due to the greater lattice thermal conductivity obtained from experimental data.

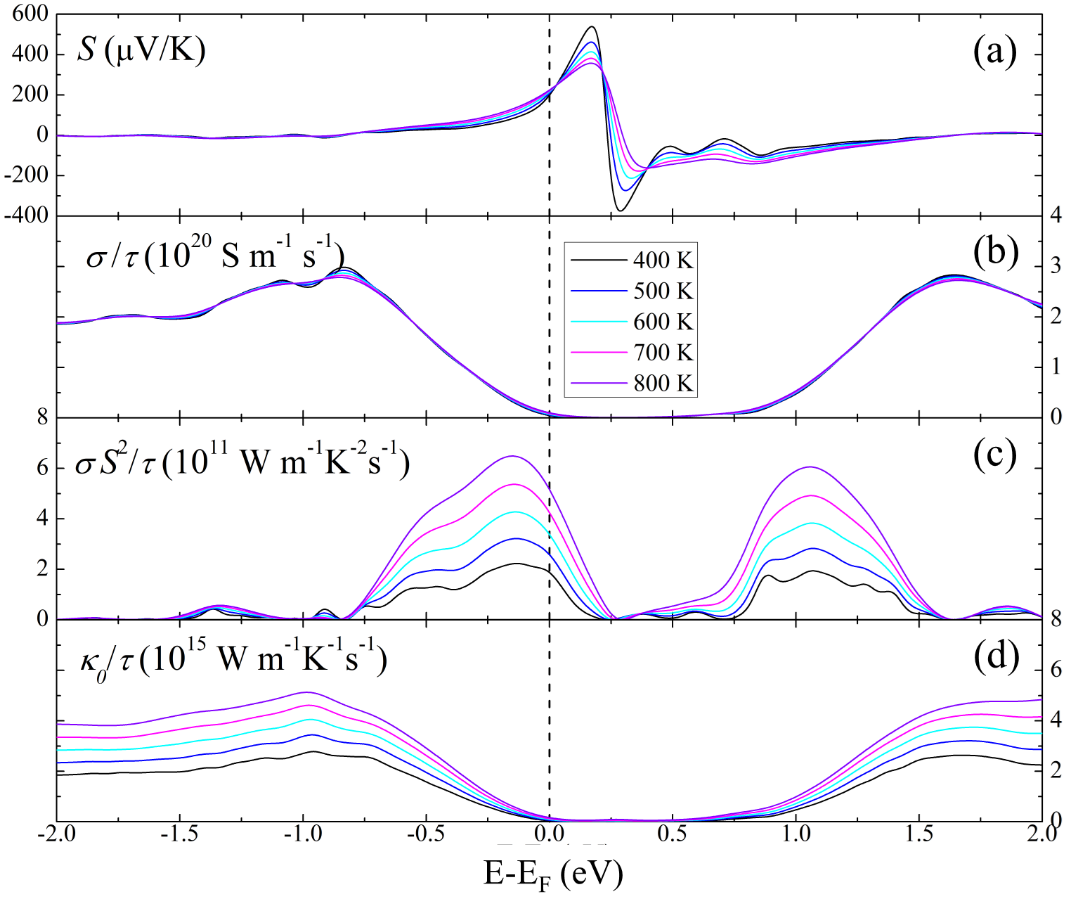

Figure 5.4: BoltzTraP calculation results of TE properties versus energy level for $ZnSnAs_2$ (a) Seebeck coefficient, and scattering independent (b) electrical conductivity, (c) power factor, and (d) electronic thermal conductivity.

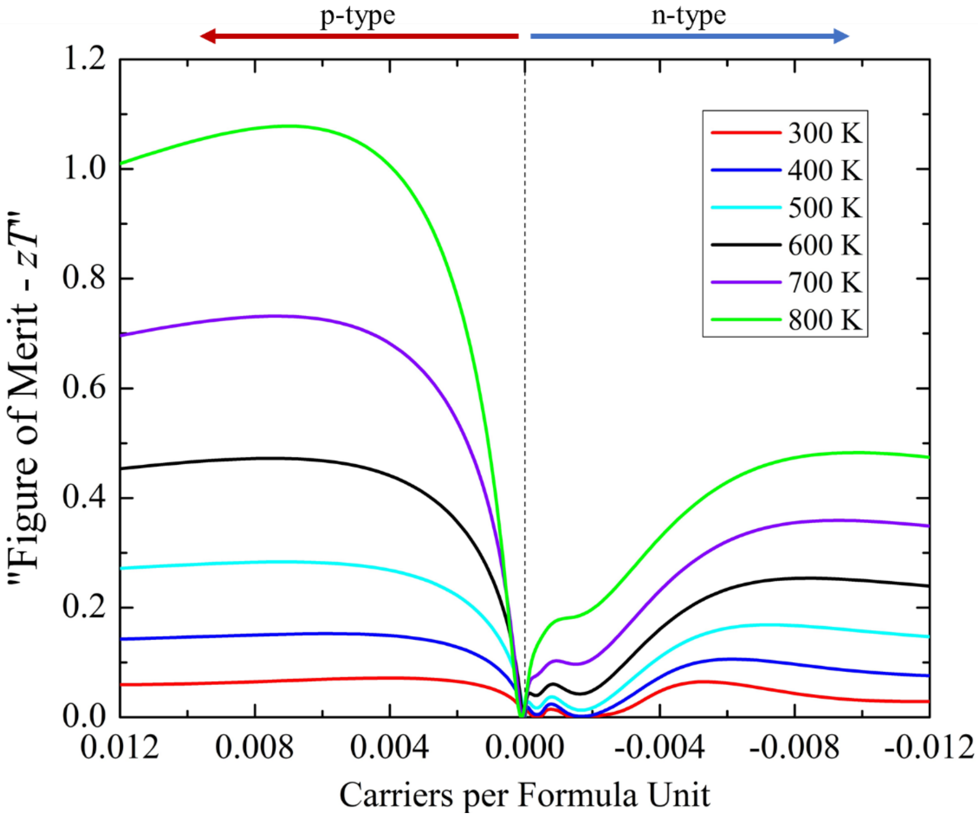

Figure 5.5: *zT* versus charge carriers per formula unit of $ZnSnAs_2$. The figure of merit is obtained from BoltzTraP calculations and experimental data for lattice thermal conductivity with a constant relaxation time of 10 fs.

5.2.3 Thermoelectric Properties

5.2.3.1 Electrical Conductivity

Electrical conductivity versus temperature measurements were made for all members of the series with results displayed in Figure 5.6. The low electrical conductivity of the phosphorus rich members required elevated temperature measurements, where minimum temperatures tend to increase with phosphorus concentration. An overall increase in conductivity with increasing arsenic concentration is seen which is expected due to the decreasing band gap. The conductivity for $ZnSnP_2$ ranges from 0.01 S cm^{-1} at 650 K to 0.1 S cm^{-1} at 800 K, while conductivity for $ZnSnAs_2$ ranges from 0.03 S cm^{-1} at 300 K to 7.0 S cm^{-1} at 650 K. Electrical conductivities withing comparable temperature ranges for all members of the series are included in Table 5.1 with relevant TE properties.

$ZnSnAs_2$ crystals synthesized by vapor transport displayed conductivity value of $1.4 \cdot 10^{-4}$ S cm^{-1} at 300 K,[228] much lower than observed in this work, likely due to the low level of impurities typically found in single crystals. Alternatively single crystals grown by the Bridgman method displayed 23.8 S cm^{-1} at 295 K which initially decreases to 15.1 S cm^{-1} at 735 K before increasing to 29.6 S cm^{-1} at 840 K.[229] Stoichiometrically synthesized $ZnSnAs_2$ bulk samples previously studied under various treatments at 300 K display conductivities ranging from 10 S cm^{-1} to 1205 S cm^{-1} with most conductivities measured around 400 S cm^{-1}.[230] Heat treatments of quenched samples tended to decrease conductivity indicating possible impurities in these samples which would result in higher electrical conductivity. Electrical conductivity for the analogous I-III-VI chalcopyrite $CuInSe_2$ single crystals were measured with values ranging from 0.15 S cm^{-1} at 300 K to 0.46 S cm^{-1} at 575 K.[227] Thermoelectric studies of vacancy doped p-type $Cu_{0.99}InSe_{2.05}$ displayed electrical conductivity ranging from 1.5 S cm^{-1} at 325 K to 6.0 S cm^{-1} at 760 K with degenerate semiconducting behavior.[222]

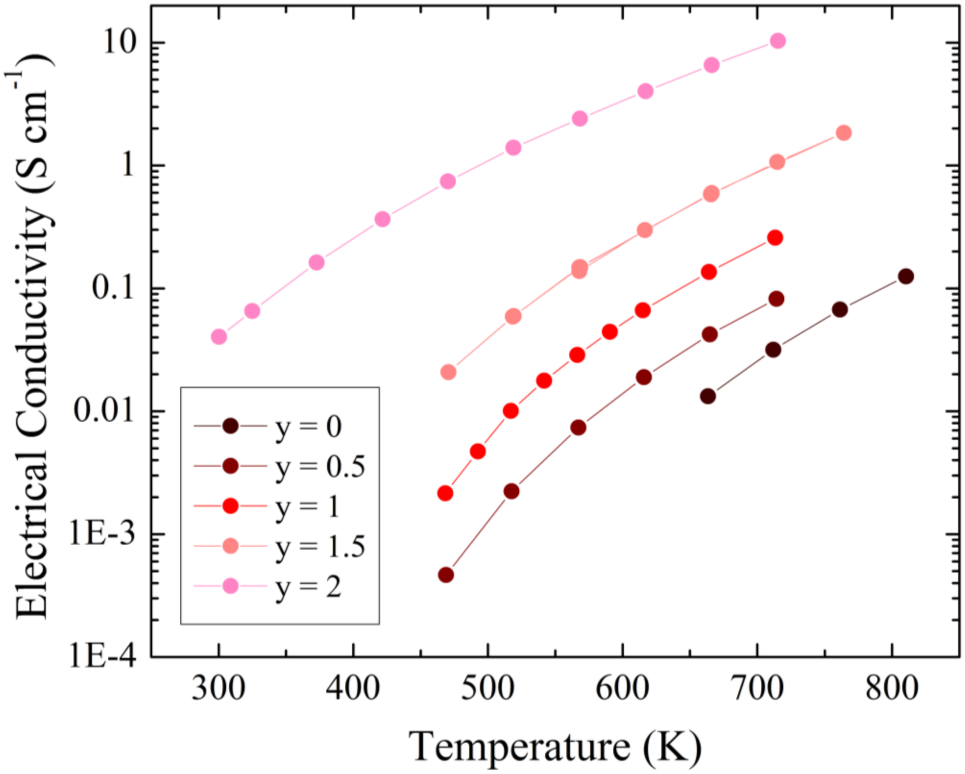

Figure 5.6: Electrical conductivity versus temperature for the $ZnSnP_{2-y}As_y$ series (y = 0, 0.5, 1, 1.5, 2). The electrical conductivity can be seen to increase with increasing As concentration.

An Arrhenius plot of ln(σ) versus T^{-1} is shown in Figure 5.7, where a linear trend is expected for intrinsic semiconductors and curved trends indicate extrinsic behavior. The series members displayed intrinsic semiconducting behavior apart from the As rich end member (y = 2) which shows extrinsic behavior. Band gaps of the series members are calculated from the slope (in the linear region) using the Arrhenius expression for activation energy. A clear trend of decreasing band gap with increasing arsenic concentration is observed as seen in Figure 5.7 (inset). The calculated band gaps for the end members; 1.4 eV for $ZnSnP_2$ and 0.7 eV for $ZnSnAs_2$ within the linear region match expectations from the literature values. $ZnSnAs_2$ displays 0.59 eV with SC and resistivity for Masumoto and 0.66 eV from IR absorption at room temperature.[229]

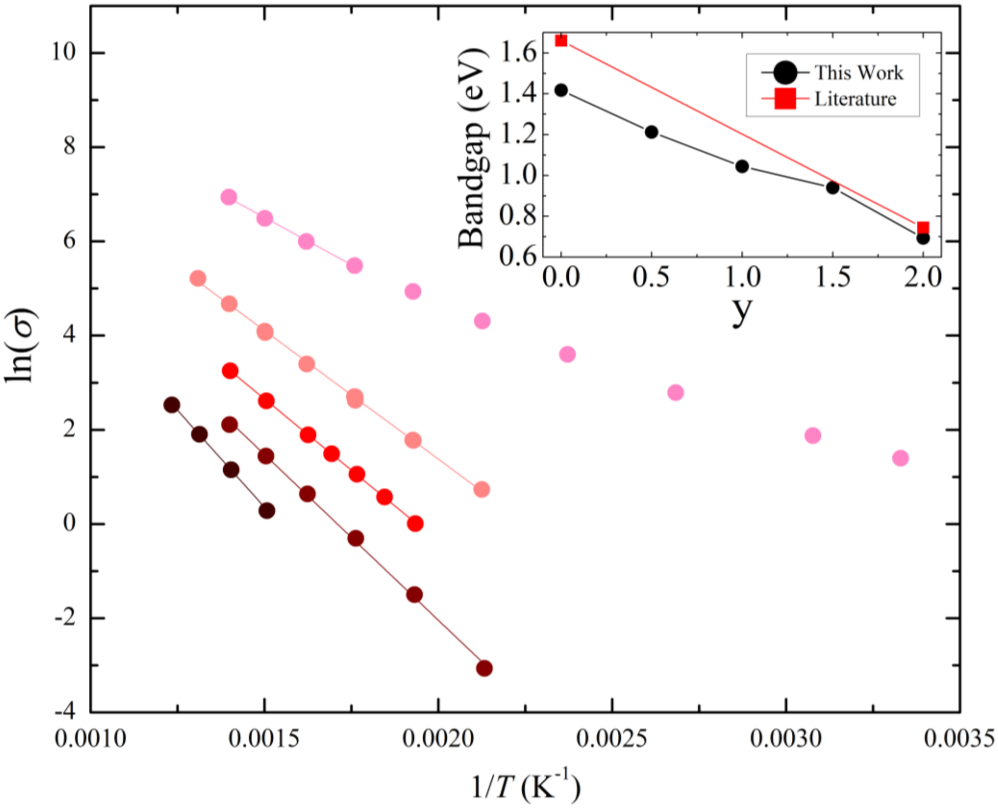

Figure 5.7: Calculation of band gap ln(σ) vs T^{-1} for the $ZnSnP_{2-y}As_y$ series. The linear response of the curves indicates intrinsic semiconducting behavior, whereas for y = 2, the nonlinear response suggests extrinsic semiconducting behavior. (Inset) Calculated band gap versus concentration for the full series with literature values of end members.

5.2.3.2 Seebeck Coefficient

The Seebeck coefficients measured for the full series are displayed in Figure 5.8. The Overall Seebeck coefficient for the compounds is shown to decrease with increasing As concentration indicating an increase in carrier concentration. The temperature dependence of Seebeck coefficient for compounds y = 0 to y = 1.5 is typical of p-type intrinsic behavior decreasing steadily with increasing temperature. A turnover of the slope in Seebeck versus temperature is indicative of bipolar conduction which is seen at 475 K for the y = 2 end member.[31]

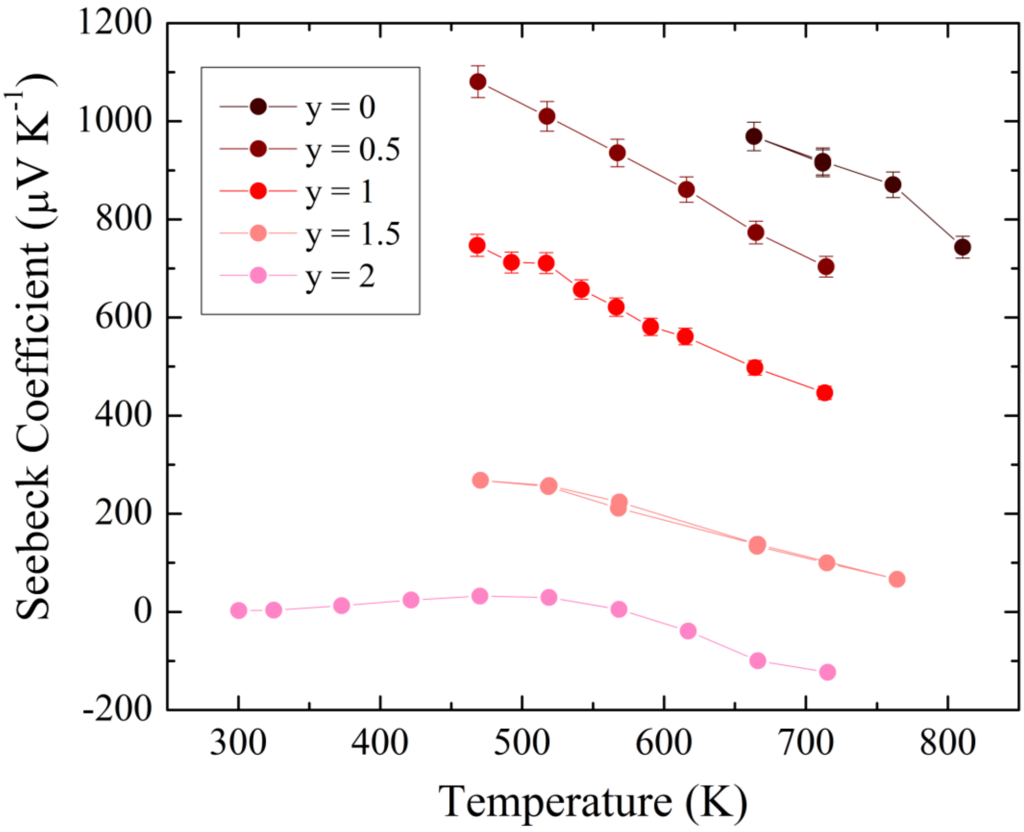

Figure 5.8: Seebeck coefficient versus temperature for the $ZnSnP_{2-y}As_y$ series (y = 0, 0.5, 1, 1.5, 2). A decrease in Seebeck coefficient with increasing As concentration is observed as expected due to increasing carrier concentrations.

A reversible p-n transition occurs for the $ZnSnAs_2$ end member between 570 K and 620 K with a steady increase from 2.6 μV K^{-1} at 300 K to 30 μV K^{-1} at 500 K before decreasing to -125 μV K^{-1} at 715 K. $ZnSnP_2$ displays the largest Seebeck coefficient with 969 μV K^{-1} at 665 K to 744 μV K^{-1} at

810 K followed by y = 0.5 ranging from 861 μV K^{-1} at 570 K to 704 μV K^{-1} at 715 K. For y = 1 the Seebeck coefficient ranges from 747 μV K^{-1} at 470 K to 446 μV K^{-1} at 715 K and for y = 1.5 ranges from 268 μV K^{-1} at 470 K to 66.3 μV K^{-1} at 765 K. These results are displayed in Figure 5.8 and summarized in Table 5.3.

Previous studies of bulk $ZnSnAs_2$ showed highly degenerate p-type semiconducting behavior, with Seebeck coefficient ranging from 41 μV K^{-1} at 300 K to 60 μV K^{-1} at 440 K similar to the results found in this work for the same temperature range. Various heat treatments and synthesis methods produced room temperature Seebeck coefficients ranging from 26 μV K^{-1} to 224 μV K^{-1} which tended to increase after heat treatments.[230] Single crystals displayed larger overall Seebeck coefficients with degenerate semiconducting behavior, ranging from 310 μV K^{-1} at 300 K to 400 μV K^{-1} at 600 K.[229] For the analogous I-III-VI chalcopyrite $CuInSe_2$ single crystals grown by vapor deposition displayed Seebeck coefficients ranging from 542 μV K^{-1} at 300 K down to 300 μV K^{-1} at 400 K increasing again to 600 μV K^{-1} at 625 K.[227] Vacancy doped p-type $Cu_{0.99}InSe_{2.05}$ thermoelectric materials displayed Seebeck coefficients of 300 μV K^{-1} at 300 K which increased to 625 μV K^{-1} at 620 K finally decreasing to 500 μV K^{-1} at 775 K.[222] A similar p-type to n-type transition was observed in one study of $CuInSe_2$, with 100 μV K^{-1} at 300 K increasing slightly to 200 μV K^{-1} at 390 K and decreasing rapidly to -200 μV K^{-1} at 560 K.[223] In comparison to $ZnSnAs_2$, $CuInSe_2$ shows much larger p-type Seebeck coefficients due to lower bipolar conduction due to the larger band gap of 0.9 eV versus 0.6 eV respectively.[150]

5.2.3.3 Power Factor

Power factor versus temperature for the members of the series are displayed in Figure 5.9, within comparable ranges the power factors show an increase with increasing As concentration between y = 0 and 1. The evenly substituted y = 1 member displays the highest power factor with 0.12 μW m^{-1} K^{-2} at 470 K to 5.1 μW m^{-1} K^{-2} at 715 K followed by the phosphorus rich y = 0.5 with 0.05 μW m^{-1} K^{-2} at 470 K to 4.1 μW m^{-1} K^{-2} at 715 K, and phosphorus end member with 1.6 μW m^{-1} K^{-2} at 675 K to 6.5 μW m^{-1} K^{-2} at 800 K. At lower temperatures the power factor y = 1.5 appears larger than lower arsenic concentration members with 0.15 μW m^{-1} K^{-2} at 470 K but as temperature increases remains low and turns over to 1.1 μW m^{-1} K^{-2} at 750 K for higher temperatures due to decreasing Seebeck coefficient possibly due to bipolar conduction.

The end member $ZnSnAs_2$ displays the largest overall power factor at high temperatures increasing to 16 μW m^{-1} K^{-2} at 715 K, however at lower temperatures before and around the p-n transition display the lowest PF due to bipolar carrier resulting in zero Seebeck coefficient. Previously studied $ZnSnAs_2$ bulk samples displayed a power factor of 8.4 μW m^{-1} K^{-2} at 300 K,[230] while single crystals measured obtained large values of 185 μW m^{-1} K^{-2} at 300 K to 271 μW m^{-1} K^{-2} at 590 K.[229] The value $2.7 \cdot 10^{-5}$ μW m^{-1} K^{-2} at 300 K obtained by this study is much lower due to both lower electrical conductivity and Seebeck coefficient of the sample. The analogous $CuInSe_2$ single crystal studied showed a power factor of 4.9 μW m^{-1} K^{-2} at 300 K,[227] while vacancy doped bulk samples $Cu_{0.99}InSe_{2.05}$ displayed power factors ranging from 10 μW m^{-1} K^{-2} at 325 K to 155 μW m^{-1} K^{-2} at 775 K.[222]

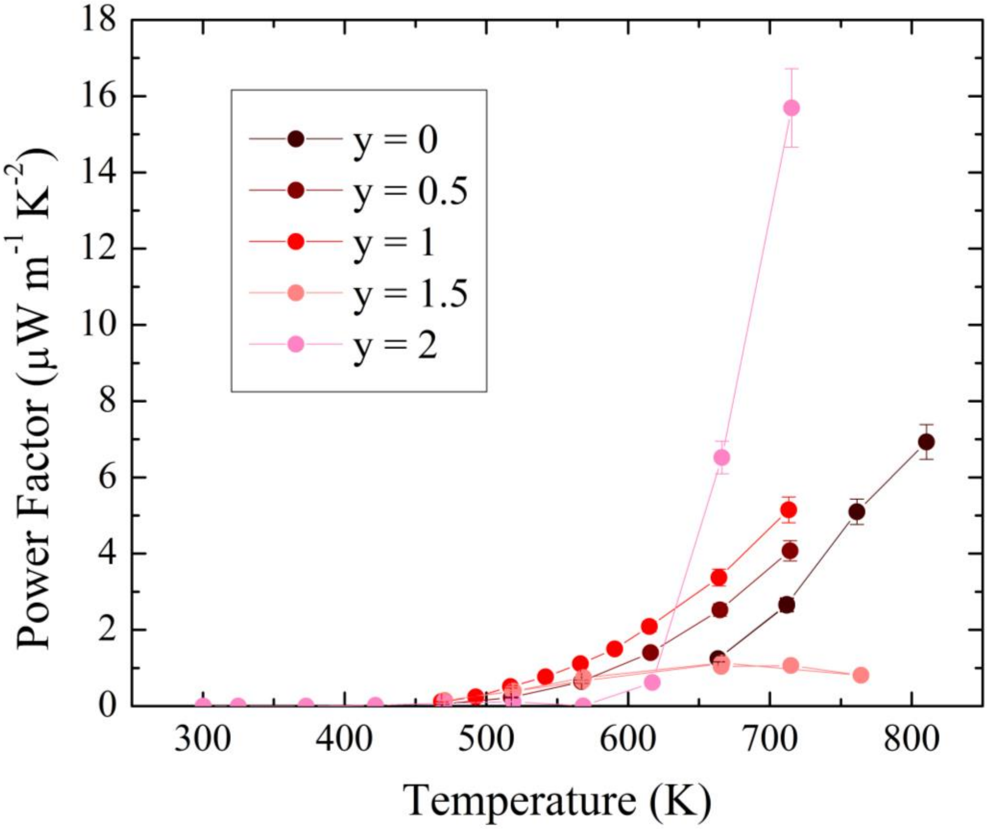

Figure 5.9: Power factor versus temperature for the $ZnSnP_{2-y}As_y$ series. An initial increase in the power factor is seen from y = 0 to y = 1 decreasing with y = 1.5. At low temperature y = 2 displays lowest which quickly increases to the greatest PF at higher temperatures.

5.2.3.4 Thermal Conductivity

Thermal conductivity versus temperature for the members of the series is shown in Figure 5.10 displaying a typical decrease with temperature due to increased phonon frequencies. The thermal conductivities of the end members display the largest values with 4.2 W m^{-1} K^{-1} and 5.6 W m^{-1} K^{-1} at 300 K to 2.4 W m^{-1} K^{-1} and 2.7 W m^{-1} K^{-1} at 825 K for y = 0 and y = 2 respectively. The lowest values of TCs are observed in y = 0.5 and y = 1 with 2.2 W m^{-1} K^{-1} and 2.3 W m^{-1} K^{-1} at 300 K respectively; and have equal values above 500 K resulting in 1.4 W m^{-1} K^{-1} at 825 K. Slightly larger than the other members, y = 1.5, displays a thermal conductivity ranging from 2.8 W m^{-1} K^{-1} at 300K decreasing to 1.7 W m^{-1} K^{-1} at 825 K. Increased phonon scattering due to mass fluctuation effects reduces the thermal conductivity by more than a factor of two at room temperature for the solid solutions compared to the end members.

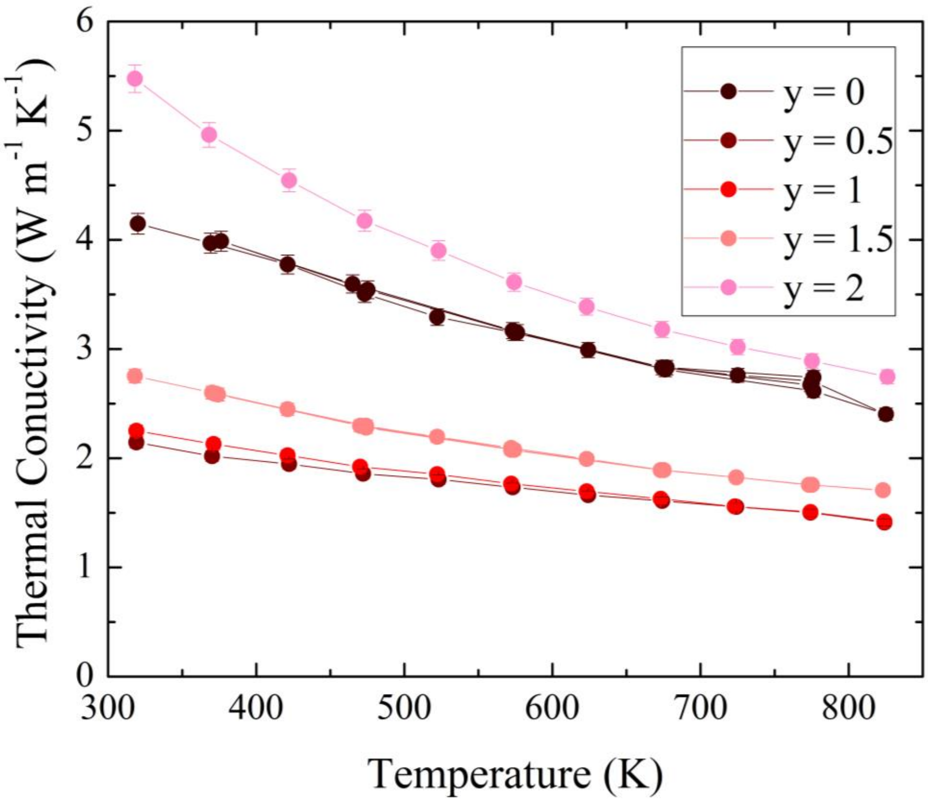

Figure 5.10: Thermal conductivity versus temperature for the ZnSnP$_{2-y}$As$_y$ series where y = 0, 0.5, 1, 1.5, 2. The solid solutions display decreased thermal conductivity compared to the end members mass fluctuation effects.

In comparison with other studies of $ZnSnAs_2$ thermal conductivity of early studies of bulk stochiometric samples measured 7.4 W m^{-1} K^{-1} and 5.8 W m^{-1} K^{-1} at room temperature.[150] Similar results were obtained by Gasson with 6.9 W m^{-1} K^{-1} at 300 K which reduced to 6.4 W m^{-1} K^{-1} at 390 K, while measurements were not performed on single crystals.[229,230] These values obtained are in agreement with other studies on $ZnSnAs_2$. Early studies of the analogous $CuInSe_2$ compound displays much lower thermal conductivity with 2.9 W m^{-1} K^{-1} at room temperature,[150] while more recent studies display TC from 4.6 W m^{-1} K^{-1} at 320 K decreasing to 1.9 W m^{-1} K^{-1} at 580 K.[223] Thermoelectric studies of $Cu_{0.99}InSe_{2.05}$ show TC ranging from 1.5 W m^{-1} K^{-1} at 320 K to 0.4 W m^{-1} K^{-1} at 775 K likely lower due to defect scattering and higher anharmonicity.[222,231,232]

The electronic thermal conductivities were calculated using the Wiedemann-Franz law and displayed as a function of temperature in Figure 5.11(a). Here the Lorenz number is estimated using the relation 1-58 from the measured Seebeck coefficient. The electronic TC of all the members is very low and contributes very little (1E-6 W m^{-1} K^{-1} – 0.01 W m^{-1} K^{-1}) due to low electrical conductivity. The lattice TCs (Figure 5.11(b)) are calculated by subtracting off electronic TC from total TC resulting in values similar to total thermal conductivity. A difference in electronic thermal conductivity of 0.09 W m^{-1} K^{-1} in comparable temperature ranges is observed between y = 0.5 and y = 1. Due to the bipolar conduction Equation 1-58 fails for y = 2 (and possibly for y = 1.5), however the electrical conductivity is so low the effect seen is minimal.

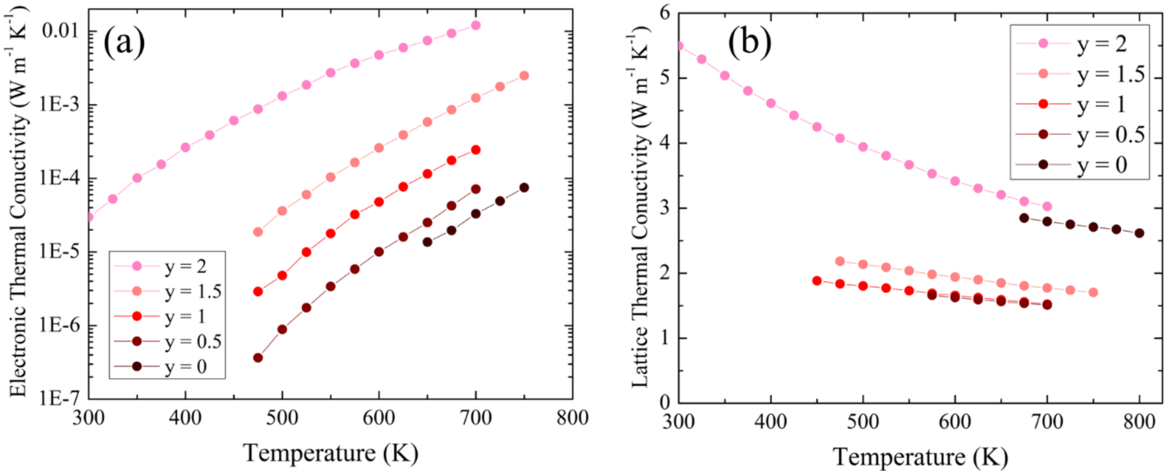

Figure 5.11: (a) Electronic thermal conductivity and (b) lattice thermal conductivity versus temperature for the $ZnSnP_{2-y}As_y$ series where y = 0, 0.5, 1, 1.5, 2.

5.2.3.5 Figure of Merit

The calculated thermoelectric figure of merit (Figure 5.12) is obtained from interpolation of relevant material data, therefore as TC data was obtained for a larger temperature range than electronic transport measurements in all samples, the data is limited to the range of electronic transport measurements. The largest and smallest observed figure of merit is found in the y = 2 end member with $zT = 1.4{\cdot}10^{-9}$ at 300 K to 0.003 at 700 K and hypothetically zero at the p-n transition temperature. At high temperatures the large electrical conductivity, increasing negative Seebeck coefficient, and decreasing thermal conductivity contribute to improving thermoelectric performance. The maximum zT found for all solid solutions were found at 700 K with $zT = 2.0{\cdot}10^{-3}$ for y = 1, $zT = 1.6{\cdot}10^{-3}$ for y = 0.5, and $zT = 4.3{\cdot}10^{-4}$ for y = 1.5. The $ZnSnP_{2-y}As_y$ solid solutions outperform the y = 0 end member as well as the $ZnGe_{1-x}Sn_xP_2$ solid solutions in comparable temperature ranges. The temperature stability of the $ZnSnP_{2-y}As_y$ solid solutions was lower than the Ge containing solid solutions, resulting in overall poorer performance due to lower temperature measurements.

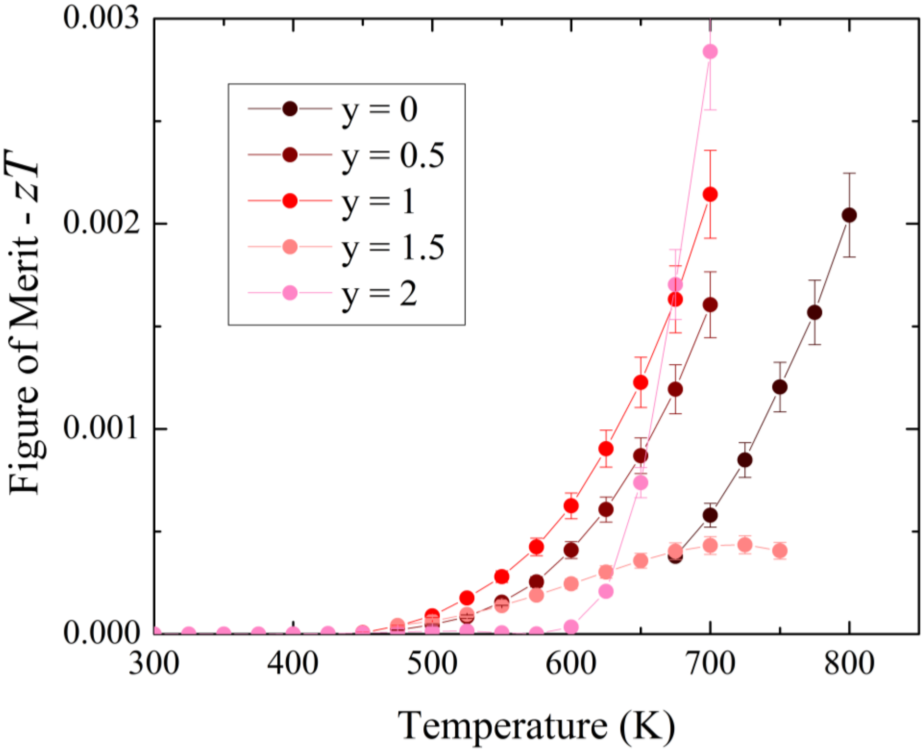

Figure 5.12: Thermoelectric figure of merit versus temperature for the $ZnSnP_{2-y}As_y$ series where y = 0, 0.5, 1, 1.5, 2.

Comparison of the results found in this work with previous studies of $ZnSnAs_2$ is unavailable as there has been no calculation of figures of merit made in literature. The work performed by Gasson on bulk $ZnSnAs_2$ provided the relevant properties to perform a calculation, however the measurements were performed on samples under different synthesis conditions. Values of zT calculated from the Gasson study results in $3.2 \cdot 10^{-4}$ at 300 K up to $5.7 \cdot 10^{-4}$ at 360 K, larger than the values obtained in this study within the limited temperature range.[230] The analogous $CuInSe_2$ has been studied significantly for thermoelectric applications. For vacancy doped $Cu_{0.99}InSe_{2.05}$ highest zT achieved is 0.31 at 773 K perpendicular to pressing direction and 0.15 parallel to pressing direction. There was little consistency with pressing direction and performance in this study however.[222] Manganese doped $CuIn_{0.95}Mn_{0.05}Se_2$ achieves zT of 0.016 at 560 K while suppressing the bipolar conduction.[223] A summary table of the thermoelectric properties is provided (Table 5.3) for y = 0.5, 1, 1.5, and 2, a summary table including y = 0 was presented in Chapter 4 (Table 4.4).

Table 5.3: Summary of thermoelectric properties for $ZnSnP_{2-y}As_y$ (y = 0.5, 1, 1.5, 2)

y	σ (S cm^{-1}) 470 K, 715 K	S (μV K^{-1}) 470 K, 715 K	$S^2\sigma$ (μW m^{-1} K^{-2}) 660 K, 810 K	κ (W m^{-1} K^{-1}) 325 K, 825 K	zT 475 K, 700 K
0.5	4.7E-4, 0.08	1080, 704	0.05, 4.08	2.13, 1.41	1.9E-5, 1.6E-3
1	2.2E-3, 0.26	747, 446	0.12, 5.15	2.24, 1.42	4.0E-5, 2.1E-3
1.5	0.15, 1.07	268, 100	2.02, 10.9	2.73, 1.70	3.7E-5, 4.3E-4
2	0.74, 10.3	32, -123	0.08, 15.7	5.41, 2.75	9.4E-6, 2.8E-3

5.2.4 Conclusion $ZnSnP_{2-y}As_y$

Successful synthesis of the $ZnSnP_{2-y}As_y$ solid solutions was achieved by the ball milling and sintering method outlined in Chapter 4. Structural changes with arsenic substitution show increase in unit cell with small differences in tetragonality due to both end members displaying a high degree. The larger unit cells decrease orbital overlap and therefore decrease band gaps verified by electrical conductivity measurements. The temperature stability of the $ZnSnP_{2-y}As_y$ solid solutions is lower and therefore measured at lower temperatures compared to $ZnGe_{1-x}Sn_xP_2$ solid solutions. Increases to the electrical conductivities are achieved compared to the $ZnGe_{1-x}Sn_xP_2$ solid solutions due to decreased band gap and therefore increasing carrier concentrations. Seebeck coefficients for the solid solutions are significantly decreased with increasing As concentrations due to increasing bipolar conduction which results in majority n-type behavior in the $ZnSnAs_2$ end member at high temperature. Thermoelectric power factors are improved in comparable temperature ranges versus to the $ZnGe_{1-x}Sn_xP_2$ solid solutions. Thermal conductivity of the solid solutions is lower when compared to the $ZnGe_{1-x}Sn_xP_2$ solid solutions, due to the end member $ZnSnAs_2$ displaying lower thermal conductivity than $ZnGeP_2$.

Resulting thermoelectric performance is improved in comparable temperature ranges when compared to the $ZnGe_{1-x}Sn_xP_2$ solid solutions, however, are still low in overall performance. Doping of the solid solutions would likely improve the performance, particularly p-type doping as expected from analysis of the electronic structure and BoltzTraP calculations. The relatively large magnitude of negative Seebeck coefficient obtained at high temperatures for $ZnSnAs_2$ is promising for n-type doping of the material as and is expected from the electronic property calculations obtained from BoltzTraP showing greater n-type Seebeck coefficient. Evidence of bipolar conduction found in y = 1.5 and y = 2 suggests arsenic rich members are less ideal for doping studies than intermediate or phosphorus rich members. If high temperature stability of the solid solutions can be improved higher performance should be achievable with P-As solid solutions.

5.3 Results and Discussion $ZnGe_{1-x}Sn_xP_{2-y}As_y$

5.3.1 Chemical and Structural Characterization

Synthesis of the compounds $ZnGe_{1-x}Sn_xP_{2-y}As_y$ were performed using the same milling, heating, and pressing conditions developed for $ZnGe_{1-x}Sn_xP_2$ for x = 0.5 and x = 0.75 in Chapter 4. The patterns were confirmed using PXRD with x = 0.5 series displayed in Figure 5.13 and x = 0.75 in Figure 5.14, end members for $ZnSnPn_2$ are included for reference. The expected trends in intensity and 2θ for the solid solutions were observed with increasing As substitution for $ZnGe_{0.5}Sn_{0.5}P_{2-y}As_y$. Singular peaks are observed for all members of the series indicating complete miscibility.

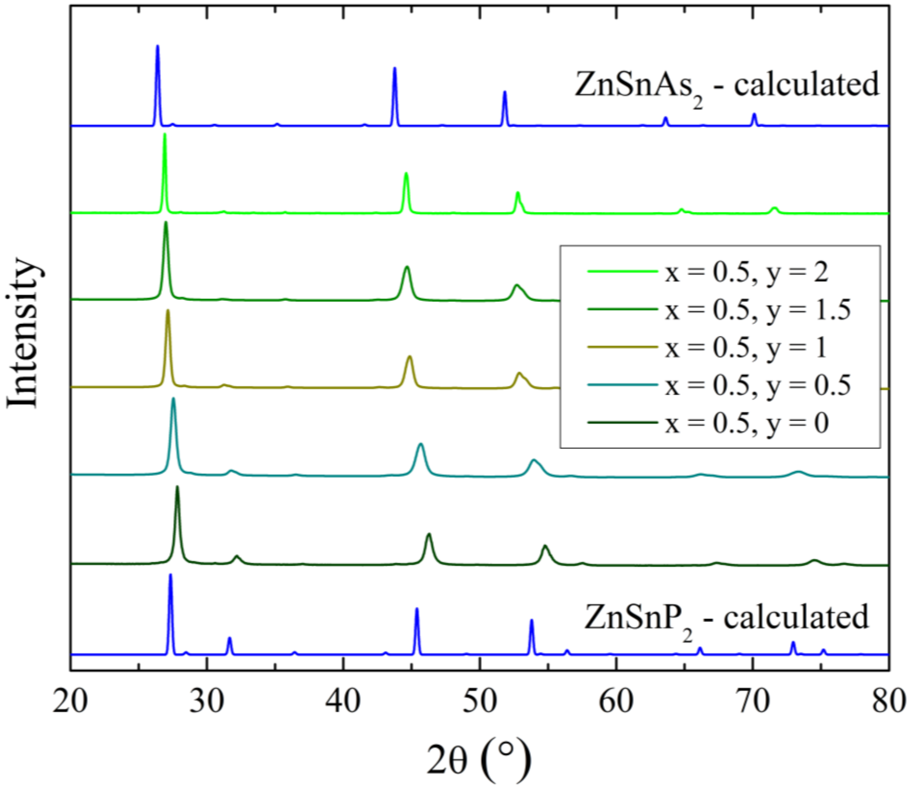

Figure 5.13: PXRD patterns for the $ZnGe_{0.5}Sn_{0.5}P_{2-y}As_y$ series (y = 0, 0.5, 1, 1.5, and 2) with the end members for $ZnSnPn_2$ included for reference.

The solid solution series for $ZnGe_{0.25}Sn_{0.75}P_{2-y}As_y$ display the expected trends in 2θ and intensity with increasing As substitution. For the y = 1 member the appearance of a shoulder on the primary peaks (2θ = 26°, 45°, 54°) suggests incomplete solubility. This is likely due to unoptimized reaction conditions or possibly a miscibility gap. The other members of the series display complete miscibility with no observable impurities.

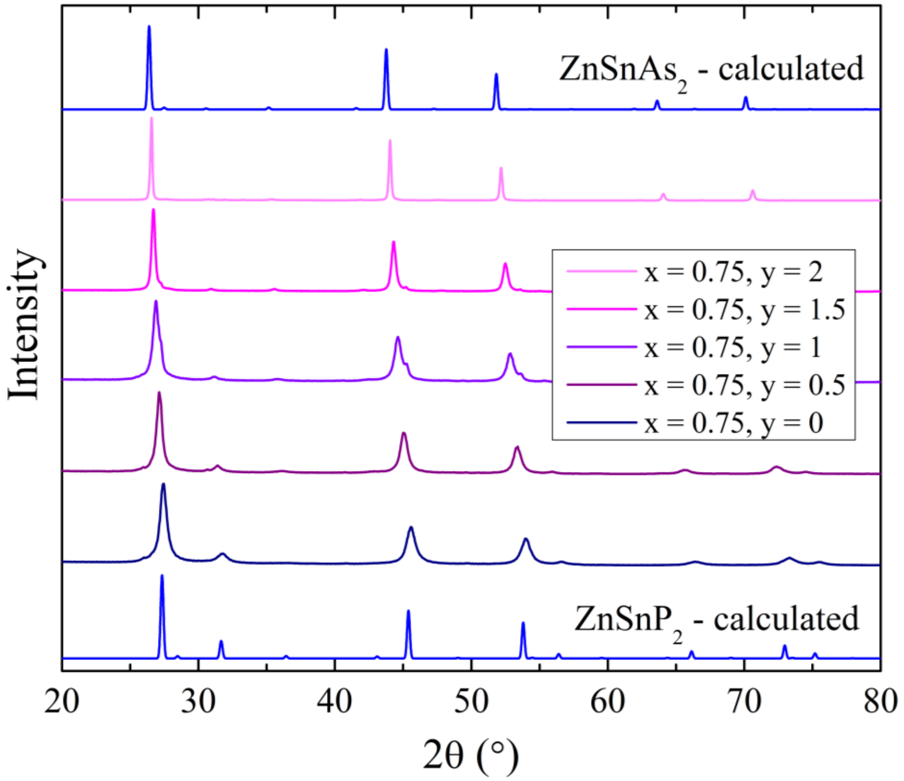

Figure 5.14: PXRD patterns for the $ZnGe_{0.25}Sn_{0.75}P_{2-y}As_y$ series (y = 0, 0.5, 1, 1.5, and 2) with the end members for $ZnSnPn_2$ included for reference.

Rietveld refinement calculations were performed for the measured compounds. The calculated unit cell parameters versus As concentration (y = 0, 0.5, 1, 1.5, and 2) is shown in Figure 5.15 for x = 0.5, 0.75, and 1. A steady increase with As concentration is seen for both x = 0.5 and x = 0.75 solid solutions. The x = 0.75 compounds have overall larger unit cell parameters and are much closer in value to the x = 1 compounds than the x = 0.5 compounds.

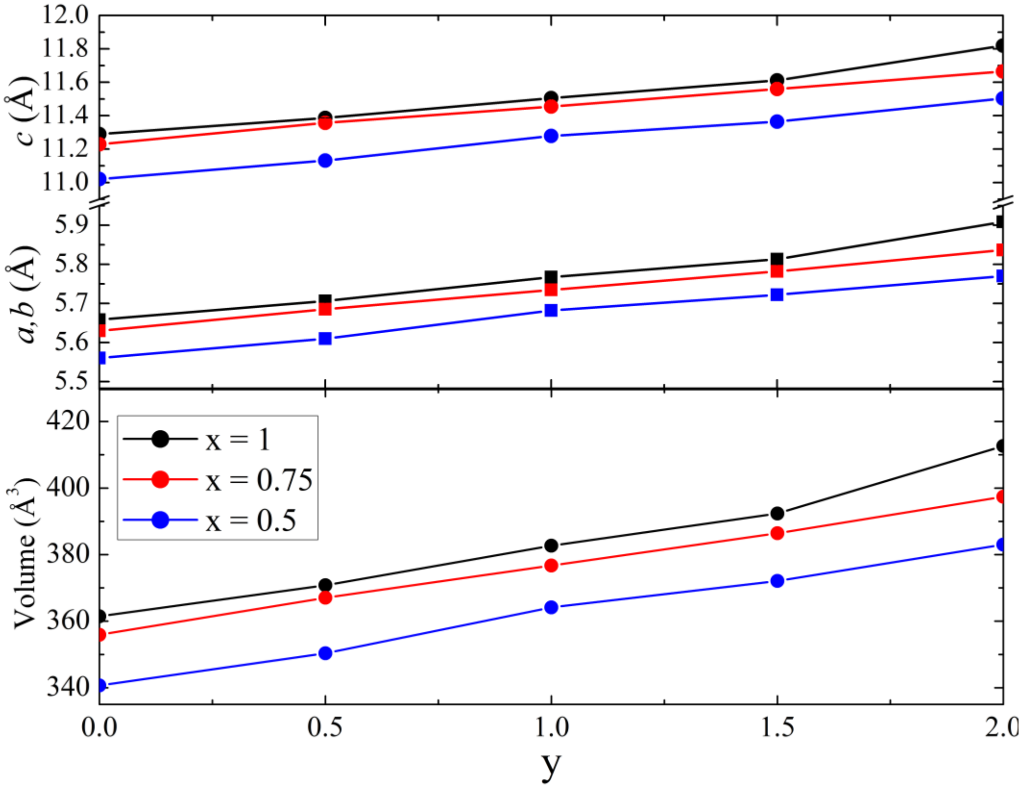

Figure 5.15: Unit cell parameters for $ZnGe_{1-x}Sn_xP_{2-y}As_y$ (x = 0.5, 0.75, 1; y = 0, 0.5, 1, 1.5, 2) versus As concentration (y) obtained from Rietveld refinements.

The calculated tetragonality of the solid solutions are shown in Figure 5.16 for x = 0.5, 0.75, and 1 versus As concentration (y = 0, 0.5, 1, 1.5, 2). For the x = 0.5 series a steady increase in tetragonality is seen between y = 0 and y = 1.5 with a greater increase between y = 1.5 and 2. The x = 0.75 series displays unexpectedly large values of tetragonality for the higher order solid solution y = 0.5 to 1.5 when compared to the x = 1 series. Overall, these materials display a high degree of tetragonality ($c/(2a) = 1$) which is beneficial for thermoelectric performance by increasing band degeneracy. Summary of the Rietveld refinement results for $ZnGe_{0.5}Sn_{0.5}P_{2-y}As_y$ and $ZnGe_{0.25}Sn_{0.75}P_{2-y}As_y$ are displayed in Table 5.4 and Table 5.5 respectively.

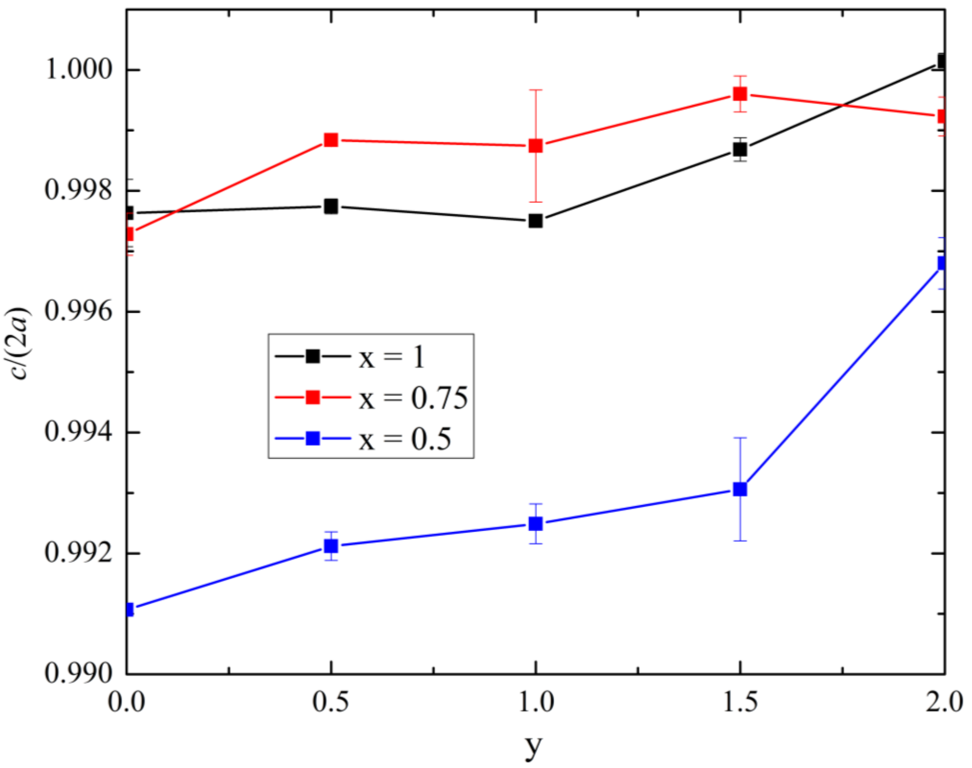

Figure 5.16: Tetragonality (*c*/(2*a*)) for $ZnGe_{1-x}Sn_xP_{2-y}As_y$ (x = 0.5, 0.75, 1; y = 0, 0.5, 1, 1.5, 2) versus As concentration (y) obtained from Rietveld refinements.

Table 5.4: Rietveld refinement results for the $ZnGe_{0.5}Sn_{0.5}P_{2-y}As_y$ series

y	*a, b* (Å)	*c* (Å)	V (Å^3)	*c*/(2*a*)
0	5.5601(3)	11.0209(8)	340.71(3)	0.9911
0.5	5.6100(6)	11.132(2)	350.33(8)	0.9921
1	5.6820(8)	11.279(3)	364.1(1)	0.9925
1.5	5.722(2)	11.365(8)	372.1(3)	0.9931
2	5.770(1)	11.503(4)	382.9(2)	0.9968

Table 5.5: Rietveld refinement results for the $ZnGe_{0.25}Sn_{0.75}P_{2-y}As_y$ series

y	*a, b* (Å)	*c* (Å)	V (Å^3)	*c*/(2*a*)
0	5.6298(9)	11.229(3)	355.89(6)	0.9973
0.5	5.6851(2)	11.357(1)	367.06(4)	0.9988
1	5.735(2)	11.455(9)	376.7(3)	0.9987
1.5	5.7819(6)	11.559(3)	386.4(1)	0.9996
2	5.8367(8)	11.664(3)	397.4(1)	0.9992

Refinement results for the x = 0.5 series showed R_{wp} = 3.6%, 16.9%, 4.6%, and 8.8% for y = 0.5, 1, 1.5 and 2 respectively. Results for the x = 0.75 series are R_{wp} = 12.3%, 8.9%, 14.9%, and 18.5% for y = 0.5, 1, 1.5, and 2 respectively. Except for y = 1 refinements for x = 0.5 displayed good quality, while the refinement results for the x = 0.75 series were lower in quality. Statistical results of the Rietveld refinements can be found in Table A.6 (x = 0.5) and Table A.7 (x = 0.75) in the Appendix, where R_p, R_{wp}, R_{exp}, x_{calc}, y_{calc}, and χ^2 are shown. Chemical composition of the series was evaluated by refining occupancy parameters during Rietveld refinements and energy dispersive x-ray spectroscopy (EDAX) analysis. Occupancies from Rietveld refinements of the x = 0.5 series were determined x_{calc} = 0.52, 0.59, 0.49, and 0.54 while y_{calc} = 0.49, 1.01, and 1.49, and 1.98 respectively. The discrepancy of x from targeted values is 18% for the y = 1 sample which may have led to sample failures experienced during property measurements. For the x = 0.75 series the x_{calc} = 0.75, 0.74, 0.73, and 0.74 while y_{calc} = 0.54, 1.01, and 1.49, and 1.91 respectively. These values show no greater than 7% discrepancy from targeted formulas.

EDAX results for the x = 0.5 and 0.75 solid solutions can be found in Table 5.6 and Table 5.7 respectively where atomic percent, and empirical formula of the constituent atoms are shown. Atom concentrations determined from EDAX measurements match well for most solid solutions with expected atomic percent. For x = 0.75, y = 1 solid solution the Ge concentration is lower than expected which matched well with the Rietveld refinement results. EDAX atomic mapping for these measurements can be found in the Appendix in Figure A.27 and Figure A.28 for x = 0.5 and x = 0.75 respectively.

Table 5.6: EDAX analysis results obtained using area scans on the $ZnGe_{1-x}Sn_xP_{2-y}As_y$ (x = 0.5) series. The table is sorted by compound nomenclature with atomic percent (At. %) and empirical formula (Emp.) for each set of measurements.

x = 0.5	y = 0.5		y = 1		y = 2	
Elem.	**At. %**	**Emp.**	**At. %**	**Emp.**	**At. %**	**Emp.**
Zn	24.24	0.97	24.47	0.98	25.24	1.01
Ge	11.05	0.44	9.54	0.38	12.76	0.51
Sn	12.28	0.49	13.15	0.53	13.07	0.52
P	39.89	1.60	27.69	1.11	-	-
As	12.54	0.50	25.15	1.01	48.92	1.96

Table 5.7: EDAX analysis results obtained using area scans on the $ZnGe_{1-x}Sn_xP_{2-y}As_y$ (x = 0.75) series. The table is sorted by compound nomenclature with atomic percent (At. %) and empirical formula (Emp.) for each set of measurements.

x = 0.75	y = 1		y = 1.5		y = 2	
Elem.	**At. %**	**Emp.**	**At. %**	**Emp.**	**At. %**	**Emp.**
Zn	24.70	0.99	24.97	1.00	26.74	1.07
Ge	5.63	0.23	5.94	0.24	6.59	0.26
Sn	19.01	0.76	19.14	0.77	18.48	0.74
P	26.47	1.06	12.72	0.51	-	-
As	24.19	0.97	37.22	1.49	48.19	1.93

5.3.2 Thermoelectric Properties of $ZnGe_{1-x}Sn_xP_{2-y}As_y$

Thermoelectric property measurements were performed for the $ZnGe_{0.5}Sn_{0.5}P_{2-y}As_y$ series (y = 0, 0.5, 1.5, 2), while only thermal conductivity measurements for $ZnGe_{0.25}Sn_{0.75}P_{2-y}As_y$ series were measured, these results are discussed in this section.

5.3.2.1 Electrical Conductivity

Electrical conductivity results are displayed in Figure 5.17 with the end members $ZnGeP_2$, $ZnSnP_2$, and $ZnSnAs_2$ for reference. The sample x = 0.5, y = 1 was not measured due to the sample breaking prior to measurement. Overall lower minimum temperatures were required for measurements of the x = 0.5 series when compared to the x = 1 series. Increasing electrical conductivity with increasing As is seen between y = 0 and y = 1.5, while for y = 2 the conductivity is unexpectedly smaller at low temperatures rising equal to y = 1.5 at 700 K and greater at higher temperatures. Conductivity ranges for y = 0.5 from $2.5 \cdot 10^{-4}$ S cm^{-1} at 370 K to 0.5 S cm^{-1} at 800 K, for y = 1.5 from 0.2 S cm^{-1} at 370 K to 2.8 S cm^{-1} at 750 K, and for y = 2 from 0.05 S cm^{-1} at 375 K to 3.3 S cm^{-1} at 750 K. The compounds show increased stability when compared to both $ZnGe_{0.5}Sn_{0.5}P_2$ and the $ZnSnP_{2-y}As_y$ series allowing for a wider temperature range of measurements.

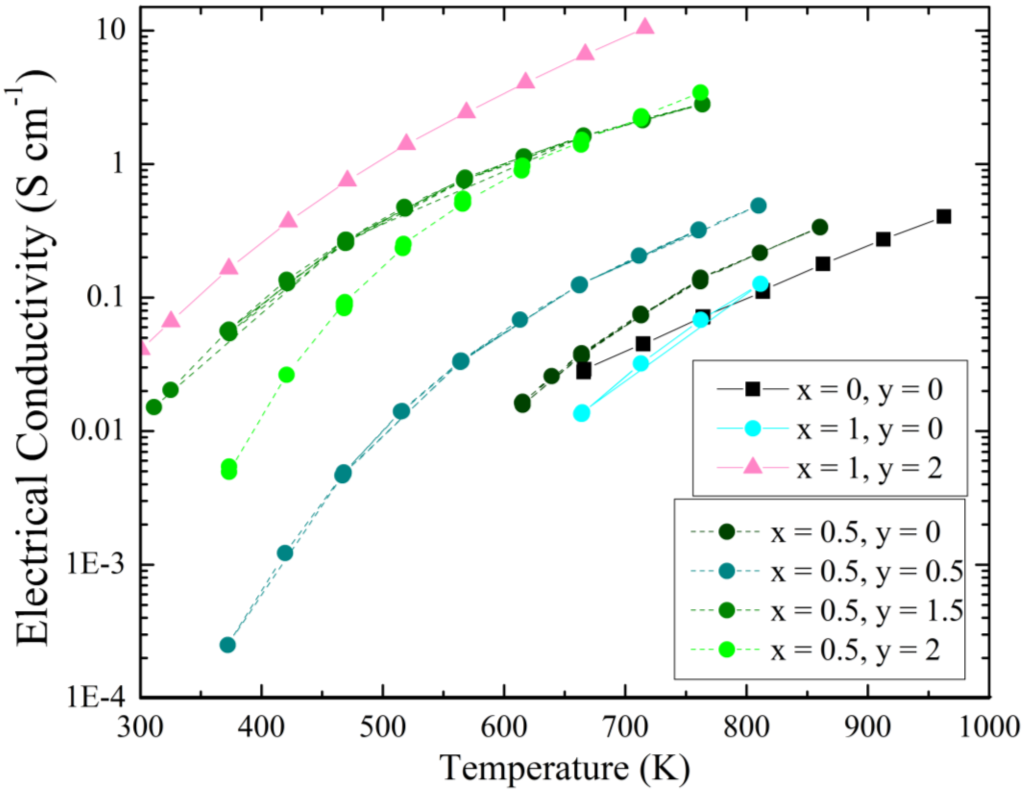

Figure 5.17: Electrical conductivity versus temperature for $ZnGe_{0.5}Sn_{0.5}P_{2-y}As_y$ (y = 0, 0.5, 1.5, 2) with end members for comparison

All measured members apart from y = 2 display intrinsic semiconducting behavior as shown from an Arrhenius plot in Figure 5.18. The band gaps of the materials are calculated using the slope from the fits in the linear regions. For y = 2 the linear fit was obtained in the high temperature linear region which should be intrinsic after depletion of extrinsic carriers. Calculated band gaps versus concentration are shown in the inset which displays decreasing band gaps with increasing As concentration. The band gaps for x = 0.5 are smaller than for x = 1 at the same As concentration with the exception of y = 2 where both are equal at about 0.7 eV. The overall nonlinear trend in the Arrhenius plot indicates non intrinsic semiconducting behavior for y = 2. The results for band gap reflect those obtained for $ZnGe_{1-x}Sn_xP_2$ solid solutions in Chapter 4, where band gap was found to increase with Sn concentration and overall, the band gaps found for x = 0.5 are lower than x = 1 at the same As concentrations.

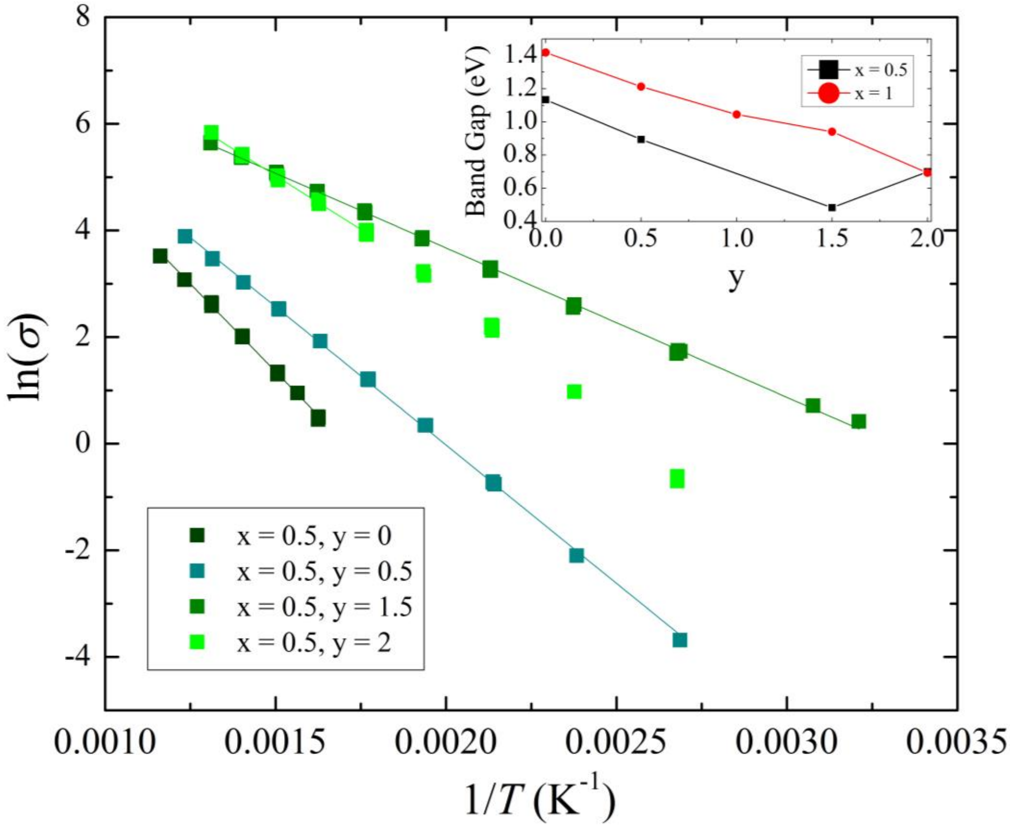

Figure 5.18: Calculation of band gaps for $ZnGe_{0.5}Sn_{0.5}P_{2-y}As_y$ (y = 0, 0.5, 1.5, 2) (a) Arrhenius plot with linear fit to intrinsic regions (b) inset band gap versus concentration with $ZnSnP_{2-y}As_y$ for comparison.

5.3.2.2 Seebeck Coefficient

Seebeck coefficients measurements for $ZnGe_{0.5}Sn_{0.5}P_{2-y}As_y$ (y = 0, 0.5, 1.5, and 2) are displayed in Figure 5.19. Overall, the Seebeck coefficients for x = 0.5 are found to decrease with increasing As concentration due to the increasing electrical conductivity similar to x = 1. The trend of Seebeck coefficient with temperature is much flatter for the x = 0.5 compounds, decreasing less with increasing temperature than the x = 1 series. The values of Seebeck coefficient for x = 0.5, y = 0.5 are lower than those found for x = 1, y = 0.5 particularly at low temperatures with a maximum of 825 μV K^{-1} at 515 K. The decrease with increasing temperatures is slight, reaching 732 μV K^{-1} at 810 K, and having greater Seebeck than x = 1 at comparable temperatures. For the other higher order solid solutions y = 1.5 and y = 2 the values of Seebeck coefficient are higher than those of the x = 1 compounds. For y = 1.5 the values range from 525 µV K^{-1} at 325 K to 550 µV K^{-1} at 765 K with a very flat temperature dependence despite the exponential increase in electrical conductivity. This simultaneous increase in Seebeck coefficient and electrical conductivity is characteristic of some HEA materials.[57,233] Values for y = 2 are very similar at low temperatures to y = 1.5 with 553 µV K^{-1} at 375 K decreasing at higher temperatures to 236 µV K^{-1} at 762 K. The decrease observed in the y = 2 sample suggests the onset of bipolar conduction as observed in $ZnSnAs_2$ end member and $ZnSnP_{0.5}As_{1.5}$ solid solution.

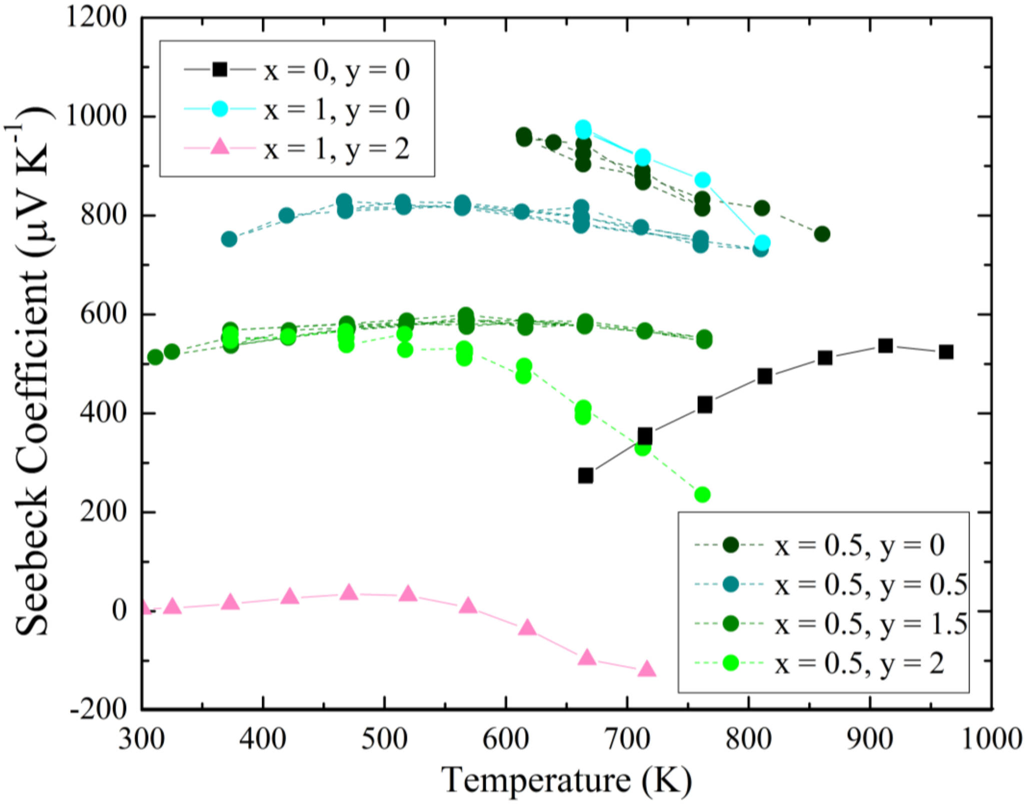

Figure 5.19: Seebeck coefficient versus temperature for $ZnGe_{0.5}Sn_{0.5}P_{2-y}As_y$ (y = 0, 0.5, 1.5, 2) with end members for comparison

5.3.2.3 Power Factor

The power factors for the series are displayed in Figure 5.20, where the power factors increase with increasing As concentration between y = 0 and y = 1.5 in comparable temperature ranges and increase with increasing temperature. The power factor for the y = 2 member is intermediate of y = 0.5 and y =

1.5 at low temperatures, decreasing Seebeck coefficient with temperature provides a maximum power factor at 650 K which decreases at higher temperatures. Overall, the power factors for the higher order solid solutions are greater compared to the end members and quaternary solid solutions.

For y = 0.5 the power factor ranges from 0.14 μW m^{-1} K^{-2} at 372 K to 26 μW m^{-1} K^{-2} at 810 K showing significant increases compared to end members and P rich solid solutions. The largest power factor is found for y = 1.5 which ranges from 0.4 μW m^{-1} K^{-2} at 310 K to 86 μW m^{-1} K^{-2} at 764 K due to a relatively flat Seebeck coefficient and exponentially increasing electrical conductivity. The effect of bipolar conduction is seen for y = 2 which ranges from 0.16 μW m^{-1} K^{-2} at 373 K reaching a maximum of 26 μW m^{-1} K^{-2} at 664 K and decreasing to 19 μW m^{-1} K^{-2} at 762 K.

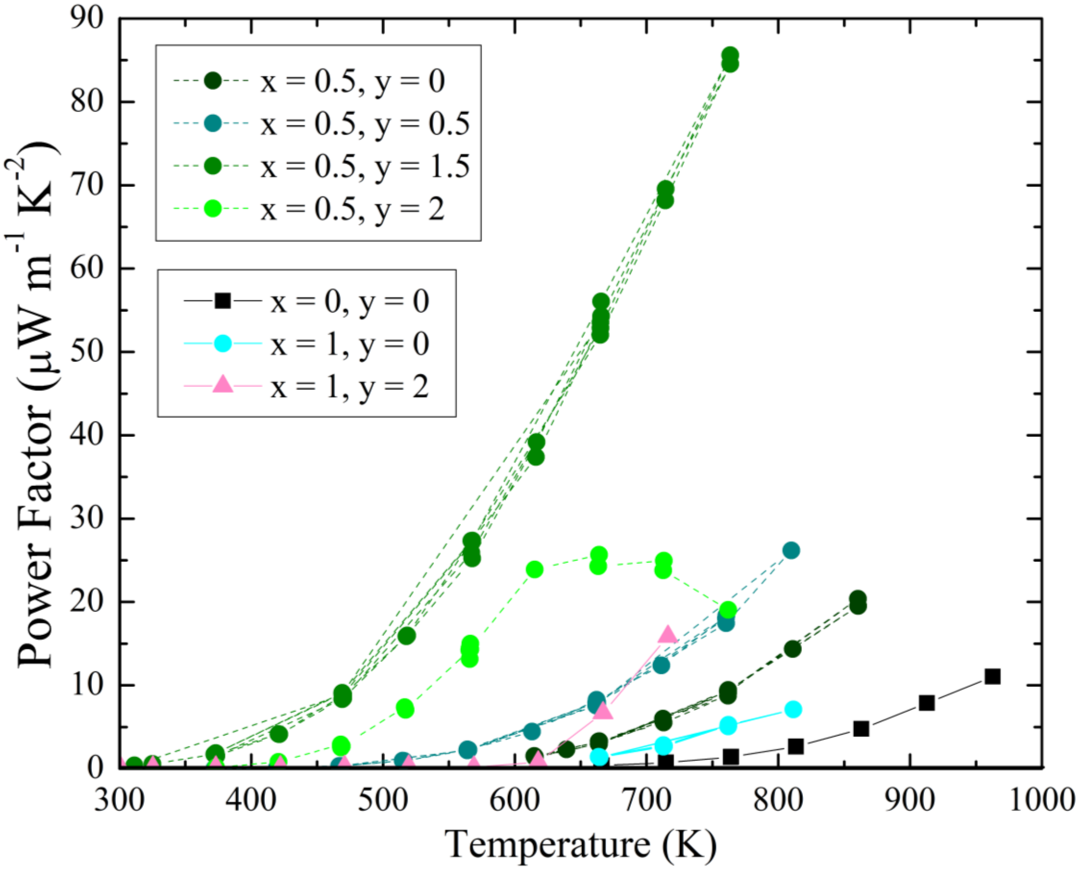

Figure 5.20: Power factor versus temperature for $ZnGe_{0.5}Sn_{0.5}P_{2-y}As_y$ (y = 0, 0.5, 1.5, 2) with end members for comparison

5.3.2.4 Thermal Conductivity

Thermal conductivity measurements were performed for the series x = 0.5, 0.75; for y = 0, 0.5, 1, 1.5, and 2, the results are displayed in Figure 5.21. The thermal conductivities display decreasing values with increasing temperatures, with the lowest conductivities for the y = 1 members. Higher order solid solutions display significantly lower thermal conductivities when compared to the other quaternary members, and the x = 0.75 series also display overall lower thermal conductivities except for y = 0 members.

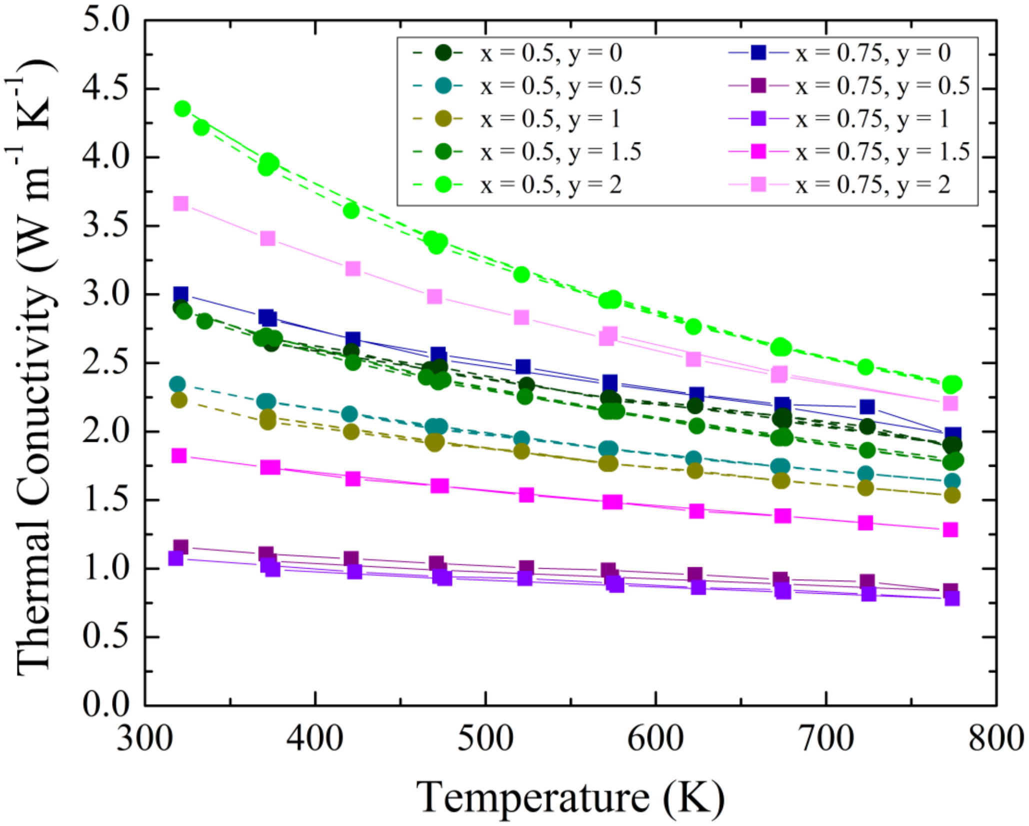

Figure 5.21: Thermal conductivity versus temperature for $ZnGe_{1-x}Sn_xP_{2-y}As_y$ (x = 0.5, 0.75; y = 0, 0.5, 1, 1.5, 2)

The difference in thermal conductivity between the x = 0.5 and x = 0.75 series may also be due to different processing conditions as discussed in Section 4.5.6. Values of TC for the higher order solid solutions x = 0.5, range from 3 W m^{-1} K^{-1} to 2.3 W m^{-1} K^{-1} at 325 K and decrease to 1.8 W m^{-1} K^{-1} to 1.5 W m^{-1} K^{-1} at 775 K, while for x = 0.75 ranges from 1.8 W m^{-1} K^{-1} to 1.1 W m^{-1} K^{-1} at 325 K and decrease to 1.3 W m^{-1} K^{-1} to 0.8 W m^{-1} K^{-1} at 775 K. The values of thermal conductivity obtained for the higher order solid solutions are very low within the glasslike regime for tin substitutions of x = 0.75 and arsenic substitutions of y = 1 and 0.5.

5.3.2.5 Figure of Merit

Thermoelectric figures of merit for the x = 0.5 series are displayed in Figure 5.22 with end members plotted for comparison. A significant increase in thermoelectric performance is found for the higher order solid solutions. Increases in zT of the higher order solid solutions are achieved through lower thermal conductivity and maintaining higher Seebeck coefficient with increased electrical conductivity when compared to the quaternary solid solutions and end members. TE performance for y = 1.5 displays the largest values for which $zT = 6.4 \cdot 10^{-5}$ at 325 K increasing to 0.034 at 750 K. $ZnGe_{0.5}Sn_{0.5}As_2$ (y = 2) displays the second-best performance at low temperature before the onset of bipolar conduction which causes a turnover starting at 700 K.

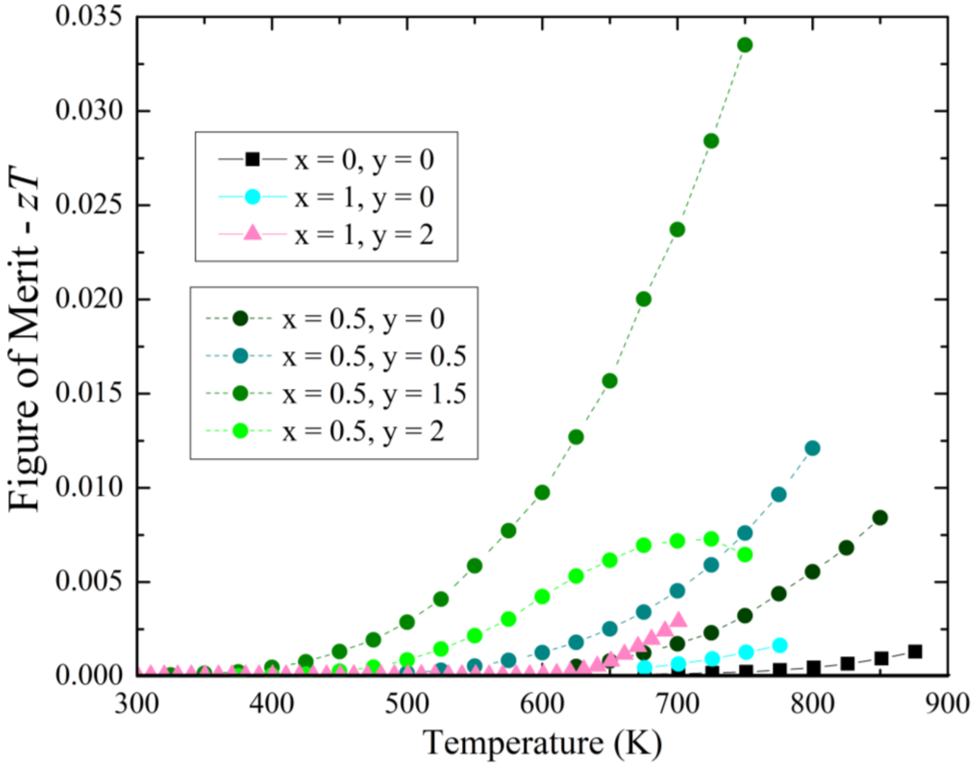

Figure 5.22: Thermoelectric figure of merit versus temperature for $ZnGe_{0.5}Sn_{0.5}P_{2-y}As_y$ (y = 0, 0.5, 1.5, 2) with end members for comparison.

Compared to other end members and solid solutions improvements to TE performance in the quinary solid solutions are the result of multiple factors. High Seebeck coefficient is maintained with a simultaneous increase in electrical conductivity, and mass fluctuation effects decrease thermal conductivity additively manner. A summary of thermoelectric properties is shown in Table 5.8 for y = 0.5, 1.5 and 2; the electrical transport properties for y = 1 sample was not measured due to sample loss.

Table 5.8: Summary of Thermoelectric properties for $ZnGe_{0.5}Sn_{0.5}P_{2-y}As_y$ (y = 0.5, 1.5, 2).

Y	σ (S^{-1} cm^{-1}) 373 K, 760 K	S ($\mu V\ K^{-1}$) 600 K, 760 K	$S^2\sigma$ ($\mu W\ m^{-1}\ K^{-2}$) 600 K, 760 K	κ ($W\ m^{-1} K^{-1}$) 325 K, 775 K	zT 375 K, 750 K
0.5	2.5E-4, 0.32	752, 740	0.14, 17.5	2.32, 1.64	6.6E-6, 7.6E-3
1.5	0.06, 2.84	569, 546	1.86, 85.6	2.86, 1.78	2.3E-4, 3.4E-2
2	5.1E-3, 3.43	550, 236	0.16, 19.1	4.32, 2.35	1.7E-5, 6.4E-3

5.3.3 Conclusion $ZnGe_{1-x}Sn_xP_{2-y}As_y$

Synthesis of higher order (quinary) chalcopyrite solid solutions was achieved using the synthetic methods developed in Chapter 4. The miscibility of the solid solutions was complete, apart from $ZnGe_{0.25}Sn_{0.75}PAs$, which may be due to unoptimized reaction conditions. Rietveld refinements displayed standard structural changes with varying composition of the solid solutions based on end members and ionic radii. Calculated tetragonality of the mixed $ZnGe_{0.25}Sn_{0.75}P_{2-y}As_y$ (y = 0.5, 1, and 0.75) members was greater than the $ZnSnP_{2-y}As_y$ members which is promising for greater band degeneracy. Increased temperature stability of the compounds was observed throughout the experiments with the inclusion of germanium.

Electrical conductivity of the materials increased with increasing arsenic concentration due to a decreasing band gap like the $ZnSnP_{2-y}As_y$ study. The Seebeck coefficients of the quinary solid solutions maintained much higher values with increasing temperature and electronic conductivity when compared to the quaternary compounds. A maintained high Seebeck coefficient with increased electrical conductivity is an observed phenomenon in high entropy alloys. Suppression of n-type carriers due to creation of acceptor states by cation rattling effects was observed in a closely related Kësterite material which was also heavily alloyed.[233] The resulting power factors observed in these compounds are much greater than the other chalcopyrite compounds studied.

Thermal conductivities of the higher order solid solutions were reduced in comparison to the quaternary compounds by increased mass fluctuation scattering on multiple crystallographic sites. A reduction down to the glasslike regime was found for the solid solutions $ZnGe_{0.25}Sn_{0.75}PAs$, and $ZnGe_{0.25}Sn_{0.75}P_{1.5}As_{0.5}$, however the thermoelectric transport properties of these compounds were not measured. The reduction of thermal conductivity combined with increased overall power factor of the measured compounds resulted in a 30-fold increase in zT when compared to other explored solid solutions. Electronic doping of these solid solutions would be necessary to improve the thermoelectric performance.

Formation of these higher order solid solutions via the methods developed provides impetus for further exploration into the pnictide chalcopyrite compounds for TE applications. High entropy alloys are typically formed using binary end members and limited synthetic methods. The ternary end members of chalcopyrite structures increase the number of available substitutions and therefore entropy of the systems. The limits of the milling techniques outlined for the formation of these HEA can be explored further. Enhancements of these systems may be achieved by alloying on the Zn site with Cd in concert with all other sites.

Chapter 6: Synthesis, Structure, and Thermoelectric Properties of Solid Solution Materials $Ca_{11}Sb_{10-x}Bi_x$, and $Ca_{11}Sb_{10-y}As_y$

This chapter explores the properties of solid solutions of the phonon glass electron crystal (PGEC) materials with the $Ho_{11}Ge_{20}$ structure. The complexity of these crystal structures is typical of compounds with low lattice thermal conductivity providing motivation for this study. Liquid-solid synthesis methods were attempted to form solid solutions of $Ca_{11}Sb_{10-x}Bi_x$ and $Ca_{11}Sb_{10-y}As_y$. PXRD analysis of the attempted reactions was performed and SCXRD analysis was performed on single crystals obtained from $Ca_{11}Sb_{10-x}Bi_x$ reactions. Site preference substitutions or coloring effects are observed from single crystal analysis. Electronic structure calculations are performed to obtain band structure and DOS. The thermoelectric properties of obtained compounds are measured and discussed with comparison to previously obtained literature results.

6.1 Experimental Methods

Preparation of materials were performed in a purified argon glovebox using elemental materials: calcium granules (99.5% Alfa Aesar), antimony lump (99.5% metals basis Alfa Aesar), bismuth needles (99.99% Alfa Aesar), and -100 mesh arsenic powder (99.98% Alfa Aesar). Synthesis of the solid solutions and end members for $Ca_{11}Sb_{10-x}Bi_x$ (x = 0, 2, 4 ,6, and 10) and $Ca_{11}Sb_{10-y}As_y$ (y = 0, 2, 4, 6, and 10) were attempted using stochiometric proportions of elemental reagents. The components were added to carbon coated fused silica tubes with the lower melting elements placed on the bottom and higher melting towards the top. Loaded tubes were vacuum sealed at $1 \cdot 10^{-3}$ mbar with container lengths of 7.5-10 cm. Reaction ampules were placed in muffle furnaces and heated quickly to 500 °C then slowly for 12 hours to 650 °C and held for 24 hours. The temperature was then raised to 850 °C over 24 hours then the heat was turned off. Low temperature (500 °C) steps were necessary to pre-react the calcium metal to reduce volatility prior to further heating. Synthesis attempts heating directly to high temperatures (> 650 °C) resulted in ampule failure due to reaction of silica with calcium vapors. The resulting ingots were brittle and grey, resembling the clumped calcium granules.

Ingots were hand ground into a uniform powder under argon atmosphere and sampled for PXRD and densification. The synthesized powders degraded under ambient conditions within a few hours which was unexpected based on previous observations of ambient stability and therefore suggests incomplete reaction. High pressure sintering was performed on samples using the OXYGON industries hot press system by applying 56 MPa of pressure at 750 °C followed by a pressure free cooldown. The resulting pellets were checked with PXRD, and density measured using Archimedes' method.

Powder X-ray diffraction was performed on polished pellets and ground samples using the Inel powder X-ray diffractometer. Single crystal studies were performed at room temperature using a Bruker Kappa APEX II CCD diffractometer with a Mo K_α radiation source. Single crystals were obtained from crushed ingots and measured using single crystal X-ray diffraction. A Bruker Kappa APEX II CCD diffractometer, with a Mo K_α monochromated radiation source is used for measurements. Structure refinements are performed using the APEX II (Bruker) software package. Thermal diffusivity of the pressed pellets was measured using the TA-instruments DLF-1200 system. Seebeck coefficient was measured by the direct method, and electrical conductivity measured by a standard 4-point with the ULVAC RIKO ZEM-3 apparatus. Rietveld refinements were performed using GSAS-II analysis software. Electronic structure calculations were performed using the Wien2k package using the full potential linearized augmented plane wave (LAPW) method.[18]

6.2 Synthesis and Structure

6.2.1 $Ca_{11}Sb_{10-x}Bi_x$ PXRD

Phase verification was performed on the powdered samples after the initial tube synthesis using PXRD. The air sensitivity of the powders limited measurement times to one hour which indicated incomplete reaction. High pressure sintering was used to complete the reaction after phase verification. The patterns resulting from series $Ca_{11}Sb_{10-x}Bi_x$ (x = 0, 2, 4, 6, 10) are shown in Figure 6.1 where the intended stoichiometries are indicated. For the x = 0 end member the successful synthesis is achieved in comparison to the calculated pattern. As bismuth concentration is increased a standard peak shift to lower 2θ values is seen as expected from an increasing unit cell. A reduction of peak intensity at 2θ = 30° and increase in peak intensity at 2θ = 23° is seen with increasing Bi concentration as expected from the calculated end member patterns. Impurity peaks are found in Bi containing samples indicative of elemental bismuth at 2θ = 24° and elemental calcium at 2θ = 26° suggesting incomplete reaction. The intensity of impurity peaks is greatest for the x = 10 end member and x = 2 stoichiometric reactions. Minor impurity peaks are found in x = 4 and x = 6 stochiometric reactions which are primarily elemental Bi reflections.

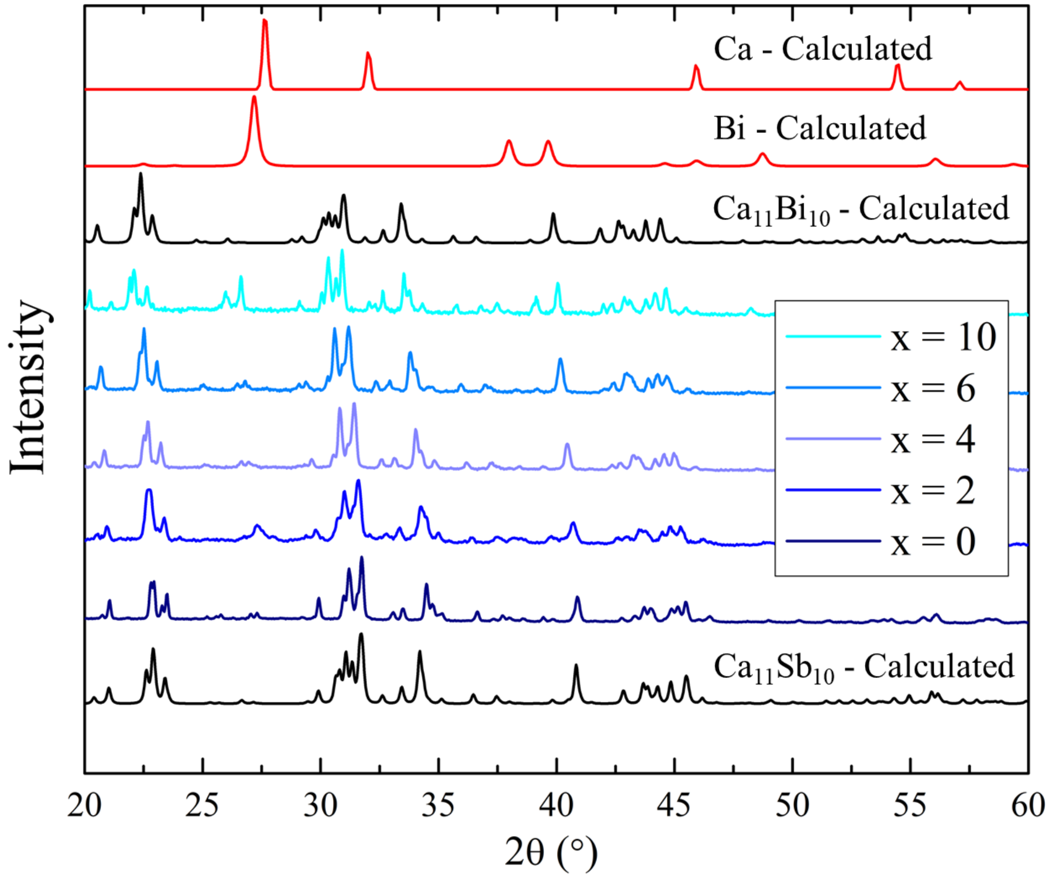

Figure 6.1: PXRD of the $Ca_{11}Sb_{10-x}Bi_x$ reaction series, the majority of reflections are associated with the target phases with a peak shift in 2θ values. End members are shown in black and identified impurities are shown in red.

6.2.2 $Ca_{11}Sb_{10-x}Bi_x$ SCXRD

Single crystals of the synthesized materials obtained from the lightly ground ingots were measured using SCXRD. The resulting structures indicated miscibility of the compounds overall Bi concentrations which were not exactly the intended stoichiometry of the reactions, indicating a variability of substitution of the crystallites within the ingot. The variability of the crystallites is not surprising due to the liquid-solid reaction conditions. The unit cell parameters are displayed in Figure 6.2 showing a general increase in *a*, *b*-axis unit cell parameter and volume with increasing Bi concentration. A slight decrease in the c-axis was seen between x = 2.6 and x = 4.8 which increases again at x = 5.6 for an overall increase with concentration.

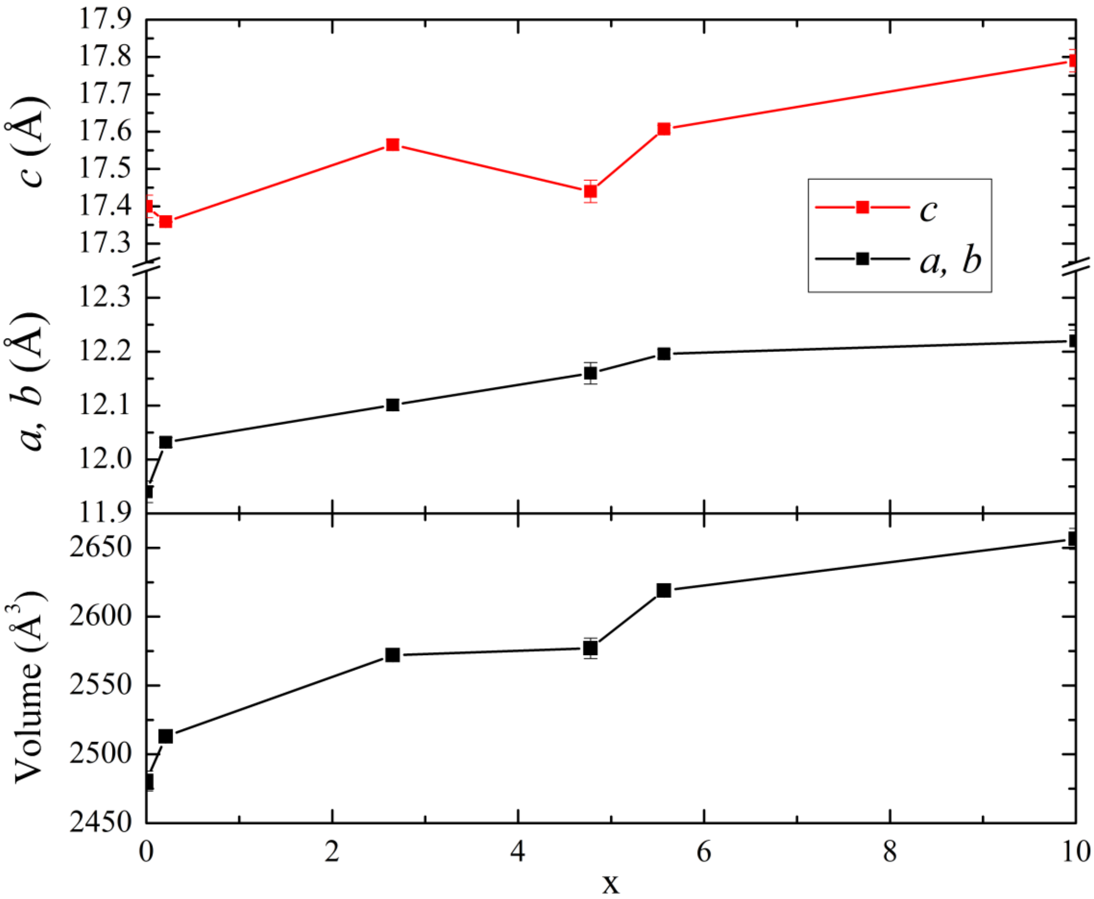

Figure 6.2: Unit cell parameters versus concentration (x) for $Ca_{11}Sb_{10-x}Bi_x$, volume and *a, b*-axis increase with increasing concentration. The *c*-axis shows a decrease between x = 2 and x = 5, and x = 0 (literature) and x = 0.21 but overall increasing trend.

Preference for Bi occupancy in the planar square Pn_4^{4-} subunits and Pn_2^{4-} linear subunits is seen from the refinements as shown in Figure 6.3. Isolated pnictide anions are shown in blue, linear subunits in green, and square planar subunits in purple. At overall crystal composition x = 2.6 the bismuth occupancy of isolated sites Pn-1, Pn-2, and Pn-4 contain little to no Bi with 0, 0.1, and 0.04 respectively, whereas Pn-3 (square) and Pn-5 (dumbbell) contain 0.52 and 0.35 respectively. This preference of bismuth occupancy is found for all other measured single crystal samples. The isolated Pn^{3-} sites maintained low concentrations of Bi with and Pn-2 containing the greatest and Pn-1 containing the lowest throughout.[234,235] Tables containing the single crystal refinement atomic parameters can be found in the Appendix in tables in Table A.12 through Table A.15.

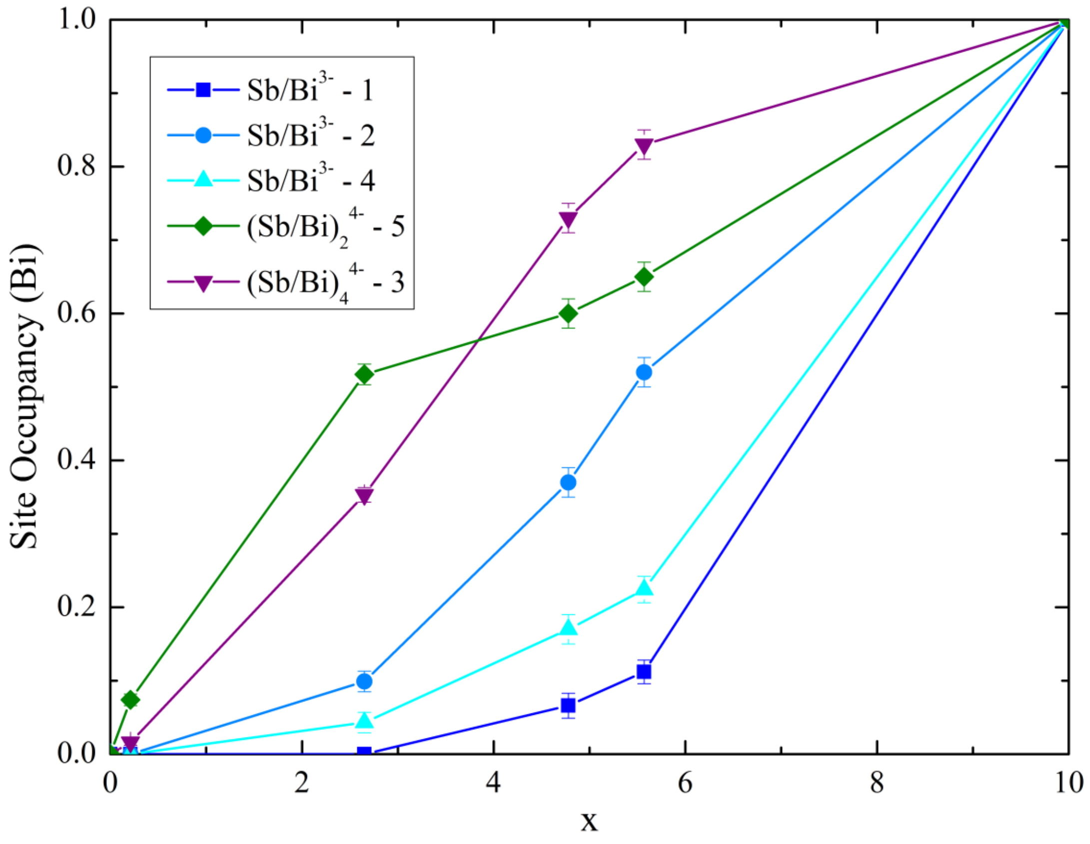

Figure 6.3: Bi site occupancy versus overall crystal stoichiometry x from $Ca_{11}Sb_{10-x}Bi_x$ single crystals. The isolated sites contain lower Bi concentration versus the polyanion sites Pn_4^{4-} and Pn_2^{4-}.

The energy differences in atomic sites can be examined using DFT methods with considerations to coordination geometry and cation-anion bond distances to predict preferred occupancy. Section 6.3 compares the electronic structure calculation results against preferred occupancy results. Bond-distance and cation-anion coordination are also known as contributing factors to site preference; however, these factors originate from the electronic orbital interactions of the atoms.

The coordination of the various pnictide anion units is shown in Figure 6.4 with Pn_4^{4-} linear square units, Pn_2^{4-} dumbbell units, and Pn^{3-} isolated atoms. The Pn_4 square units are bonded with a total of 14 Ca atoms; two Ca atoms form octahedra with a single Ca bonded to all four Pn atoms in both directions, eight Ca atoms share two bonds between adjacent Pn atoms, and four Ca atoms are bonded singly to the corners of the square unit. The Pn_2 dumbbell units contain a total of 12 Ca bonds, with each Pn atom forming a capped trigonal prism which share a rectangular face formed from sharing bonds with each atom in the dumbbell. The isolated Pn atoms are each coordinated by eight Ca atoms with average bond distances of 3.21 Å, 3.42 Å, and 3.17 Å for site 1, 2, and 4 respectively for $Ca_{11}Sb_{10}$.

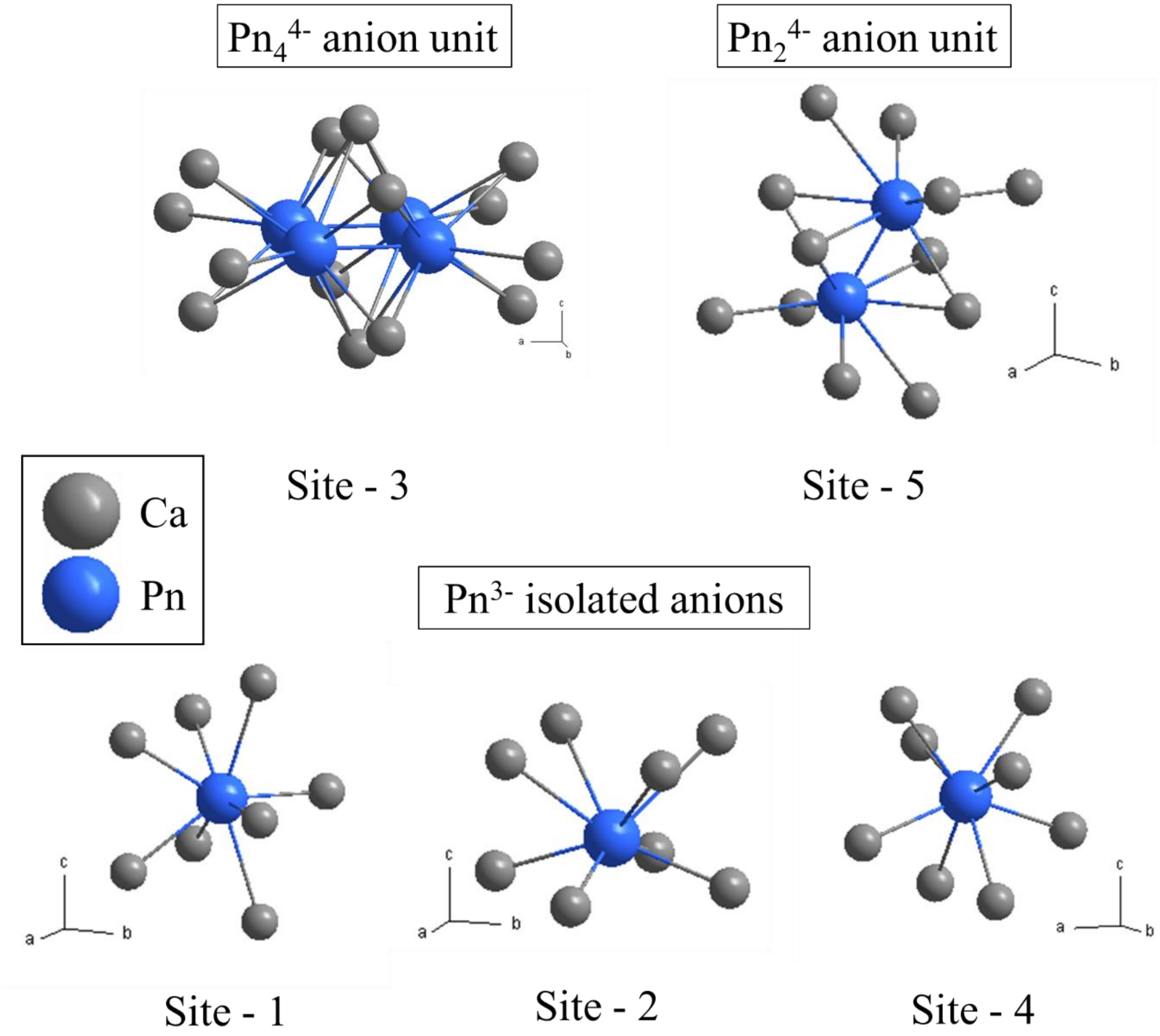

Figure 6.4: Coordination geometries of the various Pn sites with 14 Ca bonded to the Pn_4^{4-} unit, 12 Ca bonded Pn_2^{4-}, and eight Ca atoms bonded to the isolated Pn^{3-} units.

Site position, occupancy and thermal parameters can be found in Table A.8 to Table A.11 in the Appendix. Here it can be seen that the thermal displacement parameter is greatest for the Pn-3 site which forms the Sb_4^{2-} anion subunit. Structural refinements displayed large thermal displacement parameters for the Ca-2 which showed cigar shape elongation in the *a, b* planes. To obtain accurate refinement results it was required to split this site into two distinct sites. Large displacement parameters of this site are characteristic of many $M_{11}Pn_{10}$ structures.[156,159,234,235]

6.2.3 $Ca_{11}Sb_{10-y}As_y$ PXRD

Synthesis of $Ca_{11}Sb_{10-y}As_y$ solid solutions were attempted for y = 2, 4, 6, and 10 at the time of this work the compound $Ca_{11}As_{10}$ was not known to exist. Since then, the discovery and structural characterization of $Ca_{11}As_{10}$ was achieved and published in September 2022.[236] The PXRD patterns of the explored series is found in Figure 6.5. Miscibility of stoichiometries from y = 2 to y = 6 is found by comparing the resulting patterns with end members. A shift in peak positions is seen with decreasing unit cell size as expected with increasing arsenic concentration. The presence of elemental impurities, specifically calcium and antimony, were found in the attempted solid solution members. The apparent successful synthesis of the y = 6 member is an indication of the presence of As-Pn bonding because the isolated Pn sites only attribute up to four atoms in the formula $Ca_{11}Pn_{10}$.

The attempted synthesis of end member $Ca_{11}As_{10}$ was unsuccessful and resulted in synthesis of the compound CaAs. Calculated patterns are shown for CaAs and $Ca_{11}As_{10}$ for comparison with the reaction results, here it can be seen very minor peaks which could be attributed to $Ca_{11}As_{10}$; however, the majority phase is CaAs. The maximum reaction temperatures attempted here were lower than those used in the work presenting successful synthesis (850 °C versus 900 °C) which is likely the reason for unsuccessful synthesis of $Ca_{11}As_{10}$.[236] Degradation of all powdered samples under ambient conditions was observed indicating incomplete synthesis, as previously synthesized single crystals were apparently stable under ambient conditions.

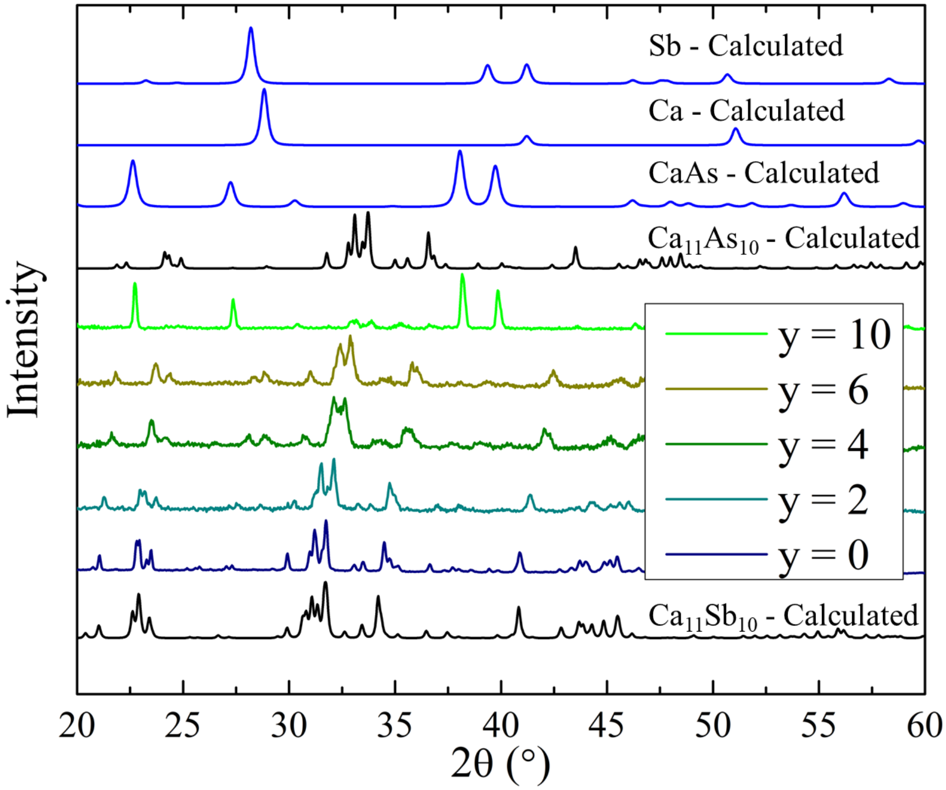

Figure 6.5: PXRD patterns of $Ca_{11}Sb_{1-y}As_y$ reaction series where the stoichiometry of the reactions is given as y.

6.3 Electronic Structure Calculations

Electronic band structure calculations for $Ca_{11}As_{10}$ (Figure 6.6), $Ca_{11}Sb_{10}$ (Figure 6.7), and $Ca_{11}Bi_{10}$ (Figure 6.8) all display multiple bands crossing the Fermi level indicating metallic electronic properties. A mixture of flat and steep bands is present at the Fermi level for all compounds which is a signature characteristic for superconducting behavior.[235] A single band displaying parabolic behavior centered at the P-point prevents a pseudo gap above the Fermi level for $Ca_{11}As_{10}$ and $Ca_{11}Sb_{10}$. The width of this region is seen to increase with decreasing unit cell size as expected due to increasing orbital overlaps. The low density of states within this region for As and Sb end members is more apparent in the DOS plots on the right sides of the figures which ranges from 0.3 eV to 0.9 eV and 0.4 eV to 0.7 eV respectively whereas DOS remains large throughout for the Bi end member. Decreasing the unit cell size further from $Ca_{11}As_{10}$ with partial phosphorus ($Ca_{11}As_{10-x}P_x$) or magnesium ($Ca_{11-x}Mg_xAs_{10}$) alloying could possibly open the pseudo gap. Further alloying with non isovalent components can be used to increase valence electron count (VEC) moving the material into degenerate or intrinsic semiconducting behavior. This strategy has been previously used to develop the metallic material Mo_3Sb_7 into the thermoelectric material $Mo_3Sb_{5.4}Te_{1.6}$ with $zT = 0.8$ at 1050 K.[237,238]

The steep bands which cross at the P-point originate from the Ca-4 *d* states and the non-isolated Pn-3 and Pn-5 *p* states. Multiple flat bands lie on the Fermi level which are primarily composed of Pn-1, Pn-3, and Pn-5 *p* states with contributions from Ca-1, Ca-2, and Ca-4 *d* states. The steep bands about the Fermi level are composed mostly from Pn-2 and Pn-4 *p* states with contributions from Ca-3 *d* states. This is illustrated well with the PDOS plots presented in each figure, where a steep drop in density of states is representative of flat electronic bands while more gradual slope corresponds to steep electronic bands. PDOS plots for each individual atom containing orbital information can be found in Figure A.30 through Figure A.33 in the Appendix. The majority of contributions for Ca and Pn atoms in each system are from *d* states and *p* states respectively. The coloring effects exhibited in these compounds are interesting since the end member $Ca_{11}Bi_{10}$ displays superconductivity at 4.1 K, and the preference for Bi substitution occurs most for the atoms contributing to the bands at the Fermi level.[233,234]

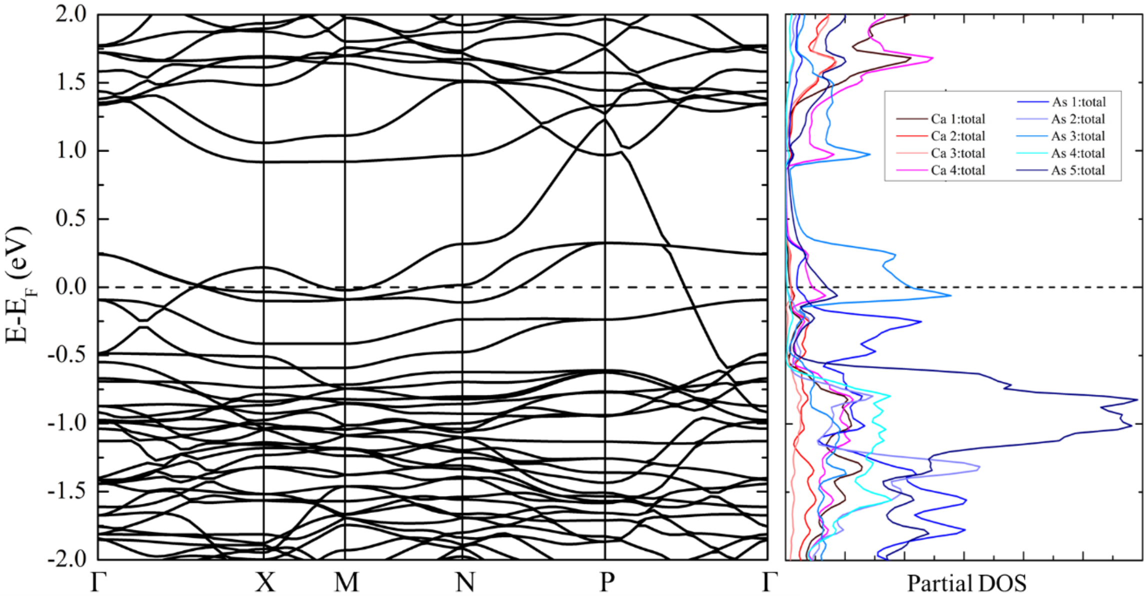

Figure 6.6: Electronic band structure for $Ca_{11}As_{10}$ (left) with partial density of states (PDOS) plotted for each atomic site (right).

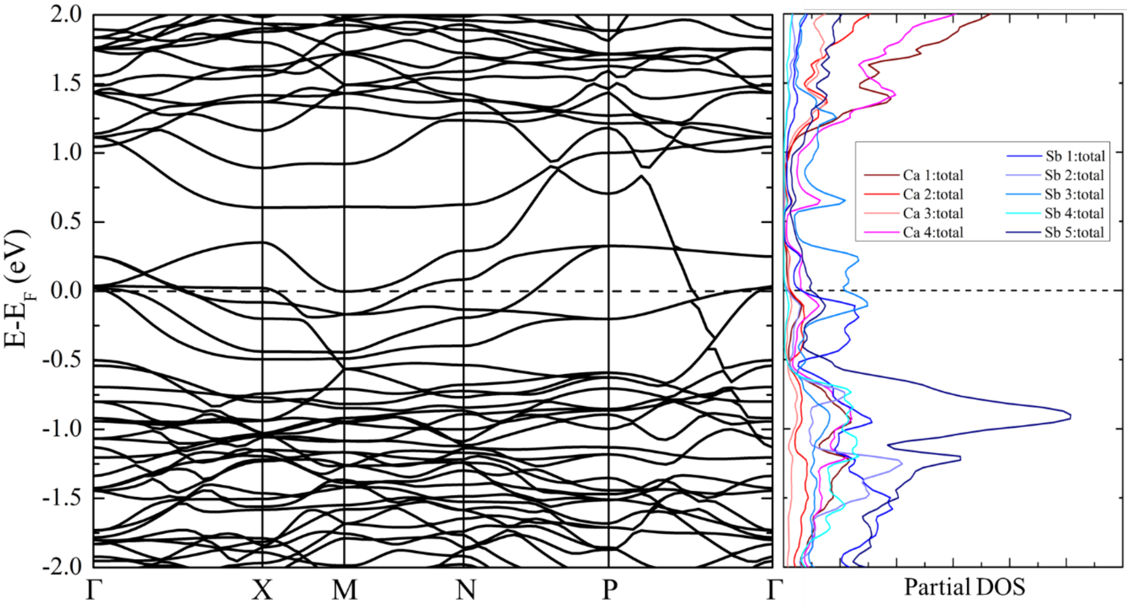

Figure 6.7: Electronic band structure for $Ca_{11}Sb_{10}$ (left) with partial density of states (PDOS) plotted for each atomic site (right)

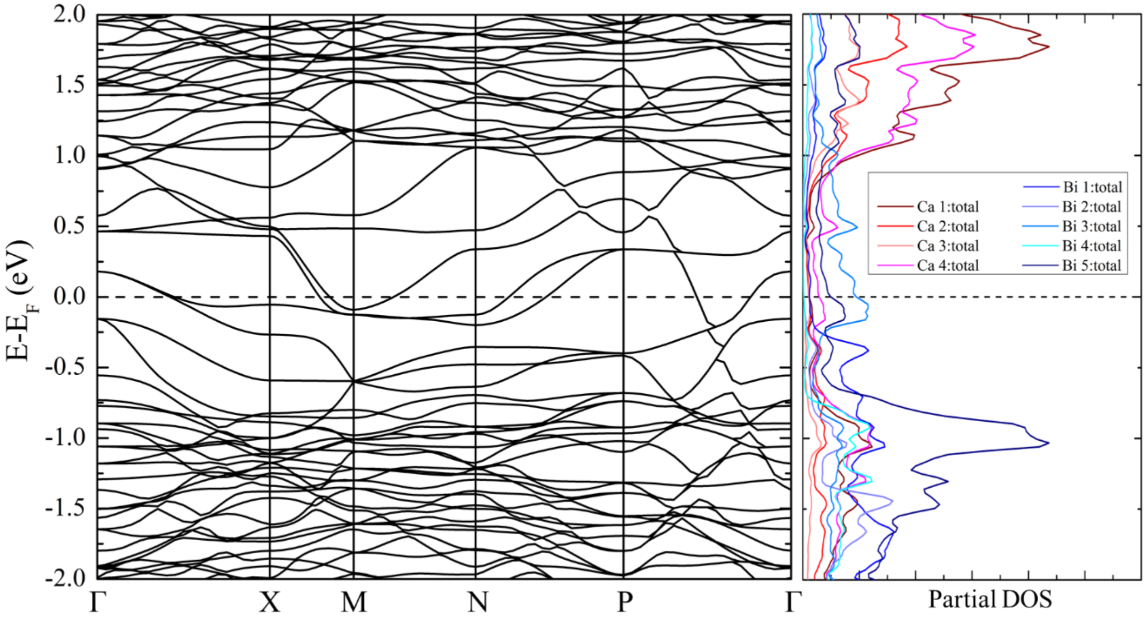

Figure 6.8: Electronic band structure for $Ca_{11}Bi_{10}$ (left) with partial density of states (PDOS) plotted for each atomic site (right)

6.3.1 Prediction of Site Preferences

The density of states was used to examine the correlations between site bonding energy and site preference obtained from SCXRD measurements. As advanced COOP (crystal orbital overlap populations) or COHP (crystal orbital Hamilton population) analysis were unattainable from WIEN2k output a simplified analysis was manually performed.[239–241] Site preference based on simple chemical reasoning suggest atoms with greater electronegativity will prefer site with higher electron density which is demonstrated to apply well for solids.[242] Atomic orbital populations (AOP) can be obtained by integrating the PDOS output from $Ca_{11}Sb_{10}$ and $Ca_{11}Bi_{10}$ electronic structure calculations. This was performed for both structures and is shown in the Appendix in Figure A.30 where the greater AOP values correlate with more Bi occupancy.[244] This correlation is opposite from what is expected, however the electronegativities of Sb (Pauling 2.05) and Bi (Pauling 2.02) are relatively close.[243]

To consider the contribution of coordinated Ca atoms to the Pn sites it was predicted that the smaller, more electronegative Sb atoms would more likely occupy sites with a greater number of close Ca atoms than Bi atoms. To consider Ca-Pn bonding the average bond distance multiplied by previously AOP values and divided by the number of coordinated Ca atoms. Site occupancy versus site number with the site energy/bonding analysis can be found in Figure 6.9, where the analysis correlates well with Bi site occupancies obtained from SCXRD specifically the magnitude for Pn-2. The primary influence of this analysis versus the AOP values is the bond distance since Pn-2 has greater average bond distances (3.4 Å) than other Pn^{3-} isolated units (3.2 Å). The unexpected results obtained by comparing the AOP values with occupancy are not too surprising considering the small electronegativity difference between Sb and Bi. Similar analysis on alloys containing complex Pn were performed for Sb/As substitutions. Larger AOP values correlated with higher degrees of As substitutions which has a larger difference in electronegativity (Pauling 2.18),[243] and also displays Pn-Pn bonding.[244,245]

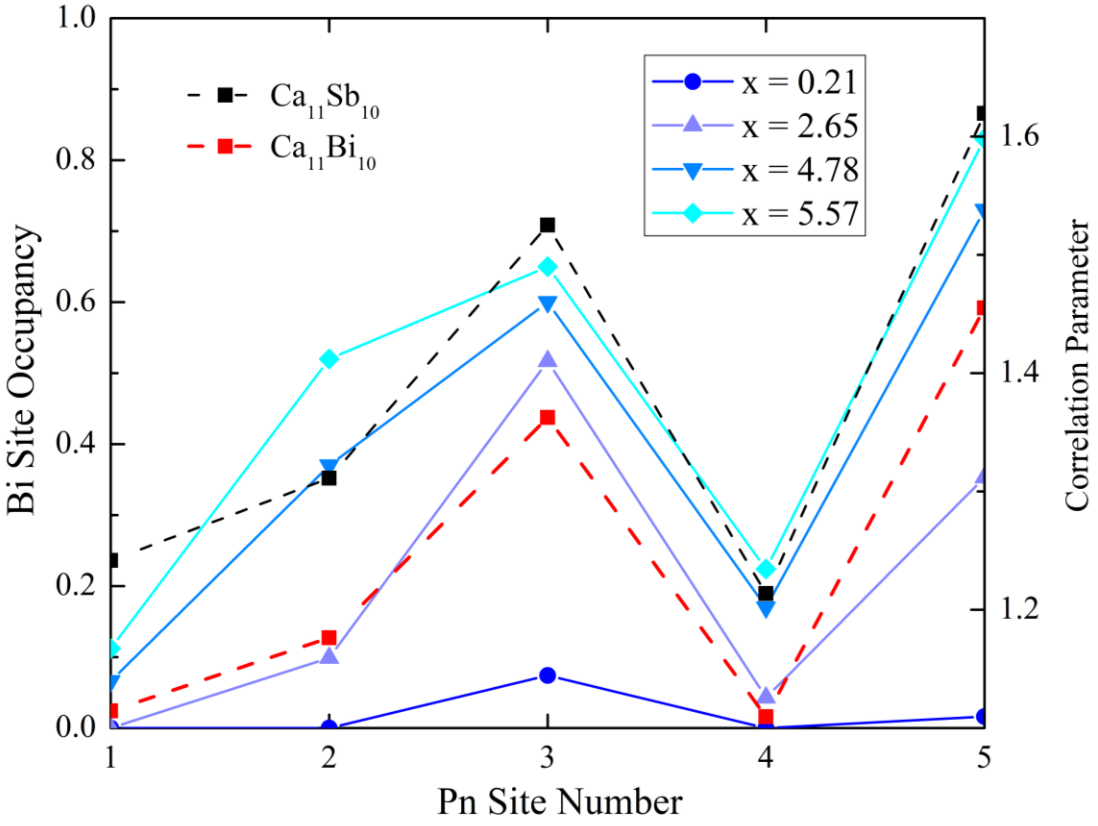

Figure 6.9: Correlation of preference of Bi site occupancy in $Ca_{11}Sb_{10-x}Bi_x$ obtained from SCXRD with parameters from DOS calculation and structural parameters for $Ca_{11}Sb_{10}$.

6.4 Thermoelectric Properties

6.4.1 Electrical Conductivity

Electrical conductivity versus temperature measurements shown in Figure 6.10 were performed on members of the $Ca_{11}Sb_{10-x}Bi_x$ (x = 0, 2, 6, and 10) series, and $Ca_{11}Sb_6As_4$ was measured as the only member of the $Ca_{11}Sb_{10-y}As_y$ series. The conductivity displays a range of values with overall increasing conductivity with increasing Bi concentration. Temperature dependence shows increasing conductivity with increasing temperature for all members of the series which suggest semiconducting behavior. The lowest values of conductivity are displayed for $Ca_{11}Sb_{10}$ which ranges from 10 S cm^{-1} at 300 K to 98 S cm^{-1} at 1000 K while $Ca_{11}Bi_{10}$ displays the largest ranging from 622 S cm^{-1} at 300 K to 696 S cm^{-1} at 615 K.

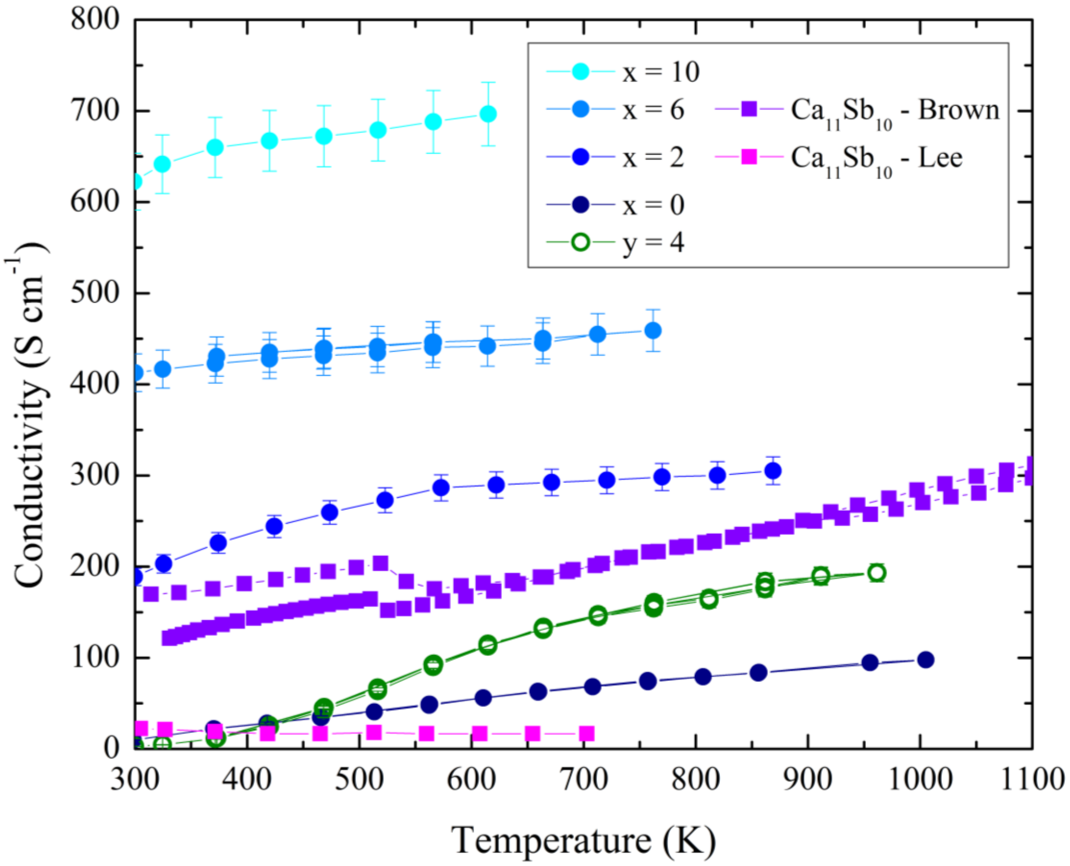

Figure 6.10: Electrical conductivity versus temperature for $Ca_{11}Sb_{10-x}Bi_x$ (x = 0, 2, 6, 10), $Ca_{11}Sb_6As_4$, and literature values for $Ca_{11}Sb_{10}$ obtained from Lee and Brown.[160,162]

Conductivity values obtained from literature are displayed for $Ca_{11}Sb_{10}$ for which the arc melted materials display lower electrical conductivity while flux synthesized materials by Brown display higher conductivity. The flux synthesized materials showed evidence of residual Sn which may account for a larger conductivity. Materials made by arc melting are anomalous as the conductivity values are low yet display a decreasing trend with temperature like that expected from metals.

$Ca_{11}Sb_6As_4$ is plotted with the other measurements for comparison which shows electrical conductivity between the Sb end member and x = 2. The large electrical conductivity was unexpected due to the greater degree of ionicity of the atomic components when compared to Sb or Bi compounds and lower density of states around the Fermi level. The compound was later found to contain a significant indication of elemental impurities as discussed previously which may account for the increased electrical conductivity in comparison with $Ca_{11}Sb_{10}$.

The Arrhenius plot of 1/T versus ln (σ) shown in Figure 6.11 was created to better understand the electrical behavior of the materials. The y-axis ln (σ) is scaled for each compound to display them within a single plot for comparison. Lower values of 1/T corresponding to higher temperatures have linear regions for x = 0, 2, and 10 and for y = 4, which may indicate intrinsic semiconducting behavior after carrier depletion. $Ca_{11}Sb_{10}$ displays linear behavior throughout most of the entire range of measured temperatures, while most other compounds display degenerate semiconducting behavior. Metallic electrical conductivity was unexpected from the DOS and BS calculations which are not in complete agreement with both literature and results found in this study.

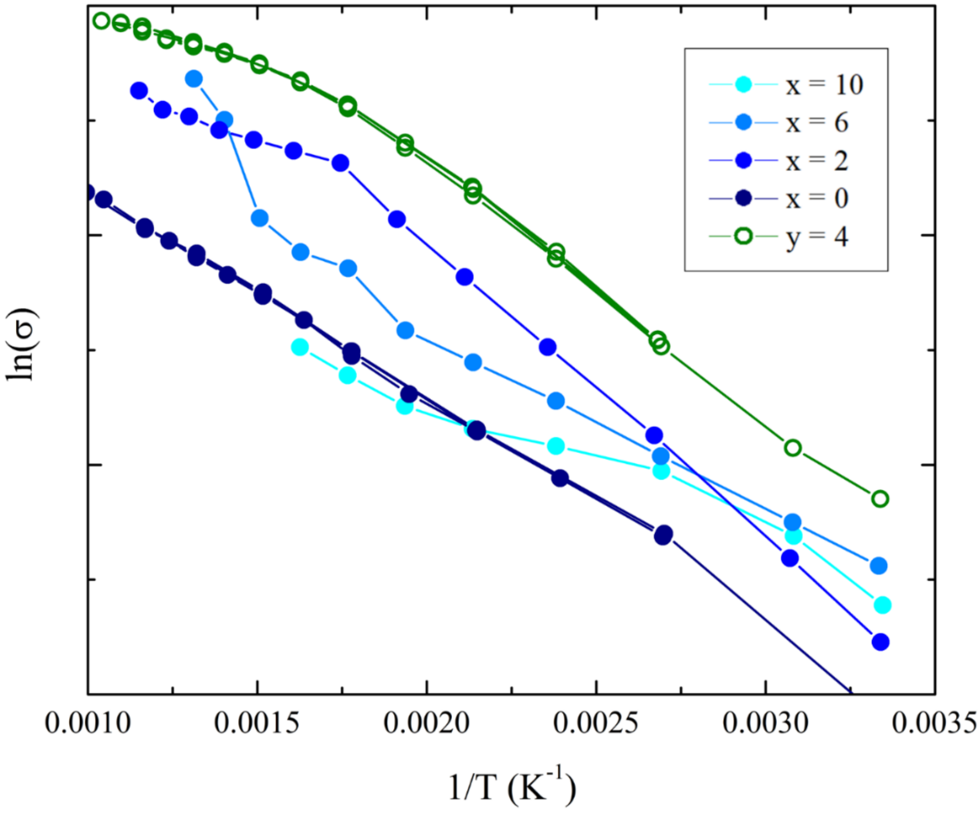

Figure 6.11: 1/T versus $ln(\sigma)$ for $Ca_{11}Sb_{10-x}Bi_x$ (x = 0, 2, 6, 10) and $Ca_{11}Sb_6As_4$ with y-axis scaled for visibility.

6.4.2 Seebeck Coefficient

Seebeck coefficient versus temperature was measured as shown in Figure 6.12 for the $Ca_{11}Sb_{1-x}Bi_x$ series (x = 0, 2, 6, and 10) and for $Ca_{11}Sb_6As_4$. Seebeck coefficients indicate p-type conductivity for x = 0, 2, and 6 with an n-type to p-type transition observed for the $Ca_{11}Bi_{10}$ material. Increasing positive values of Seebeck are observed for all $Ca_{11}Sb_{10-x}Bi_x$ materials. Seebeck values for the Sb-rich end member ranged from 19 $\mu V\ K^{-1}$ at 300 K to 80 $\mu V\ K^{-1}$ at 1000 K. Low level substitution of Bi for x = 2 decreased Seebeck resulting in 11 $\mu V\ K^{-1}$ at 300 K which increased to 31 $\mu V\ K^{-1}$ at 870 K. Further Bi substitution with x = 6 results in 0.8 $\mu V\ K^{-1}$ at 300 K to 12 $\mu V\ K^{-1}$ at 760 K. The Bi end member $Ca_{11}Bi_{10}$ displayed an n-p transition with -3.3 $\mu V\ K^{-1}$ at 300K increasing 5.5 $\mu V\ K^{-1}$ at 615 K.

$Ca_{11}As_4Sb_6$ has the largest low temperature Seebeck coefficient of 60 at 300 K which quickly decreases and levels out to 20 between 700 K and 850 K after which a slight upturn is seen between 900 K and 1000 K. The Seebeck coefficient obtained by Brown displayed an n-type to p-type transition which starts at -5 at 300 K eventually increasing to 20 at 1075 K.[160] The lower value and n-p transition may be due to the reported residual tin flux observed. In comparison the results obtained by Lee show a flatter slightly decreasing Seebeck coefficient around 20 which fits well with the electrical conductivity.[162]

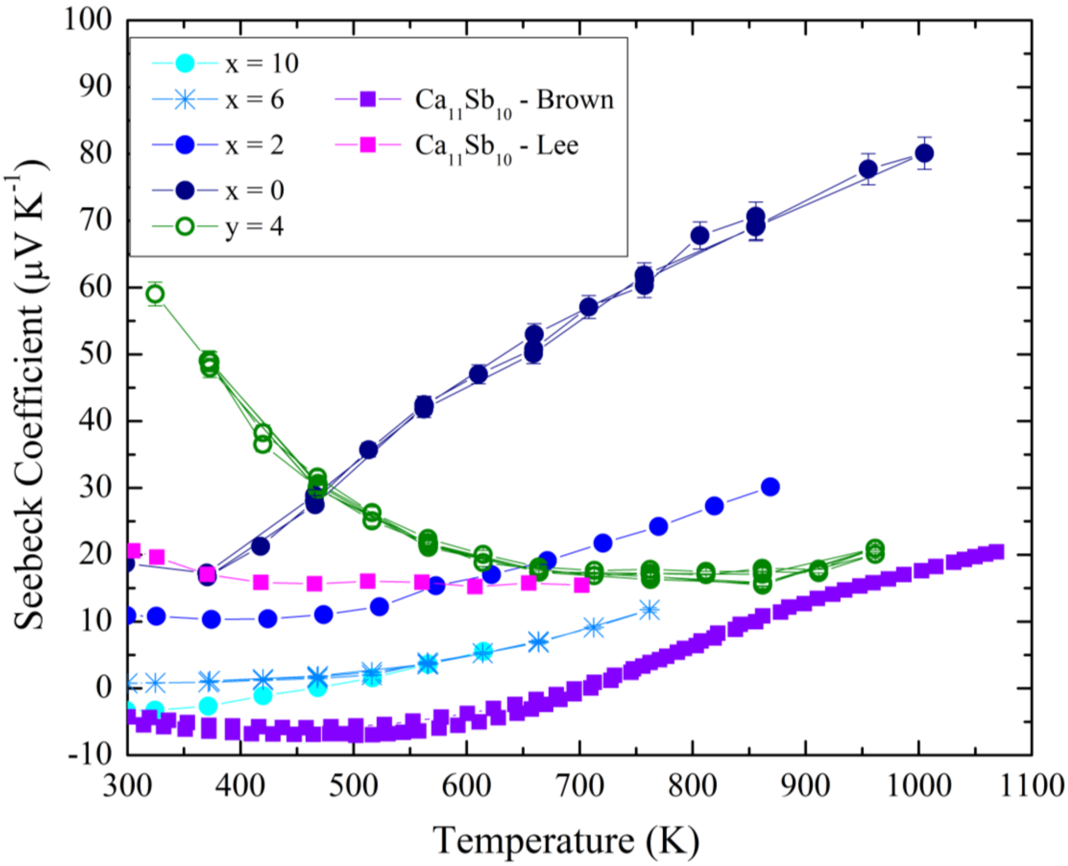

Figure 6.12: Seebeck coefficient versus temperature for $Ca_{11}Sb_{10-x}Bi_x$ series (x = 0, 2, 6, and 10), $Ca_{11}As_4Sb_6$, and literature values for $Ca_{11}Sb_{10}$ obtained from Lee and Brown.[160,162]

6.4.3 Power Factor

Power factors obtained are presented in Figure 6.13 which displays varying results for the members of the $Ca_{11}Sb_{10-x}Bi_x$ series. The largest power factors obtained are for $Ca_{11}Sb_{10}$ which starts at 0.4 μW m^{-1} K^{-2} and rapidly increases to 62 μW m^{-1} K^{-2} at 1000 K due to simultaneously increasing electrical conductivity and Seebeck coefficient. A similar increase but lower magnitude is seen for x = 2 which begins at 2.2 μW m^{-1} K^{-2} at 300 K and increases to 26 μW m^{-1} K^{-2} at 850 K. Low power factors are found for x = 6 and x = 10 due to the low Seebeck coefficient and n-p carrier transition respectively. $Ca_{11}As_4Sb_6$ also displays a low overall power factor with relatively flat temperature dependence between 0.8 μW m^{-1} K^{-2} and 7.5 μW m^{-1} K^{-2} over the temperature range. This is due to rapidly decreasing Seebeck coefficient and moderate increasing electrical conductivity with temperature.

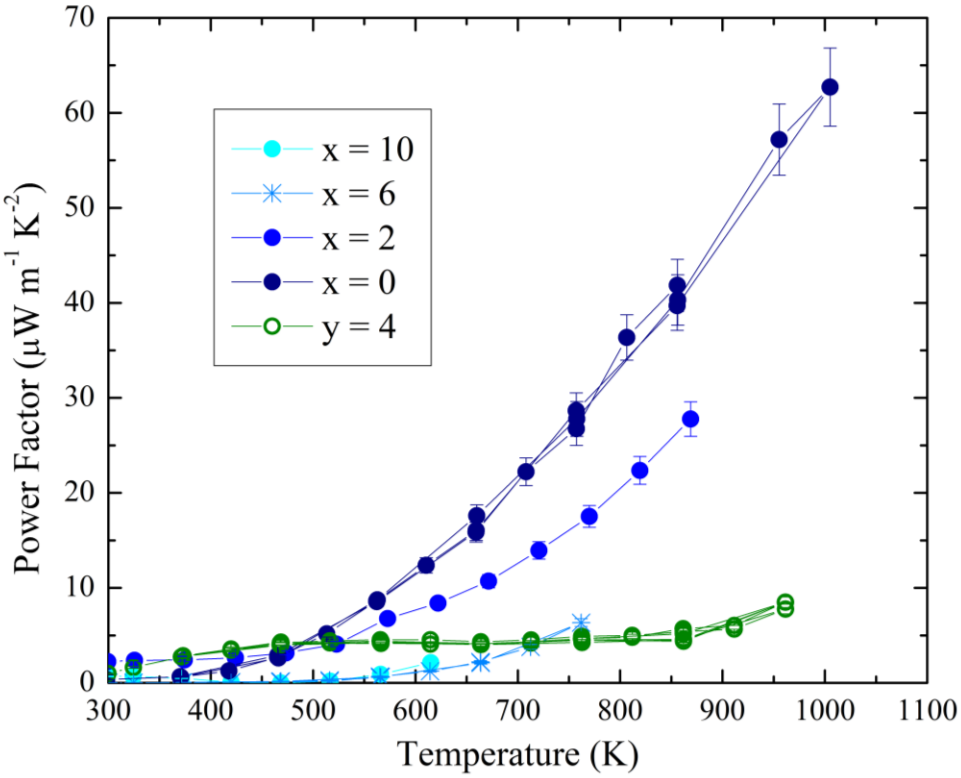

Figure 6.13: Power factor versus temperature for $Ca_{11}Sb_{10-x}Bi_x$ series (x = 0, 2, 6, 10) and $Ca_{11}As_4Sb_6$.

6.4.4 Thermal Conductivity

Thermal conductivity versus temperature was measured for $Ca_{11}Sb_{10-x}Bi_x$ (x = 0, 2, 4, 6, 10) and $Ca_{11}As_4Sb_6$ from 300K to 1050 K which is displayed in Figure 6.14 along with literature results for $Ca_{11}Sb_{10}$. The compounds display overall low TC values with the Sb rich end member display glasslike values ranging from 0.61 W m^{-1} K^{-1} at 300 K increasing slightly to 0.72 W m^{-1} K^{-1} at 1050 K. The total thermal conductivity values are found to increase with increasing Bi concentration with the $Ca_{11}Bi_{10}$ sample ranging from 0.92 W m^{-1} K^{-1} at 300 K to 2.4 W m^{-1} K^{-1} at 1050 K. $Ca_{11}Sb_{10-x}Bi_x$ samples apart from $Ca_{11}Sb_{10}$ display a linear increase in TC with increasing temperature due to the presence of charge carriers in the Bi rich samples.

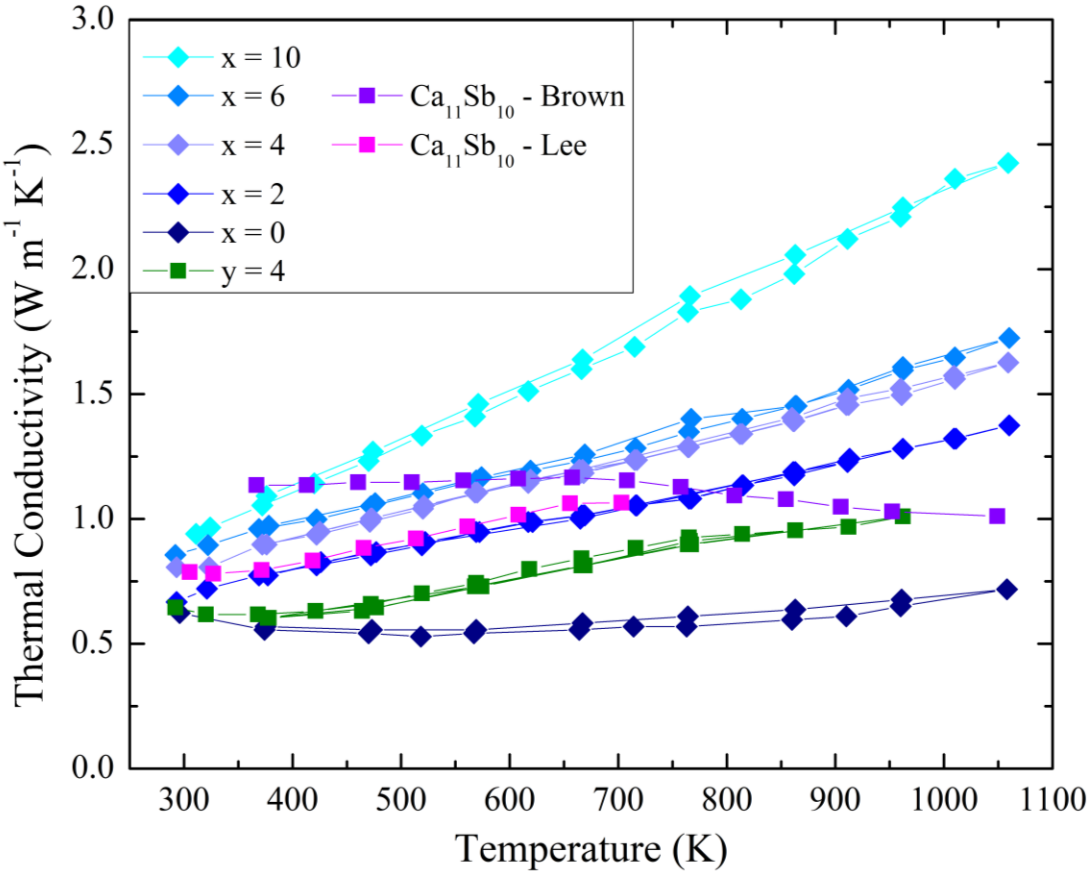

Figure 6.14: Total thermal conductivity versus temperature for $Ca_{11}Sb_{10-x}Bi_x$ series (x = 0, 2, 4, 6, 10), $Ca_{11}As_4Sb_6$, and literature values for $Ca_{11}Sb_{10}$ from Brown and Lee.[160,162]

Comparison of $Ca_{11}Sb_{10}$ samples with literature and this work display significantly different results. The samples grown by flux method (Brown) and arc melting (Lee) display larger overall thermal conductivities with a decreasing versus increasing temperature trend respectively.[160,162] At 415 K, flux grown samples displayed 1.1 W m^{-1} K^{-1} versus the ones measured here 0.55 W m^{-1} K^{-1}, while at 700 K arc melted samples displayed TC of 1.06 W m^{-1} K^{-1} versus 0.57 W m^{-1} K^{-1} obtained here. $Ca_{11}As_4Sb_6$ displayed the second lowest TC which ranged from 0.64 W m^{-1} K^{-1} at 300 K increasing to 1.0 W m^{-1} K^{-1} at 950 K.

Calculations of lattice and electrical thermal conductivities were performed using the Wiedemann-Franz law with estimates of the Lorenz number from Equation 1-58. Electrical conductivity was interpolated resulting in temperature ranges limited to those measurements. The results are displayed in Figure 6.15 for $Ca_{11}Sb_{10-x}Bi_x$ (x = 0, 2, 6, and 10) and $Ca_{11}As_4Sb_6$. The electronic TCs (triangles) increase systematically with increasing Bi concentrations as expected due to larger electrical conductivities. The As containing sample displays similar trends due to higher electrical conductivity. The lowest lattice thermal conductivity (boxes) is found in the Bi-rich end member $Ca_{11}Bi_{10}$ which displays a flat temperature dependence of 0.46 W m^{-1} K^{-1}. At low temperatures both alloyed samples display lower lattice TC than the Sb-rich end member, however $Ca_{11}Sb_{10}$ decreases from 0.60 W m^{-1} K^{-1} at 300 K to 0.47 W m^{-1} K^{-1} at 750 K before increasing very slightly at higher temperatures. Overall, none of the alloyed samples displayed lower lattice TC values which is surprising due to the expected mass fluctuation effects.

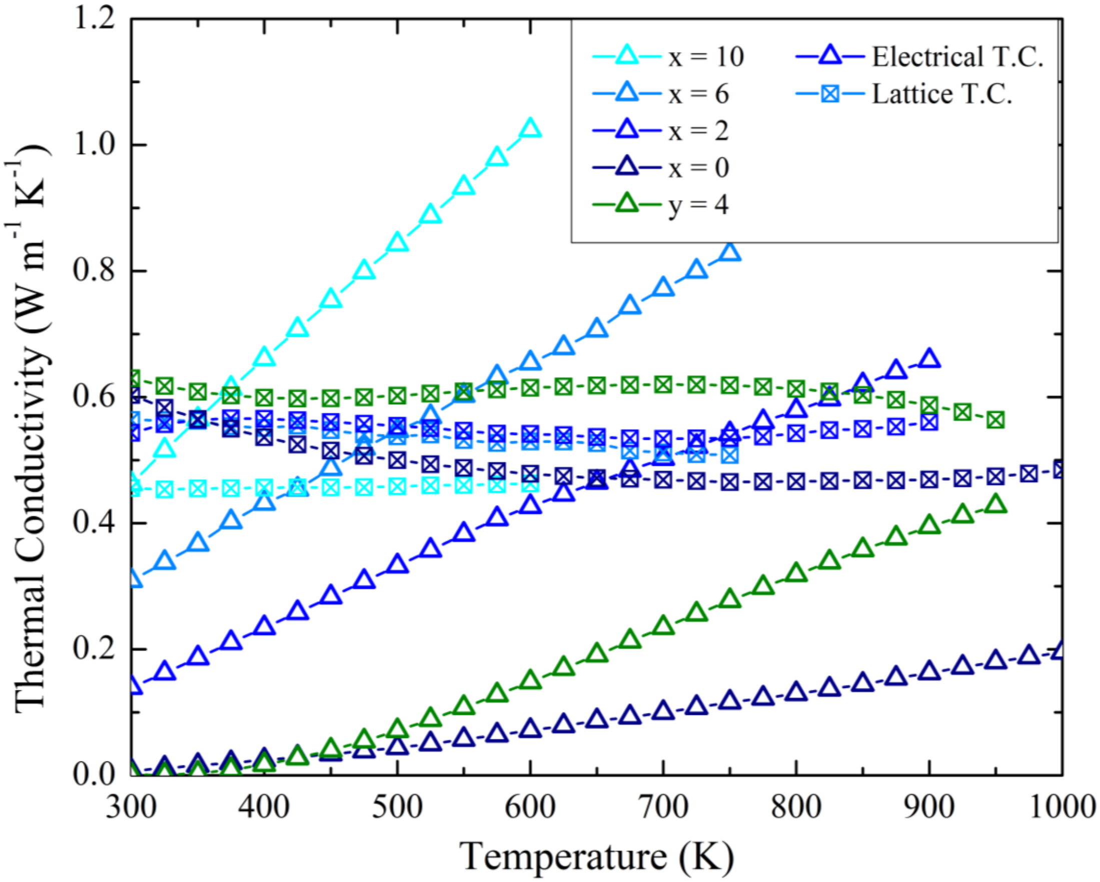

Figure 6.15: Lattice (boxes) and Electronic (triangles) components of thermal conductivity versus temperature for $Ca_{11}Sb_{10-x}Bi_x$ (x = 0, 2, 6, 10) and $Ca_{11}As_4Sb_6$.

6.4.5 Thermoelectric Figure of Merit

Values of *zT* versus temperature were obtained from interpolating relevant data which is plotted in Figure 6.16 for $Ca_{11}Sb_{10-x}Bi_x$ (x = 0, 2, 6, and 10) and $Ca_{11}As_4Sb_6$. The obtained values display similar trends to the power factors with $Ca_{11}Sb_{10}$ becoming much larger than the other measured samples due to overall lower thermal conductivity values. At 300 K $zT = 1\cdot10^{-3}$ which rapidly increases to 0.093 at 1000 K due to simultaneous increase in Seebeck coefficient and electrical conductivity while thermal conductivity remains relatively flat. The Sb rich solid solution x = 2 displays the second best *zT* which reaches a maximum of 0.02 at 850 K.

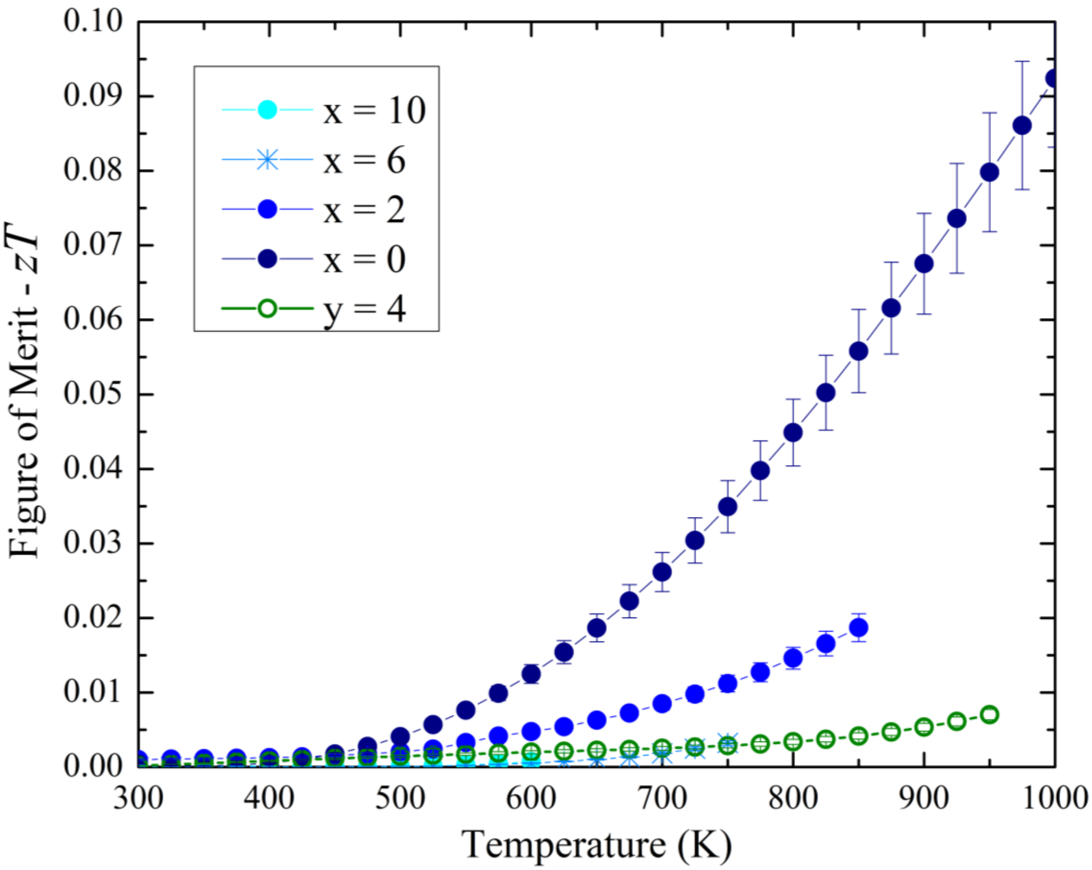

Figure 6.16: Figure of Merit versus temperature for the $Ca_{11}Sb_{10-x}Bi_x$ (x = 0, 2, 6, 10) series, Se-doped $Ca_{11}Sb_{9.7}Se_{0.3}$, and $Ca_{11}Sb_6As_4$ materials. The Sb rich end member displays the largest figure of merit *zT* = 0.093 at 1000 K.

6.5 Conclusion

The direct liquid-solid synthesis method applied in this study was shown to successfully produce solid solutions of $Ca_{11}Sb_{10-x}Bi_x$ and $Ca_{11}Sb_{10-y}As_y$. Some elemental impurities were identified in both sets of solid solutions, with CaAs impurities when attempting synthesis of $Ca_{11}As_{10}$. Refined synthesis procedures were likely needed for more consistent results. The material produced from the direct synthesis approach is brittle and therefore easily crushed in comparison with malleable calcium metal. Ball milling techniques in conjunction with the described direct synthesis procedures would be an interesting process for future exploration of these materials. Forming solid solutions of incongruently melting and congruently melting compounds was shown to be achievable with milling techniques in Chapter 4. Since $Ca_{11}Sb_{10}$ is congruently melting and $Ca_{11}Bi_{10}$ is incongruently melting milling approaches would be an interesting synthesis avenue to explore for these solid solutions. Extensive alloying of $Ca_{11}Sb_{10-y}As_y$ was achieved despite synthetic hurdles which provides another avenue of exploration of this interesting class of materials.

Electronic structure calculations predicted metallic properties from all synthesized materials which did not agree well with measured semiconducting properties. The materials are charge balanced through Zintl formalism and therefore semiconducting properties are a reasonable result. The density of states crossing the Fermi level increased with increasing pnictide mass which correlated well with conductivity measurements of the solid solutions where conductivity increased with increasing Bi concentration. Evidence of bipolar conductivity was present for all the compounds studied which. Previous studies of $Ca_{11}Bi_{10}$ found the structure was stable while deficient in Bi atoms which gave rise to metallic properties and superconductivity. The preferential substitutions of the pnictide sites were studied with SCXRD and electronic structure calculations. The preference of Bi substitution on higher energy sites was observed with most of the preference for sites participating in Pn-Pn bonding. The preferred Bi substitution may have potential use for developing the material as a superconductor as the activity occurs at the Fermi level.

The thermoelectric properties of the end member $Ca_{11}Sb_{10}$ were the most promising of all the studied materials. A simultaneous increase in electrical conductivity and Seebeck coefficient with temperature was an interesting result which was highly beneficial to thermoelectric performance. Decreasing lattice thermal conductivity with temperature was also observed at intermediate temperatures improving performance further. The origin of these effects may be tied to the Sb-Sb bonding and their vibrational modes. The Pn-3 site has large thermal displacement parameters which may be indicative of rattling effects particularly at higher temperatures. Rattling of atoms has been shown to create localized charge deficiencies which would create acceptor states leading to a p-type doping effect. In the case of $Ca_{11}Sb_{10}$, the Ca electrons would compensate for the Sb charge deficiency; increasing hole concentration, suppressing bipolar conductivity, and simultaneously increase Seebeck coefficient and electrical conductivity. Phonon dispersion relations can be examined further using first principles methods which may provide valuable insight into this phenomenon.[246] This effect was observed in all $Ca_{11}Sb_{10-x}Bi_x$ materials studied.

The reduction in lattice thermal conductivity with temperature for $Ca_{11}Sb_{10}$ would also be explained with a rattling effect as low frequency phonons modes would dissipate lattice energy. Low overall thermal conductivity resembles PGEC concept which arises from the complex crystal structure. Reduction of lattice thermal conductivity by alloying was not achieved, however direct measurements were not performed. The compounds possibly deviate from Wiedemann-Franz law or calculation of the Lorenz number by the applied method. The end member $Ca_{11}Sb_{10}$ displays promising thermoelectric performance for an unoptimized material. Insights into the variability of properties based on different synthesis methods were obtained suggesting underlying material complexities which may be exploited for property enhancement.

Chapter 7: Summary and Outlook

The goal of this body of work has been to understand and develop solid solutions as thermoelectric materials. Properties influencing the performance of TE materials are discussed with focus on principles for optimization. The importance of carrier concentration is highlighted from this discussion as a primary influence on electrical conductivity, Seebeck coefficient, and electronic thermal conductivity. Degenerate semiconductors are identified as the material of choice due to the opposing influence of charge carriers on key properties. Electronic band structure and density of states are shown to influence charge carrier concentration as well as carrier mobility and Seebeck coefficient through effective carrier mass. Band degeneracies are identified as beneficial for thermoelectric properties and strategies to engineer them are discussed. Thermal conductivity and importantly lattice thermal conductivity is presented as a key property which can be reduced using a variety of strategies with little negative influencing other properties. Solid solutions are shown to be a class of materials which can be used to optimize thermoelectric properties. Carrier concentration, carrier effective mass, and lattice thermal conductivity can all be positively influenced by utilization of the outlined solid solution engineering strategies. The methods utilized for the thermoelectric studies within this work are outlined before presenting the experimental results and discussions.

Chapter 3 presents a large-scale method employed for the synthesis of established thermoelectric solid solution $Mg_2Si_{0.3}Sn_{0.67}Bi_{0.03}$. An in-house reactor system was developed for high through-put synthesis of the material. The material was then pressed on a large scale and the thermoelectric properties were studied. The methods developed produced a consistent high performing thermoelectric material as shown by statistical analysis. The average zT of over 1 kg of material produced was 1.2 at 773 K which shows the viability of this process for large scale manufacturing and eventual device application.

Chapter 4 explored the wide band gap solid solutions $ZnGe_{1-x}Sn_xP_2$ for development of pnictide based chalcopyrite thermoelectric materials. A synthetic method was developed which produced full miscibility of the differently melting end members. The structures were studied and indicated a preference towards tetragonality which is expected to be beneficial for TE properties. Electronic structure calculations were performed on end members and hypothetical alloy configurations. For samples with higher tetragonality, BoltzTraP calculation of electronic properties showed that p-type carriers are expected to have better thermoelectric performance than n-type carriers, due to greater band valley convergences in the valence band edge versus the conduction band edge. Thermoelectric property measurements were limited to elevated temperatures as the samples displayed low electrical conductivities. Improvements to TE performance was achieved through alloying for both the power factors and thermal conductivity when compared to the end members. Larger Ge concentration was also found to increase thermal stability of the compounds allowing for higher maximum performance. Extensive milling was also shown to drastically reduce the thermal conductivity values to more than half of those found by standard milling techniques. It was concluded from this study that higher carrier concentration and doping would be needed for improving the TE properties.

Chapter 5 extended the exploration of pnictide chalcopyrite solid solution thermoelectric materials, with the goal of increasing carrier concentrations. Arsenic substitution was explored by employing the synthesis techniques developed in Chapter 4. The materials studied for TE properties were $ZnGe_{1-x}Sn_xP_{2-y}As_y$ with x = 0.5, 0.75, 1; and y = 0.5, 1, 1.5, and 2. The study found improvements to electrical conductivity with As substitution, however bipolar conduction of As rich members resulted in moderate improvements to TE properties. Changes in carrier concentrations could be studied for these materials with Hall effect measurements. The rapid increase in Seebeck coefficient with increasing n-type behavior for $ZnSnAs_2$ which displays the viability of n-type doping for these materials. The milling techniques were found to successfully synthesize quinary solid solutions which is a novel result for this class of materials. Improvements to all key thermoelectric properties are seen by maintained high Seebeck coefficient, electrical conductivity and further reduction of thermal conductivity resulting in $zT = 0.034$ at 700 K for $ZnGe_{0.5}Sn_{0.5}P_{1.5}As_{0.5}$. Incomplete study of the $ZnGe_{0.25}Sn_{0.75}P_{2-y}As_y$ series was performed which displayed further reduction of TC and is expected produce higher Seebeck coefficients due to greater tetragonality. The improvements resemble results found for materials characterized as high entropy alloys (HEA) which have been shown to produce promising TE performance. The results uncovered in this chapter provide an impetus for more extensive alloying and doping for pnictide chalcopyrite materials. Unexplored series for ABC_2 includes A = Cd, B = Si, Mg, and C = Sb which gives rise to potential six-component systems. Dopants are available for both types with n-type doping of S, Se, and Te for C-site, or compatible M^{3+} atoms for A-site; while p-type dopants include Cu or Ag on A-site, and Al, Ga, or In on B-site. The ball milling technique developed was shown to be a powerful tool for development of solid solutions and therefore may be viable for these further explorations.

The chalcopyrite materials explored in Chapters 4 and 5 showed interesting potential as thermoelectric materials. Broader findings of these studies on solid solution semiconductors offer applications beyond thermoelectrics. Chalcopyrites have been studied previously for their promise as second harmonic generation materials, and band gap control such as shown in Chapter 5, is important for tuning materials towards specific applications. Tuning of band gaps for energy absorption in photovoltaics is also important, as harvesting a broad spectrum of radiation is key for efficient solar cell application. High entropy alloy (HEA) materials are quickly becoming a topic of interest in solid state sciences, where little focus has been on high entropy semiconducting materials. As mentioned previously the unexplored potential of multiple mixed sites within these materials gives rise to a pathway for formation of HEA materials. HEA properties have been shown beneficial for thermoelectric applications; however, the emergence of alternative properties is possible. Further experimental studies of these chalcopyrite solid solutions are warranted. Charge carrier concentration and carrier mobility are important to consider for TE applications and beyond. Hall transport measurements would provide a deeper insight into the effects of solid solution formation has on these properties. Physical properties such as the thermal stability of these materials were observed to be sensitive to substitution levels. Experiments such as differential scanning calorimetry (DSC) would be informative for synthesis, solid solution effects on stability, and application within devices. Mechanical properties are often overlooked in the study of thermoelectric materials; however, the formation of solid solutions would likely influence these properties as well.

Finally, Chapter 6 was focused on the $Ca_{11}Sb_{10-x}Bi_x$ and $Ca_{11}Sb_{10-y}As_y$ series as thermoelectric materials. Successful synthesis was achieved for only some members of the solid solution series, while others showed signs of elemental impurities in the PXRD and by degrading at ambient conditions. There were signs of elemental impurities for $x = 2$ and $x = 10$ and in all samples for the $Ca_{11}Sb_{10-y}As_y$ series. Majority peaks resembling the target phase was achieved for As rich $y = 6$, which was unprecedented as As was not known to be stable in these structures. A direct liquid solid synthesis method was utilized, which due to the differing melting behaviors of the end members was unlikely to achieve full miscibility. The ball milling methods developed in previous chapters would be difficult to apply to such a calcium rich compound as softer metals do not crush easily. The liquid solid synthesis however, produced an embrittled ingot in all cases, which would likely contain a small enough portion of elemental Ca to further process via ball milling. SCXRD of single crystals extracted from the ingots was performed and refined structures were obtained. A trend of preferred occupancy was observed for samples of various Bi concentration, and along with electronic structure calculations a correlation parameter was found to predict the trend well. Electronic transport measurements indicated semiconducting behavior with signs of bipolar conductivity which result in low Seebeck coefficients. A simultaneous increase in temperature and Seebeck coefficients with temperature indicate underlying structural complexities which suppresses bipolar conductivity with increasing temperature. Comparison of the properties of the end member $Ca_{11}Sb_{10}$ with those from literature identifies inconsistencies which may be the result of different synthesis methods. Thermoelectric performance was moderate and promising for an unoptimized material displaying $zT = 0.093$ at 1000 K. This class of materials is very interesting, especially with the introduction of the newly discovered $Ca_{11}As_{10}$ which provides more avenues for optimization and tuning of properties.

References

1. *Thermoelectrics Handbook: Macro to Nano*. *Thermoelectrics Handbook Macro to Nano* (CRC Press, Taylor & Francis Group, 2005).
2. Beretta, D., Neophytou, N., Hodges, J. M., Kanatzidis, M. G., Narducci, D., Martin-Gonzalez, M., Beekman, M., Balke, B., Cerretti, G., Tremel, W., Zevalkink, A., Hofmann, A. I., Müller, C., Dörling, B., Campoy-Quiles, M., *et al.* Thermoelectrics: From History, a Window to the Future. *Mat Sci Eng R* **138**, 210–255 (2019).
3. He, J. & Tritt, T. M. Advances in Thermoelectric Materials Research: Looking Back and Moving Forward. *Science* **357**, 1–9 (2017).
4. Ioffe, A. F., Stil'bans, L. S., Iordanishvili, E. K. & Stavitskaya, T. S. *Semiconductor Thermoelements and Thermoelectric Cooling*. (Infosearch Ltd., 1957).
5. Francioso, L., De Pascali, C., Farella, I., Martucci, C., Cret, P., Siciliano, P. & Perrone, A. Flexible Thermoelectric Generator for Ambient Assisted Living Wearable Biometric Sensors. *J Power Sources* **196**, 3239–3243 (2011).
6. Suarez, F., Nozariasbmarz, A., Vashaee, D. & Öztürk, M. C. Designing Thermoelectric Generators For Self-Powered Wearable Electronics. *Energy Environ Sci* **9**, 2099–2113 (2016).
7. Yang, Y., Wei, X. J. & Liu, J. Suitability of a Thermoelectric Power Generator for Implantable Medical Electronic Devices. *J Phys D Appl Phys* **40**, 5790–5800 (2007).
8. Bell, L. E. Cooling, Heating, Generating Power, and Recovering Waste Heat with Thermoelectric Systems. *Science* **321**, 1457–1461 (2008).
9. Sharma, S., Dwivedi, V. K. & Pandit, S. N. A Review of Thermoelectric Devices for Cooling Applications. *Int J Green Energy* **11**, 899–909 (2014).
10. Dai, Y. J., Wang, R. Z. & Ni, L. Experimental Investigation on a Thermoelectric Refrigerator Driven By Solar Cells. *Renew Energy* **28**, 949–959 (2003).

11. Hamid Elsheikh, M., Shnawah, D. A., Sabri, M. F. M., Said, S. B. M., Haji Hassan, M., Ali Bashir, M. B. & Mohamad, M. A Review on Thermoelectric Renewable Energy: Principle Parameters That Affect Their Performance. *Renewable and Sustainable Energy Reviews* **30**, 337–355 (2014).
12. Mao, J., Liu, Z., Zhou, J., Zhu, H., Zhang, Q., Chen, G. & Ren, Z. Advances in Thermoelectrics. *Adv Phys* **67**, 69–147 (2018).
13. Kittel, C. *Introduction to Solid State Physics*. (Wiley, 1996).
14. Ashcroft, N. W. & Mermin, N. D. *Solid State Physics*. (Rinehart and Winston, 1975).
15. West, A. R. *Solid State Chemistry and its Applications*. *Acta Crystallographica Section B Structural Science* (John Wiley and Sons, Ltd, 2014).
16. Snyder, G. J. & Toberer, E. S. Complex thermoelectric materials. *Nat Mater* **7**, 105–114 (2008).
17. Antonov, V., Harmon, B. & Yaresko, A. *Electronic Structure and Magneto-Optical Properties of Solids*. (Kluwer Academic Publishers, 2004).
18. Schwarz, K. DFT calculations of solids with LAPW and WIEN2k. *J Solid State Chem* **176**, 319–328 (2003).
19. Lee, P. M. Electronic Structure of Magnesium Silicide and Magnesium Germanide. *Physical Review* **135**, 1110–1114 (1964).
20. Seeger, K. *Semiconductor Physics*. (Springer, 1991).
21. Nebel, C. E. Electrons Dance in Diamond. *Nat Mater* **12**, 690–691 (2013).
22. Wood, C. Materials for Thermoelectric Energy Conversion. *Reports on Progress in Physics* **51**, 459–539 (1988).
23. Kim, H. S., Gibbs, Z. M., Tang, Y., Wang, H. & Snyder, G. J. Characterization of Lorenz Number with Seebeck Coefficient Measurement. *APL Mater* **3**, 041506/1–5 (2015).
24. Flage-Larsen, E. & Prytz. The Lorenz Function: Its Properties at Optimum Thermoelectric Figure-of-Merit. *Appl Phys Lett* **99**, 202108/1–3 (2011).

25. Franz, R. & Wiedemann, G. Ueber die Wärme-Leitungsfähigkeit der Metalle. *Ann Phys* **165**, 497–531 (1853).

26. Sze, S. M. & Ng, K. K. *Physics of Semiconductor Devices*. (Wiley-Interscience, 2007).

27. Fistul, V. *Heavily Doped Semiconductors*. (Plenum Press, 1969).

28. Blakemore, J. S. & Henisch, H. K. *Semiconductor Statistics: International Series of Monographs on Semiconductors*. (Elsevier Science, 2016).

29. Reif-Acherman, S. Augustus Matthiessen: His Studies on Electrical Conductivities and the Origins of His 'Rule'. *Proceedings of the IEEE* **103**, 713–721 (2015).

30. Mott, N. F. The Conduction Band in Non-Crystalline Semiconductors. *Philosophical Magazine B* **58**, 369–384 (1988).

31. Zevalkink, A., Smiadak, D. M., Blackburn, J. L., Ferguson, A. J., Chabinyc, M. L., Delaire, O., Wang, J., Kovnir, K., Martin, J., Schelhas, L. T., Sparks, T. D., Kang, S. D., Dylla, M. T., Snyder, G. J., Ortiz, B. R., *et al.* A Practical Field Guide to Thermoelectrics: Fundamentals, Synthesis, and Characterization. *Appl Phys Rev* **5**, 021303/1–50 (2018).

32. Pei, Y., Wang, H. & Snyder, G. J. Band Engineering of Thermoelectric Materials. *Advanced Materials* **24**, 6125–6135 (2012).

33. Wu, D., Zhao, L. D., Tong, X., Li, W., Wu, L., Tan, Q., Pei, Y., Huang, L., Li, J. F., Zhu, Y., Kanatzidis, M. G. & He, J. Superior Thermoelectric Performance in PbTe-PbS Pseudo-Binary: Extremely Low Thermal Conductivity and Modulated Carrier Concentration. *Energy Environ Sci* **8**, 2056–2068 (2015).

34. Heremans, J. P., Jovovic, V., Toberer, E. S., Saramat, A., Kurosaki, K., Charoenphakdee, A., Yamanaka, S. & Snyder, G. J. Enhancement of Thermoelectric Efficiency in PbTe by Distortion of the Electronic Density of States. *Science* **321**, 554–557 (2008).

35. Suwardi, A., Cao, J., Zhao, Y., Wu, J., Chien, S. W., Tan, X. Y., Hu, L., Wang, X., Wang, W., Li, D., Yin, Y., Zhou, W. X., Repaka, D. V. M., Chen, J., Zheng, Y., *et al.* Achieving High Thermoelectric Quality Factor Toward High Figure of Merit in GeTe. *Materials Today Physics* **14**, 100239/1–9 (2020).

36. Liu, W., Tan, X., Yin, K., Liu, H., Tang, X., Shi, J., Zhang, Q. & Uher, C. Convergence of Conduction Bands as a Means of Enhancing Thermoelectric Performance of n-type $Mg_2Si_{1-x}Sn_x$ Solid Solutions. *Phys Rev Lett* **108**, 166601/1–5 (2012).

37. Pei, Y., Shi, X., Lalonde, A., Wang, H., Chen, L. & Snyder, G. J. Convergence of Electronic Bands for High Performance Bulk Thermoelectrics. *Nature* **473**, 66–69 (2011).

38. Zeier, W. G., Zhu, H., Gibbs, Z. M., Ceder, G., Tremel, W. & Snyder, G. J. Band Convergence in the Non-Cubic Chalcopyrite Compounds Cu_2MGeSe_4. *J Mater Chem C Mater* **2**, 10189–10194 (2014).

39. Kim, C. E., Soon, A. & Stampfl, C. Unraveling the Origins of Conduction Band Valley Degeneracies in $Mg_2Si_{1-x}Sn_x$ Thermoelectrics. *Physical Chemistry Chemical Physics* **18**, 939–946 (2015).

40. McKinney, R. W., Gorai, P., Stevanovic, V. & Toberer, E. Search for New Thermoelectric Materials with Low Lorenz Number. *J Mater Chem A* **5**, 17302–17311 (2017).

41. Borup, K. A., de Boor, J., Wang, H., Drymiotis, F., Gascoin, F., Shi, X., Chen, L., Fedorov, M. I., Müller, E., Iversen, B. B. & Snyder, G. J. Measuring Thermoelectric Transport Properties of Materials. *Energy Environ Sci* **8**, 423–435 (2015).

42. Wang, H., Porter, W. D., Böttner, H., König, J., Chen, L., Bai, S., Tritt, T. M., Mayolett, A., Senawiratne, J., Smith, C., Harris, F., Gilbert, P., Sharp, J. W., Lo, J., Kleinke, H., *et al.* Transport Properties of Bulk Thermoelectrics: An International Round-Robin Study, Part II: Thermal Diffusivity, Specific Heat, and Thermal Conductivity. *J Electron Mater* **42**, 1073–1084 (2013).

43. Slack, G. A. Nonmetallic Crystals with High Thermal Conductivity. *Journal of Physics and Chemistry of Solids* **34**, 321–335 (1973).

44. Klemens, P. G. The Thermal Conductivity of Dielectric Solids at Low Temperatures. *Proc R Soc Lond A Math Phys Sci* **208**, 108–133 (1951).

45. Klemens, P. G. Thermal Conductivity and Lattice Vibrational Modes. *Solid State Physics - Advances in Research and Applications* **7**, 1–98 (1958).

46. Klemens, P. G. The Scattering of Low-Frequency Lattice Waves by Static Imperfections. *Proceedings of the Physical Society. Section A* **68**, 1113–1128 (1955).

47. Chen, Z., Zhang, X. & Pei, Y. Manipulation of Phonon Transport in Thermoelectrics. *Advanced Materials* **30**, 1705617/1–12 (2018).

48. Feng, T., Lindsay, L. & Ruan, X. Four-Phonon Scattering Significantly Reduces Intrinsic Thermal Conductivity of Solids. *Phys Rev B* **96**, 161201(R)/1–6 (2017).

49. Grüneisen, E. Theorie des Festen Zustandes Einatomiger Elemente. *Ann Phys* **344**, 257–306 (1912).

50. Callister, W. D. *Material Science and Engineering: An Introduction*. (John Wiley & Sons, Inc., 2007).

51. Ramirez, D. C., Macario, L. R., Cheng, X., Cino, M., Walsh, D., Tseng, Y. C. & Kleinke, H. Large Scale Solid State Synthetic Technique for High Performance Thermoelectric Materials: Magnesium-Silicide-Stannide. *ACS Appl Energy Mater* **3**, 2130–2136 (2020).

52. Vegard, L. Die Konstitution der Mischkristalle und die Raumfüllung der Atome. *Zeitschrift für Physik* **5**, 17–26 (1921).

53. Magomedov, M. N. On the Deviation from the Vegard’s Law for the Solid Solutions. *Solid State Commun* **322**, 114060/1–5 (2020).

54. Tsai, M. H. & Yeh, J. W. High-Entropy Alloys: A Critical Review. *Mater Res Lett* **2**, 107–123 (2014).

55. Tsai, M. H. Physical Properties of High Entropy Alloys. *Entropy* **15**, 5338–5345 (2013).

56. Singh, A. K. & Subramaniam, A. On the Formation of Disordered Solid Solutions in Multi-Component Alloys. *J Alloys Compd* **587**, 113–119 (2014).

57. Fan, Z., Wang, H., Wu, Y., Liu, X. & Lu, Z. Thermoelectric Performance of PbSnTeSe High-Entropy Alloys. *Mater Res Lett* **5**, 187–194 (2017).

58. Karati, A., Nagini, M., Ghosh, S., Shabadi, R., Pradeep, K. G., Mallik, R. C., Murty, B. S. & Varadaraju, U. v. $Ti_2NiCoSnSb$ - A New Half-Heusler Type High-Entropy Alloy

Showing Simultaneous Increase in Seebeck Coefficient and Electrical Conductivity for Thermoelectric Applications. *Sci Rep* **9**, 1–12 (2019).

59. Fan, Z., Wang, H., Wu, Y., Liu, X. J. & Lu, Z. P. Thermoelectric High-Entropy Alloys with Low Lattice Thermal Conductivity. *RSC Adv* **6**, 52164–52170 (2016).

60. Miller, G. J. The 'Coloring Problem' in Solids: How It Affects Structure, Composition and Properties. *Eur J Inorg Chem* 523–536 (1998).

61. Ponou, S. & Fässler, T. F. Nonclassical Bonding in the Novel Structure of Ba_2Bi_3 and Unexpected Site Preference in the Coloring Variant Ba_2BiSb_2. *Inorg Chem* **43**, 6124–6126 (2004).

62. Kanatzidis, M. G., Pöttgen, R. & Jeitschko, W. The Metal Flux: A Preparative Tool for the Exploration of Intermetallic Compounds. *Angew Chem Int Ed* **44**, 6996–7023 (2005).

63. Baláž, M. Mechanochemistry. in *Environmental Mechanochemistry* 1–52 (Springer International Publishing, 2021).

64. Grigorieva, T. F., Barinova, A. P. & Lyakhov, N. Z. Mechanochemical Synthesis of Intermetallic Compounds. *Usp Khim* **70**, 65–71 (2001).

65. Michalchuk, A. A. L., Boldyreva, E. V., Belenguer, A. M., Emmerling, F. & Boldyrev, V. V. Tribochemistry, Mechanical Alloying, Mechanochemistry: What is in a Name? *Front Chem* **9**, 685789/1–29 (2021).

66. Takacs, L. The Historical Development of Mechanochemistry. *Chem Soc Rev* **42**, 7649–7659 (2013).

67. Alrbaihat, M., Khalil Al-Zeidaneen, F. & Abu-Afifeh, Q. Reviews of the Kinetics of Mechanochemistry: Theoretical and Modeling Aspects. *Mater Today Proc* **65**, 3651–3656 (2022).

68. Baláž, P. *Mechanochemistry in Nanoscience and Minerals Engineering*. (Springer, 2008).

69. Zhang, L., Xiao, P., Shi, L., Henkelman, G., Goodenough, J. B. & Zhou, J. Suppressing the Bipolar Contribution to the Thermoelectric Properties of $Mg_2Si_{0.4}Sn_{0.6}$ by Ge Substitution. *J Appl Phys* **117**, 155103/1–11 (2015).

70. Kim, S. il, Lee, K., Mun, H., Kim, H., Hwang, S., Roh, J., Yang, D., Shin, W., Li, X., Lee, Y., Snyder, J. & Kim, S. Dense Dislocation Arrays Embedded Ingrain Boundaries for High-Performance Bulk Thermoelectrics. *Science* **348**, 109–114 (2015).

71. Han, C., Sun, Q., Li, Z. & Dou, S. X. Thermoelectric Enhancement of Different Kinds of Metal Chalcogenides. *Adv Energy Mater* **6**, 1600498/1–36 (2016).

72. Hong, M., Chen, Z. G. & Zou, J. Fundamental and Progress of Bi_2Te_3-Based Thermoelectric Materials. *Chinese Physics B* **27**, 1–25 (2018).

73. Hu, L., Zhu, T., Liu, X. & Zhao, X. Point Defect Engineering of High-Performance Bismuth-Telluride-Based Thermoelectric Materials. *Adv Funct Mater* **24**, 5211–5218 (2014).

74. LaLonde, A. D., Pei, Y., Wang, H. & Snyder, J. Lead Telluride Alloy Thermoelectrics. *Materials Today* **14**, 526–532 (2011).

75. Hsu, K. F., Loo, S., Guo, F., Chen, W., Dyck, J. S., Uher, C., Hogan, T., Polychroniadis, E. & Kanatzidis, M. Cubic $AgPb_mSbTe_{2+m}$: Bulk Thermoelectric Materials with High Figure of Merit. *Science* **303**, 818–820 (2004).

76. Zhang, Q., Wang, H., Liu, W., Wang, H., Yu, B., Zhang, Q., Tian, Z., Ni, G., Lee, S., Esfarjani, K., Chen, G. & Ren, Z. Enhancement of Thermoelectric Figure-of-Merit by Resonant States of Aluminium Doping in Lead Selenide. *Energy Environ Sci* **5**, 5246–5251 (2012).

77. Zhao, L. D., Lo, S. H., Zhang, Y., Sun, H., Tan, G., Uher, C., Wolverton, C., Dravid, V. P. & Kanatzidis, M. G. Ultralow Thermal Conductivity and High Thermoelectric Figure of Merit in SnSe Crystals. *Nature* **508**, 373–377 (2014).

78. Duong, A. T., Nguyen, V. Q., Duvjir, G., Duong, V. T., Kwon, S., Song, J. Y., Lee, J. K., Lee, J. E., Park, S., Min, T., Lee, J., Kim, J. & Cho, S. Achieving ZT = 2.2 with Bi-doped n-Type SnSe Single Crystals. *Nat Commun* **7**, 13713/1–6 (2016).

79. Kim, J. H. & Rhyee, J. S. Enhancement of the Thermoelectric Properties in a Mid-Temperature Range in a Phase-Separated $In_4Se_{3-x}Cl_y/BaIn_2Se_4$ Composite. *Electronic Mater Lett* **10**, 801–805 (2014).

80. Heyding, R. D. & Maclaren Murray, R. The Crystal Structures of $Cu_{1.8}Se$, Cu_3Se_2, α- and γCuSe, $CuSe_2$, and $CuSe_2$II. *Can J Chem* **54**, 841–848 (1976).

81. Oliveria, M., Mcmullan, R. K. & Wuensch, B. J. Single Crystal Neutron Diffraction Analysis of the Cation Distribution in the High-Temperature Phases α-$Cu_{2-x}S$, α-$Cu_{2-x}Se$, AND α-Ag_2Se. *Solid State lonics* **28**, 1332–1337 (1988).

82. Liu, H., Shi, X., Xu, F., Zhang, L., Zhang, W., Chen, L., Li, Q., Uher, C., Day, T. & Snyder, G. J. Copper Ion Liquid-Like Thermoelectrics. *Nat Mater* **11**, 422–425 (2012).

83. Qin, Y., Yang, L., Wei, J., Yang, S., Zhang, M., Wang, X. & Yang, F. Doping Effect on Cu_2Se Thermoelectric Performance: A Review. *Materials* **13**, 1–32 (2020).

84. Papoian, G. A. & Hoffmann, R. Hypervalent Bonding in One, Two and Three Dimensions: Extending the Zintl-Klemm Concept to Nonclassical Electron-Rich Networks. *Angew Chem Int Ed* **112**, 2500–2544 (2000).

85. Kauzlarich, S. M., Brown, S. R., Jeffrey Snyder, G., Morton, S. A., Waddill, G. D. & Tobin, J. G. Zintl Phases for Thermoelectric Devices. *Dalton Transactions* **84**, 2099–2107 (2007).

86. Toberer, E. S., May, A. F. & Snyder, G. J. Zintl Chemistry for Designing High Efficiency Thermoelectric Materials. *Chemistry of Materials* **22**, 624–634 (2010).

87. Zevalkink, A., Aydemir, U. & Snyder, G. J. Chain-Forming A_3MPn_3 and $A_5M_2Pn_6$ Zintl Phases. in *Materials Aspect of Thermoelectricity* (ed. Uher, C.) vol. 1 (CRC Press., 2016).

88. Zevalkink, A., Toberer, E. S., Zeier, W. G., Flage-Larsen, E. & Snyder, G. J. Ca_3AlSb_3: An Inexpensive, Non-Toxic Thermoelectric Material for Waste Heat Recovery. *Energy Environ. Sci.* **4**, 510–518 (2011).

89. Zevalkink, A., Zeier, W. G., Pomrehn, G., Schechtel, E., Tremel, W. & Snyder, G. J. Thermoelectric Properties of Sr_3GaSb_3 – A Chain-Forming Zintl Compound. *Energy Environ Sci* **5**, 9121–9128 (2012).

90. Peng, W., Chanakian, S. & Zevalkink, A. Crystal Chemistry and Thermoelectric Transport of Layered AM_2X_2 Compounds. *Inorg Chem Front* **5**, 1744–1759 (2018).

91. Kleinke, H. Metal Pnictides: Structures and Thermoelectric Properties. in *Handbook of Solid State Chemistry* (eds. Dronskowski, R., Kikkawa, S. & Stein, A.) (2017).

92. Wang, X. J., Tang, M. B., Chen, H. H., Yang, X. X., Zhao, J. T., Burkhardt, U. & Grin, Y. Synthesis and High Thermoelectric Efficiency of Zintl Phase $YbCd_{2-x}Zn_xSb_2$. *Appl Phys Lett* **94**, 092106/1–3 (2009).

93. Shi, X., Zhang, X., Ganose, A., Park, J., Sun, C., Chen, Z., Lin, S., Li, W., Jain, A. & Pei, Y. Compromise Between Band Structure and Phonon Scattering in Efficient n-$Mg_3Sb_{2-x}Bi_x$ Thermoelectrics. *Materials Today Physics* **18**, 100362/1–6 (2021).

94. Brown, S. R., Kauzlarich, S. M., Gascoin, F. & Jeffrey Snyder, G. $Yb_{14}MnSb_{11}$: New High Efficiency Thermoelectric Material for Power Generation. *Chem Mater* **18**, 1873–1877 (2006).

95. Grebenkemper, J. H., Hu, Y., Barrett, D., Gogna, P., Huang, C. K., Bux, S. K. & Kauzlarich, S. M. High Temperature Thermoelectric Properties of $Yb_{14}MnSb_{11}$ Prepared from Reaction of MnSb with the Elements. *Chem Mater* **27**, 5791–5798 (2015).

96. Grebenkemper, J. H., Hu, Y., Barrett, D., Gogna, P., Huang, C. K., Bux, S. K. & Kauzlarich, S. M. The Remarkable Crystal Chemistry of the $Ca_{14}AlSb_{11}$ Structure Type, Magnetic and Thermoelectric Properties. *J Solid State Chem* **271**, 88–102 (2019).

97. Zaitsev, V. K., Fedorov, M. I., Gurieva, E. A., Eremin, I. S., Konstantinov, P. P., Samunin, A. Y. & Vedernikov, M. V. Highly Effective $Mg_2Si_{1-x}Sn_x$ Thermoelectrics. *Phys Rev B* **74**, 045207/1–5 (2006).

98. Liu, W., Tang, X., Li, H., Sharp, J., Zhou, X. & Uher, C. Optimized thermoelectric properties of Sb-doped $Mg_{2(1+z)}Si_{0.5-y}Sn_{0.5}Sb_y$ through adjustment of the Mg content. *Chem Mater* **23**, 5256–5263 (2011).

99. Khan, A. U., Kobayashi, K., Tang, D. M., Yamauchi, Y., Hasegawa, K., Mitome, M., Xue, Y., Jiang, B., Tsuchiya, K., Golberg, D., Bando, Y. & Mori, T. Nano-Micro-Porous Skutterudites With 100% Enhancement in ZT for High Performance Thermoelectricity. *Nano Energy* **31**, 152–159 (2017).

100. Kubouchi, M., Ogawa, Y., Hayashi, K., Takamatsu, T. & Miyazaki, Y. Effect of Interstitial Mg in $Mg_{2+x}Si$ on Electrical Conductivity and Seebeck Coefficient. *J Electron Mater* **45**, 1589–1593 (2016).

101. Stefanaki, E. C., Polymeris, G. S., Ioannou, M., Pavlidou, E., Hatzikraniotis, E., Kyratsi, T. & Paraskevopoulos, K. M. Inhomogeneities and Effective Mass in Doped Mg_2Si. *J Electron Mater* **45**, 1900–1906 (2016).

102. Liu, W., Chi, H., Sun, H., Zhang, Q., Yin, K., Tang, X., Zhang, Q. & Uher, C. Advanced Thermoelectrics Governed by a Single Parabolic Band: $Mg_2Si_{0.3}Sn_{0.7}$, A Canonical Example. *PCCP* **16**, 6893–6897 (2014).

103. Noda, Y., Kon, H., Furukawa, Y., Otsuka, N., Nishida, I. A. & Masumoto, K. Preparation and thermoelectric properties of $Mg_2Si_{1-x}Ge_x$ (x=0.0~0.4) Solid Solution Semiconductors. *Mater Trans* **33**, 845–850 (1992).

104. Kubouchi, M., Hayashi, K. & Miyazaki, Y. Quantitative Analysis of Interstitial Mg in Mg_2Si Studied by Single Crystal X-ray Diffraction. *J Alloys Compd* **617**, 389–392 (2014).

105. Farahi, N., VanZant, M., Zhao, J., Tse, J. S., Prabhudev, S., Botton, G. A., Salvador, J. R., Borondics, F., Liu, Z. & Kleinke, H. Sb- and Bi-doped Mg_2Si: Location of the Dopants, Micro- and Nanostructures, Electronic Structures and Thermoelectric Properties. *J Chem Soc, Dalton Trans* **43**, 14983–14991 (2014).

106. Khan, A. U., Vlachos, N. v., Hatzikraniotis, E., Polymeris, G. S., Lioutas, C. B., Stefanaki, E. C., Paraskevopoulos, K. M., Giapintzakis, I. & Kyratsi, T. Thermoelectric Properties of Highly Efficient Bi-doped $Mg_2Si_{1-x-y}Sn_xGe_y$ Materials. *Acta Mater* **77**, 43–53 (2014).

107. Pulikkotil, J. J., Singh, D. J., Auluck, S., Saravanan, M., Misra, D. K., Dhar, A. & Budhani, R. C. Doping and Temperature Dependence of Thermoelectric Properties in $Mg_2(Si,Sn)$. *Phys Rev B* **86**, 155204/1–7 (2012).

108. Jung, I. H., Kang, D. H., Park, W. J., Kim, N. J. & Ahn, S. H. Thermodynamic Modeling of the Mg-Si-Sn System. *CALPHAD* **31**, 192–200 (2007).

109. Liu, W., Tang, X., Li, H., Yin, K., Sharp, J., Zhou, X. & Uher, C. Enhanced Thermoelectric Properties of n-type $Mg_{2.16}(Si_{0.4}Sn_{0.6})_{1-y}Sb_y$ Due to Nano-Sized Sn-Rich Precipitates and an Optimized Electron Concentration. *J Mater Chem* **22**, 13653–13661 (2012).

110. Liu, W., Zhang, Q., Yin, K., Chi, H., Zhou, X., Tang, X. & Uher, C. High Figure of Merit and Thermoelectric Properties of Bi-doped $Mg_2Si_{0.4}Sn_{0.6}$ Solid Solutions. *J Solid State Chem* **203**, 333–339 (2013).

111. Khan, A. U., Vlachos, N. & Kyratsi, Th. High Thermoelectric Figure of Merit of $Mg_2Si_{0.55}Sn_{0.4}Ge_{0.05}$ Materials Doped with Bi and Sb. *Scr Mater* **69**, 606–609 (2013).

112. Farahi, N., Prabhudev, S., Botton, G. A., Salvador, J. R. & Kleinke, H. Nano- and Microstructure Engineering: An Effective Method for Creating High Efficiency Magnesium Silicide Based Thermoelectrics. *ACS Appl Mater Interfaces* **8**, 34431–34437 (2016).

113. Cheng, X., Farahi, N. & Kleinke, H. Mg_2Si-Based Materials for the Thermoelectric Energy Conversion. *JOM* **68**, 2680–2687 (2016).

114. Zhang, Q., Cheng, L., Liu, W., Zheng, Y., Su, X., Chi, H., Liu, H., Yan, Y., Tang, X. & Uher, C. Low Effective Mass and Carrier Concentration Optimization for High Performance p-Type $Mg_{2(1-x)}Li_{2x}Si_{0.3}Sn_{0.7}$ Solid Solutions. *PCCP* **16**, 23576–23583 (2014).

115. You, S. W. & Kim, I. H. Solid-State Synthesis and Thermoelectric Properties of Bi-doped Mg_2Si Compounds. *Current Applied Physics* **11**, 392–395 (2011).

116. Tani, J. I. & Kido, H. Thermoelectric Properties of Bi-doped Mg_2Si Semiconductors. *Physica B Condens Matter* **364**, 218–224 (2005).

117. Luo, W., Yang, M., Chen, F., Shen, Q., Jiang, H. & Zhang, L. Preparation and Thermoelectric Properties of Bi-Doped $Mg_2Si_{0.8}Sn_{0.2}$ Compound. *Mater Trans* **51**, 288–291 (2010).

118. Gao, P., Lu, X., Berkun, I., Schmidt, R. D., Case, E. D. & Hogan, T. P. Reduced Lattice Thermal Conductivity in Bi-doped $Mg_2Si_{0.4}Sn_{0.6}$. *Appl Phys Lett* **105**, 202104/1–7 (2014).

119. Kozlov, A., Gröbner, J. & Schmid-Fetzer, R. Phase Formation in Mg-Sn-Si and Mg-Sn-Si-Ca Alloys. *J Alloys Compd* **509**, 3326–3337 (2011).

120. Li, J., Li, X., Chen, C., Hu, W., Yu, F., Zhao, Z., Zhang, L., Yu, D., Tian, Y. & Xu, B. Enhanced Thermoelectric Performance of Bismuth-Doped Magnesium Silicide Synthesized Under High Pressure. *J Mater Sci* **53**, 9091–9098 (2018).

121. Tseng, Y., Razavi-tousi, S. S., Greenwood, M. & Sears, J. Phase Separation and its Relationship with Thermoelectric Properties in Tin-Substituted Magnesium Silicide Synthesized from Melt. *Scr Mater* **166**, 128–133 (2019).

122. Farahi, N., Prabhudev, S., Bugnet, M., Botton, G. A., Zhao, J., Tse, J. S., Salvador, J. R. & Kleinke, H. Enhanced Figure of Merit in $Mg_2Si_{0.877}Ge_{0.1}Bi_{0.023}$/Multi Wall Carbon Nanotube Nanocomposites. *RSC Adv* **5**, 65328–65336 (2015).

123. Macario, L. R., Cheng, X., Ramirez, D., Mori, T. & Kleinke, H. Thermoelectric Properties of Bi-Doped Magnesium Silicide Stannides. *ACS Appl Mater Interfaces* **10**, 40585–40591 (2018).

124. Liu, W., Yin, K., Zhang, Q., Uher, C. & Tang, X. Eco-Friendly High-Performance Silicide Thermoelectric Materials. *Natl Sci Rev* **4**, 611–626 (2017).

125. Kim, G., Lee, H., Kim, J., Roh, J. W., Lyo, I., Kim, B. W., Lee, K. H. & Lee, W. Up-Scaled Solid State Reaction for Synthesis of Doped Mg_2Si. *Scr Mater* **128**, 53–56 (2017).

126. Farahi, N., Stiewe, C., Truong, D. Y. N., de Boor, J. & Müller, E. High Efficiency $Mg_2(Si,Sn)$-Based Thermoelectric Materials: Scale-up Synthesis, Functional Homogeneity, and Thermal Stability. *RSC Adv* **9**, 23021–23028 (2019).

127. Byer, R. L. Nonlinear Optical Phenomena and Materials. *Ann Rev Mater Sci* **4**, 147–190 (1974).

128. Kildal, H. & Mikkelsen, J. C. The Nonlinear Optical Coefficient, Phasematching, and Optical Damage in the Chalcopyrite $AgGaSe_2$. *Opt Commun* **9**, 315–318 (1973).

129. Luo, X., Li, Z., Guo, Y., Yao, J. & Wu, Y. Recent Progress on New Infrared Nonlinear Optical Materials with Application Prospect. *J Solid State Chem* **270**, 674–687 (2019).

130. Kumar, V., Tripathy, S. K. & Jha, V. Second Order Nonlinear Optical Properties of $A^{I}B^{III}C_2^{VI}$ Chalcopyrite Semiconductors. *Appl Phys Lett* **101**, 192105/1–5 (2012).

131. Nakamura, M., Yamaguchi, K., Kimoto, Y., Yasaki, Y., Kato, T. & Sugimoto, H. Cd-Free $Cu(In,Ga)(Se,S)_2$ Thin-Film Solar Cell With Record Efficiency of 23.35%. *IEEE J Photovolt* **9**, 1863–1867 (2019).

132. Wada, T. $CuInSe_2$ and Related I-III-VI_2 Chalcopyrite Compounds for Photovoltaic Application. *Jpn J Appl Phys* **60**, 080101/1–11 (2021).

133. Shay, J. L., Wagner, S. & Kasper, H. M. Efficient $CuInSe_2$/CdS Solar Cells. *Appl Phys Lett* **27**, 89–90 (1975).

134. Abou-Ras, D., Wagner, S., Stanbery, B. J., Schock, H. W., Scheer, R., Stolt, L., Siebentritt, S., Lincot, D., Eberspacher, C., Kushiya, K. & Tiwari, A. N. Innovation Highway: Breakthrough Milestones and Key Developments in Chalcopyrite Photovoltaics from a Retrospective Viewpoint. *Thin Solid Films* **633**, 2–12 (2017).

135. Sandroni, M., Wegner, K. D., Aldakov, D. & Reiss, P. Prospects of Chalcopyrite-Type Nanocrystals for Energy Applications. *ACS Energy Lett* **2**, 1076–1088 (2017).

136. Wagner, S. Preparation and Properties of Green-Light-Emitting CdS-$CuGaS_2$ Heterodiodes. *J Appl Phys* **45**, 246–251 (1974).

137. Thomas, S. R., Chen, C. W., Date, M., Wang, Y. C., Tsai, H. W., Wang, Z. M. & Chueh, Y. L. Recent Developments in the Synthesis of Nanostructured Chalcopyrite Materials and Their Applications: A Review. *RSC Adv* **6**, 60643–60656 (2016).

138. Plata, J. J., Posligua, V., Márquez, A. M., Fernandez Sanz, J. & Grau-Crespo, R. Charting the Lattice Thermal Conductivities of I-III-VI_2 Chalcopyrite Semiconductors. *Chem Mater* **34**, 2833–2841 (2022).

139. Shay, J. L. & Wernick, J. H. *Ternary Chalcopyrite Semiconductors: Growth, Electronic Properties, and Applications*. (Pergamon Press, 1975).

140. Cao, Y., Su, X., Meng, F., Bailey, T. P., Zhao, J., Xie, H., He, J., Uher, C. & Tang, X. Origin of the Distinct Thermoelectric Transport Properties of Chalcopyrite $ABTe_2$ (A = Cu, Ag; B = Ga, In). *Adv Funct Mater* **30**, 2005861/1–13 (2020).

141. Lu, Y., Chen, S., Wu, W., Du, Z., Chao, Y. & Cui, J. Enhanced Thermoelectric Performance of a Chalcopyrite Compound $CuIn_3Se_{5-x}Te_x$ (x = 0~0.5) Through Crystal Structure Engineering. *Sci Rep* **7**, 40224/1–8 (2017).

142. Nomura, A., Choi, S., Ishimaru, M., Kosuga, A., Chasapis, T., Ohno, S., Snyder, G. J., Ohishi, Y., Muta, H., Yamanaka, S. & Kurosaki, K. Chalcopyrite $ZnSnSb_2$: A Promising Thermoelectric Material. *ACS Appl Mater Interfaces* **10**, 43682–43690 (2018).

143. Kosuga, A., Plirdpring, T., Higashine, R., Matsuzawa, M., Kurosaki, K. & Yamanaka, S. High-Temperature Thermoelectric Properties of $Cu_{1-x}InTe_2$ with a Chalcopyrite Structure. *Appl Phys Lett* **100**, 2012–2015 (2012).

144. Plirdpring, T., Kurosaki, K., Kosuga, A., Day, T., Firdosy, S., Ravi, V., Snyder, G. J., Harnwunggmoung, A., Sugahara, T., Ohishi, Y., Muta, H. & Yamanaka, S. Chalcopyrite $CuGaTe_2$: A High-Efficiency Bulk Thermoelectric Material. *Adv Mater* **24**, 3622–3626 (2012).

145. Parker, D. & Singh, D. J. Thermoelectric Properties of $AgGaTe_2$ and Related Chalcopyrite Structure Materials. *Phys Rev B Condens Matter Mater Phys* **85**, 125209/1–7 (2012).

146. Yusufu, A., Kurosaki, K., Kosuga, A., Sugahara, T., Ohishi, Y., Muta, H. & Yamanaka, S. Thermoelectric Properties of $Ag_{1-x}GaTe_2$ With Chalcopyrite Structure. *Appl Phys Lett* **99**, 061902/1–3 (2011).

147. Qiu, P., Qin, Y., Zhang, Q., Li, R., Yang, J., Song, Q., Tang, Y., Bai, S., Shi, X. & Chen, L. Intrinsically High Thermoelectric Performance in $AgInSe_2$ n-Type Diamond-Like Compounds. *Adv Sci* **5**, 1700727/1–8 (2018).

148. Su, X., Zhao, N., Hao, S., Stoumpos, C. C., Liu, M., Chen, H., Xie, H., Zhang, Q., Wolverton, C., Tang, X. & Kanatzidis, M. G. High Thermoelectric Performance in the Wide Band-Gap $AgGa_{1-x}Te_2$ Compounds: Directional Negative Thermal Expansion and Intrinsically Low Thermal Conductivity. *Adv Funct Mater* **29**, 1806534/1–9 (2019).

149. NIST Inorganic Crystal Structure Database. NIST Standard Reference Database Number 3. (2022).

150. Berger, L. I. & Prochukhan, V. D. *Ternary Diamond-Like Semiconductors*. *Ternary Diamond-Like Semiconductors / Troinye Almazopodobnye Poluprovodniki / Тройные Алмазоподобные Полупроволники* (Springer US, 1969).

151. Novotortsev, V. M., Marenkin, S. F., Fedorchenko, I. v. & Kochura, A. v. Physicochemical Foundations of Synthesis of New Ferromagnets from Chalcopyrites $A^{II}B^{IV}C_2^V$. *Russ J Inorg Chem* **55**, 1762–1773 (2010).

152. Pamplin, B. R. Critical Review of the Growth of II-IV-V_2 Compounds. *J Cryst Growth* **26**, 239–242 (1974).

153. Mukherjee, M., Yumnam, G. & Singh, A. K. High Thermoelectric Figure of Merit via Tunable Valley Convergence Coupled Low Thermal Conductivity in $A^{II}B^{IV}C_2^V$ Chalcopyrites. *J Phys Chem C* **122**, 29150–29157 (2018).

154. Sreeparvathy, P. C., Kanchana, V. & Vaitheeswaran, G. Thermoelectric Properties of Zinc Based Pnictide Semiconductors. *J Appl Phys* **119**, 085701/1–8 (2016).

155. Sreeparvathy, P. C., Kanchana, V., Vaitheeswaran, G. & Christensen, N. E. $ZnGeSb_2$: A Promising Thermoelectric Material with Tunable Ultra-High Conductivity. *PCCP* **18**, 26275–26283 (2016).

156. Deller, K. & Eisenmann, B. Zur Kenntnis von $Ca_{11}Sb_{10}$ und $Ca_{11}Bi_{10}$. *Z Naturforsch, B: Chem Sci* **31**, 29–34 (1976).

157. Sharp, J. W., Jones, E. C., Williams, R. K., Martin, P. M. & Sales, B. C. Thermoelectric Properties of $CoSb_3$ and Related Alloys. *J Appl Phys* **78**, 1013–1018 (1995).

158. Snyder, G. J., Christensen, M., Nishibori, E., Caillat, T. & Iversen, B. B. Disordered Zinc in Zn_4Sb_3 with Phonon-Glass and Electron-Crystal Thermoelectric Properties. *Nat Mater* **3**, 458–463 (2004).

159. Derrien, G., Tillard-Charbonnel, M., Manteghetti, A., Monconduit, L. & Belin, C. Synthesis and Crystal Structure of $M_{11}X_{10}$ Compounds, M = Sr, Ba and X = Bi, Sb. Electronic Requirements and Chemical Bonding. *J Solid State Chem* **164**, 169–175 (2002).

160. Brown, S. R., Kauzlarich, S. M., Gascoin, F. & Jeffrey Snyder, G. High-Temperature Thermoelectric Studies of $A_{11}Sb_{10}$ (A=Yb, Ca). *J Solid State Chem* **180**, 1414–1420 (2007).

161. Rauscher, J. F., Kauzlarich, S. M., Ikeda, T. & Snyder, G. J. Synthesis, Structure, and High Temperature Thermoelectric Properties of $Yb_{11}Sb_{9.3}Ge_{0.5}$. *Z Anorg Allg Chem* **633**, 1587–1594 (2007).

162. Lee, J., Ahn, K., Kim, K., Jo, H., Yoon, J. S., Moon, D., Shin, W. H., Ok, K. M. & You, T. S. Effect of Rare-Earth Metals Substitution for Ca on the Crystal Structure and Thermoelectric Properties of the $Ca_{11-x}RE_xSb_{10-y}$ System. *Cryst Growth Des* **19**, 3498–3508 (2019).

163. Massalski, T.B. *Binary Alloy Phase Diagrams*. (ASM International, 1990).

164. Mio, H., Kano, J., Saito, F. & Kaneko, K. Effects of Rotational Direction and Rotation-to-Revolution Speed Ratio in Planetary Ball Milling. *Mater Sci Eng* **332**, 75–80 (2002).

165. Schneider, F., Szuppa, T., Stolle, A., Ondruschka, B. & Hopf, H. Energetic Assessment of the Suzuki–Miyaura Reaction: A Curtate Life Cycle Assessment as an Easily Understandable and Applicable Tool for Reaction Optimization. *Green Chemistry* **11**, 1894–1899 (2009).

166. Szuppa, T., Stolle, A., Ondruschka, B. & Hopfe, W. Solvent-Free Dehydrogenation of γ-Terpinene in a Ball Mill: Investigation of Reaction Parameters. *Green Chemistry* **12**, 1288–1294 (2010).

167. Mio, H., Kano, J., Saito, F. & Kaneko, K. Optimum Revolution and Rotational Directions and Their Speeds in Planetary Ball Milling. *Int J Miner Process* **74**, 85–92 (2004).

168. Jiang, X., Trunov, M. A., Schoenitz, M., Dave, R. N. & Dreizin, E. L. Mechanical Alloying and Reactive Milling in a High Energy Planetary Mill. *J Alloys Compd* **478**, 246–251 (2009).

169. Rosenkranz, S., Breitung-Faes, S. & Kwade, A. Experimental Investigations and Modelling of the Ball Motion in Planetary Ball Mills. *Powder Technol* **212**, 224–230 (2011).

170. Burmeister, C. F. & Kwade, A. Process engineering with planetary ball mills. *Chem Soc Rev* **42**, 7660–7667 (2013).

171. Stender, H. H., Kwade, A. & Schwedes, J. Stress Energy Distribution in Different Stirred Media Mill Geometries. *Int J Miner Process* **74** S103–S117 (2004).

172. Mio, H., Kano, J. & Saito, F. Scale-up Method of Planetary Ball Mill. *Chem Eng Sci* **59**, 5909–5916 (2004).

173. Kano, J., Mio, H. & Saito, F. Correlation of Grinding Rate of Gibbsite with Impact Energy of Balls Simulation of Balls Motion by PEM. *AIChE* **46**, 1694–1697 (2000).

174. Kano, J. & Saito, F. Correlation of Powder Characteristics of Talc During Planetary Ball Milling with the Impact Energy of the Balls Simulated by the Particle Element Method. *Powder Technol* **98**, 166–170 (1998).

175. Matsuoka, M., Hirata, J. & Yoshizawa, S. Kinetics of Solid-State Polymorphic Transition of Glycine in Mechano-Chemical Processing. *Chem Eng Res Des* **88**, 1169–1173 (2010).

176. Briggs, J. Hot Pressing: An Overview. in *Concise Encyclopedia of Advanced Ceramic Materials* 219–222 (Elsevier, 1991).

177. Broiek, J., Grande, F., Anderson, J. T. & Keys, A. Densitometric Analysis of Body Composition: Revision of Some Quantitative Assumptions. *Ann N Y Acad Sci* **110**, 113–140 (1963).

178. Sartorius AG. *Density Determination Kit User's Manual*. (1998).

179. Egerton, R. F. *Physical Principles of Electron Microscopy*. (Springer US, 2005).

180. Bragg, W. H. & Bragg Apr, W. L. The Reflection of X-rays by Crystals. *Proc R Soc A* **88**, 428–438 (1913).

181. Stout, G. H. & Jensen, L. H. *X-Ray Structure Determination: A Practical Guide*. (John Wiley & Sons, Inc., 1989).

182. Young, R. A. *The Rietveld Method*. (Oxford University Press, 2002).

183. Rietveld, H. M. A Profile Refinement Method for Nuclear and Magnetic Structures. *J Appl Crystallogr* **2**, 65–71 (1969).

184. Larson, A. C. & Von Dreele, R. B. *General Structure Analysis System (GSAS)*. (2004).

185. Toby, B. H. R Factors in Rietveld analysis: How Good is Good Enough? *Powder Diffr* **21**, 67–70 (2006).

186. Wang, H., Porter, W. D., Böttner, H., König, J., Chen, L., Bai, S., Tritt, T. M., Mayolett, A., Senawiratne, J., Smith, C., Harris, F., Gilbert, P., Sharp, J. W., Lo, J., Kleinke, H., *et al.* Transport Properties of Bulk Thermoelectrics – An International Round-Robin Study, Part I: Seebeck Coefficient and Electrical Resistivity. *J Electron Mater* **42**, 654–664 (2013).

187. De Boor, J. & Müller, E. Data Analysis for Seebeck Coefficient Measurements. *Rev Sci Instrum* **84**, 065102/1–9 (2013).

188. Parker, W. J., Jenkins, R. J., Butler, C. P. & Abbott, G. L. Flash Method of Determining Thermal Diffusivity, Heat Capacity, and Thermal Conductivity. *J Appl Phys* **32**, 1679–1684 (1961).

189. Chu, F. I., Taylor, R. E. & Donaldson, A. B. Thermal Diffusivity Measurements at High Temperatures by the Radial Flash Method. *J Appl Phys* **51**, 336–341 (1980).

190. Wang, H., Porter, W. D., Böttner, H., König, J., Chen, L., Bai, S., Tritt, T. M., Mayolet, A., Senawiratne, J., Smith, C., Harris, F., Gilbert, P., Sharp, J., Lo, J., Kleinke, H., *et al.* Transport properties of bulk thermoelectrics: An international round-robin study, part II: Thermal diffusivity, specific heat, and thermal conductivity. *J Electron Mater* **42**, 1073–1084 (2013).

191. Mackey, J., Dynys, F. & Sehirlioglu, A. Uncertainty Analysis for Common Seebeck and Electrical Resistivity Measurement Systems. *Rev Sci Instrum* **85**, 085119/1–10 (2014).

192. Wang, H., Bai, S., Chen, L., Cuenat, A., Joshi, G., Kleinke, H., König, J., Lee, H. W., Martin, J., Oh, M. W., Porter, W. D., Ren, Z., Salvador, J., Sharp, J., Taylor, P., *et al.* International Round-Robin Study of the Thermoelectric Transport Properties of an n-Type Half-Heusler Compound from 300 K to 773 K. *J Electron Mater* **44**, 4482–4491 (2015).

193. Hohenbergt Ecole, P. & Konnt, W. Inhomogeneous Electron Gas. *Physical Review* **136**, 864–871 (1964).

194. Perdew, J. P., Burke, K. & Ernzerhof, M. Generalized Gradient Approximation Made Simple. *Phys Rev Lett* **77**, 3865–3868 (1996).

195. Blaha, P., Schwarz, K., Madsen, G. K. H., Kvasnicka, D., Luitz, J., Laskowsk, R., Tran, F. & Marks, L. *WIEN2k: An Augmented Plane Wave Plus Local Orbitals Program for Calculating Crystal Properties*. *Materials Science and Engineering* (Techn. Universitat, 2019).

196. Blaha, P., Schwarz, K., H Madsen, G. K., Kvasnicka, D., Luitz, J., Laskowski, R., Tran, F. & Marks, L. D. *WIEN2k User Guide*. (2021).

197. Madsen, G. K. H., Carrete, J. & Verstraete, M. J. BoltzTraP2, A Program for Interpolating Band Structures and Calculating Semi-Classical Transport Coefficients. *Comput Phys Commun* **231**, 140–145 (2018).

198. Scheidemantel, J., Ambrosch-Draxl, C., Thonhauser, T., Badding, V. & Sofo, O. Transport Coefficients from First-Principles Calculations. *Phys Rev B Condens Matter Mater Phys* **68**, 125210/1–6 (2003).

199. Farahi, N., Prabhudev, S., Botton, G., Zhao, J., Tse, J. S., Liu, Z., Salvador, J. R. & Kleinke, H. Local Structure and Thermoelectric Properties of $Mg_2Si_{0.977-x}Ge_xBi_{0.023}$ ($0.1 \leq x \leq 0.4$). *J Alloys Compd* **644**, 249–255 (2015).

200. Vaipolin, A. A., Goryunova, N. A., Kleshchinskii, L. I., Loshakova, G. v. & Osmanov, E. O. The Structure and Properties of the Semiconducting Compound ZnSnP2. *Physica Status Solidi (B)* **29**, 435–442 (1968).

201. Rubenstein, M. & Ure, R. W. Preparation and Characteristics of $ZnSnP_2$. *J Phys Chem Solids* **29**, 551–555 (1968).

202. Ryan, M. A., Peterson, M. W., Williamson, D. L., Frey, J. S., Maciel, G. E. & Parkinson B. A. Metal site disorder in zinc tin phosphide. *Materials Research Society* **2**, 528–537 (1987).

203. Nakatsuka, S., Nakamoto, H., Nose, Y., Uda, T. & Shirai, Y. Bulk Crystal Growth and Characterization of $ZnSnP_2$ Compound Semiconductor by Flux Method. *Physica Status Solidi (C)* **12**, 520–523 (2015).

204. Mughal, S. A., Payne, A. J. & Ray, B. Preparation and Phase Studies of the Ternary Semiconducting Compounds $ZnSnP_2$, $ZnGeP_2$, $ZnSiP_2$, $CdGeP_2$, and $CdSiP_2$. *J Mater Sci* **4**, 895–901 (1969).

205. Verozubova, G. A., Gribenyukov, A. I., Korotkova, V. v. & Ruzaikin, M. P. $ZnGeP_2$ Synthesis and Growth from Melt. *Mater Sci Eng, B* **48**, 191–197 (1997).

206. Masumoto, K., Isomura, S. & Goto, W. The Preparation and Properties of $ZnSiAs_2$, $ZnGeP_2$ and $CdGeP_2$ Semiconducting Compounds. *J Phys Chem Solids* **27**, 1939–1947 (1966).

207. Verozubova G.A., Okunev A.O., Gribenyukov A.I., Trofimiv A.Yu., Trukhanov E.M., Kolesnikov A.V. Growth and defect structure of ZnGeP2 crystals. *Journal of Crystal Growth* **312**, 1122–1126 (2010).

208. Wei, L., Zhang, G., Fan, W., Li, Y., Yang, L. & Zhao, X. Anisotropic Thermal Anharmonicity of $CdSiP_2$ and $ZnGeP_2$: Ab Initio Calculations. *J Appl Phys* **114**, 233501/1–6 (2013).

209. Buehler, E., Wernick, J. H. & Wiley, J. D. The ZnP_2-Ge System and Growth of Single Crystals of $ZnGeP_2$. *J Electron Mater* **2**, 445–454 (1973).

210. Wang, T. Y., Sivakumar, R., Rai, D. K., Hsu, W. T. & Lan, C. W. A New Single Step Process for Synthesis and Growth of $ZnGeP_2$ Crystal. *J Chin Inst Chem Eng* **39**, 385–387 (2008).

211. Benameur, K., Mouchaal, Y., Benchouk, K., Laafer, A. & Barille, R. Synthesized and Characterizations Nanoparticles of Chalcopyrite Alloy $CuIn_{1-x}Fe_xSe_2$. *Inorg Chem Commun* **136**, 109265/1–7 (2022).

212. Landry, C. C., Lockwood, J. & Barron, A. R. Synthesis of Chalcopyrite Semiconductors and Their Solid Solutions by Microwave Irradiation. *Chem Mater* **7**, 699–706 (1995).

213. Li, Y., Meng, Q., Deng, Y., Zhou, H., Gao, Y., Li, Y., Yang, J. & Cui, J. High Thermoelectric Performance of Solid Solutions $CuGa_{1-x}In_xTe_2$ (x = 0-1.0). *Appl Phys Lett* **100**, 231903/1–4 (2012).

214. Shay, J. L. & Wernick, J. H. *Ternary Chalcopyrite Semiconductors: Growth, Electronic Properties, and Applications*. (Pergamon Press Inc., 1975).

215. Robbins, M., Phillips, J. C. & Lambrecht, V. G. Solid Solution Formation in the Systems $CuM^{III}X_2$-$AgM^{III}X_2$ Where M^{III} = AI, Ga, In and X_2 = S, Se. *J. Phys. Chem. Solids* **34**, 1205–1209 (1973).

216. Jacob, K. T., Raj, S. & Rannesh, L. Vegard's law: A Fundamental Relation or an Approximation? *Int J Mater Res* **98**, 776–779 (2007).

217. Berger, L. I. *Semiconductor Materials*. (CRC Press, 2020).

218. *CRC Handbook of Chemistry and Physics*. (CRC Press, 2017).

219. Petousis, I., Mrdjenovich, D., Ballouz, E., Liu, M., Winston, D., Chen, W., Graf, T., Schladt, T. D., Persson, K. A. & Prinz, F. B. High-Throughput Screening of Inorganic Compounds for the Discovery of Novel Dielectric and Optical Materials. *Sci Data* **4**, 160134/1–12 (2017).

220. Ricci, F., Chen, W., Aydemir, U., Snyder, G. J., Rignanese, G.-M., Jain, A. & Hautier, G. An ab initio Electronic Transport Database for Inorganic Materials. *Sci Data* **4**, 170085/1–13 (2017).

221. Piyathilaka, H. P., Sooriyagoda, R., Dewasurendra, V., Johnson, M. B., Zawilski, K. T., Schunemann, P. G. & Bristow, A. D. Terahertz Generation by Optical Rectification in Chalcopyrite Crystals $ZnGeP_2$, $CdGeP_2$ and $CdSiP_2$. *Opt Express* **27**, 16958/1–8 (2019).

222. Wang, K., Qin, P., Ge, Z. H. & Feng, J. Highly Enhanced Thermoelectric Properties of p-Type $CuInSe_2$ Alloys by the Vacancy Doping. *Scr Mater* **149**, 88–92 (2018).

223. Yao, J., Takas, N. J., Schliefert, M. L., Paprocki, D. S., Blanchard, P. E. R., Gou, H., Mar, A., Exstrom, C. L., Darveau, S. A., Poudeu, P. F. P. & Aitken, J. A. Thermoelectric Properties of p-Type $CuInSe_2$ Chalcopyrites Enhanced by Introduction of Manganese. *Phys Rev B* **84**, 075203/1–10 (2011).

224. Zhang, J., Liu, R., Cheng, N., Zhang, Y., Yang, J., Uher, C., Shi, X., Chen, L. & Zhang, W. High-Performance Pseudocubic Thermoelectric Materials from Non-Cubic Chalcopyrite Compounds. *Adv Mater* **26**, 3848–3853 (2014).

225. Carr, W. D. & Morelli, D. T. Influence of Doping and Solid Solution Formation on the Thermoelectric Properties of Chalcopyrite Semiconductors. *J Alloys Compd* **630**, 277–281 (2015).

226. Nomura, A., Choi, S., Ishimaru, M., Kosuga, A., Chasapis, T., Ohno, S., Snyder, G. J., Ohishi, Y., Muta, H., Yamanaka, S. & Kurosaki, K. Chalcopyrite $ZnSnSb_2$: A Promising Thermoelectric Material. *ACS Appl Mater Interfaces* **10**, 43682–43690 (2018).

227. Shaban, H. T., Mobarak, M. & Nassary, M. M. Characterization of $CuInSe_2$ single crystal. *Physica B Condens Matter* **389**, 351–354 (2007).

228. Manimaran, M., Kalkura, S. N. & Ramasamy, P. Crystallization of $ZnSnAs_2$ by Physical Vapour Transport. *J Mater Sci Lett* **14**, 1366–1368 (1995).

229. Masumoto, K. & Isomura, S. The Preparation and Semiconducting Properties of Single Crystals of $ZnSnAs_2$ Compound B. *J Phys Chem Solids* **26**, 163–171 (1965).

230. Gasson, D. B., Holmes, P. J., Jennings, I. C., Marathe, B. R. & Parrott, J. E. The Properties of $ZnSnAs_2$ and $CdSnAs_2$. *J Phys Chem Solids* **23**, 1291–1302 (1962).

231. Elalfy, L., Music, D. & Hu, M. Metavalent Bonding Induced Abnormal Phonon Transport in Diamondlike Structures: Beyond Conventional Theory. *Phys Rev B* **103**, 075203/1–8 (2021).

232. Liu, H., Zhao, B., Yu, Y., He, Z., Xiao, J., Huang, W., Zhu, S., Chen, B. & Xie, L. Theoretical Investigations on Elastic, Thermal and Lattice Dynamic Properties of

Chalcopyrite $ZnSnX_2$ (X = P, As, Sb) Under Pressure and Temperature: The First-Principles Calculation. *Int J Mod Phys B* **32**, 1850329/1–28 (2018).

233. Isotta, E., Mukherjee, B., Fanciulli, C., Ataollahi, N., Sergueev, I., Stankov, S., Edla, R., Pugno, N. M. & Scardi, P. Origin of a Simultaneous Suppression of Thermal Conductivity and Increase of Electrical Conductivity and Seebeck Coefficient in Disordered Cubic Cu2ZnSnS4. *Phys Rev Appl* **14**, (2020).

234. Rehr, A. & Kauzlarich, S. M. $Sr_{11}Sb_{10}$. *Acta Crystallogr C* **50**, 1859–1861 (1994).

235. Sturza, M., Han, F., Malliakas, C. D., Chung, D. Y., Claus, H. & Kanatzidis, M. G. Superconductivity in the Intermetallic Pnictide Compound $Ca_{11}Bi_{10-x}$. *Phys Rev B* **89**, 054512/1–6 (2014).

236. Hoffmann, A. V., Hlukhyy, V. & Fassler, T. F. Crystal Structure of Undecacalcium Decaarsenide, $Ca_{11}As_{10}$. *Z Kristallogr - New Cryst Struct* **238**, 1–3 (2023).

237. Gascoin, F., Rasmussen, J. & Snyder, G. J. High temperature thermoelectric properties of Mo3Sb7-xTex for x = 1.6 and 1.5. *J Alloys Compd* **427**, 324–329 (2007).

238. Dashjav, E., Szczepenowska, A. & Kleinke, H. Optimization of the Thermopower of the Antimonide Mo_3Sb_7 by a Partial Sb/Te Substitution. *J Mater Chem* **12**, 345–349 (2002).

239. Nelson, R., Ertural, C., George, J., Deringer, V. L., Hautier, G. & Dronskowski, R. LOBSTER: Local Orbital Projections, Atomic Charges, and Chemical-Bonding Analysis from Projector-Augmented-Wave-Based Density-Functional Theory. *J Comput Chem* **41**, 1931–1940 (2020).

240. Maintz, S., Deringer, V. L., Tchougréeff, A. L. & Dronskowski, R. Analytic Projection from Plane-Wave and PAW Wavefunctions and Application to Chemical-Bonding Analysis in Solids. *J Comput Chem* **34**, 2557–2567 (2013).

241. Börnsen, N. & Fähnle, M. E_{cov}-A New Tool for the Analysis of Electronic Structure Data in a Chemical Language. *J Phys: Condens. Matter* **11**, 287–293 (1999).

242. Misra, S. & Miller, G. J. $Gd_{5-x}Y_xTt_4$ (Tt = Si or Ge): Effect of Metal Substitution on Structure, Bonding, and Magnetism. *J Am Chem Soc* **130**, 13900–13911 (2008).

243. Pauling, L. *The Nature of Chemical Bonding*. (Cornell University Press, 1960).

244. Cooley, J., Kazem, N., Zaikina, J. V., Fettinger, J. C. & Kauzlarich, S. M. Effect of Isovalent Substitution on the Structure and Properties of the Zintl Phase Solid Solution $Eu_7Cd_4Sb_{8-x}As_x$ ($2 \leq x \leq 5$). *Inorg Chem* **54**, 11767–11775 (2015).

245. Christensen, M., Johnsen, S. & Iversen, B. B. Synthesis, Crystallographic and Theoretical Studies of the New Zintl Phases $Ba_2Cd_2Pn_3$ (Pn=As, Sb), and the solid solutions $(Ba_{1-x}Sr_x)_2Cd_2Sb_3$ and Ba2Cd2(Sb1–xAsx)3. *Dalton Transactions* **39**, 978–992 (2010).

246. Togo, A. & Tanaka, I. First Principles Phonon Calculations in Materials Science. *Scr Mater* **108**, 1–5 (2015).

Appendix A: Supplemental Figures and Tables

A.1 Chapter 1 Supplemental

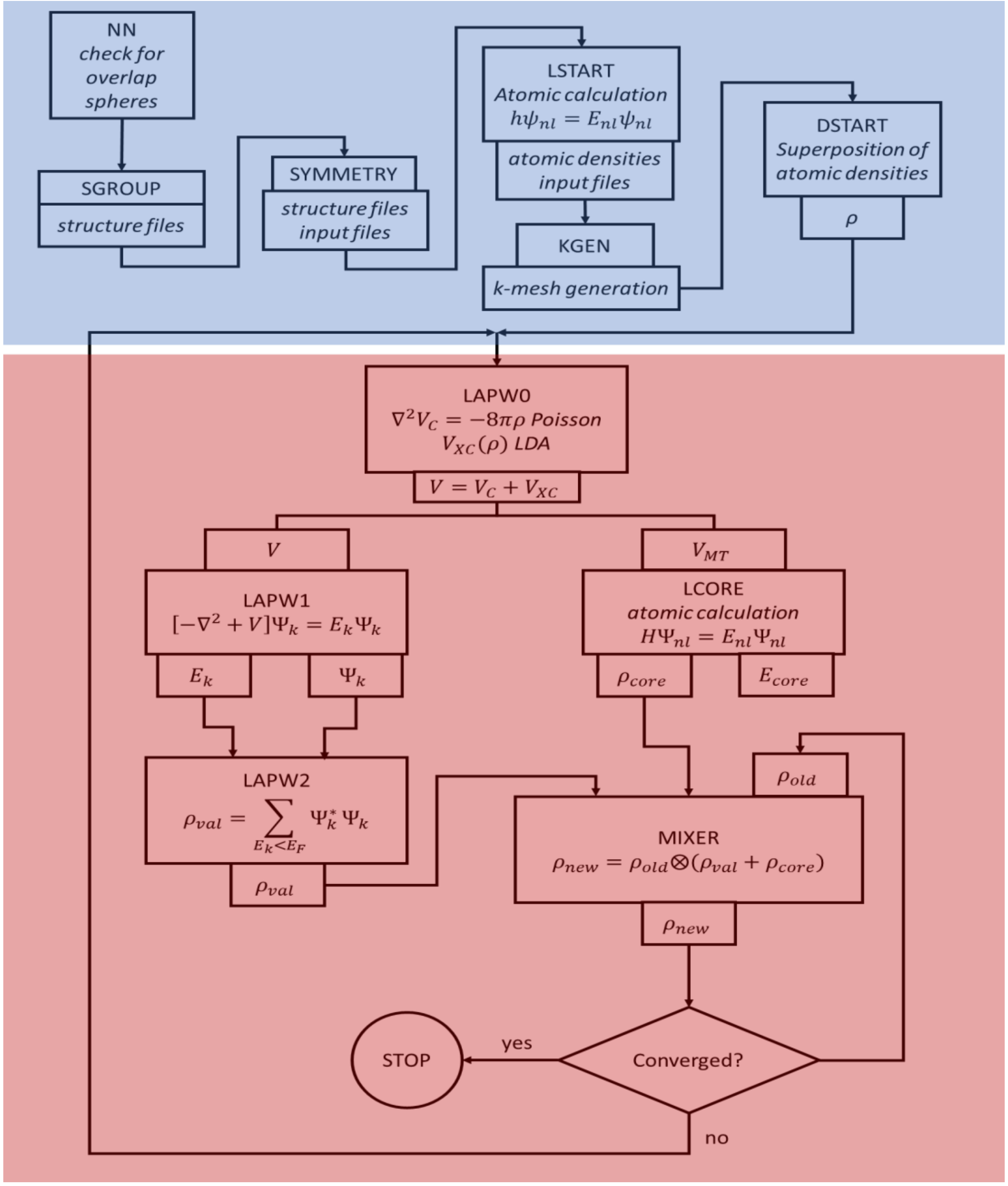

Figure A.1: Flowchart of basic WIEN2k suite operation with the initialization programs highlighted blue and self-consistent field (SCF) programs highlighted in red.

A.2 Chapter 3 Supplemental

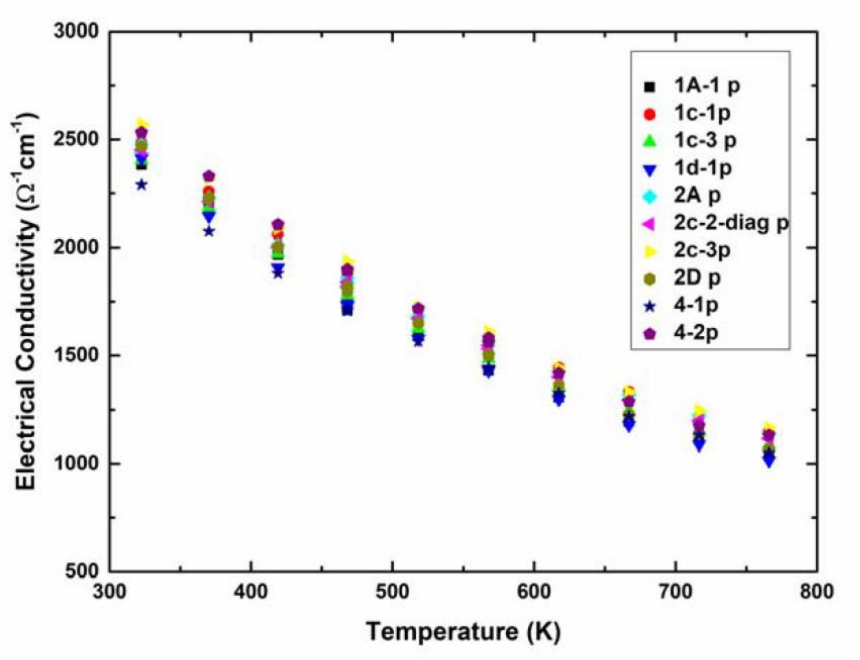

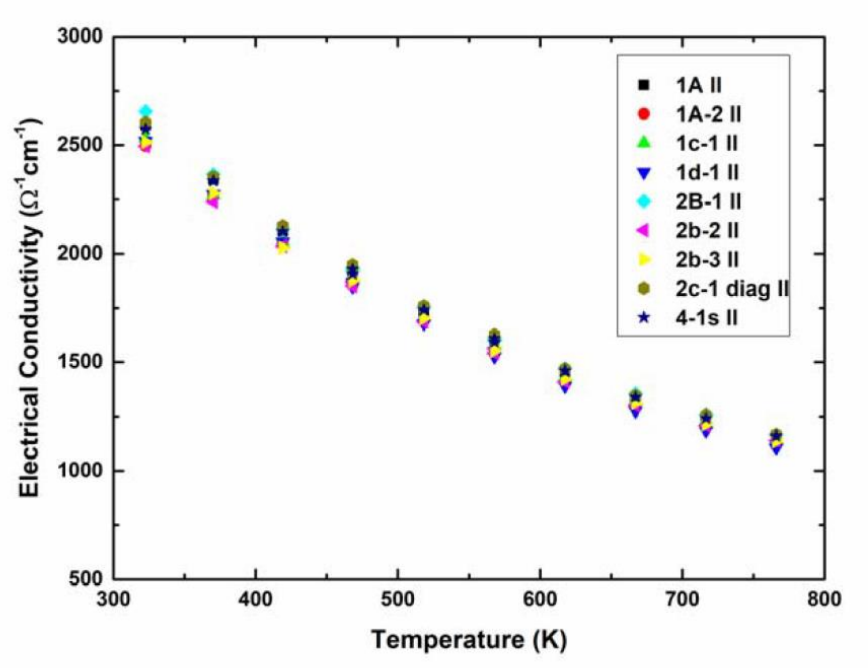

Figure A.2: Electrical conductivity vs temperature measurements on machined samples (Figure 3.2) obtained perpendicular (top) and parallel (bottom).

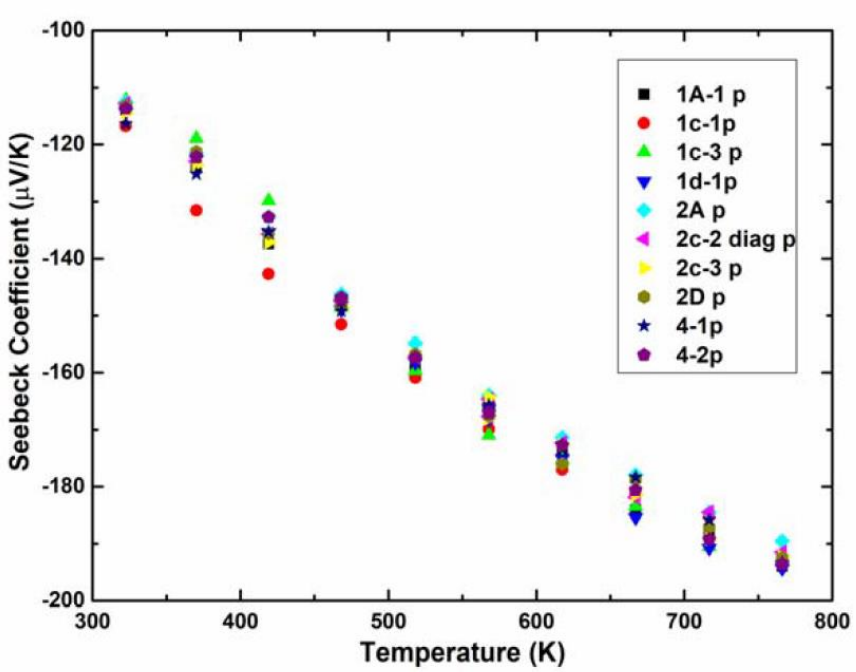

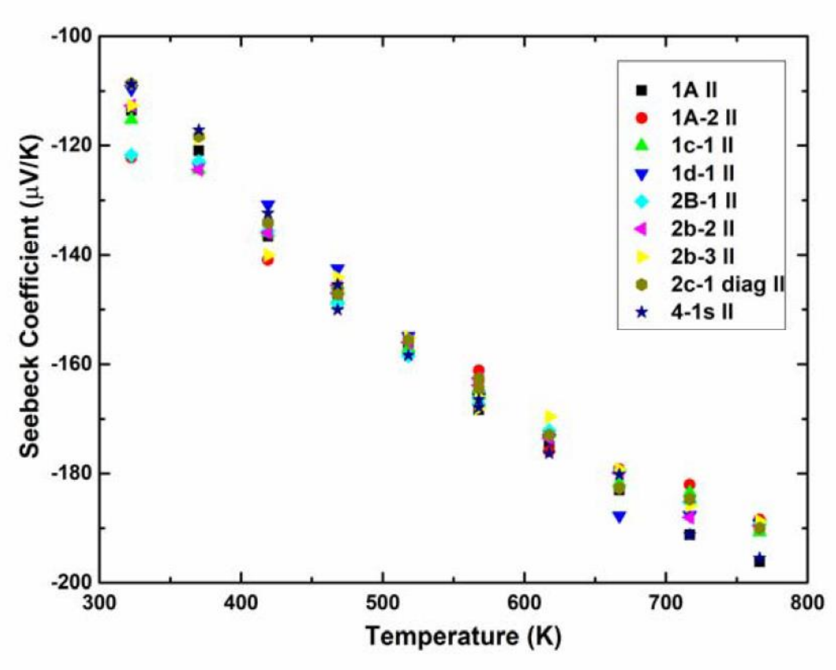

Figure A.3: Seebeck coefficient vs temperature measurements on machined samples (Figure 3.2) obtained perpendicular (top) and parallel (bottom).

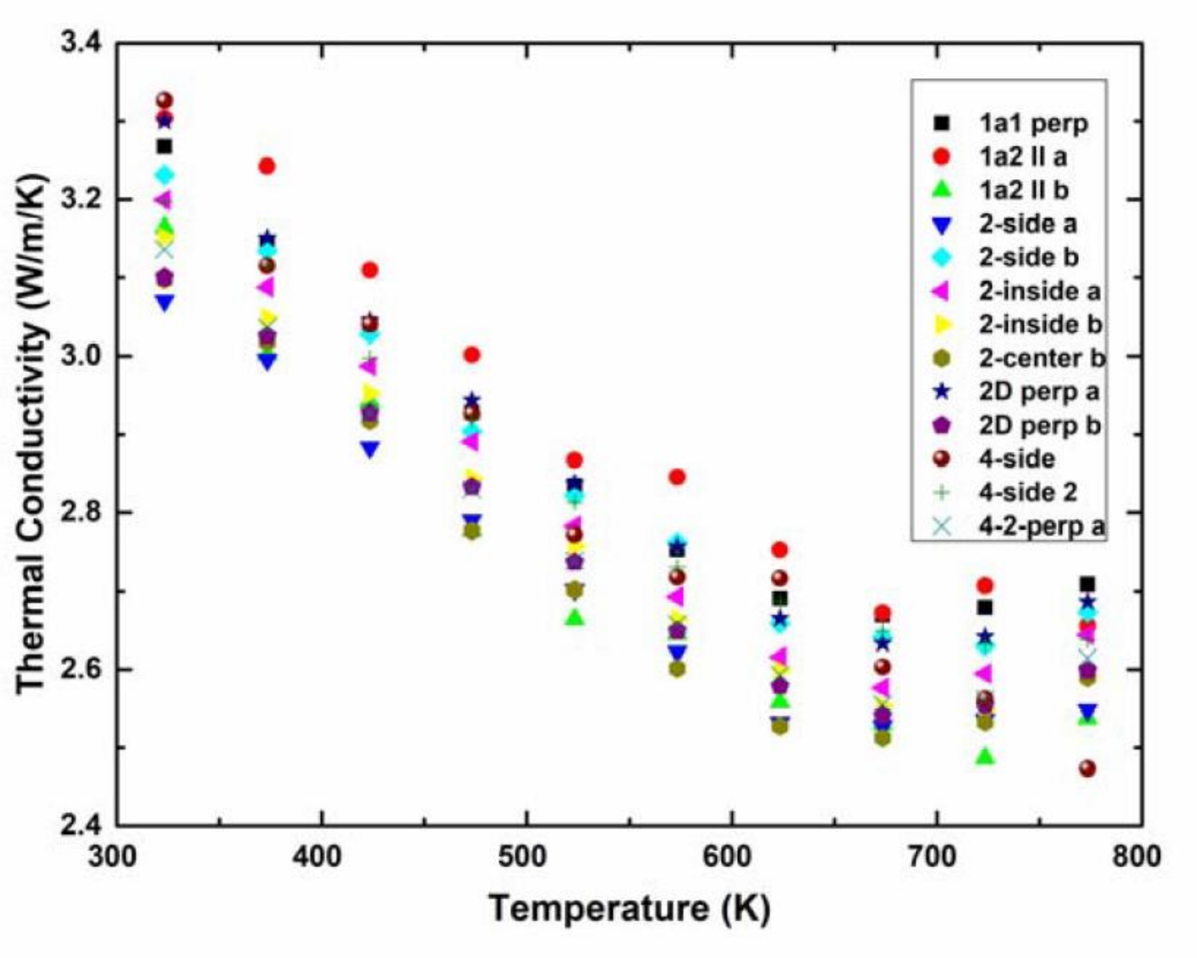

Figure A.4: Thermal conductivity versus temperature measurements for samples machined from large pressed piece (Figure 3.2); samples are named according to their position and orientation within the large pressed piece.

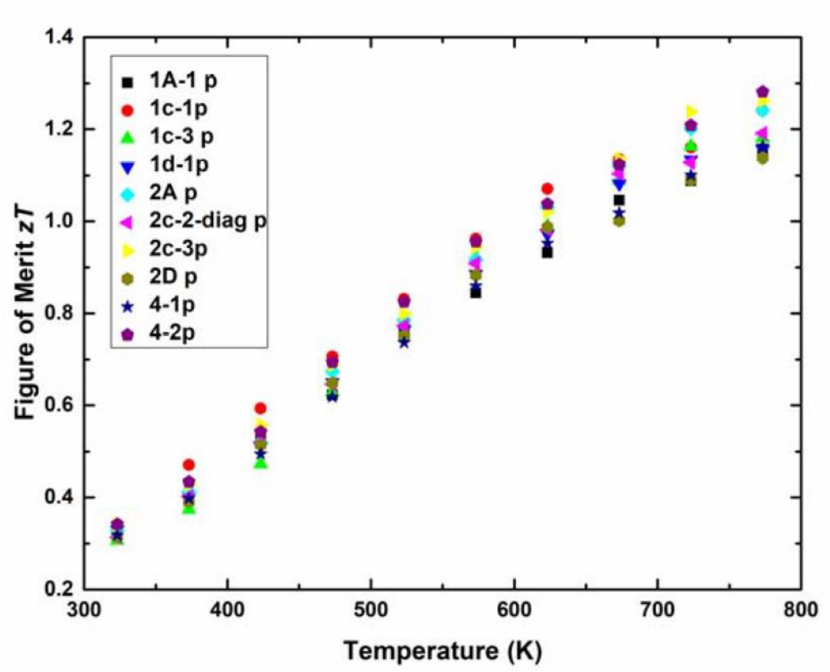

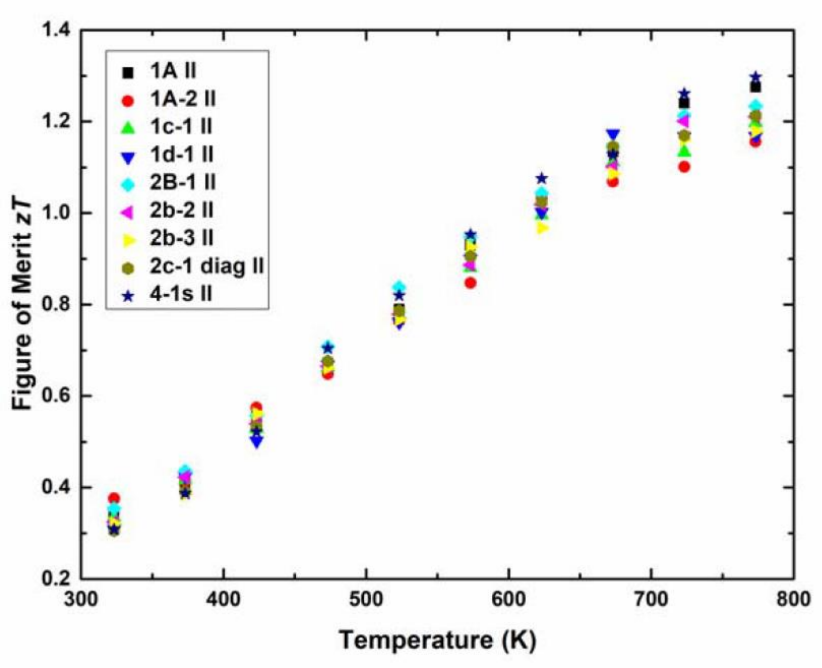

Figure A.5: Figure of merit vs temperature measurements on machined samples (Figure 3.2) obtained perpendicular (top) and parallel (bottom) calculated using average thermal conductivity values.

Table A.1: Parameters for samples cut perpendicular (Figure 3.2) to pressing direction.

Sample	Mass (g)	Depth (mm)	Width (mm)	Length (mm)	Density (g cm^{-3})
1a-1 p	0.198	3.15	2.30	8.64	3.16
1c-1p	0.151	2.29	2.34	8.86	3.18
1c-3 p	0.143	2.35	2.14	9.02	3.15
1d-1 p	0.142	2.35	2.19	8.91	3.10
2a p	0.091	1.78	1.83	8.88	3.15
2c-2-diag p	0.149	2.33	2.31	8.73	3.17
2c-3 p	0.137	2.32	2.12	8.63	3.23
2d p	0.137	2.10	2.29	8.94	3.19
4-1 p	0.145	2.22	2.35	8.83	3.15
4-2 p	0.143	2.29	2.23	8.90	3.15

Table A.2: Parameters for samples cut parallel (Figure 3.2) to pressing direction.

Sample	Mass (g)	Depth (mm)	Width (mm)	Length (mm)	Density (g cm^{-3})
1A ll	0.170	1.82	2.86	10.32	3.16
1a-2 ll	0.312	2.28	2.19	19.74	3.17
1c-1 ll	0.221	2.36	2.25	13.02	3.20
1d-1 ll	0.353	2.18	2.36	21.73	3.16
2b-1 ll	0.126	2.09	1.82	10.65	3.11
2b-2 ll	0.123	2.08	1.82	10.50	3.09
2b-3 ll	0.339	2.21	2.29	21.11	3.17
2c-1-diag ll	0.218	2.25	2.33	12.97	3.21
4-1s ll	0.230	2.30	2.22	14.22	3.17

Table A.3: Parameters for samples cut at various orientations to pressing direction corresponding to Figure 3.2, used for thermal diffusivity measurements.

Sample	Mass (g)	Depth (mm)	Width (mm)	Length (mm)	Density (g cm^{-3})
1-A-1 perp	3.08	8.69	9.98	0.838	3.14
1-A-2 ll a	0.69	8.89	8.82	0.149	2.75
1-A-2 ll b	0.79	9.85	8.15	0.190	3.00
2-side a	1.06	6.13	9.51	0.187	3.03
2-side b	1.17	9.08	6.47	0.217	3.16
2-inside a	1.76	7.80	9.21	0.396	3.13
2-inside b	1.78	9.17	9.83	0.503	3.13
2-center b	0.94	9.18	9.83	0.272	3.21
2D perp a	2.09	9.67	9.00	0.584	3.21
2D perp b	2.09	9.27	9.57	0.579	3.12
4 side	0.52	9.16	8.63	0.120	2.92
4 side 2	1.22	9.04	9.57	0.329	3.12
4-2-perp a	2.20	9.02	8.87	0.558	3.17

A.3 Chapter 4 Supplemental

Table A.4: Rietveld refinement statistics of final calculations for $ZnGe_{1-x}Sn_xP_2$ solid solutions.

x	R_p	R_{wp}	R_{exp}	χ^2	x_{calc}
0	0.153	0.185	0.022	8.47	--
0.25	0.051	0.073	0.009	8.37	0.223
0.5	0.032	0.044	0.009	4.72	0.454
0.75	0.043	0.059	0.009	6.44	0.737
1	0.060	0.085	0.009	9.69	--

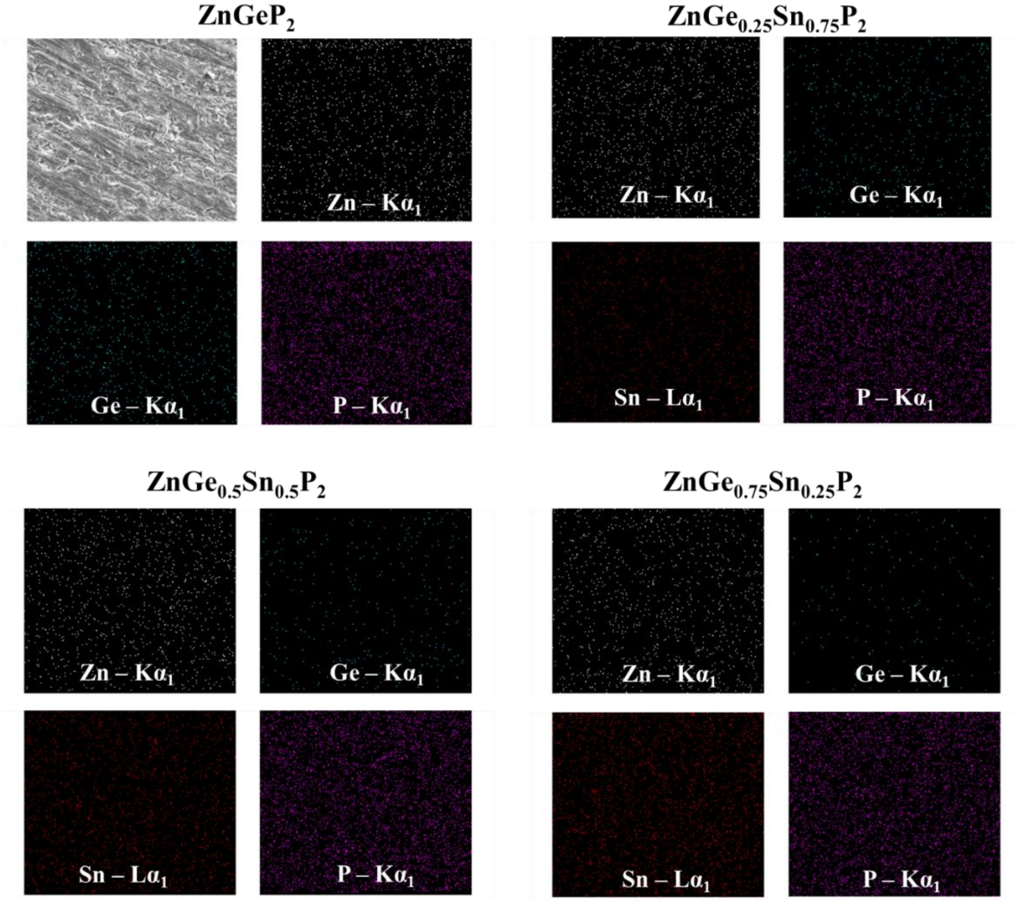

Figure A.6: EDAX mapping of $ZnGe_{1-x}Sn_xP_2$ series with homogeneous distribution of elements.

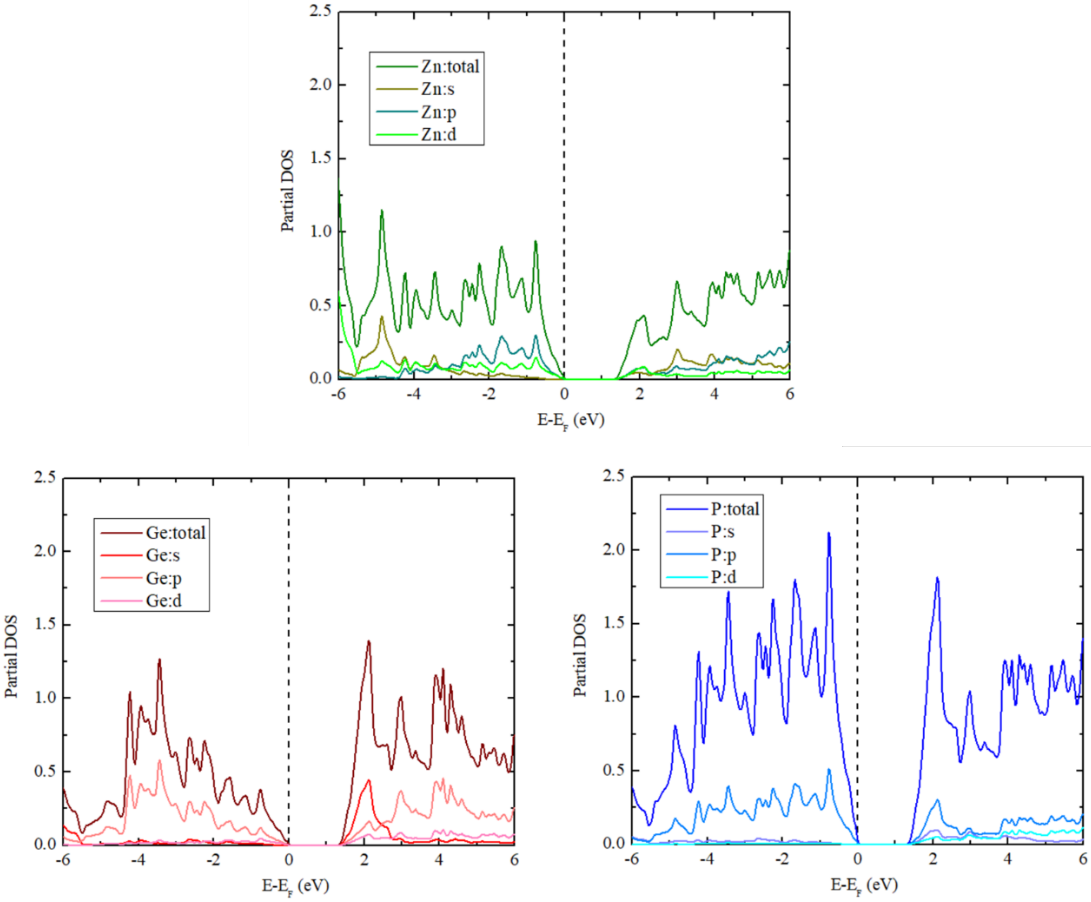

Figure A.7: PDOS calculation for $ZnGeP_2$

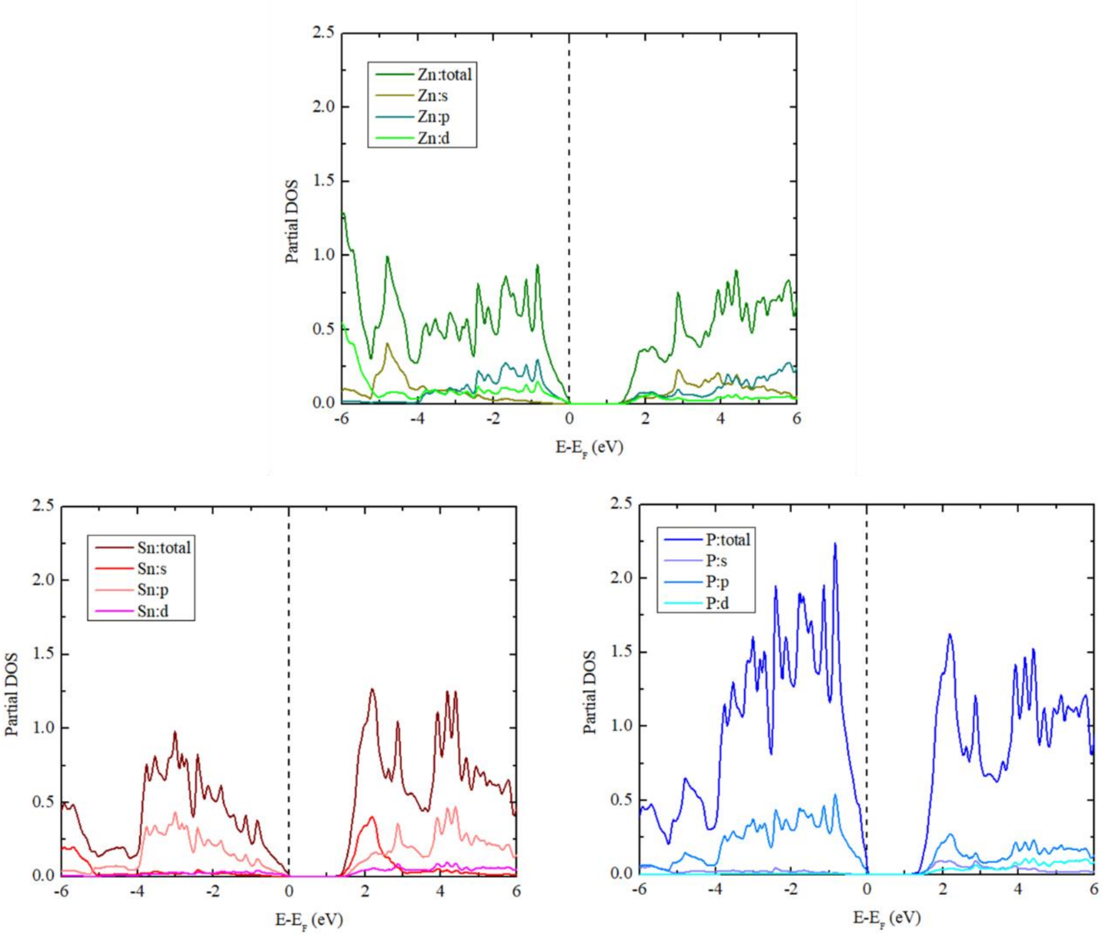

Figure A.8: PDOS calculation for $ZnSnP_2$

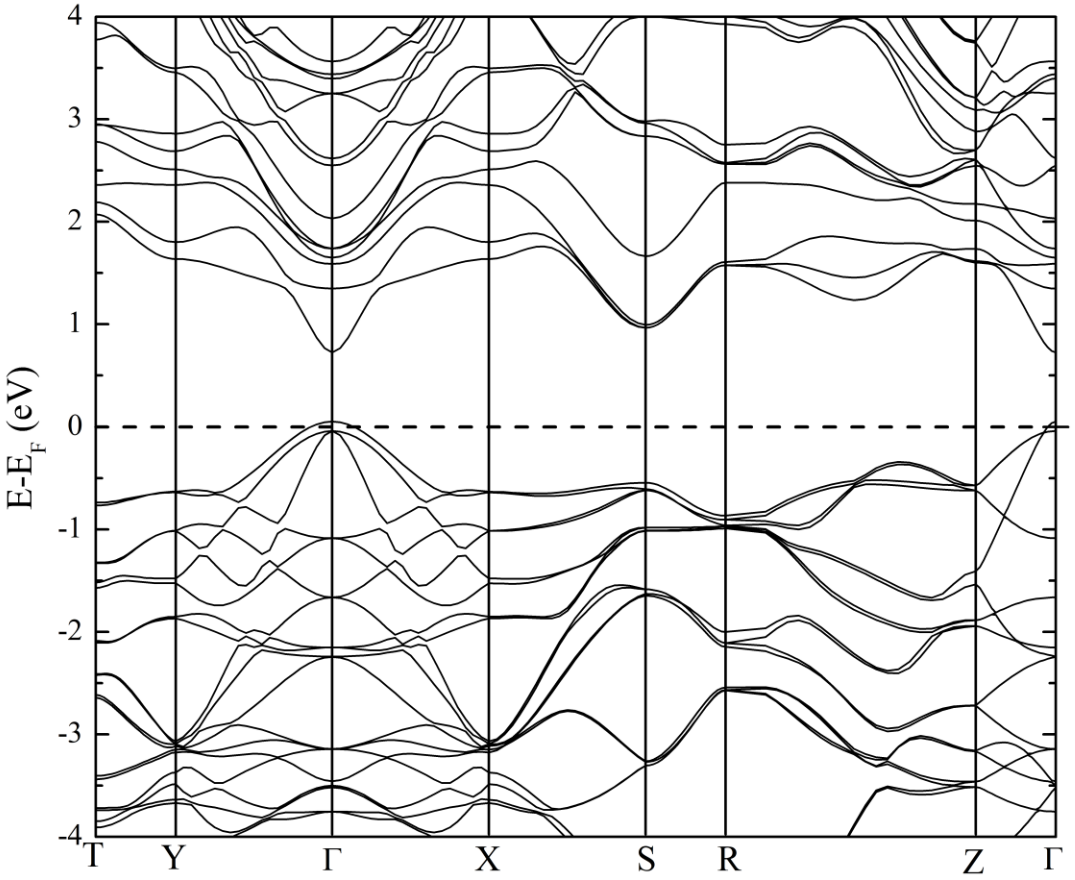

Figure A.9: Electronic band structure results for $ZnGe_{0.75}Sn_{0.25}P_2$ using the orthorhombic basis $P222_1$.

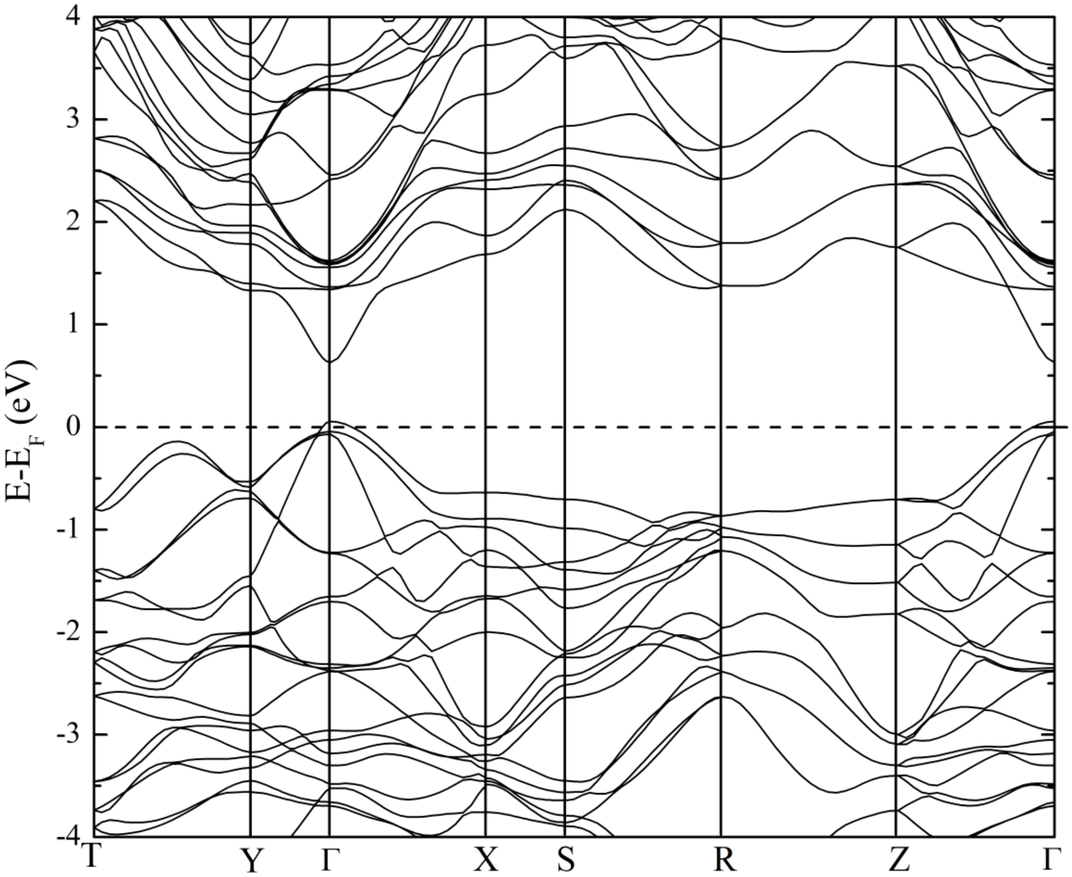

Figure A.10: Electronic band structure result for the first unique $ZnGe_{0.5}Sn_{0.5}P_2$ structure using the orthorhombic basis $P222_1$.

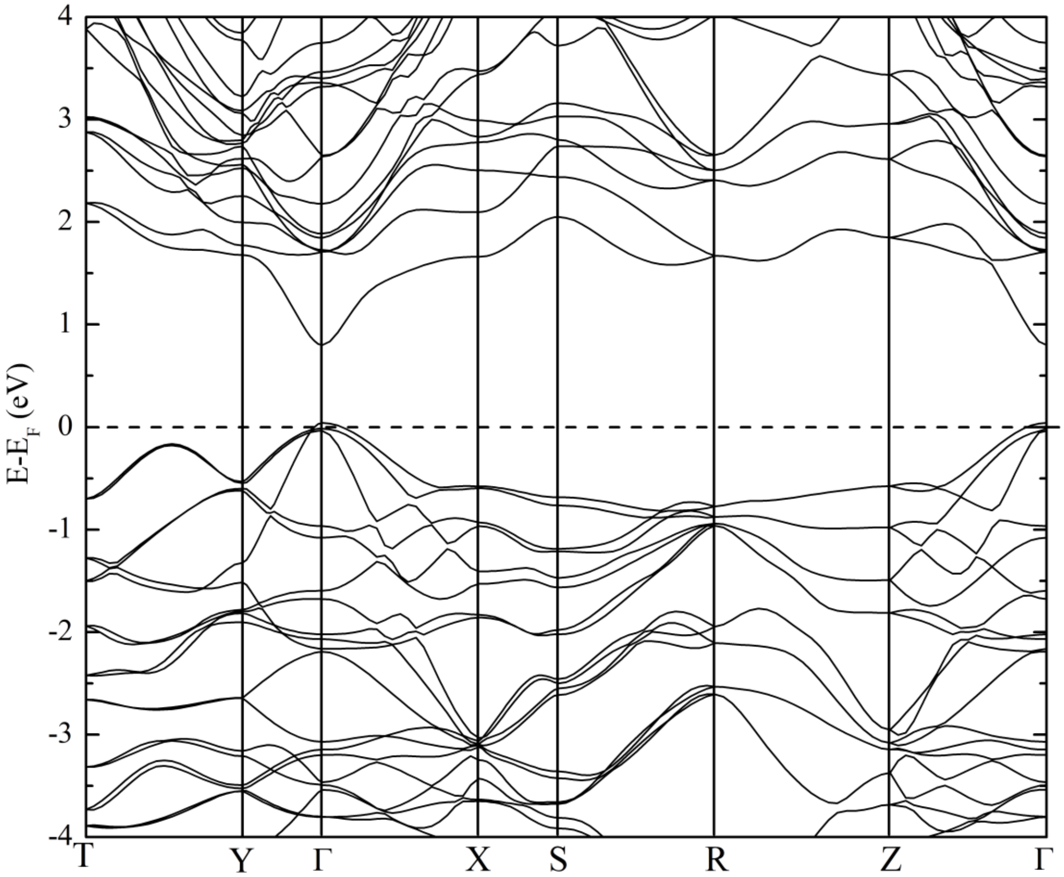

Figure A.11: Electronic band structure result for the second unique $ZnGe_{0.5}Sn_{0.5}P_2$ structure using the orthorhombic basis $P222_1$.

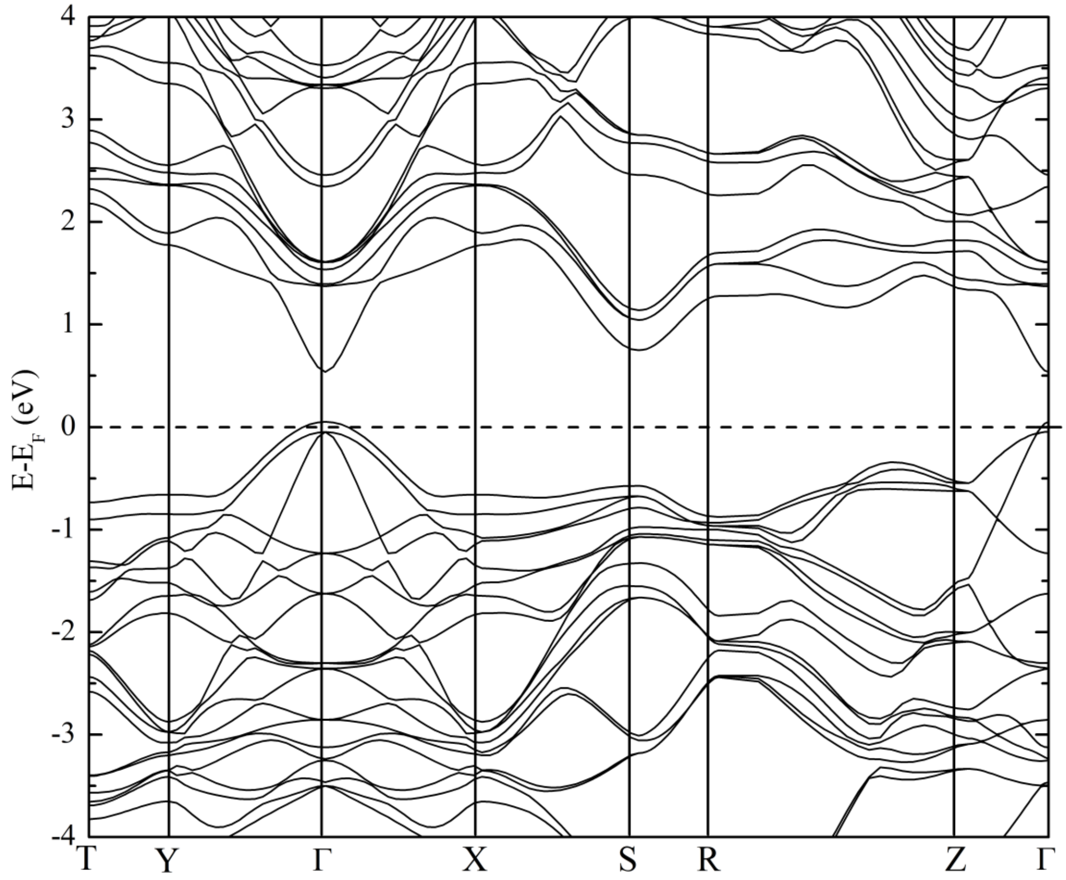

Figure A.12: Electronic band structure result for the unique $ZnGe_{0.25}Sn_{0.75}P_2$ structure using the orthorhombic basis $P222_1$.

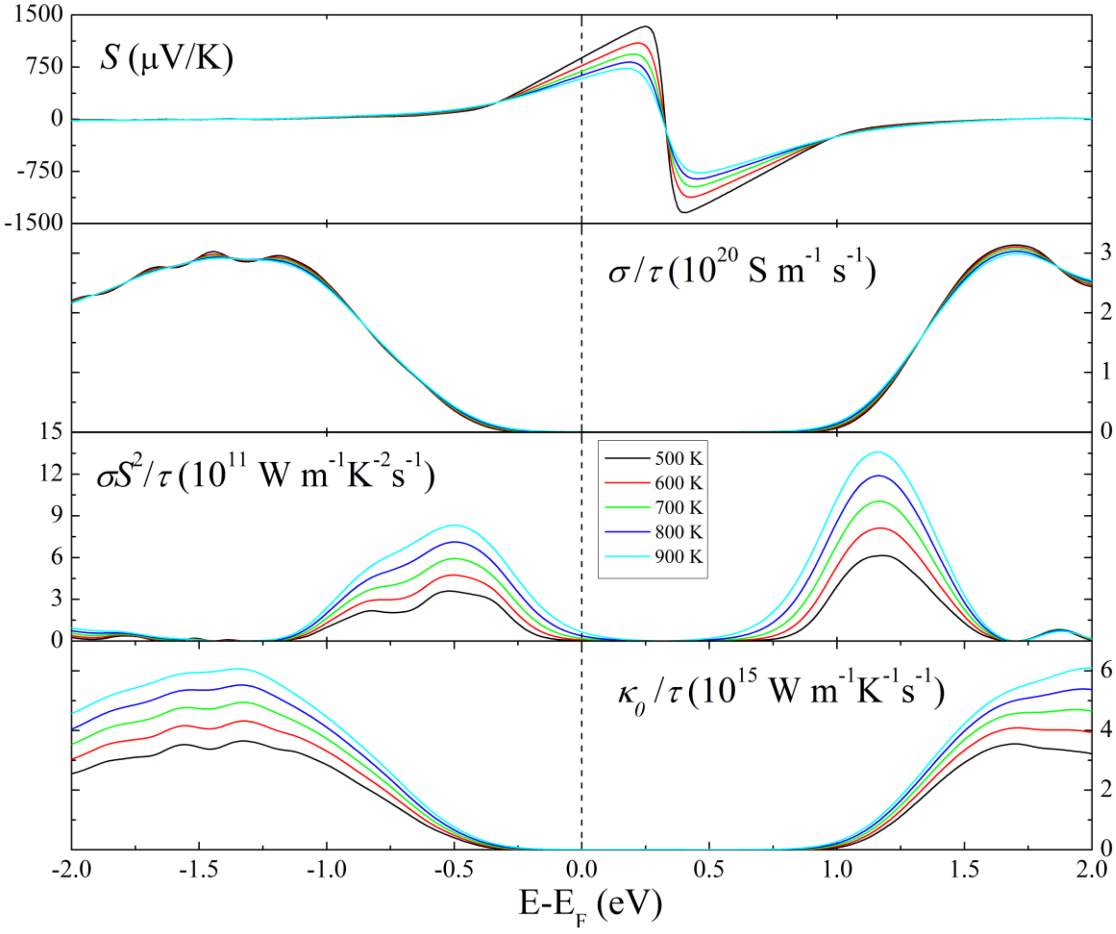

Figure A.13: Boltztrap calculation results of $ZnGeP_2$ properties versus Fermi level including Seebeck coefficient and scattering independent electrical conductivity, power factor, and electronic thermal conductivity. Calculation details described in Chapter 4, Section 4.4, Electronic Structure and Properties.

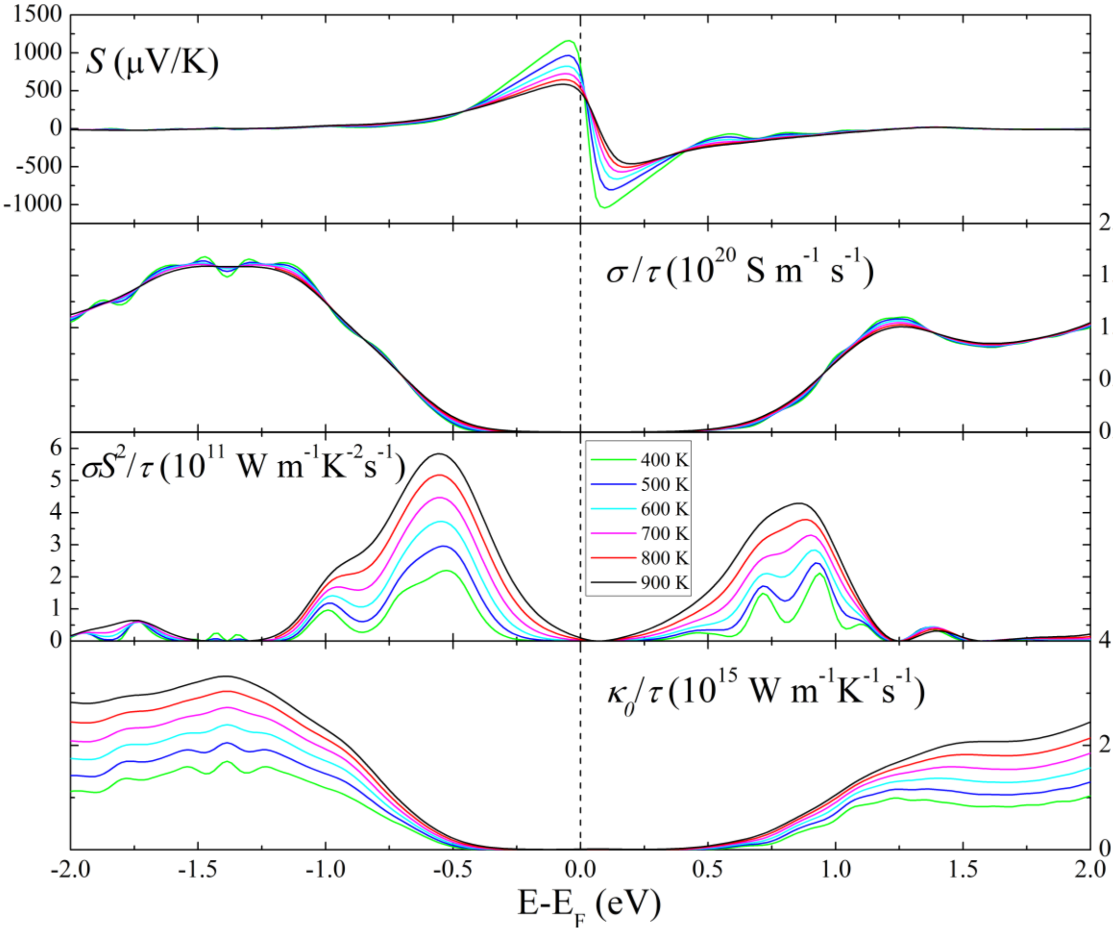

Figure A.14: Boltztrap calculation results of $ZnGe_{0.75}Sn_{0.25}P_2$ properties versus Fermi level including Seebeck coefficient and scattering independent electrical conductivity, power factor, and electronic thermal conductivity. Calculation details described in Chapter 4, Section 4.4, Electronic Structure and Properties.

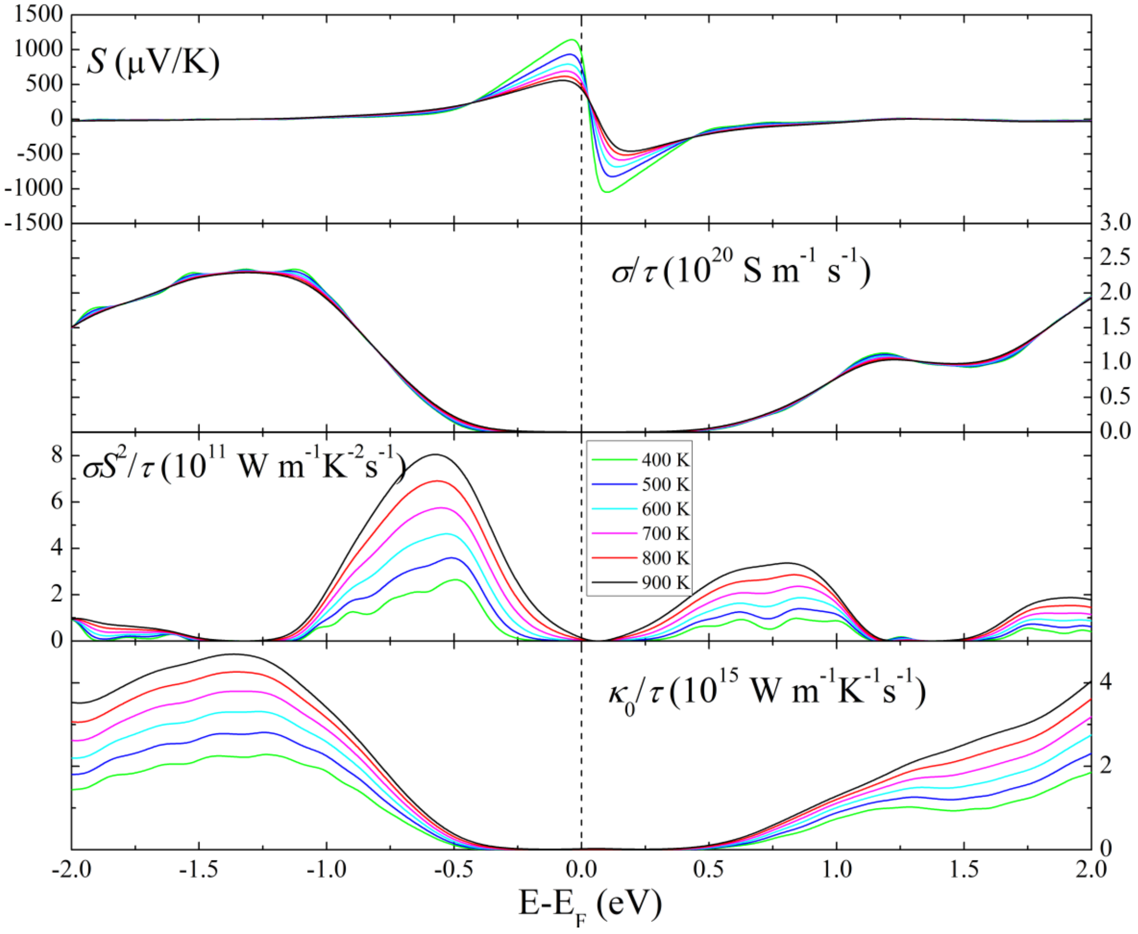

Figure A.15: Boltztrap calculation results of $ZnGe_{0.5}Sn_{0.5}P_2$-1 properties versus Fermi level including Seebeck coefficient and scattering independent electrical conductivity, power factor, and electronic thermal conductivity. Calculation details described in Chapter 4, Section 4.4, Electronic Structure and Properties.

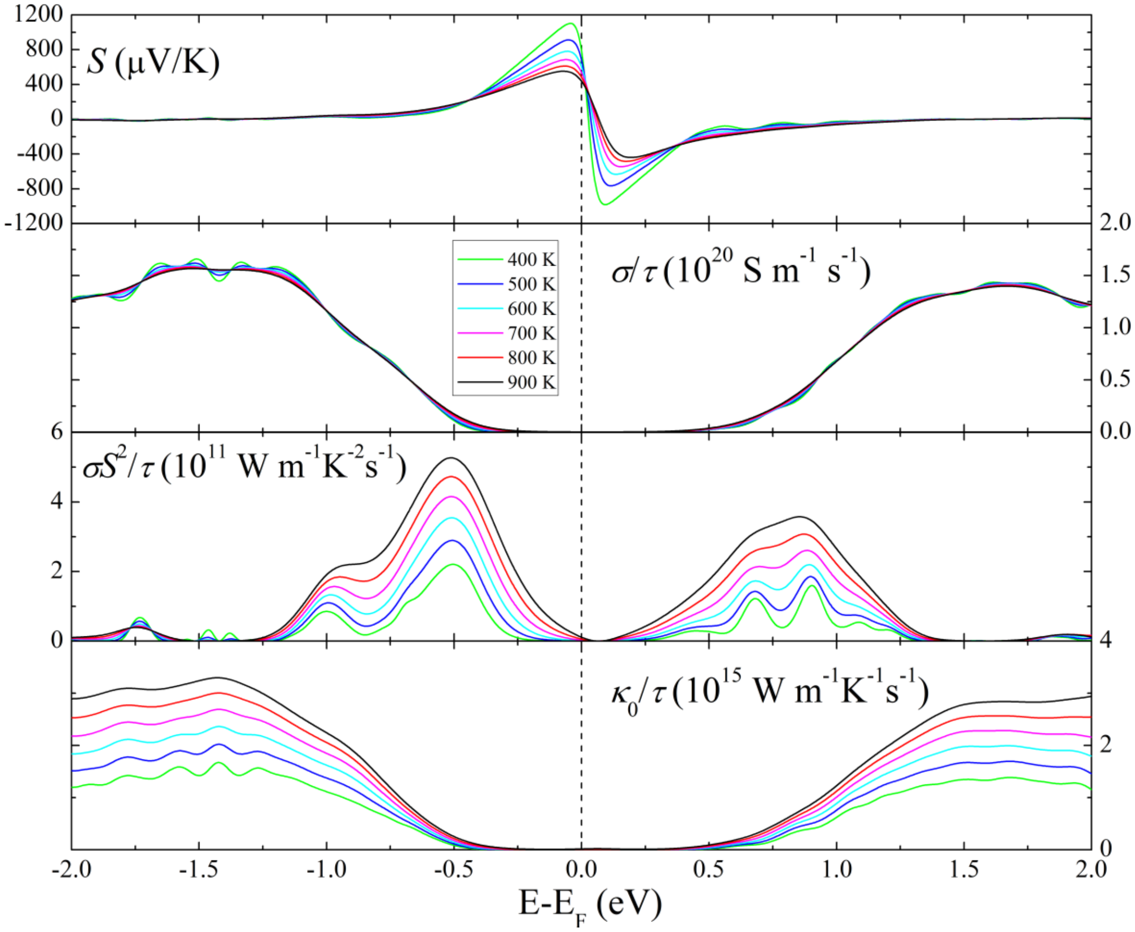

Figure A.16: Boltztrap calculation results of ZnGe$_{0.5}$Sn$_{0.5}$P$_2$-2 properties versus Fermi level including Seebeck coefficient and scattering independent electrical conductivity, power factor, and electronic thermal conductivity. Calculation details described in Chapter 4, Section 4.4, Electronic Structure and Properties.

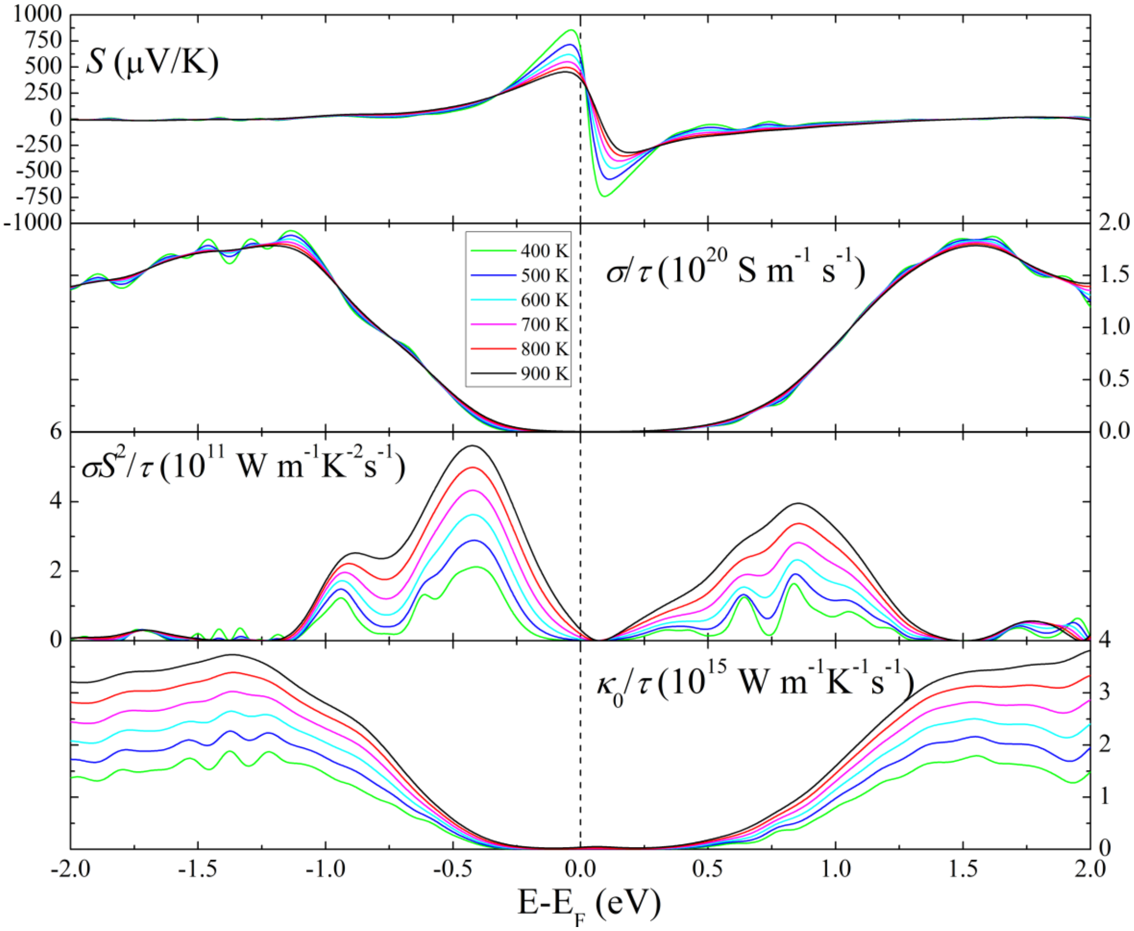

Figure A.17: Boltztrap calculation results of $ZnGe_{0.25}Sn_{0.75}P_2$ properties versus Fermi level including Seebeck coefficient and scattering independent electrical conductivity, power factor, and electronic thermal conductivity. Calculation details described in Chapter 4, Section 4.4, Electronic Structure and Properties.

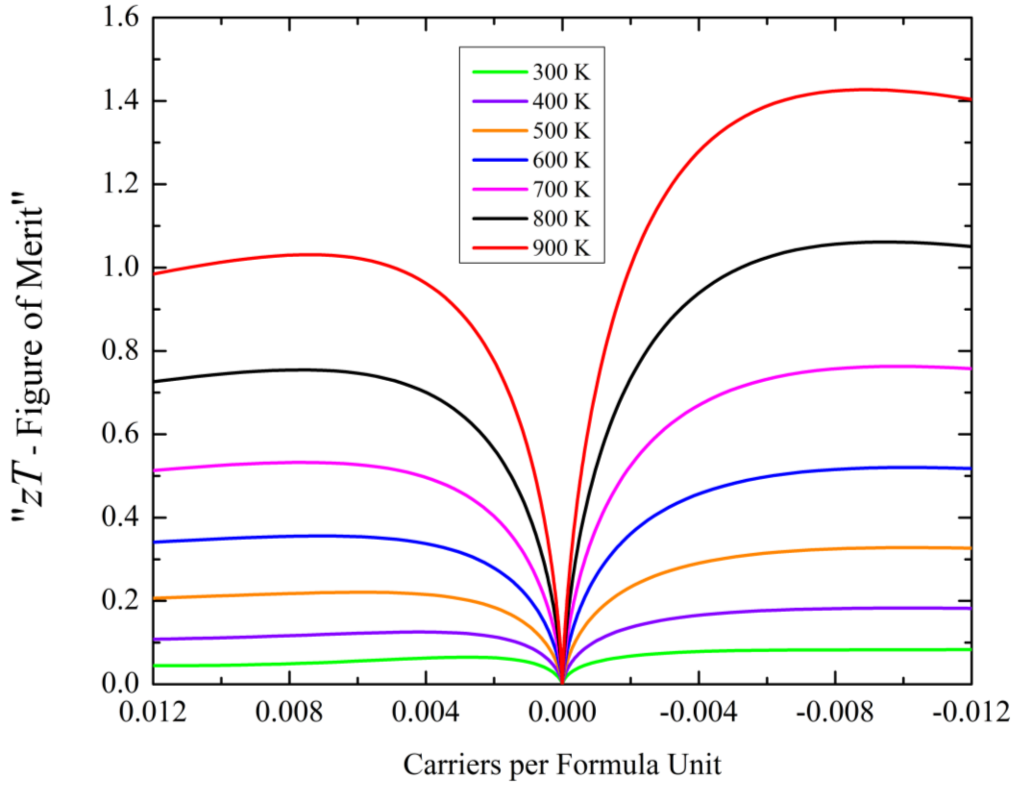

Figure A.18: Figure of merit calculated from experimental lattice TC versus carriers per formula unit for $ZnGeP_2$. Calculation details described in Chapter 4, Section 4.4, Electronic Structure and Properties.

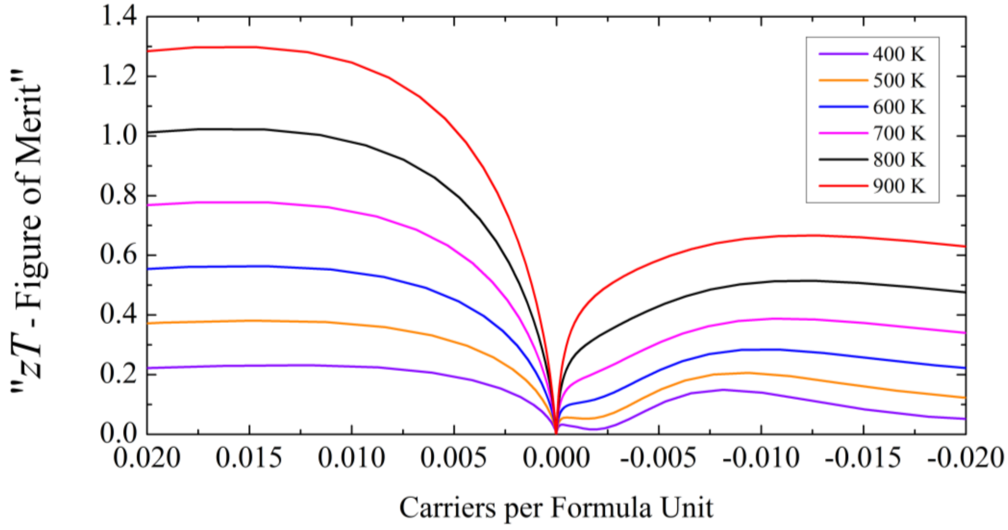

Figure A.19: Figure of merit calculated from experimental lattice TC versus carriers per formula unit for $ZnGe_{0.75}Sn_{0.25}P_2$. Calculation details described in Chapter 4, Section 4.4, Electronic Structure and Properties.

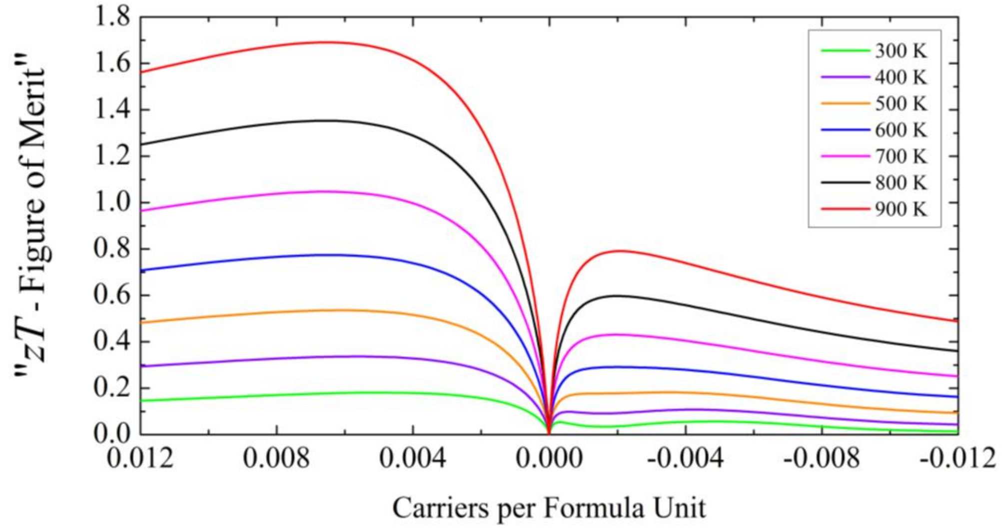

Figure A.20: Figure of merit calculated from experimental lattice TC versus carriers per formula unit for $ZnGe_{0.5}Sn_{0.5}P_2$-1. Calculation details described in Chapter 4, Section 4.4, Electronic Structure and Properties.

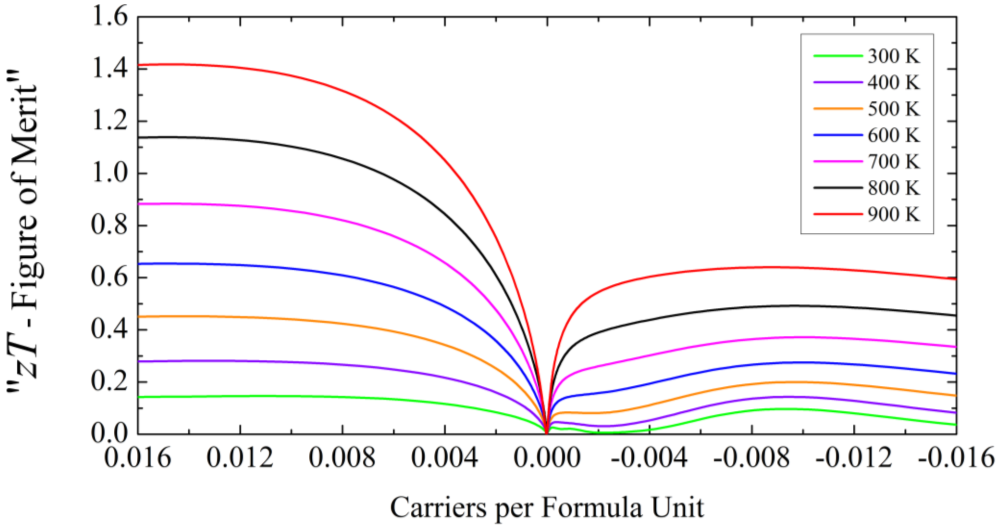

Figure A.21: Figure of merit calculated from experimental lattice TC versus carriers per formula unit for $ZnGe_{0.5}Sn_{0.5}P_2$-2. Calculation details described in Chapter 4, Section 4.4, Electronic Structure and Properties.

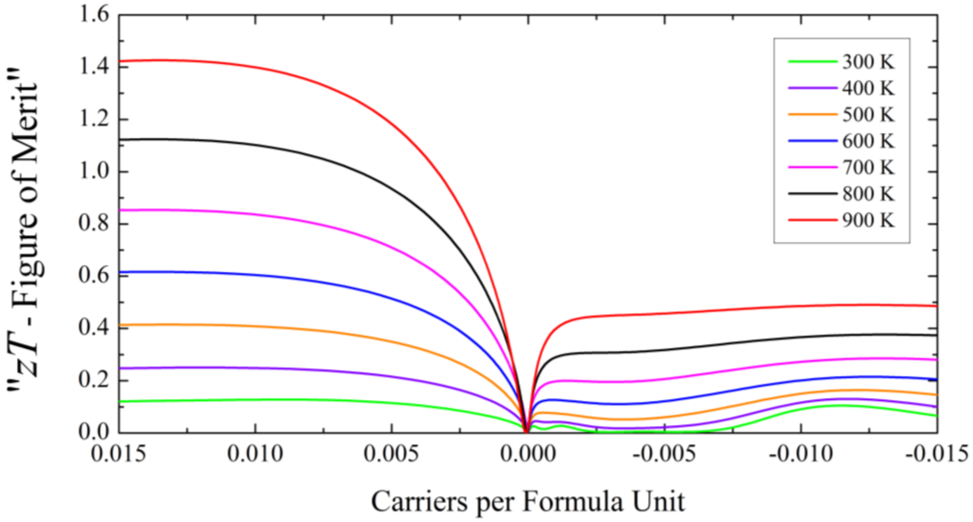

Figure A.22: Figure of merit calculated from experimental lattice TC versus carriers per formula unit for $ZnGe_{0.25}Sn_{0.75}P_2$. Calculation details described in Chapter 4, Section 4.4, Electronic Structure and Properties.

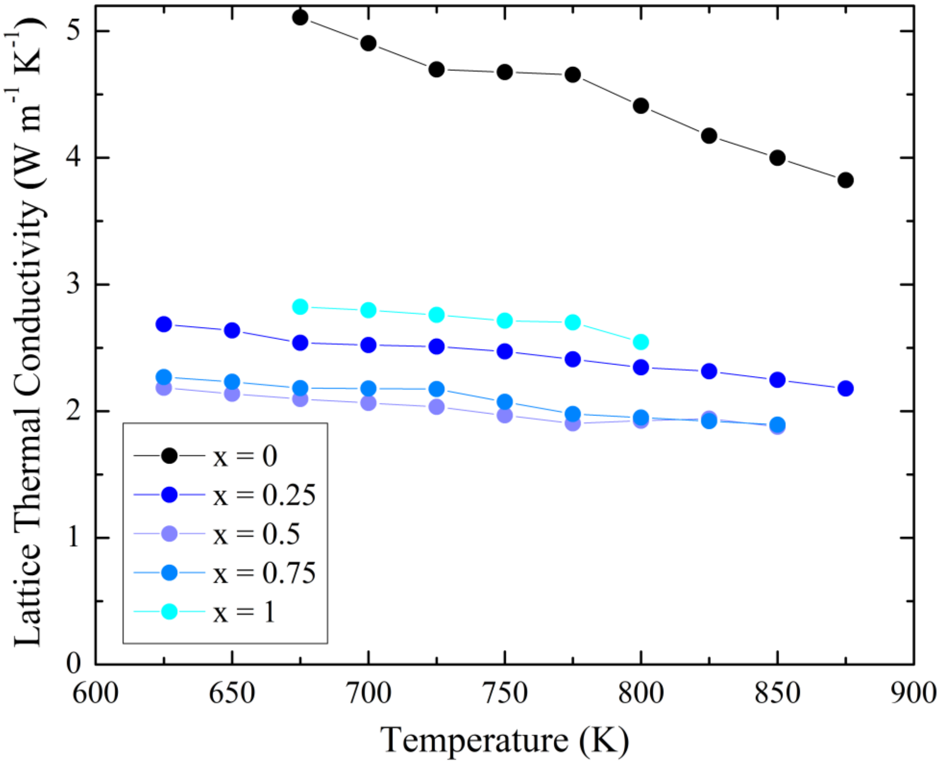

Figure A.23: Lattice thermal conductivity calculated for $ZnGe_{1-x}Sn_xP_2$ series.

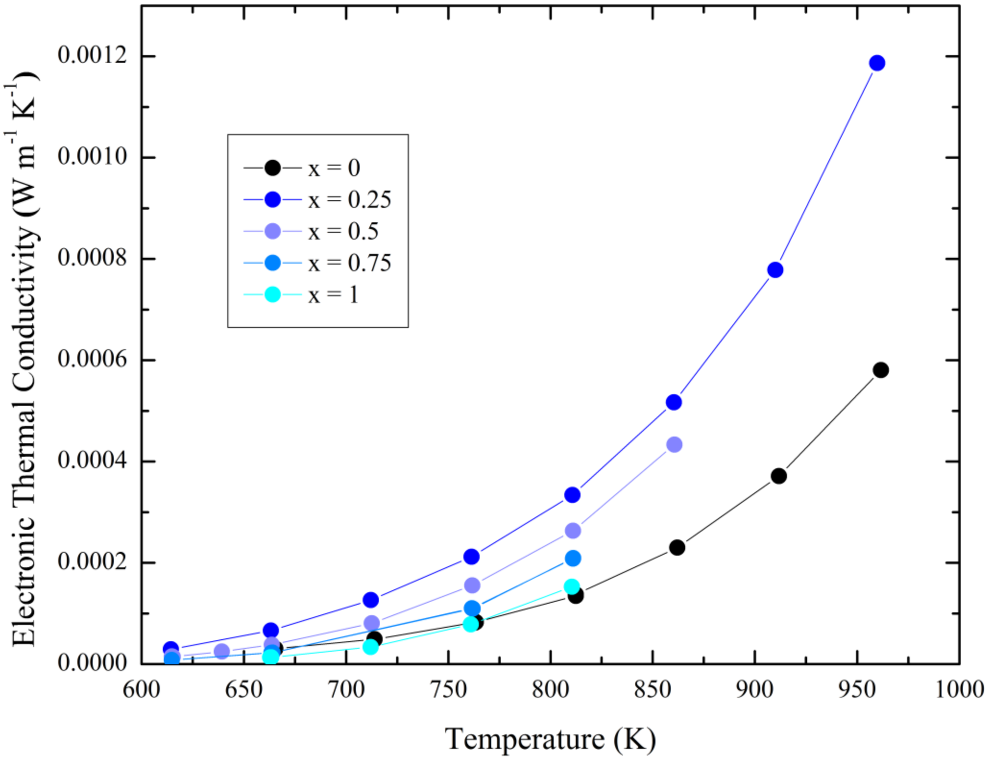

Figure A.24: Electronic thermal conductivity for $ZnGe_{1-x}Sn_xP_2$

A.4 Chapter 5 Supplemental

Table A.5: Rietveld refinement statistics from final calculations for $ZnGeSnP_{2-y}As_y$ series.

x = 1, y	R_p	R_{wp}	R_{exp}	χ^2	y_{calc}
0.5	0.053	0.075	0.009	7.57	0.533
1	0.166	0.218	0.204	1.07	0.959
1.5	0.069	0.095	0.011	8.29	1.521
2	0.095	0.144	0.033	4.34	1.845

Table A.6: Rietveld refinement statistics from final calculations for $ZnGe_{1-x}Sn_xP_{2-y}As_y$ (x = 0.5) series.

x = 0.5, y	R_p	R_{wp}	R_{exp}	χ^2	x_{calc}	y_{calc}
0.5	0.025	0.036	0.026	1.38	0.515	0.489
1	0.139	0.169	0.047	16.58	0.589	1.005
1.5	0.033	0.046	0.028	1.69	0.497	1.492
2	0.055	0.088	0.031	2.84	0.540	1.979

Table A.7: Rietveld refinement statistics from final calculations for $ZnGe_{1-x}Sn_xP_{2-y}As_y$ (x = 0.75) series.

x = 0.75, y	R_p	R_{wp}	R_{exp}	χ^2	x_{calc}	y_{calc}
0.5	0.091	0.123	0.009	13.34	0.748	0.535
1	0.064	0.089	0.009	9.82	0.738	1.017
1.5	0.097	0.149	0.009	17.09	0.729	1.487
2	0.146	0.185	0.009	20.56	0.735	1.910

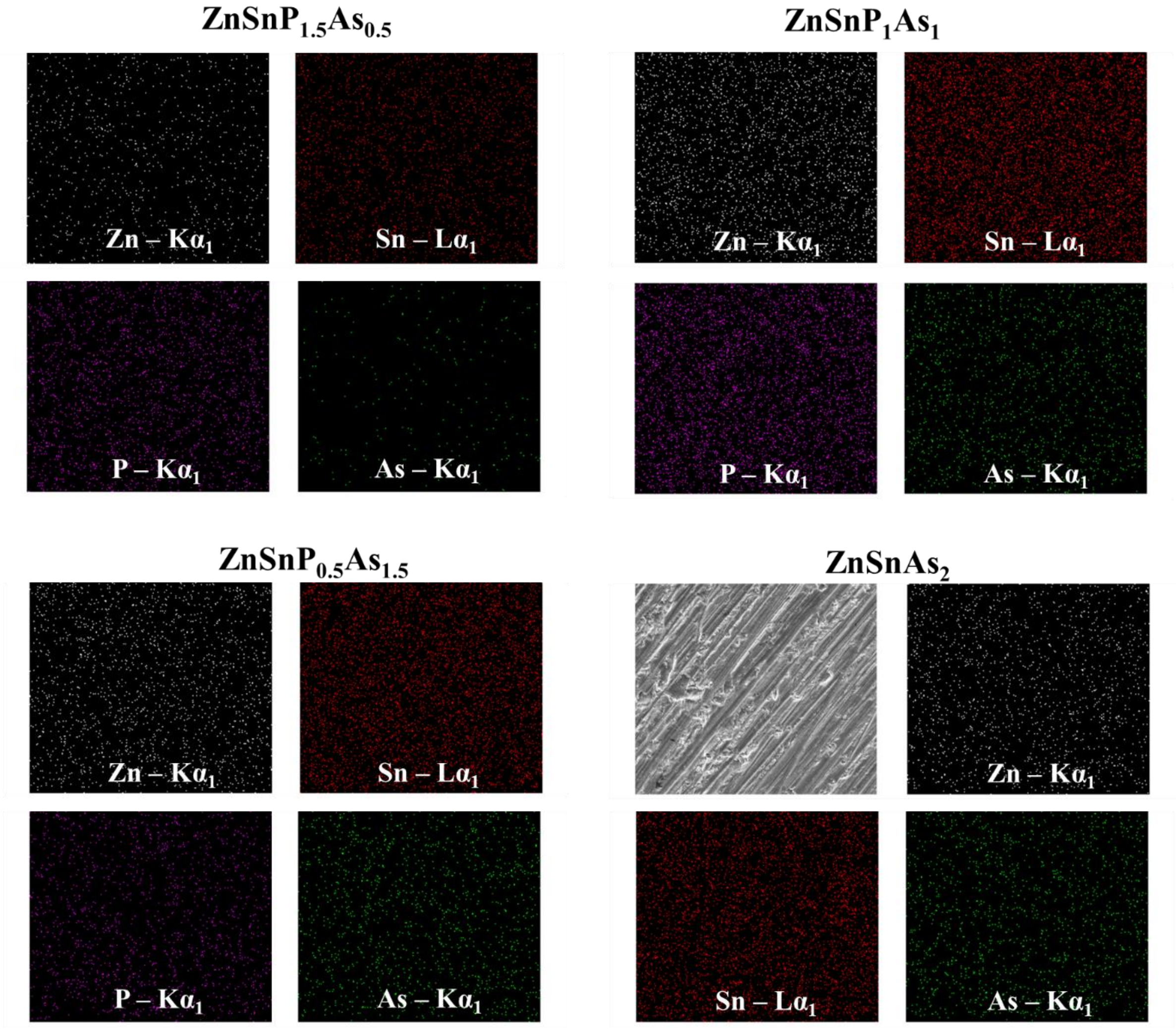

Figure A.25: EDAX mapping of ZnSnP$_{2\text{-}y}$As$_y$ series with homogeneous distribution of elements.

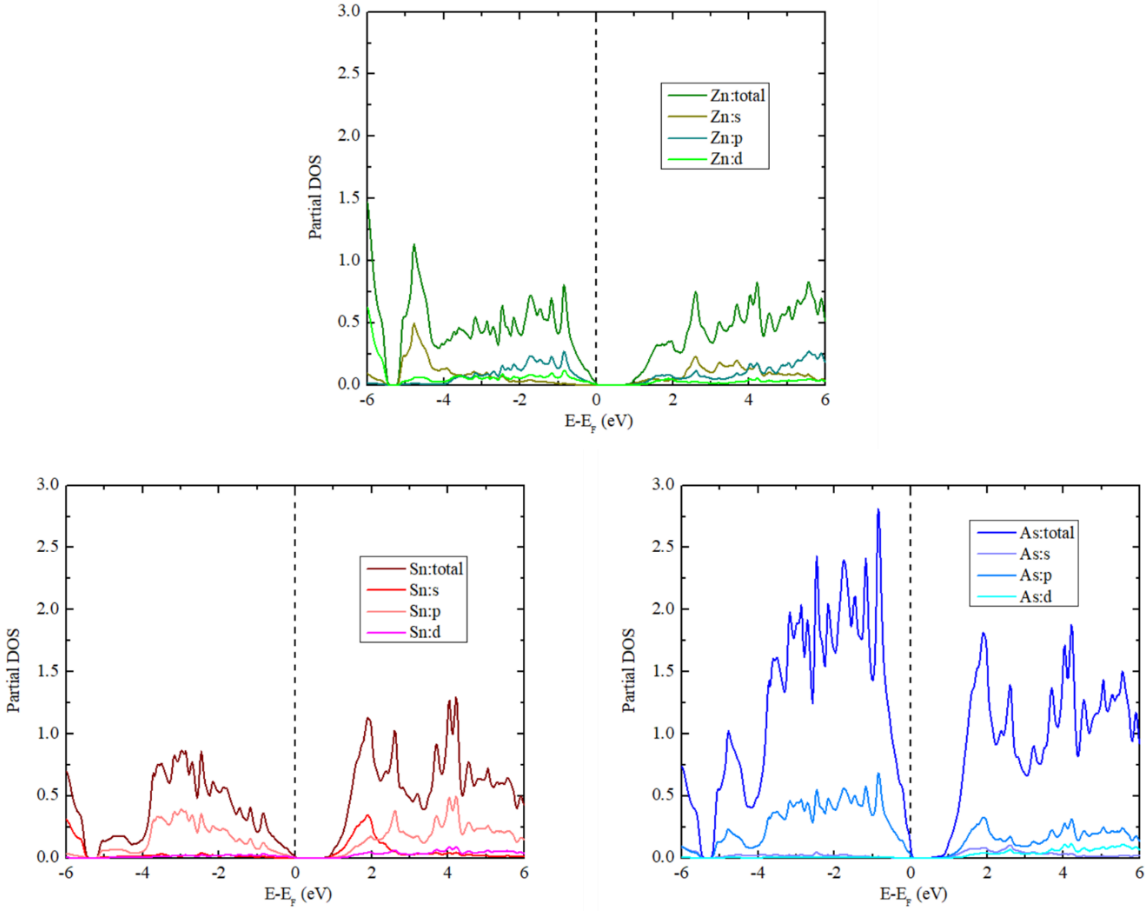

Figure A.26: PDOS calculated for $ZnSnAs_2$.

$ZnGe_{0.5}Sn_{0.5}P_{1.5}As_{0.5}$

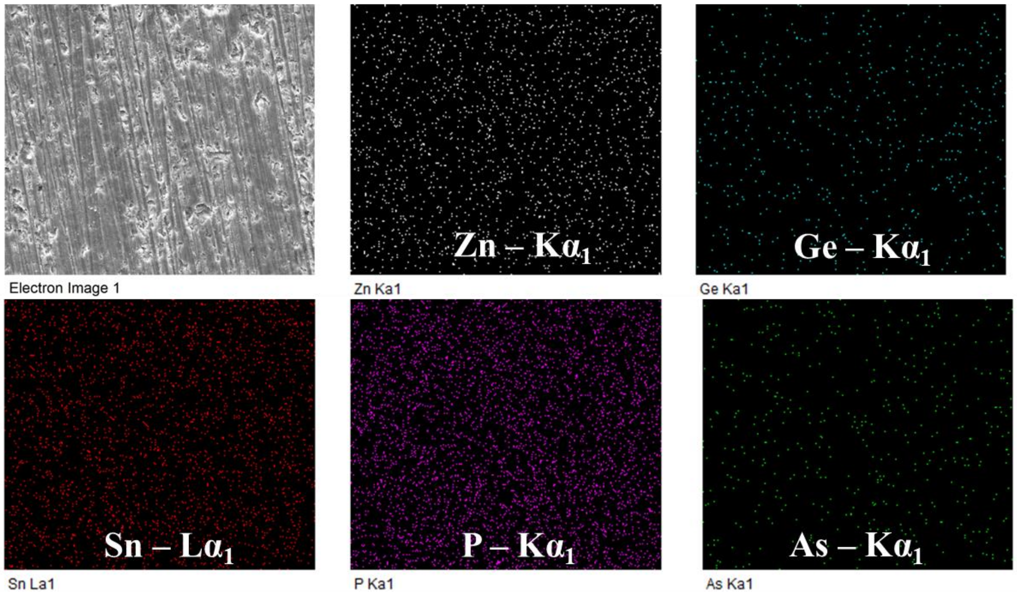

$ZnGe_{0.5}Sn_{0.5}P_1As_1$

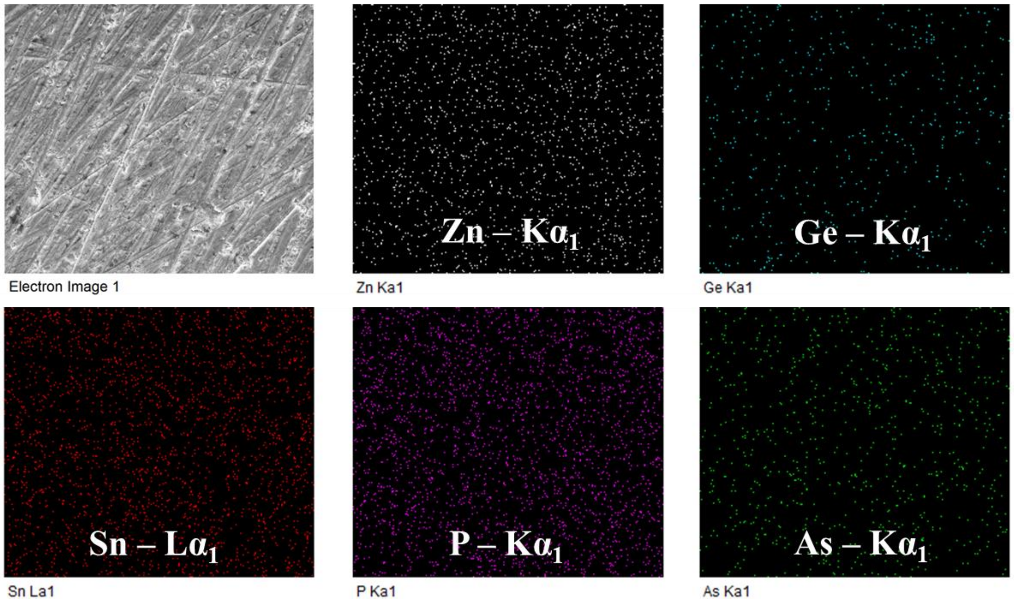

Figure A.27: EDAX mapping of $ZnGe_{1-x}Sn_xP_{2-y}As_y$ (x = 0.5) series with homogeneous distribution of elements.

$ZnGe_{0.25}Sn_{0.75}P_1As_1$

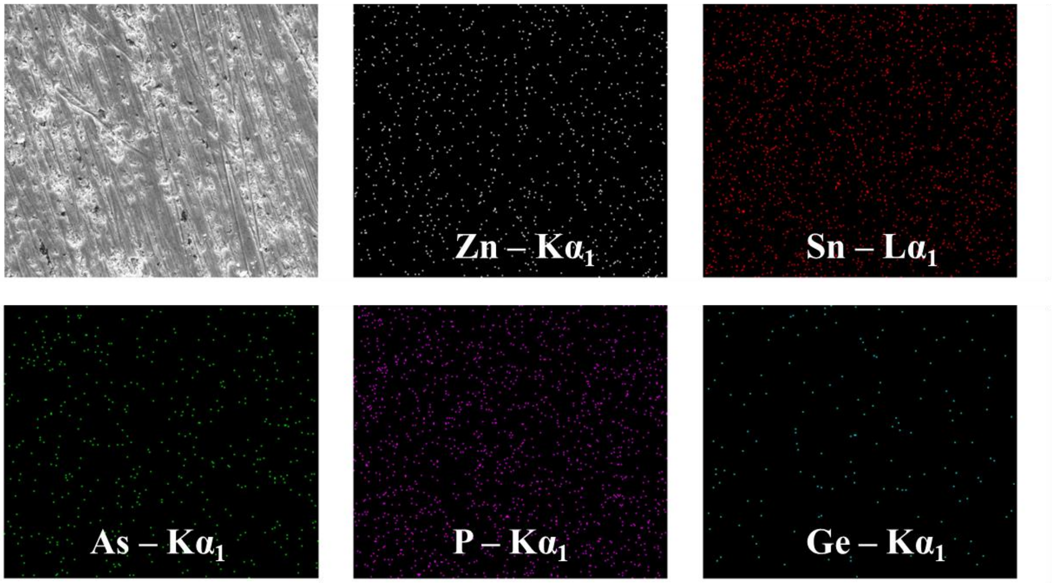

$ZnGe_{0.25}Sn_{0.75}P_{0.5}As_{1.5}$

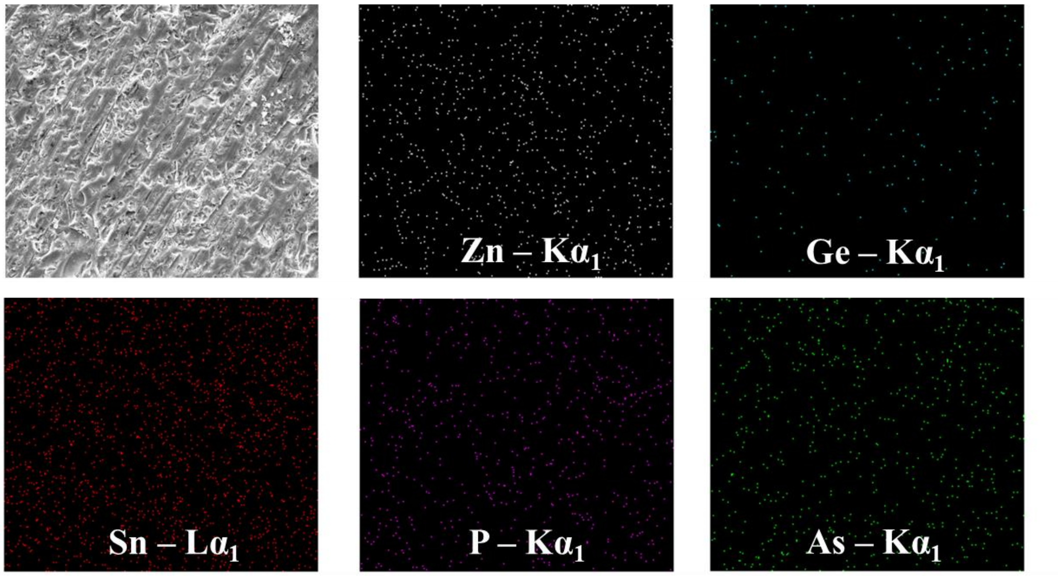

Figure A.28: EDAX mapping of $ZnGe_{1-x}Sn_xP_{2-y}As_y$ (x = 0.75) series with homogeneous distribution of elements.

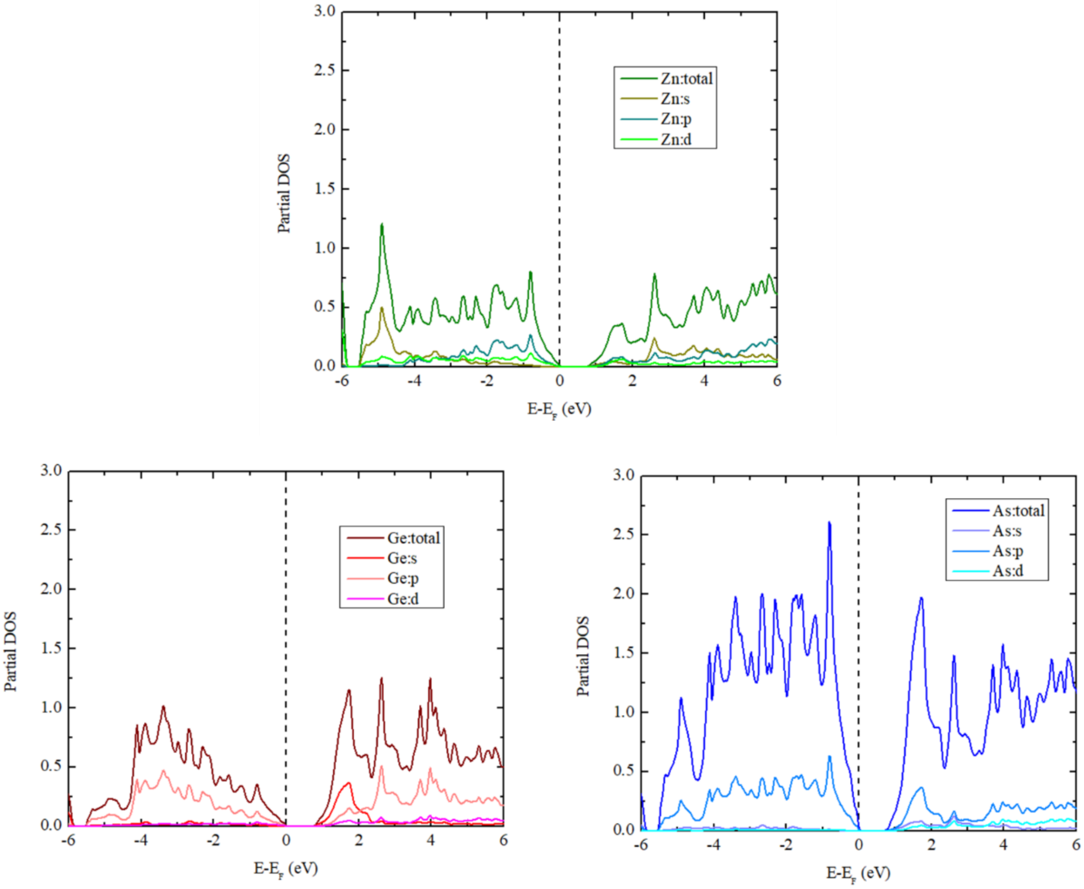

Figure A.29: PDOS calculated for ZnGeAs$_2$.

A.5 Chapter 6 Supplemental

Table A.8: Atomic positions, site occupancies, and isotropic thermal displacement parameters from $Ca_{11}Sb_{10-x}Bi_x$ (x = 0.21) SCXRD refinements.

Atom	x	y	z	Occ.	U_{eq} (10^{-3} Å^2)
Ca1	0	0.25247(10)	0.31109(7)	1	18(1)
Ca2A	0.3575(6)	0.3575(6)	0	0.551(9)	44(2)
Ca2B	0.3126(7)	0.3126(7)	0	0.449(9)	44(2)
Ca3	0.0000	0	0.16602(15)	1	18(1)
Ca4	0	0.33996(11)	0.10356(6)	1	16(1)
Sb1	0.15448(5)	0.5	0	1	16(1)
Sb2	0	0	0.36598(5)	1	13(1)
Sb3	0.12982(8)	0.12982(8)	0	0.926(8)	59(1)
Bi3	0.12982(8)	0.12982(8)	0	0.074(8)	59(1)
Sb4	0	0.5	0.25	1	10(1)
Sb5	0.20579(2)	0.20579(2)	0.17622(2)	0.984(4)	16(1)
Bi5	0.20579(2)	0.20579(2)	0.17622(2)	0.016(4)	16(1)

Table A.9: Atomic positions, site occupancies, and isotropic thermal displacement parameters from $Ca_{11}Sb_{10-x}Bi_x$ (x = 2.60) SCXRD refinements.

Atom	x	y	z	Occ.	U_{eq} (10^{-3} Å^2)
Ca1	0	0.2525(2)	0.31106(15)	1	20(1)
Ca2A	0.3548(13)	0.3548(13)	0	0.64(2)	55(4)
Ca2B	0.306(2)	0.306(2)	0	0.36(2)	55(4)
Ca3	0	0	0.1667(3)	1	19(1)
Ca4	0	0.3413(2)	0.10332(13)	1	16(1)
Sb1	0.15524(10)	0.5	0	1	14(1)
Sb2	0	0	0.36571(9)	0.901(14)	15(1)
Bi2	0	0	0.36571(9)	0.099(14)	15(1)
Sb3	0.12968(9)	0.12968(9)	0	0.483(14)	48(1)
Bi3	0.12968(9)	0.12968(9)	0	0.517(14)	48(1)
Sb4	0	0.5	0.25	0.957(14)	10(1)
Bi4	0	0.5	0.25	0.043(14)	10(1)
Sb5	0.20513(4)	0.20513(4)	0.17480(4)	0.647(10)	18(1)
Bi5	0.20513(4)	0.20513(4)	0.17480(4)	0.353(10)	18(1)

Table A.10: Atomic positions, site occupancies, and isotropic thermal displacement parameters from $Ca_{11}Sb_{10-x}Bi_x$ (x = 4.78) SCXRD refinements.

Atom	x	y	z	Occ.	U_{eq} (10^{-3} Å^2)
Ca1	0	0.2522(3)	0.81098(16)	1	22(1)
Ca2A	0.351(2)	0.351(2)	0.5	0.69(5)	64(7)
Ca2B	0.307(4)	0.307(4)	0.5	0.31(5)	64(7)
Ca3	0	0	0.6656(3)	1	24(2)
Ca4	0	0.3425(3)	0.60288(14)	1	19(1)
Sb1	0.15527(11)	0.5	0.5	0.934(17)	17(1)
Bi1	0.15527(11)	0.5	0.5	0.066(17)	17(1)
Sb2	0	0	0.86659(8)	0.63(2)	18(1)
Bi2	0	0	0.86659(8)	0.37(2)	18(1)
Sb3	0.13004(9)	0.13004(9)	0.5	0.40(2)	43(1)
Bi3	0.13004(9)	0.13004(9)	0.5	0.60(2)	43(1)
Sb4	0	0.5	0.75	0.83(2)	14(1)
Bi4	0	0.5	0.75	0.17(2)	14(1)
Sb5	0.20466(4)	0.20466(4)	0.67343(3)	0.27(2)	21(1)
Bi5	0.20466(4)	0.20466(4)	0.67343(3)	0.73(2)	21(1)

Table A.11: Atomic positions, site occupancies, and isotropic thermal displacement parameters from $Ca_{11}Sb_{10-x}Bi_x$ (x = 5.57) SCXRD refinements.

Atom	x	y	z	Occ.	U_{eq} (10^{-3} Å^2)
Ca1	0	0.2524(2)	0.31076(14)	1	21(1)
Ca2A	0.351(2)	0.351(2)	0	0.65(5)	56(5)
Ca2B	0.313(3)	0.313(3)	0	0.35(5)	56(5)
Ca3	0	0	0.1651(3)	1	22(1)
Ca4	0	0.3424(2)	0.10284(12)	1	17(1)
Sb1	0.15512(8)	0.5	0	0.888(16)	15(1)
Bi1	0.15512(8)	0.5	0	0.112(16)	15(1)
Sb2	0	0	0.36712(6)	0.48(2)	16(1)
Bi2	0	0	0.36712(6)	0.52(2)	16(1)
Sb3	0.13063(7)	0.13063(7)	0	0.35(2)	40(1)
Bi3	0.13063(7)	0.13063(7)	0	0.65(2)	40(1)
Sb4	0	0.5	0.25	0.776(18)	12(1)
Bi4	0	0.5	0.25	0.224(18)	12(1)
Sb5	0.20450(3)	0.20450(3)	0.17316(3)	0.17(2)	19(1)
Bi5	0.20450(3)	0.20450(3)	0.17316(3)	0.83(2)	19(1)

Table A.12: Crystallographic data and details from structure refinement of single crystals obtained from $Ca_{11}Sb_8Bi_2$ stochiometric reactions.

Empirical formula	$Ca_{11}Sb_{9.79}Bi_{0.21}$
Formula weight	1676.82
Temperature	296(2) K
Wavelength	0.71073 Å
Crystal system	Tetragonal
Space group	*I*4/*mmm*
Unit cell dimensions	$a = b$ =12.0320(9) Å, c = 17.3586(13) Å
Volume	2513.0(4) $Å^3$
Z	4
Density (calculated)	4.432 g/cm^3
Absorption coefficient	14.047 mm^{-1}
F(000)	2947
Crystal size	0.108 x 0.065 x 0.010 mm^3
Theta range for data collection	2.347 to 29.991°.
Index ranges	-16<=h<=16, -16<=k<=16, -24<=l<=24
Reflections collected	15596
Independent reflections	1087 [R(int) = 0.0263]
Completeness to theta = 25.242°	99.9 %
Absorption correction	Semi-empirical from equivalents
Max. and min. transmission	0.7460 and 0.5134
Refinement method	Full-matrix least-squares on F^2
Data / restraints / parameters	1087 / 6 / 44
Goodness-of-fit on F^2	1.064
Final R indices [I>2sigma(I)]	R1 = 0.0253, wR2 = 0.0526
R indices (all data)	R1 = 0.0270, wR2 = 0.0535
Extinction coefficient	0.00027(2)
Largest diff. peak and hole	4.978 and -3.718 e.$Å^{-3}$

Table A.13: Crystallographic data and details from structure refinement of single crystals obtained from $Ca_{11}Sb_6Bi_4$ stochiometric reactions.

Empirical formula	$Ca_{11}Sb_{7.4}Bi_{2.6}$
Formula weight	1884.74
Temperature	296(2) K
Wavelength	0.71073 Å
Crystal system	Tetragonal
Space group	*I*4/*mmm*
Unit cell dimensions	$a = b$ = 12.101(10) Å, c = 17.565(14) Å
Volume	2572(5) Å^3
Z	4
Density (calculated)	4.867 g/cm^3
Absorption coefficient	27.504 mm^{-1}
F(000)	3252
Crystal size	0.080 x 0.030 x 0.010 mm^3
Theta range for data collection	2.319 to 30.000°.
Index ranges	-17<=h<=12, -16<=k<=14, -24<=l<=24
Reflections collected	12122
Independent reflections	1104 [R(int) = 0.0420]
Completeness to theta = 25.242°	99.9 %
Absorption correction	Semi-empirical from equivalents
Max. and min. transmission	0.7460 and 0.4699
Refinement method	Full-matrix least-squares on F^2
Data / restraints / parameters	1104 / 6 / 46
Goodness-of-fit on F^2	2.956
Final R indices [I>2σ(I)]	R1 = 0.0459, wR2 = 0.0786
R indices (all data)	R1 = 0.0536, wR2 = 0.0794
Extinction coefficient	n/a
Largest diff. peak and hole	12.946 and -8.778 e.Å^{-3}

Table A.14: Crystallographic data and details from structure refinement of single crystals obtained from $Ca_{11}Sb_5Bi_5$ stochiometric reactions.

Empirical formula	$Ca_{11}Sb_{5.22}Bi_{4.78}$
Formula weight	2075.00
Temperature	296(2) K
Wavelength	0.71073 Å
Crystal system	Tetragonal
Space group	*I*4/*mmm*
Unit cell dimensions	$a = b = 12.16(2)$ Å, $c = 17.44(3)$ Å
Volume	2577(11) $Å^3$
Z	4
Density (calculated)	5.348 g/cm^3
Absorption coefficient	40.036 mm^{-1}
F(000)	3531
Crystal size	0.040 x 0.040 x 0.020 mm^3
Theta range for data collection	2.336 to 30.000°.
Index ranges	-15<=h<=17, -9<=k<=17, -24<=l<=23
Reflections collected	7215
Independent reflections	1115 [R(int) = 0.0559]
Completeness to theta = 25.242°	99.7 %
Absorption correction	Semi-empirical from equivalents
Max. and min. transmission	0.7460 and 0.5908
Refinement method	Full-matrix least-squares on F^2
Data / restraints / parameters	1115 / 6 / 46
Goodness-of-fit on F^2	1.131
Final R indices [I>2sigma(I)]	R1 = 0.0415, wR2 = 0.0800
R indices (all data)	R1 = 0.0566, wR2 = 0.0862
Extinction coefficient	n/a
Largest diff. peak and hole	9.078 and -6.255 e.$Å^{-3}$

Table A.15: Crystallographic data and details from structure refinement of single crystals obtained from $Ca_{11}Sb_4Bi_6$ stochiometric reactions.

Empirical formula	$Ca_{11}Sb_{4.43}Bi_{5.57}$
Formula weight	2144.39
Temperature	296(2) K
Wavelength	0.71073 Å
Crystal system	Tetragonal
Space group	*I*4/*mmm*
Unit cell dimensions	*a* = *b* = 12.196(8) Å, *c* = 17.607(10) Å
Volume	2619(4) $Å^3$
Z	4
Density (calculated)	5.438 g/cm^3
Absorption coefficient	43.914 mm^{-1}
F(000)	3633
Crystal size	0.080 x 0.040 x 0.020 mm^3
Theta range for data collection	2.313 to 29.882°.
Index ranges	-14<=h<=13, -4<=k<=17, -8<=l<=24
Reflections collected	5958
Independent reflections	1120 [R(int) = 0.0248]
Completeness to theta = 25.242°	99.9 %
Absorption correction	Semi-empirical from equivalents
Max. and min. transmission	0.7460 and 0.5123
Refinement method	Full-matrix least-squares on F^2
Data / restraints / parameters	1120 / 6 / 46
Goodness-of-fit on F^2	1.062
Final R indices [I>2sigma(I)]	R1 = 0.0333, wR2 = 0.0810
R indices (all data)	R1 = 0.0390, wR2 = 0.0839
Extinction coefficient	n/a
Largest diff. peak and hole	11.528 and -4.969 e.$Å^{-3}$

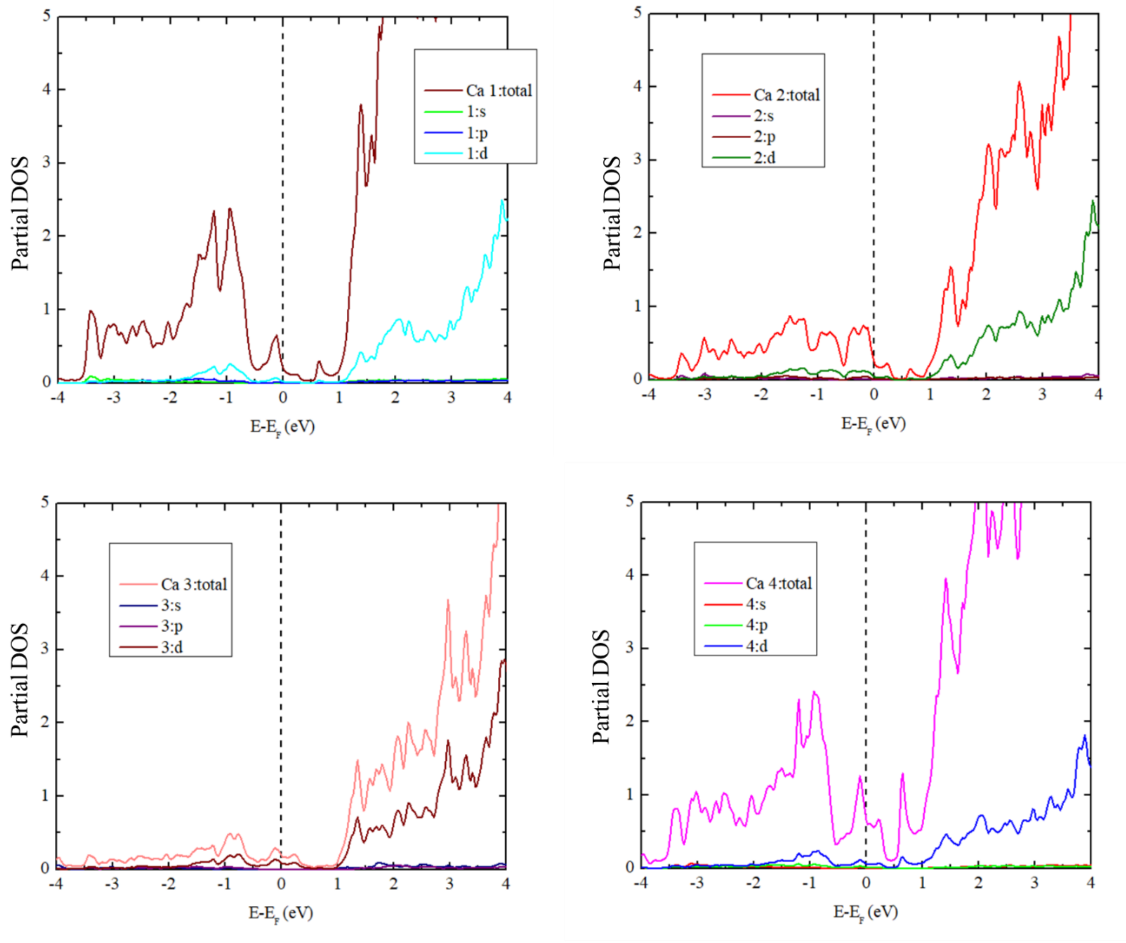

Figure A.30: Partial Density of States for Ca atom sites including *s*, *p*, and *d* states for $Ca_{11}Sb_{10}$.

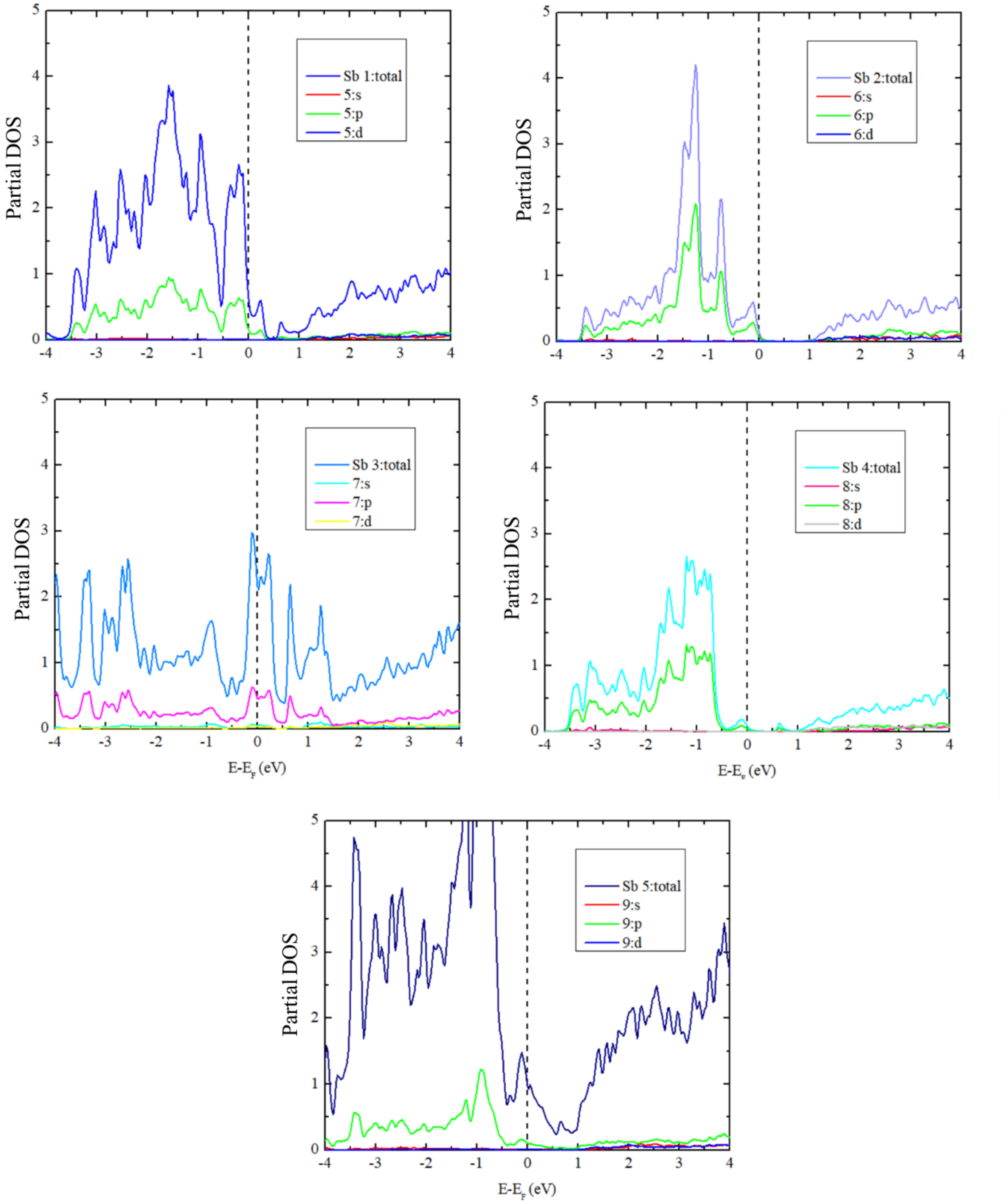

Figure A.31: Partial Density of States for Sb atom sites including *s*, *p*, and *d* states for $Ca_{11}Sb_{10}$.

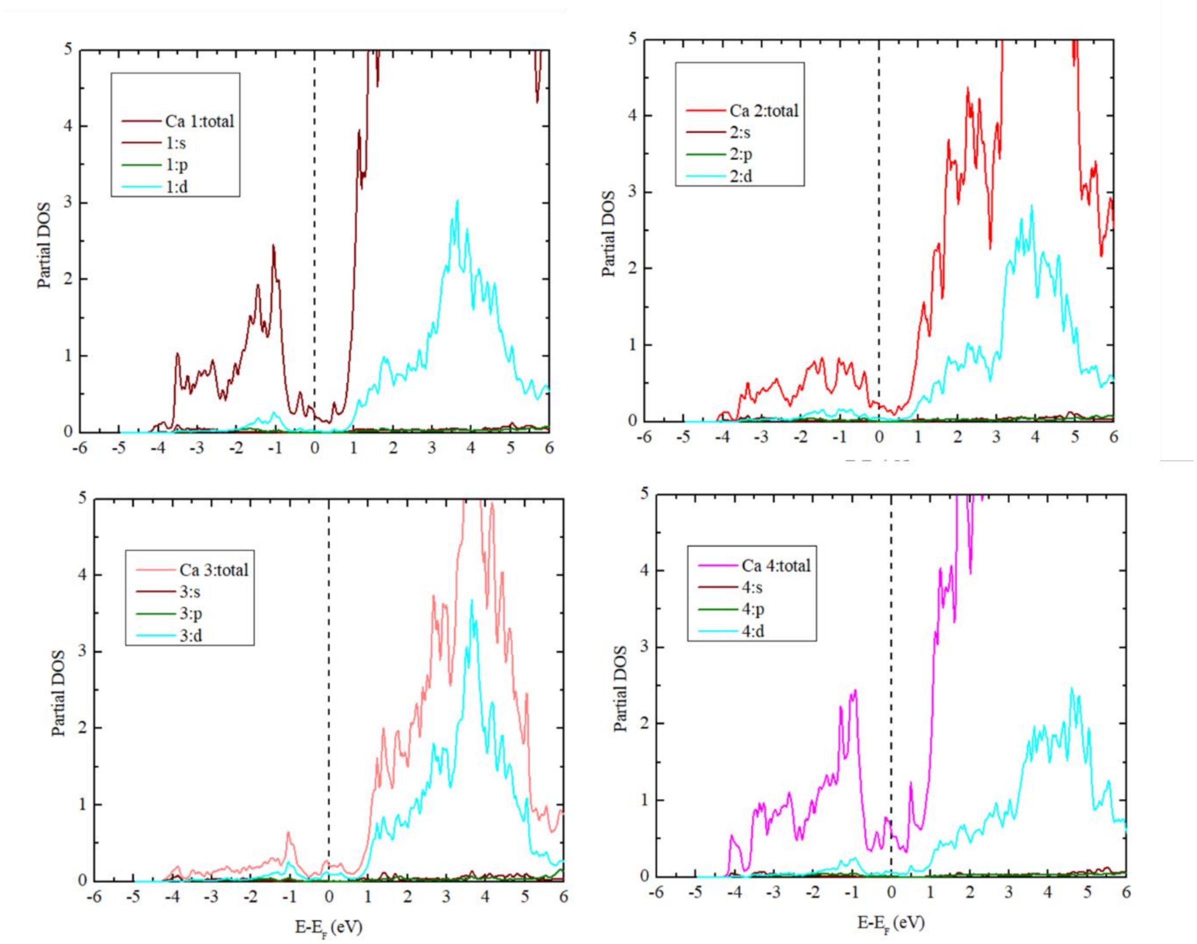

Figure A.32: Partial Density of States for Ca atom sites including *s*, *p*, and *d* states for $Ca_{11}Bi_{10}$.

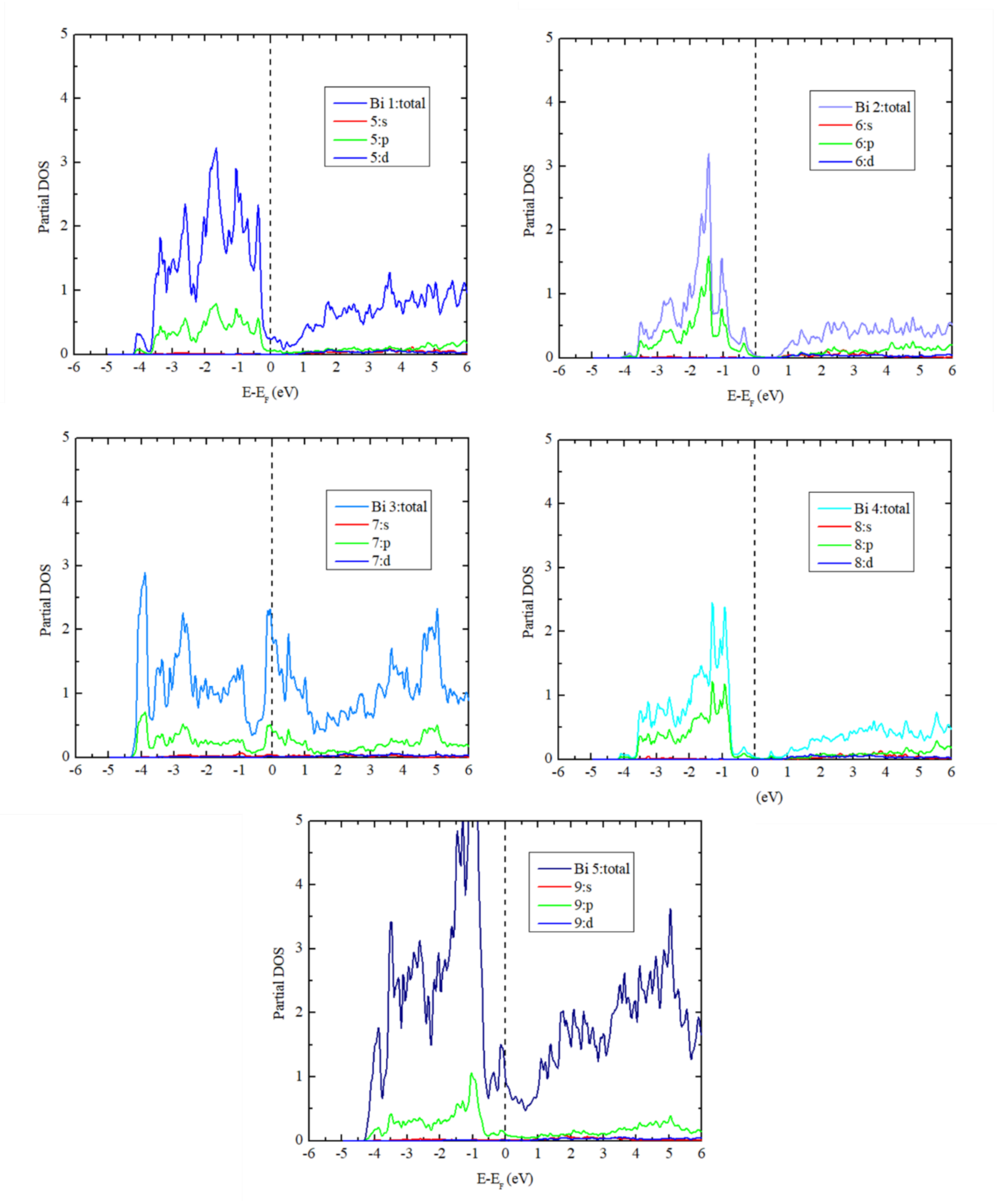

Figure A.33: Partial Density of States for Bi atom sites including *s*, *p*, and *d* states for $Ca_{11}Bi_{10}$.

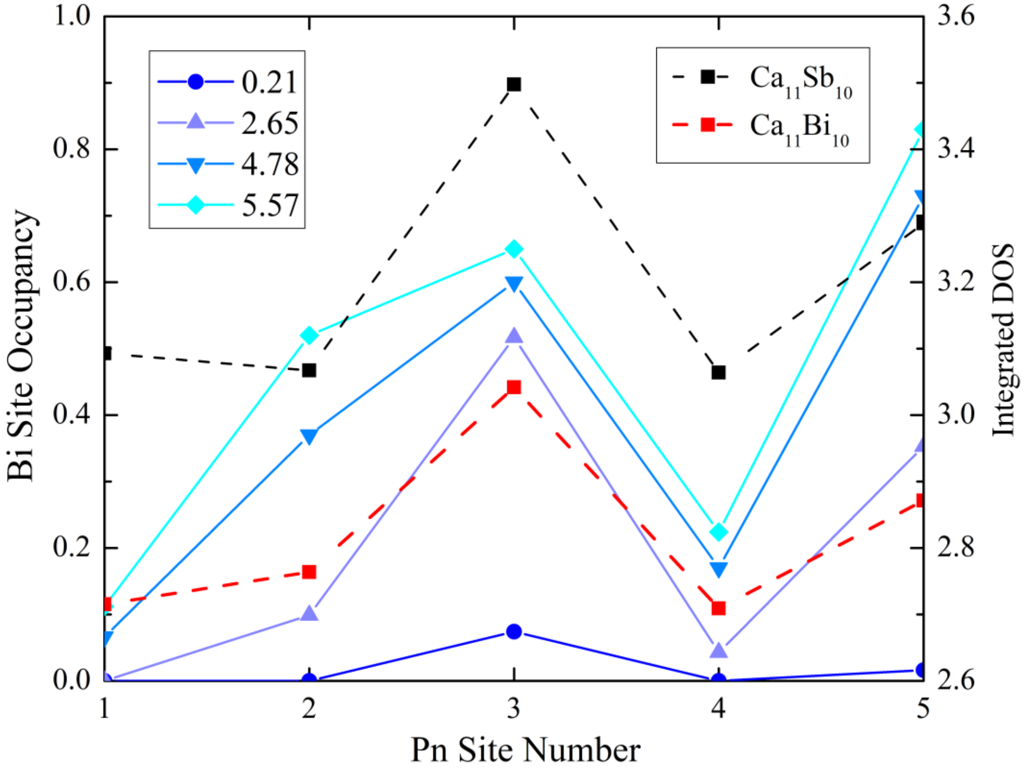

Figure A.34: Considering the orbital occupations of the Pn sites using integrated density of states vs SCXRD Pn site occupation.